Auroral and Ionospheric Flow Measurements of Magnetopause Reconnection During Intervals of Northward Interplanetary Magnetic Field

Thesis submitted for the degree of
Doctor of Philosophy
at the University of Leicester

by

Suzanne M. Imber

Radio and Space Plasma Physics Group
University of Leicester

August 2008

Abstract

Auroral and Ionospheric Flow Measurements of Magnetopause Reconnection
During Intervals of Northwards Interplanetary Magnetic Field

Suzanne M. Imber

This thesis investigates the coupling between the solar wind and the magnetosphere during intervals of northward interplanetary magnetic field (IMF). The first section uses Super Dual Auroral Radar Network (SuperDARN) data to estimate the high latitude single lobe reconnection rate and relates this to upstream solar wind conditions measured by the Advanced Composition Explorer (ACE) spacecraft. The reconnection rate was found to depend on the IMF direction and magnitude, as well as the solar wind electric field and the length of the merging gap. The second study combines a modified version of the Lockwood ion dispersion model with the Cooling model to characterise the expected ion dispersion signature observed by low or mid altitude spacecraft during intervals of northward IMF. The dependence of the modelled signature on upstream conditions was analysed and found to be in agreement with a small statistical study undertaken using dispersion signature observed by Cluster. A very clear dispersion signature observed by FAST was compared with the predicted modelled signature and found to be in good agreement. The final study presents the theoretical and first observational evidence of dual lobe reconnection at Earth. The threshold clock angle for dual lobe reconnection is calculated for two case studies, as well as the amount of magnetic flux closed. An estimate of the number of particles captured demonstrated that dual lobe reconnection could be the plasma capture mechanism for the cold, dense plasma sheet, although this is thought to require a prolonged period of northward IMF. This study increases our understanding of solar wind-magnetosphere coupling during northward IMF; it also raises further interesting questions and suggests avenues for further work which are discussed at the end of the thesis.

Declaration

I, Suzanne M. Imber, confirm that the work presented in this thesis is my own. Information derived from other sources has been suitably referenced. The following scientific papers have been published based on work included in this thesis:

Imber, S. M., Milan, S. E., and Hubert, B., The auroral and ionospheric flow signatures of dual lobe reconnection, *Ann. Geophys.*, *24*, 3115-3129, 2006.

Imber, S. M., Milan, S. E., and Hubert, B., Observations of significant flux closure by dual lobe reconnection, *Ann. Geophys.*, *25*, 1617-1627, 2007.

Acknowledgements

I would first and foremost like to thank Steve Milan for honestly being the best supervisor I could have asked for and never once closing his door or being too busy. I am so grateful for his friendship and good humour as well as all of his help and advice over the last three years.

The Leicester Radio and Space Plasma Physics group is full of friendly and helpful people however I would like to thank a few of those in particular. Firstly I am grateful to my second supervisor Mark Lester for his help and advice. My officemates Lisa Baddeley, Caitriona Jackman and Steph Kellett have had a lot to put up with over the last three years, and without their help and chocolate supplies this thesis would have taken considerably longer to write! I would like to thank Sarah Badman, for sharing so many laughs, rambles and ergos, and baking so many awesome cakes! I would also like to thank Ade Grocott, Colin Forsyth, Darren Wright and Rob Fear for being such good friends, knowing so much more than I do and always being there to help.

I would also like to thank my oldest friends Louisa Kent and Kim Jelfs for always being there. Dani Fuller, for climbing such incredible mountains with me (bring on the seven summits!), most importantly always getting me safely back down again, and always planning the next big adventure. Finally my cycling buddies, Dani, Peter Russell-Wilks and Steve Porteous for training rides, tractor chasing, and finally beasting John O'Groats to Lands End.

Many other friends have also contributed to this thesis in different ways, in particular Gavin, for red wine and good films, Ferg and all of Team Alpha for always Getting Awesome, as well as fantastic Tanya, Kate and Kat and my wonderful housemates Dave, Si, Steve and Bertie for all the good times at Imperial.

Finally I would like to thank my parents, Cathy and Ian, and my brother, James, for unfailing support and encouragement; without them this thesis would not have been written.

Table of Contents

Chapter 1. Introduction

This thesis is concerned with dayside reconnection processes during northward interplanetary magnetic field (IMF). The purpose of this introductory chapter is to introduce both the fundamental plasma physics and the relevant magnetospheric structures in the solar terrestrial system.

1.1 Plasma Physics

1.1.1 Maxwell's equations

Maxwell's equations (Maxwell, 1891) define the evolution of electric fields (**E**) and magnetic fields (**B**) with time, t:

$$\nabla \cdot \mathbf{B} = 0 \qquad \text{Gauss' Law for magnetism} \quad [1.1]$$

$$\nabla \cdot \mathbf{E} = \frac{\rho_q}{\varepsilon_0} \qquad \text{Gauss' Law} \qquad [1.2]$$

$$\nabla \times \mathbf{E} = -\frac{\partial \mathbf{B}}{\partial t} \qquad \text{Faraday's Law} \qquad [1.3]$$

$$\nabla \times \mathbf{B} = \mu_0 \varepsilon_0 \frac{\partial \mathbf{E}}{\partial t} + \mu_0 \mathbf{J} \quad \text{Ampere's Law} \qquad [1.4]$$

where μ_0 is the permeability of free space, ε_0 is the permittivity of free space, ρ_q is the charge density and **J** is the current density.

1.1.2 Particle gyration and $E \times B$ drift

The motion of a particle with charge q in an electromagnetic field is given by:

$$m\frac{d\mathbf{v}}{dt} = q(\mathbf{E} + \mathbf{v} \times \mathbf{B}) \qquad [1.5]$$

where m is the mass and **v** is the velocity of the particle. The first term on the right hand side is the Coulomb force due to the electric field, and the second term is the Lorentz force acting on the particle due to the magnetic field.

In the absence of an electric field, particles in a magnetic field obey a reduced form of [1.5]:

$$m\frac{d\mathbf{v}}{dt} = q(\mathbf{v} \times \mathbf{B}) \qquad [1.6]$$

This can be manipulated (taking the dot product with $\mathbf{v}$ and using $\mathbf{v}.(\mathbf{v} \times \mathbf{B}) = 0$) to show that the kinetic energy of a particle in a magnetic field does not change, i.e. v is constant:

$$m\frac{d\mathbf{v}}{dt} \cdot \mathbf{v} = \frac{d}{dt}\left(\frac{m\mathbf{v}^2}{2}\right) = 0 \qquad [1.7]$$

Assuming a Cartesian coordinate system, such that the velocity $\mathbf{v}$ has components v_x, v_y, v_z, and assuming that $\mathbf{B}$ is directed along $\hat{\mathbf{z}}$, [1.6] yields:

$$m\frac{dv_x}{dt} = qBv_y$$
$$m\frac{dv_y}{dt} = -qBv_x \qquad [1.8]$$
$$m\frac{dv_z}{dt} = 0$$

Further, these equations combine to yield:

$$\frac{d^2v_x}{dt^2} = -\omega_g^2 v_x$$
$$\frac{d^2v_y}{dt^2} = -\omega_g^2 v_y \qquad [1.9]$$
$$\omega_g = \frac{qB}{m}$$

Particles therefore gyrate around a field line, with gyrofrequency given by ω_g and gyroradius given by:

$$r_g = \frac{mv_\perp}{|q|B} \qquad [1.10]$$

where $\qquad v_\perp = \left(v_x^2 + v_y^2\right)^{1/2}$

(Baumjohann and Treumann, 1997) while also drifting along a field line.

Imposing an electric field, $\mathbf{E}$, and taking the cross product of [1.5] with $\mathbf{B}$ yields:

$$m\frac{d\mathbf{v}}{dt} \times \mathbf{B} = q(\mathbf{E} \times \mathbf{B} + \mathbf{v} \times \mathbf{B} \times \mathbf{B}) \qquad [1.11]$$

Now using the vector identity $\mathbf{v} \times \mathbf{B} \times \mathbf{B} = (\mathbf{v}.\mathbf{B})\mathbf{B} - \mathbf{v}B^2$ the motion of the particle perpendicular to the field can be written as:

$$\mathbf{v}_\perp = \frac{\mathbf{E} \times \mathbf{B}}{B^2} - \frac{m}{qB^2} \frac{d\mathbf{v}}{dt} \times \mathbf{B} \qquad [1.12]$$

The second term on the right hand side is the particle gyration around the field line and the first term is a drift velocity (Baumjohann and Treumann, 1997). This $\mathbf{E} \times \mathbf{B}$ drift is independent of charge, mass or energy and therefore all particles move together and there is no net current. It is due to acceleration of particles as they move parallel to the electric field, and deceleration as they move antiparallel to it which increases and decreases the gyroradius of the particles and results in an overall drift perpendicular to both the electric and magnetic field directions.

1.1.3 Gradient and Curvature drift

The general expression for the drift velocity generated by any force, **F**, acting on a particle in a magnetic field is given by:

$$\mathbf{v}_d = \frac{\mathbf{F} \times \mathbf{B}}{qB^2} \qquad [1.13]$$

A particle on a curved field line will experience a centrifugal force perpendicular to the direction of the field line, which generates a drift motion given by:

$$\mathbf{v}_d = \frac{v_\parallel^2}{\omega_g B} \frac{\mathbf{R}_c \times \mathbf{B}}{R_c^2} \qquad [1.14]$$

where m is the mass of the particle, $v_\parallel$ is the velocity of the particle parallel to the direction of the field, and R_c is the radius of curvature of the field line. ω_g is the gyrofrequency of the particle around the field line, given by [1.9] (Dendy et al., 1993). This plasma drift leads to a net current in a plasma as the gyrofrequency depends upon the charge of the particle.

A gradient in the magnetic field strength perpendicular to the direction of the field will also generate a particle drift, known as grad-B drift. The expression for the grad-B drift is:

$$\mathbf{v}_d = \frac{mv_\perp^2}{2qB^3} (\mathbf{B} \times \nabla B) \qquad [1.15]$$

The direction of this drift is perpendicular to the magnetic field and the gradient in that field, and leads to a net current with ions and electrons drifting in opposite directions (Baumjohann and Treumann, 1997).

3

1.1.4 Magnetic mirroring

Charged particles travelling along a magnetic field line experience Coulomb and Lorentz forces which result in a helical particle trajectory (see Section 1.1.2). The velocity of the particle therefore has both field-parallel and perpendicular components, $v_{\parallel}$ and $v_{\perp}$. The pitch angle is the angle between the particle velocity and the magnetic field line, and is therefore defined as:

$$\alpha = \tan^{-1}\left(\frac{v_{\perp}}{v_{\parallel}}\right) \qquad [1.16]$$

Gauss' Law for magnetism [1.1] implies that **B** cannot diverge. The dipole nature of the Earth's magnetic field means that the magnetic field strength decreases with increasing distance from the Earth (see Section 1.3.1). In order to prevent divergence of **B**, the density of field lines is proportional to the magnetic field strength. A trapped particle travelling along a dipolar geomagnetic field line therefore experiences a gradient in the magnetic field strength parallel to the field line. The magnetic moment (or first adiabatic invariant) of this particle can be written as:

$$\mu = \frac{mv^2 \sin^2 \alpha}{2B} \qquad [1.17]$$

where α is the pitch angle of the particle, *m* and *v* are the mass and velocity of the particle and *B* is the total magnetic field (Baumjohann and Treuman, 1997). The magnetic moment of the particle is conserved as the particle moves, as is the total energy of the particle, given by $\frac{1}{2}mv^2$. As this particle approaches a region of higher magnetic field, its pitch angle must increase in order to conserve the first adiabatic invariant. The field-parallel component of the particle velocity therefore decreases as the field-perpendicular component increases, until all of the energy of the particle is in the field-perpendicular direction; this point is called the mirror point. The force on the particle due to the gradient in the field acts to reflect the particle from this point back along the field line in the opposite direction.

The motion of a trapped particle on a dipolar field line therefore consists of three components. The particle gyrates around the field line due to the Lorentz force, while also bouncing between hemispheres due to the gradient in the magnetic field parallel to the field lines. In addition the trapped particle drifts azimuthally

around the Earth due to curvature and gradient drifting (see Section 1.1.3). These motions are summarised in Figure 1.1.

Particles with lower pitch angles reach lower altitudes before mirroring and may even reach a sufficiently low altitude to impact with an atmospheric neutral. The loss cone is defined as the pitch angle range within which particles are lost to the upper atmosphere in this way.

1.1.5 The MHD induction equation

Most space plasmas obey a set of equations which make up the theorem of ideal magnetohydrodynamics (MHD). The basic principles behind ideal MHD are that the plasma is studied on large scales and is non-relativistic, quasi-neutral and infinitely conducting, slowly varying on timescales of the gyrofrequency. By considering a population of particles of one species it is possible to rewrite [1.5] including the forces due to gravity and plasma pressure:

$$\rho \frac{d\mathbf{v}}{dt} = nq(\mathbf{E} + \mathbf{v} \times \mathbf{B}) - \nabla p + \rho \mathbf{g} \qquad [1.18]$$

where ρ is the mass density, n is the number density of that species, q is the charge on each particle, $\mathbf{g}$ is the gravitational acceleration and p is the plasma pressure. In ideal MHD we assume quasi-neutrality, i.e. the number density of electrons is the same as the number density of ions, or $n_e \approx n_i \approx n$. [1.18] for electrons and ions can be combined:

$$\rho \frac{d\mathbf{v}}{dt} = en_i(\mathbf{v}_i - \mathbf{v}_e) \times \mathbf{B} - \nabla(p_i + p_e) + \rho \mathbf{g} \qquad [1.19]$$

with the assumption that $m_i >> m_e$.

Defining the current density of the plasma, $\mathbf{J}$:

$$\mathbf{J} = en_i(\mathbf{v}_i - \mathbf{v}_e) \qquad [1.20]$$

and $p = p_i + p_e$, [1.19] can be simplified to:

$$\rho \frac{d\mathbf{v}}{dt} = \mathbf{J} \times \mathbf{B} - \nabla p + \rho \mathbf{g} \qquad [1.21]$$

Using the non-relativistic form of Ampere's law ($\nabla \times \mathbf{B} = \mu_0 \mathbf{J}$) it is possible to eliminate $\mathbf{J}$ from [1.21]:

$$\rho \frac{d\mathbf{v}}{dt} = \frac{(\nabla \times \mathbf{B}) \times \mathbf{B}}{\mu_0} - \nabla p + \rho \mathbf{g} \qquad [1.22]$$

N

S

Mirror point

N

S

Ions

Electrons

Ring current
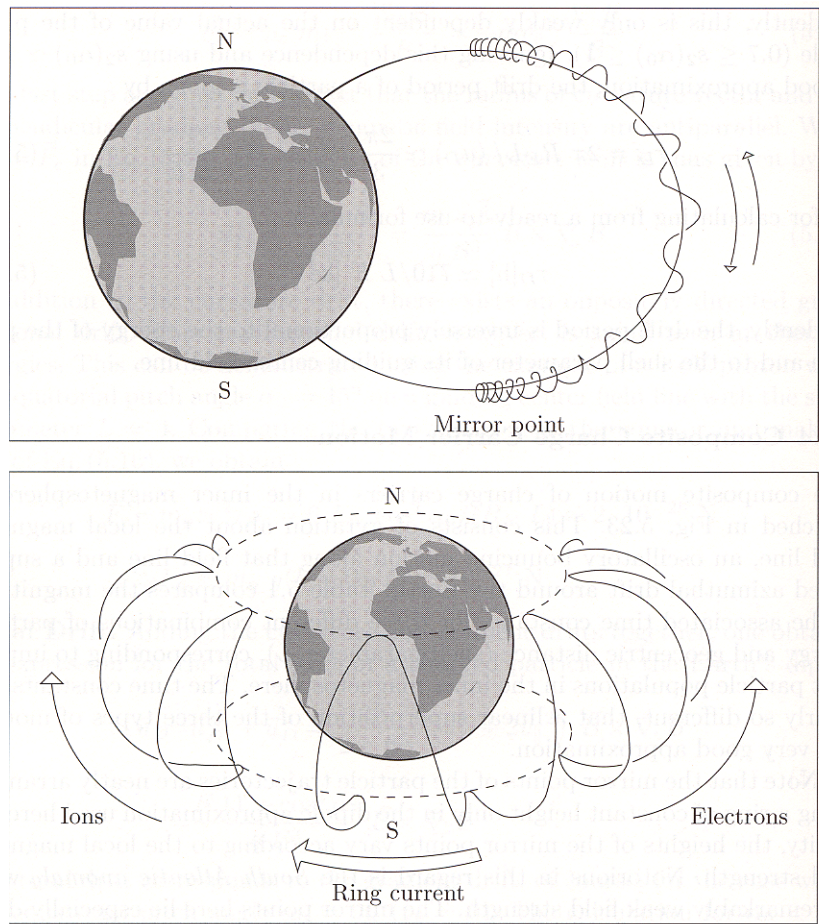
Figure 1.1. A schematic to show the trajectory of charged particles trapped on closed field lines. The top panel shows particles gyrating around the field line as well as mirroring between hemispheres. The lower panel shows the particles drifting azimuthally around the Earth due to gradient and curvature drift, also mirroring between hemispheres. From Prölss, 2004.

This is the transport equation, and is one of the fundamental laws of ideal MHD as it can be used to determine the flow velocity of a plasma (Prölss, 2004).

Ohm's law states that:

$$\mathbf{J} = \sigma(\mathbf{E} + \mathbf{v} \times \mathbf{B})$$
[1.23]

where σ is the conductivity of the plasma. In ideal MHD the plasma is taken to be collisionless so that $\sigma \to \infty$ (an approximation that is extremely good in most space plasma environments) and therefore $\mathbf{J}/\sigma \to 0$, such that:

$$\mathbf{E} = -\mathbf{v} \times \mathbf{B}$$
[1.24]

(Kivelson and Russell, 1995).

1.1.6 Frozen-in flow

It is possible to show that under ideal MHD the plasma and the field lines are "frozen" such that the plasma cannot cross field lines but may travel along them. The magnetic flux threading through a surface *s* is given by:

$$\phi = \int_s \mathbf{B}.d\mathbf{s}$$
[1.25]

The vector *ds*:

$$d\mathbf{s} = \mathbf{v}dt dl \sin\theta = (\mathbf{v} \times d\mathbf{l})dt$$
[1.26]

is normal to the surface, and has a length which corresponds to the change in area of a small section of the surface when a small length *dl* moves with a velocity **v** in time *dt* (Figure 1.2). This distortion of the surface then results in a rate of change of flux given by:

$$\frac{d\phi}{dt} = \int_s \frac{\partial \mathbf{B}}{\partial t} \cdot d\mathbf{s} + \int_c \mathbf{B}.(\mathbf{v} \times d\mathbf{l})$$
[1.27]

where the first term takes into account the change in the magnetic field with time, and the second term comes about due to the change in surface area of the loop with time. Finally using the vector identity:

$$\mathbf{B}.(\mathbf{v} \times d\mathbf{l}) = -(\mathbf{v} \times \mathbf{B}).d\mathbf{l}$$
[1.28]

combined with Stoke's theorem it is possible to obtain:

$$\frac{d\phi}{dt} = \int_s \frac{\partial \mathbf{B}}{\partial t}.d\mathbf{s} - \int_s \nabla \times (\mathbf{v} \times \mathbf{B}).d\mathbf{s}$$
[1.29]

which when combined with [1.25] yields:
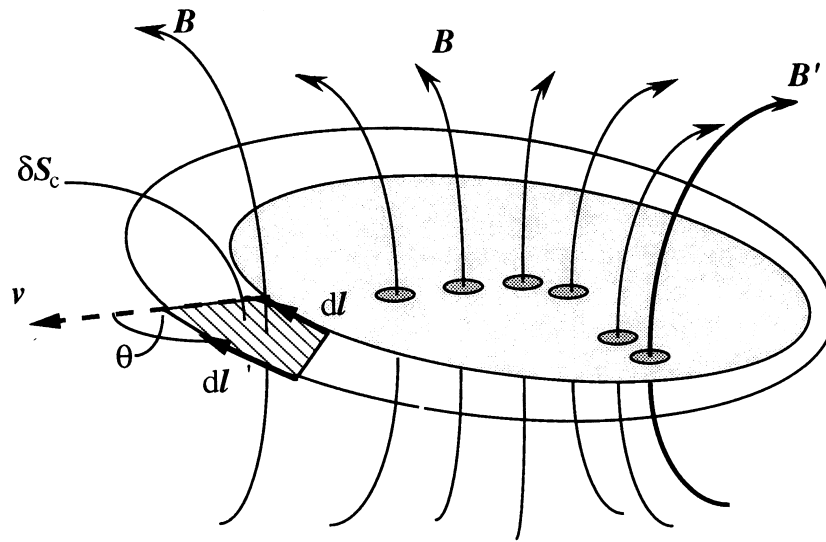
Figure 1.2. A schematic to show the change in area of a surface enclosing magnetic field lines. *dl* is a small length tangential to the loop which moves with velocity **v** in time *dt*. From Dendy, 1993.

$$\frac{d\phi}{dt} = 0 \qquad\qquad [1.30]$$

Plasma is therefore tied to the field lines, such that moving the plasma does not change the magnetic flux threading through a surface. This is known as Alfven's Theorem. It implies that within the limitations of MHD, plasma and field lines are tied together such that they cannot move independently. This theorem is therefore fundamental to the understanding of the interaction of magnetic fields in the Sun-Earth system.

1.1.7 Magnetic Reynolds Number

Combining Faraday's Law [1.3] with Ohm's Law [1.23] yields:

$$\frac{\partial \mathbf{B}}{\partial t} = \nabla \times \left(\mathbf{v} \times \mathbf{B} - \frac{\mathbf{J}}{\sigma} \right) \qquad\qquad [1.31]$$

Now using the non-relativistic Ampere's Law and Gauss' Law [1.1] combined with the vector identity $\nabla \times \nabla \times \mathbf{B} = \nabla(\nabla . \mathbf{B}) - \nabla^2 \mathbf{B}$ leads to:

$$\frac{\partial \mathbf{B}}{\partial t} = \nabla \times (\mathbf{v} \times \mathbf{B}) + \frac{1}{\mu_0 \sigma} \nabla^2 \mathbf{B} \qquad\qquad [1.32]$$

This is the magnetic induction equation for non-ideal MHD; the first term describes convective motion of the field with the plasma, and the second term describes the diffusion of the field through the plasma (Baumjohann and Treuman, 1997).

Rewriting these terms as ratios in dimensional form:

$$\frac{B}{T} : \frac{VB}{L} : \frac{B}{\mu_0 \sigma L^2} \qquad\qquad [1.33]$$

The magnetic Reynolds number is the ratio of the second and third terms:

$$R_m = \mu_0 \sigma L V \qquad\qquad [1.34]$$

where V is the average velocity perpendicular to the magnetic field, T is the characteristic time of magnetic field variations, and L is the characteristic length scale of the variations. The magnetic Reynolds number gives an indication of the extent to which Alfven's theorem is valid in a plasma; a large value of R_m indicates that the field and the plasma are frozen, while a small value is indicative of a diffusion dominated plasma (Baumjohann and Treuman, 1997).

1.1.8 Magnetic Reconnection

Magnetic reconnection takes place between oppositely directed field lines when Alfven's theorem breaks down, i.e. in a non-infinitely conducting plasma considered on small length scales. The region where this approximation breaks down is called the diffusion region which is characterised by a small value of the magnetic Reynolds number R_m, meaning that plasma and magnetic field lines can move independently. The oppositely directed field lines "break" and reconnect in a different topology. Figure 1.3 is a schematic showing the reconnection process. In this Figure, field lines move into the diffusion region from above and below the reconnection site, then the magnetic field lines reconnect. The two newly-reconnected field lines are highly kinked and therefore move at high speed under the magnetic tension force away from the reconnection site to the left and the right. It is generally accepted that in order for reconnection to take place there must be a significant shear in the magnetic field therefore this process only takes place under specific conditions in the terrestrial system; mainly at the magnetopause and in the geomagnetic tail. Reconnection at the magnetopause is the primary solar wind-magnetosphere coupling mechanism and is therefore responsible for the entry of solar wind plasma into the terrestrial magnetosphere. This will be discussed in more detail in Chapter 2.

1.2 The Sun and the solar wind

1.2.1 The structure of the Sun

The Sun is made up of 91% hydrogen, 8% helium and small fractions of heavier elements (Prölss, 2004). It is thought to be composed of a number of layers; the core rotates rigidly, with the outer regions rotating differentially such that the equatorial region has a rotation period of 26 days and the polar regions closer to 37 days (Kivelson and Russell, 1995). The Sun is a prodigious source of energy due to the high temperature and pressure in the core that result in the nuclear fusion of hydrogen to form helium:

$$4\,^1\mathrm{H} \rightarrow\, ^4\mathrm{He} + 2\gamma + 2\nu_e + 2\,\mathrm{e}^+ + 26.5\,\mathrm{MeV} \qquad [1.35]$$

ion diffusion region   electron diffusion region

inflow region

plasma jet
midplane

X-line

jet   jet

Hall current

inflow region

observed
electron beam

observed Hall magnetic fields
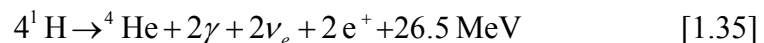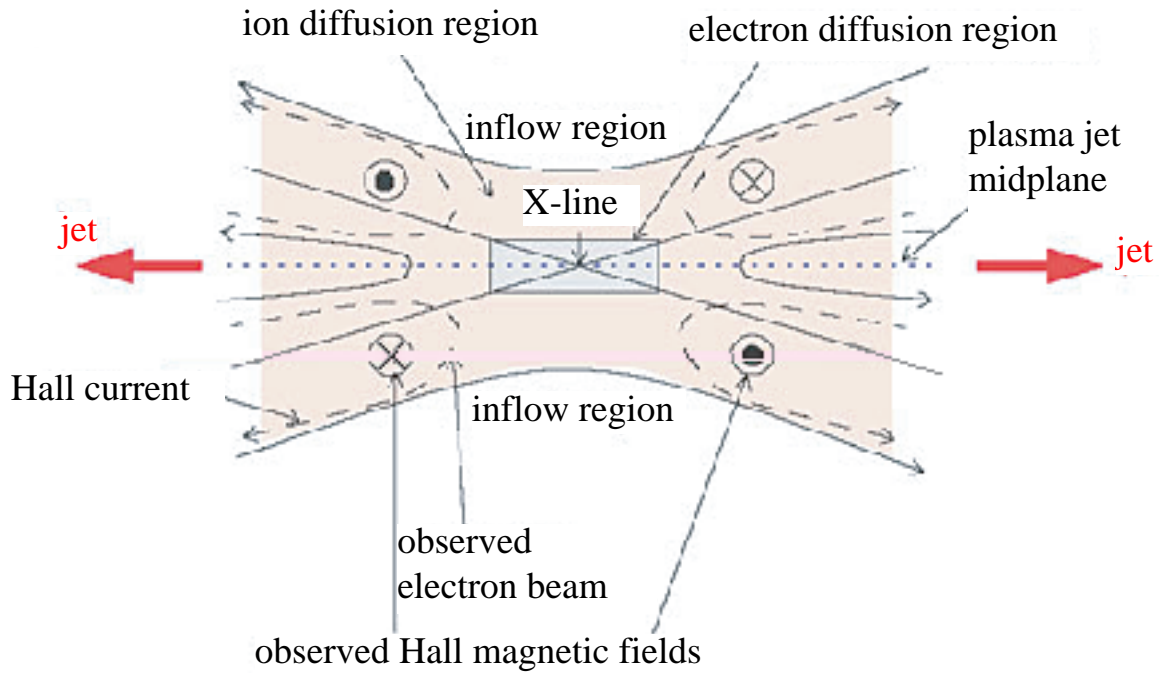
Figure 1.3.   A schematic to demonstrate the process of magnetic reconnection. Oppositely directed horizontal field lines are separated by a thin current sheet. On small spatial scales the plasma does not act as an infinite conductor and Alfven's Theorem breaks down. The oppositely directed field lines break and reconnect and the result is one field line which travels to the left and another which travels to the right due to the strong magnetic tension force on the bent field lines. This process also accelerates particles along the field lines and generates standing shock waves to the left and right of the schematic. From Øieroset, 2001.

where γ is a photon, ν_e is an electron neutrino and e^+ is a positron (Parnell, 1999). The core temperature is ~150 million K, and the density is ~160,000 kg m^{-3}.

The energy generated by fusion in the core is transferred by radiative diffusion as photons and neutrinos travel outwards from the core. The neutrinos are able to pass from the core to the surface without interacting with other particles, however the photons interact with protons, neutrons and heavier elements. Photons are absorbed by these particles and subsequently reemitted with lower energy, resulting in an increase in the photon wavelength. Away from the core however, the temperature and density decrease until photons are absorbed by atoms and not re-emitted. From this radius (~0.7 R_S) outwards the primary energy transfer mechanism is convection. Heat transferred from the upper radiative zone drives convective cells where plasma rises to the surface, cools, sinks, then is heated and rises again. Figure 1.4 outlines the different regions of the solar interior and atmosphere.

The photosphere is the region above the convective zone which is the coolest and densest part of the atmosphere. Radiation is emitted from this region mainly in the visible waveband, although significant amounts of emission have also been detected in UV and IR wavelengths. Imaging of this region both in white light and magnetograms enables the top of the convective cells to be identified as well as features such as sunspots: regions of high magnetic field and low temperature generated by the effect of differential rotation on the internal magnetic field. The photosphere is approximately 500 km thick and in this region the density decreases from $\sim 2.5 \times 10^{-4}$ to 4.3×10^{-5} kg m^{-3} and the plasma temperature varies from ~6400 to 4300 K (Parnell, 1999).

The boundary between the photosphere and the chromosphere is marked by a dramatic increase in plasma temperature. Over a height of only 2500 km, the temperature increases to over 30,000 K and the density falls to less than 1×10^{-9} kg m^{-3}. The reason for this increase in temperature is unknown, but it is thought to be generated by the release of magnetic energy as field lines are twisted by the convective motion of the plasma, possibly via magnetic waves (Parnell, 1999).

Above the chromosphere is the solar corona. This region sees an increase in temperature to over 1×10^{6} K and significant features such as prominances and solar
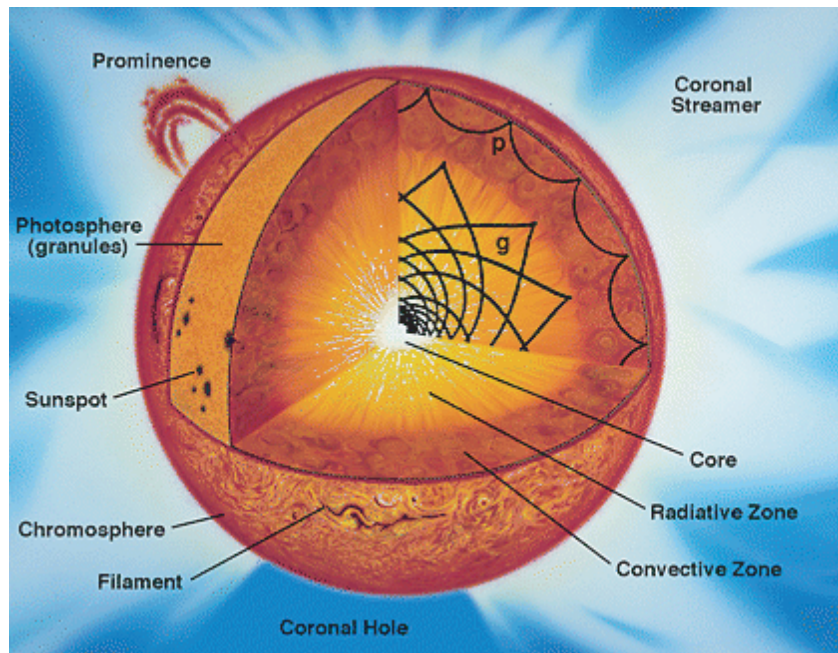
Figure 1.4. A schematic of the structure of the Sun. Energy is generated in the core and travels outward initially by radial diffusion and subsequently by convection. The photosphere is the visible part of the Sun, above this is the chromosphere and finally the corona. Coronal holes are visible at high latitudes, as are large scale structures such as sunspots, prominences (flares) and coronal streamers (related to coronal mass ejections). From Haubold and Mathai, 1997.

flares are observed. Plasma is continually escaping from the solar atmosphere into space, forming the solar wind.

1.2.2 The solar wind and the IMF

The solar wind consists of plasma streaming radially away from the solar surface. Simple gas dynamic modelling demonstrates that the high coronal pressure (and temperature) accelerate the solar wind to supersonic speeds by the time it reaches the Earth at 1 AU (Parker, 1958). High speed solar wind is thought to be generated by outflow from coronal holes which are regions of open magnetic field lines, whereas low speed solar wind is formed at low latitudes where field lines are closed. The average radial velocity of the solar wind is ~470 km s^{-1} and its average density and temperature are 6 cm^{-3} and 10^5 K at 1 AU (Prölss, 2004).   In an infinitely conducting plasma the magnetic field and the plasma are frozen together such that a parcel of plasma is always tied to the same magnetic field line (Section 1.1.6). Embedded within the plasma emitted from the Sun, and frozen to it, are magnetic field lines which have footprints mapping to fixed points on the solar surface. As the Sun rotates the field lines wind up to form a topology called the Parker Spiral (Figure 1.5). The average angle of the field lines to the Sun-Earth line is ~45° at 1 AU, contained within the ecliptic plane, although this is highly variable (Kivelson and Russell, 1995). These solar field lines extending out into the solar system form the interplanetary magnetic field (IMF), the direction and strength of which has important implications for processes occurring at Earth.

At the magnetic equator there exists a current sheet separating regions of opposing magnetic field direction. This current sheet is known as the heliospheric current sheet (Figure 1.6) and is tilted with respect to the equatorial plane as the Sun's magnetic axis is offset with respect to its rotational axis. It is also rippled as the Sun's magnetic field has higher order terms than the simple dipole we use as an approximation. A combination of the rippled and tilted nature of this current sheet results in the Earth being alternately above and below the current sheet and therefore experiencing periods of interplanetary magnetic field (IMF) directed towards and away from the Sun.
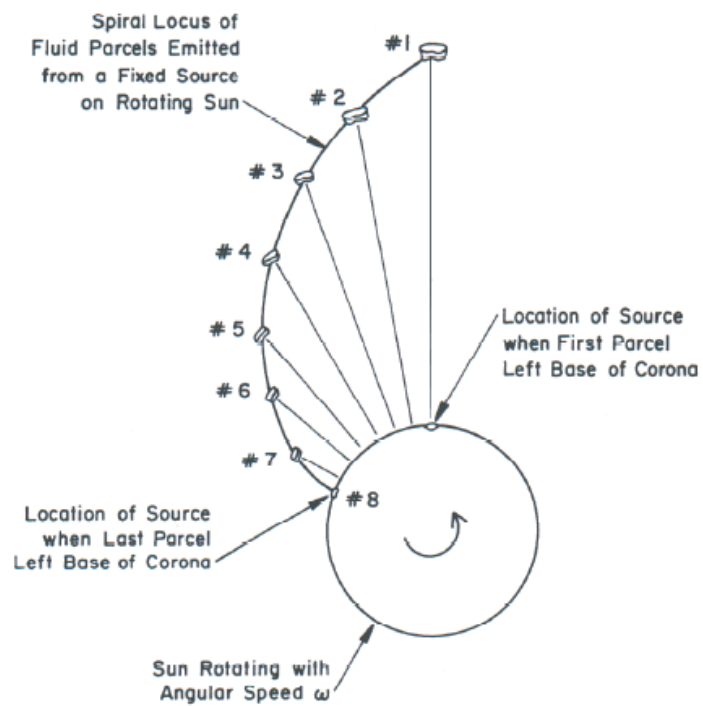
Figure 1.5. Solar rotation causes magnetic field lines frozen to radially outflowing plasma to be twisted into the Parker Spiral. From Kivelson and Russell, 1995.
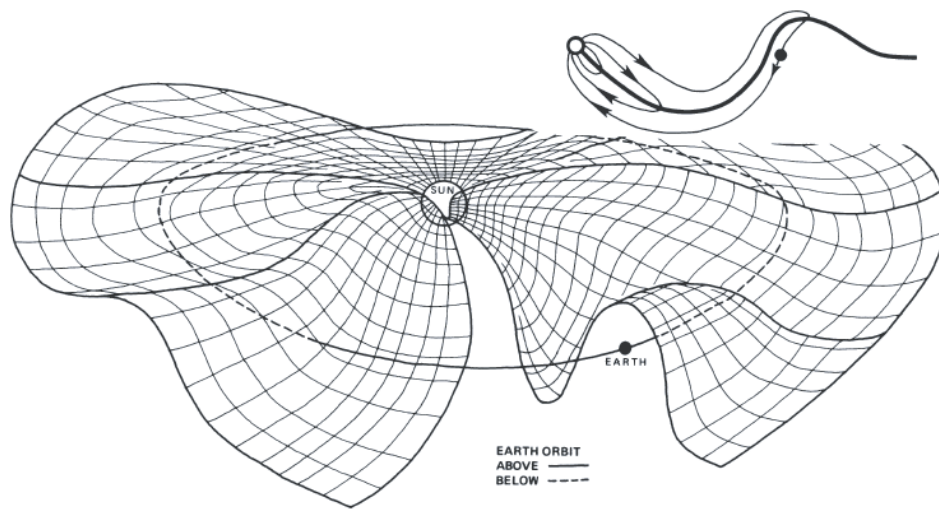
Figure 1.6. A schematic of the heliospheric current sheet to demonstrate how the Earth alternately experiences northward and southward directed interplanetary magnetic field regimes. By S.-I. Akasofu.

Processes occurring in the solar corona also have a significant impact on the direction of the IMF. There are three main processes which may influence the solar wind; solar flares, corotating interaction regions and coronal mass ejections:

1. Solar flares are continually erupting from the solar corona. They usually erupt close to sunspots and other regions of high magnetic shear. The energy of a solar flare is thought to be $\sim 10^{25}$ Joules and high energy particles as well as radiation are emitted.

2. Corotating interaction regions (CIRs) are regions in the solar wind where a flow of fast solar wind (produced for example by a coronal hole) catches up with slow solar wind in front of it. The fast solar wind cannot overtake the slow wind and compresses the plasma ahead, creating a compression region at the leading edge and a rarefaction region behind that. Gradually a pair of shocks are formed, one of which propagates forward (in the frame of reference of the compression region) and the other propagates back and acts to slow the fast solar wind (Kivelson and Russell, 1995).

3. Coronal mass ejections are thought to be due to reconnection taking place in the solar corona. Huge amounts of mass (up to 10^{13} kg) are radially emitted from the Sun, embedded within which is a magnetic flux rope. As this plasma moves away from the Sun at high speed it forms a shock wave ahead of it and a high density compression region similar to a corotating interaction region. By the time the flux rope (also called a magnetic cloud in the solar wind) reaches 1 AU it is a massive structure. The helical field within the flux rope results in a slowly rotating interplanetary magnetic field at Earth which can result in stable northward or southward directed IMF for hours and even days, and provides a good opportunity for research into solar wind-magnetosphere coupling.

1.3. The Structure of the Magnetosphere

The Earth's magnetic field acts as an obstacle to the supersonic flow of the magnetised solar wind. The first indication that an obstacle to the flow exists is the bowshock (typically ~ 15 R_E upstream of the Earth) which acts to slow and redirect the flow of the solar wind around the Earth, in a similar way to acoustic shock waves in aerodynamical systems. The shocked solar wind typically has a density

and magnetic field approximately 4 times that of the upstream solar wind (Kivelson and Russell, 1995).

The Earth has a magnetic field which we approximate to a dipole. The cavity carved in the solar wind flow by the geomagnetic field is called the magnetosphere, and the region between the bowshock and the magnetopause is known as the magnetosheath. Between the interplanetary magnetic field (IMF) and the geomagnetic field is a current sheet called the magnetopause. Geomagnetic field lines within the magnetopause on the dayside are closed, such that both ends map to high latitudes at the Earth. The dayside magnetopause is compressed due to the ram pressure of the solar wind, and the nightside is stretched out into a long magnetotail. The field lines within the magnetotail lobes are open, such that one end maps to high latitudes in the northern or southern hemisphere, and the other end is connected into the solar wind, far downtail (Figure 1.7). When the interplanetary magnetic field (IMF) is directed southwards, reconnection takes place at low latitudes on the dayside, where the IMF and the geomagnetic field are antiparallel (Section 1.1.8). This reconnection causes field lines to break and reconnect, such that closed, dayside field lines are opened and have one end mapping to high latitudes while the other end is out in the solar wind. These newly opened field lines are swept anti-sunward and added to the lobes of the tail which extends many hundreds of Earth radii (R_E). Reconnection in the tail then acts to close these open field lines and they return to the dayside at low latitudes, thereby completing a process called the Dungey Cycle (Dungey, 1961). Magnetospheric interaction with the solar wind is extremely important in the Earth's environment as it allows energy and momentum to be transferred from the solar wind into geospace. The main aim of this thesis is to better understand dayside reconnection processes and therefore more detail can be found in Chapter 2.

1.3.1 The Earth's magnetic field

The Earth's dipolar magnetic field can be expressed in spherical polar coordinates by:

$$(B_r, B_\theta, B_\phi) = \frac{m}{r^3}(-2\sin\theta, \cos\theta, 0) \qquad [1.36]$$

18
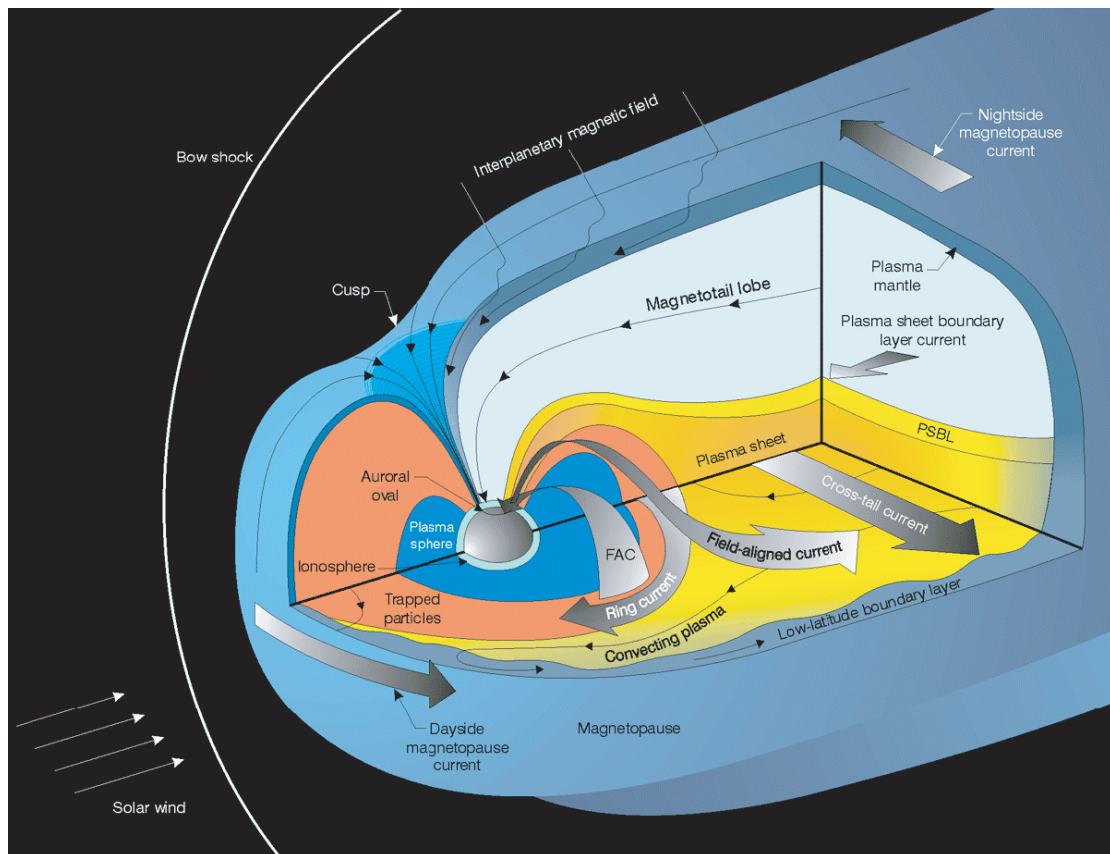
Figure 1.7. A schematic to show the boundaries, plasma populations and current systems within the Earth's magnetosphere. By J. Burch, Southwest Research Institute, San Antonio,USA.

where m is the magnetic moment of the Earth, r is the radial distance from the centre of the Earth and θ is the latitude (Baumjohann and Treumann, 1999).

1.3.2 The Magnetopause

The magnetopause is a current sheet which separates the shocked solar wind and the magnetosphere. The location of this current sheet depends on the balance between the solar wind dynamic pressure and the magnetic pressure of the compressed geomagnetic field. The location of the magnetopause changes such that these forces balance, for example a stronger solar wind dynamic pressure will force the magnetopause Earthwards and enhance the magnetopause current, which will act to increase the magnetic pressure at the magnetopause until equilibrium is reached.

The current at the dayside magnetopause is called the Chapman-Ferraro current, the direction of which can be calculated by considering particles incident on the magnetopause from the solar wind. As the particles approach the magnetopause they feel the Lorentz force

$$\mathbf{F} = q(\mathbf{v} \times \mathbf{B}) \hspace{3cm} [1.37]$$

This force acts in opposite directions on protons and electrons which perform half a gyro-rotation in opposite directions (Figure 1.8). This leads to a dawn-dusk current flowing across the surface of the magnetopause, the width of which is approximately half of an ion gyroradius. This dawn-dusk current flowing on the dayside magnetopause closes over the tail lobes in both hemispheres (Figure 1.7).

1.3.3 The Magnetotail

The flow of the solar wind past the magnetosphere drags open geomagnetic field lines anti-sunward to form a magnetotail hundreds of Earth radii (R_E) in length (Figure 1.7). The tail is composed of two lobes of open field lines, which map to either the northern or southern polar region. Some distance from the planet these field lines no longer influence the Earth system and are not considered further. The field lines within the two lobes are oppositely directed, therefore between the lobes exists a current sheet called the cross-tail, or neutral current sheet which is directed

solar wind $\quad\quad \mathbf{B} = 0$ $\quad\quad\quad$ magnetopause $\quad$ magnetosphere $\quad\quad \mathbf{B} = B_z\mathbf{e}_z$

$\rho = n(m_p + m_e)$ $\quad\quad\quad\quad\quad$ t $\quad\quad\quad\quad\quad\quad\quad\quad\quad$ $\rho = 0$

J_y $\quad\quad\quad\quad\quad$ $\odot$ B

r_{Le}

electron $\ominus$

proton $\oplus$ $\quad\quad\quad\quad\quad\quad\quad\quad\quad\quad\quad\quad$ x $\quad\quad$ $\odot$ z

$y = y_0$

v $\quad\quad\quad\quad\quad\quad\quad\quad\quad$ y

r_{Lp}
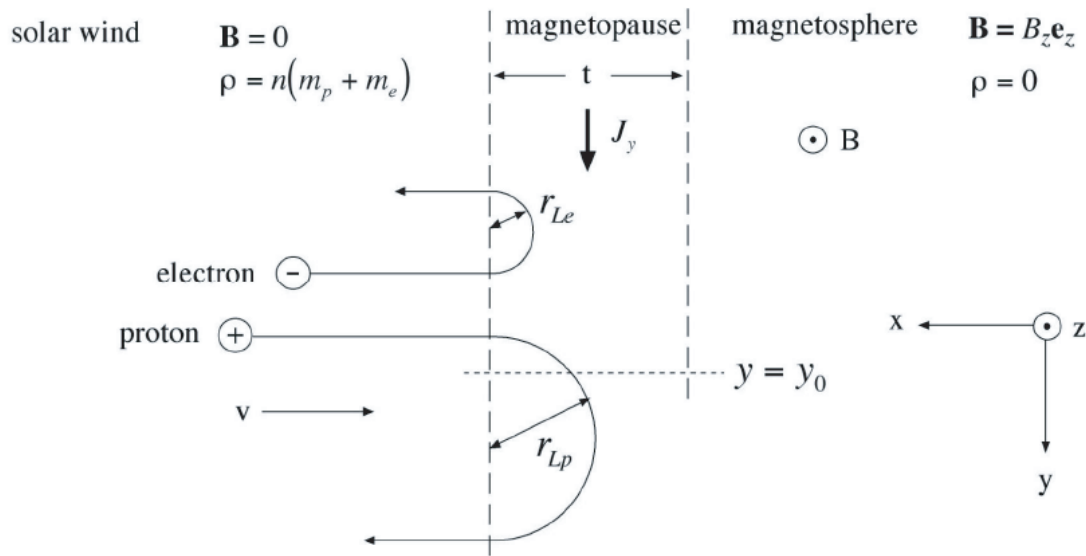
Figure 1.8. A schematic to show the trajectory of electrons and ions as they approach the magnetopause. Incoming solar wind electrons and ions approach from the left, feel the Lorentz force and perform half a gyro-rotation before leaving the current sheet. This leads to a dawn-dusk current across the dayside magnetopause called the Chapman-Ferraro current; the thickness of the magnetopause is given by the thickness of this current sheet. From Kivelson and Russell, 1995.

from dawn to dusk. The currents flowing within this current sheet close with the dayside Chapman-Ferraro currents and they also help to close the Region I and Region II field aligned current systems (Section 1.3.7). The tail lobes are only sparsely populated with plasma, as ions and electrons moving Earthward will mirror once at the Earth and then travel downtail and be lost. The near-Earth current sheet is embedded in closed field lines however, which have a trapped plasma population mirroring between hemispheres. This plasma population forms the plasma sheet, which has an average ion temperature of a few keV and an average density of ~0.3 cm^{-3} (Øieroset et al., 2005).

The diameter of the magnetotail increases with distance downtail. Near the Earth it is determined by the balance between the magnetic pressure of the lobes and the solar wind dynamic pressure. With distance downtail, the solar wind flow is increasingly parallel to the magnetopause therefore the solar wind dynamic pressure decreases, and the lobe magnetic pressure approaches the solar wind static pressure. The average near-Earth lobe magnetic field strength is ~ 20 nT (Slavin et al., 1985).

1.3.4 The near-Earth plasma environment

Radiation belts

The radiation belts were discovered by James Van Allen in 1958. There are two radiation belts, an inner one consisting mainly of protons 700-10,000 km above the Earth's surface, and an outer one consisting mainly of electrons, extending from 13,000 to 65,000 km (Figure 1.9a). Ions and electrons within these belts are trapped on closed geomagnetic field lines, mirroring as they approach low altitude and drifting azimuthally around the Earth. They are high energy particles in the MeV range, therefore can perform a complete orbit of the Earth in a few minutes (Liemohn and Chan, 2007). Sources of radiation belt particles include injection from the plasma sheet, cosmic ray neutron decay, and radiative diffusion. Radiation belt particles are also affected by interaction with waves; some of the more important loss processes into the atmosphere are due to interaction of radiation belt particles with electromagnetic ion cyclotron waves and ELF and VLF plasma waves. It is also these waves which create the electron slot region; that is the cavity between the two radiation belts (Liemohn and Chan, 2007).
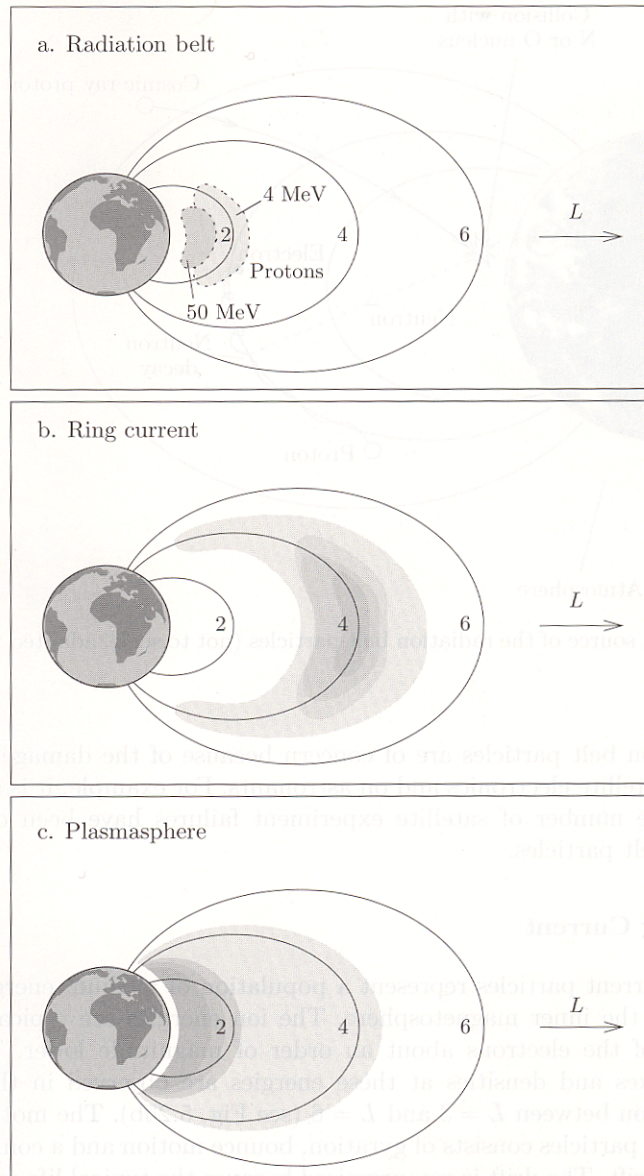
Figure 1.9. A schematic to show the location of the inner magnetosphere plasma populations in the GSM X-Z plane. The lines are magnetic field lines and the numbers mark the L-shell of these field lines. From Prölss, 2004.

The Ring Current

The ring current is formed by particles on trapped field lines gradient and curvature drifting around the Earth (Section 1.1.3). The electrons drift eastwards and the ions drift westwards, thereby causing a net westward azimuthal current (Figure 1.9b).

The source of the ring current particles has been shown to be the tail plasma sheet. Plasma downtail from the Earth experiences an $\mathbf{E} \times \mathbf{B}$ force due to the dawn-dusk electric field in the current sheet which acts in the same direction on both ions and electrons and results in an Earthward particle drift. These particles will eventually drift close enough to the Earth to be added to the ring current. There are many ring current loss processes however, such as charge exchange and scattering into the loss cone by collisions and wave interactions (Prölss, 2004).

The plasmasphere

The plasmasphere is a region close to the Earth in which corotation dominates over reconnection-driven convection. It is characterised by cold, dense plasma, mainly made up of protons that escaped from the ionosphere. The lower boundary of the plasmasphere is defined as the altitude at which the primary ion changes from atomic oxygen to atomic hydrogen and is usually between 500 and 2000 km. (Prölss, 2004). The outer boundary of the plasmasphere is called the plasmapause and its variable location depends on the relative strengths of the corotation and the convection-driven electric fields (Figure 1.9c).

1.3.5 The polar caps and the geomagnetic cusps

Open, lobe field lines map to the polar caps in the northern and southern hemispheres (Figure 1.7). These regions are characterised by a low flux of precipitating electrons with energy ~few hundred eV, called "polar rain" (with no appreciable ion signature) which are thought to originate at the solar corona (Fairfield and Scudder, 1985). The closed field lines outside the polar cap contain high fluxes of trapped, high energy particles (tens to hundreds of keV). The open/closed field line boundary (OCB) is the boundary between the open field lines

in the polar cap, and the closed field lines at lower latitudes, and this boundary can therefore be identified as the poleward edge of the diffuse electron aurora (see Section 1.3.7). This identification can become much more complex when reconnection is taking place (see Chapter 2).

The region between the closed, dayside geomagnetic field lines, and the open lobe field lines is called the cusp (see Figure 1.7). This region has a very low magnetic field, and is particularly important when considering magnetic reconnection and momentum transfer between the IMF and the geomagnetic field. The cusp structure depends on the location and rate of reconnection taking place, as newly reconnected field lines under both north- and southward IMF conditions pass through the cusp as they convect away from the reconnection site. Ions and electrons may travel down these newly reconnected field lines and will mirror at low altitudes or precipitate into the upper atmosphere. A low altitude spacecraft located on a cusp field line may therefore see particle signatures of reconnection, both in the initial downward travelling particles, and those upward moving particles that have mirrored at lower altitudes. These particle signatures are an extremely useful tool in understanding the nature of dayside reconnection processes and will be discussed in more detail later in this thesis.

1.3.6. Current systems in the magnetosphere

The distortion of the geomagnetic field from the dipole indicates the flow of currents in near-Earth space. These current systems arise due to a variety of mechanisms related to the interaction of the solar wind with the magnetosphere. The magnetopause, cross-tail and ring currents have already been discussed in Sections 1.3.2, 1.3.3 and 1.3.4. There are several other important current systems in the magnetosphere which will be described below.

Pedersen and Hall Currents in the ionosphere

Dungey cycle flows during southward IMF are driven primarily by reconnection at the subsolar point and in the tail. Anti-sunward flow over the polar cap combined with the Earth's magnetic field in the GSM-Z direction leads to an electric field in the direction given by:

$$\mathbf{E} = -\mathbf{v} \times \mathbf{B} \qquad\qquad [1.40]$$

assuming ideal MHD. This electric field is dawn-dusk in the northern polar cap. Equatorward of the OCB, sunward flow generates an electric field given by [1.40] which is directed from dusk to dawn in the northern hemisphere.

Currents are generated in different regions of the ionosphere due to these electric fields. The importance of collisions in the motion of particles is related to the ratio of the collision frequency between charged particles and neutrals, v, with the gyrofrequency ω_g given by [1.9]. If $v \ll \omega_g$ then the particle will $\mathbf{E} \times \mathbf{B}$ drift. If $v \gg \omega_g$ then the particle will begin to feel the impact of collisions with neutrals. As ions are so much heavier than electrons, the height at which collisions become important is ~150 km, compared to ~80 km for electrons. The result is that between these altitudes ions are impeded by collisions where electrons are not, therefore a net current is generated called the Hall current which flows perpendicular to the direction of both the electric and the magnetic field. The Hall currents are represented by dashed lines in Figure 1.10.

An additional effect is felt by ions due to increased collisions with atmospheric neutrals. Following a collision, the ion will begin its gyromotion again, and if the collision frequency is larger than the gyrofrequency then it will be unlikely to complete a full gyroperiod before it undergoes a further collision. This leads to a net motion of ions in the direction of motion parallel to the electric field and a current called the Pedersen current which is shown by the black arrows in Figure 1.10.

Region I and II field aligned currents

Closure of Pedersen currents is achieved by magnetic field aligned currents (FACs). Dawn-dusk Pedersen currents within the polar cap lead to a convergence of current along the duskside open/closed field line boundary (OCB) and divergence along the dawn side of the OCB (Figure 1.10), as first detected by Ijima and Potemra (1978) (Figure 1.11). Field aligned currents known as Region I currents flow up and out of the ionosphere on the dusk side of the OCB, over the northern or southern magnetopause tail lobe in the dusk-dawn direction, closing by a downward
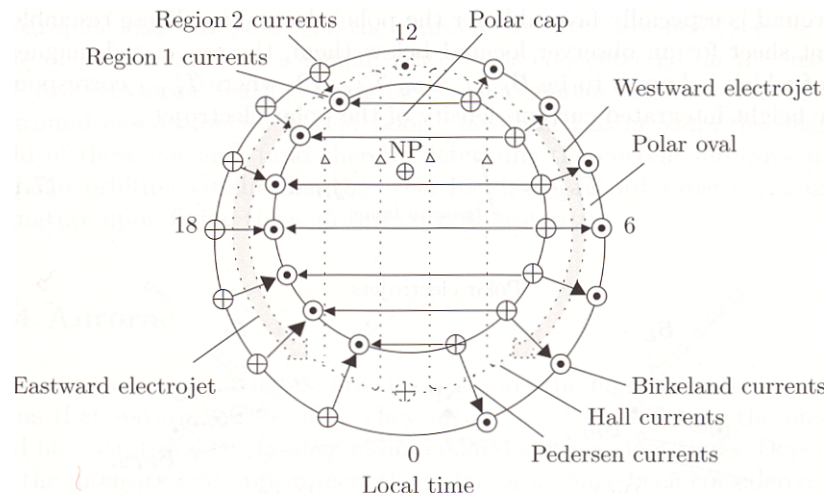
Figure 1.10. A schematic to show field aligned current systems in the ionosphere. Region I field aligned currents flow up on the dusk side of the open/closed field line boundary (OCB) and down on the dawn side. Region II currents are equatorward of the Region I currents and flow in the opposite direction. Pedersen currents are represented by black arrows and flow parallel to the electric field direction in the ionosphere, so dawn-dusk across the polar cap and perpendicular to the OCB in the section between the Region I and Region II currents. Hall currents are shown by dotted lines with white arrows and these flow perpendicular to both electric and magnetic fields. The Hall current system in the polar cap is therefore sunward within the OCB and azimuthally tailward between the Region I and Region II current systems. From Prölss, 2004.

27
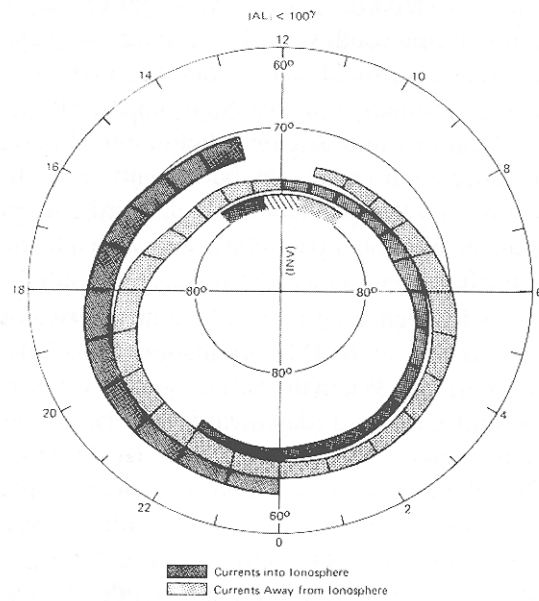
Figure 1.11. Statistical location of the Region 1 and Region 2 field aligned currents. Poleward of these is the NB_Z or Region 0 current system, upward currents in the pre-noon sector and downward field aligned currents in the post-noon sector. From Iijima and Potemra, 1978.

field aligned current at the dawn side of the OCB (Baumjohann and Treumann, 1997).

Region II currents are located at lower latitudes than the Region I currents in the ionosphere and are also driven by electric fields generated by southward IMF Dungey cycle flow. These electric fields outside the OCB are directed from dusk to dawn as the return convection flow is sunward at low latitudes. The electric fields therefore generate field aligned currents flowing in the opposite direction to the corresponding Region I currents; downward at dusk and upward at dawn. The upward field aligned current on the dawn side flows via the dawn-dusk equatorial partial ring current to meet the downward field aligned current on the dusk side. Pedersen currents in the ionosphere link the Region I and Region II field aligned currents and the circuit is completed by the Region I current system (Baumjohann and Treumann, 1997).

Current systems under northward IMF

When the IMF turns northward it is expected that twin reverse convection cells will be formed in the polar caps, as will be discussed in further detail in Chapter 2. These twin reverse cells are completely contained within the polar cap with sunward flow at high latitudes and antisunward flow at lower latitudes. A new current system is therefore formed, known as the Region 0 current system, or NB_Z current system. This is located just poleward of the Region I current system in the dayside portion of the polar cap. The sunward flow at high latitudes sets up a dusk-dawn electric field which generates downward directed field aligned currents at dusk and upward directed field aligned currents at dawn, opposite to the Region I currents and only over a very small portion of the dayside polar cap (Figure 1.11). These currents close across the dayside magnetopause.

Geomagnetic Indices

During magnetically active times such as geomagnetic storms, the ring current density is observed to increase. This increase in the ring current introduces a southwards directed magnetic field at the Earth's surface which can be detected as a negative excursion in the H (horizontal) component magnetograms from the

equator (see Section 1.4.6 for an explanation of coordinate systems) (Paschmann et al., 2003). The average H component magnetic field measured hourly at four magnetometers near the equator is known as the D_{st} index which is primarily used for the identification of magnetic storms. The SYM-H index is similar to D_{st}, although different stations are used and it is available at 1 minute time resolution.

The AU and AL geomagnetic indices are measured using twelve magnetometers situated near the northern hemisphere auroral oval at different local times (Baumjohann and Treumann, 1997). The H component of the magnetic field from each station is measured, and the maximum measured excursion from the quiet day value at any station is known as the AU index, while the minimum excursion is the AL index. These indices are available at 1 minute time resolution, and measure the extent of the eastward and westward electrojets associated with substorms (Chapter 2.1), therefore are used as a proxy for the substorm activity level.

1.3.7 The Aurora

Many types of auroral features have been identified using both ground and space-based instrumentation. There are two main types of aurora, diffuse and discrete and these are generated by different mechanisms.

Diffuse Aurora

As described in Section 1.3.4, plasma sheet particles on closed field lines in the tail feel a dawn-dusk electric field and therefore $\mathbf{E} \times \mathbf{B}$ drift towards the Earth. High energy particles also experience significant gradient and curvature drift forces which cause them to drift azimuthally, as well as bouncing between hemispheres. Particles with a lower pitch angle will be able to travel further down the closed field line towards the Earth before mirroring and returning to high altitudes again. Particles in the loss cone (i.e. with a very small pitch angle) will precipitate down field lines into the upper atmosphere and can generate auroral emission by the processes described below. Interaction of particles with plasma waves (such as gyro-resonance with Whistler-mode waves) can result in particles being accelerated parallel to the magnetic field lines and therefore being injected into the loss cone from outside of it (Dendy, 1995). This causes electrons to be continually lost from

these closed field lines and they are replenished by $\mathbf{E} \times \mathbf{B}$ drifting particles from the plasma sheet. The aurora generated by precipitating electrons on closed field lines interacting with the neutral atmosphere is known as diffuse aurora, and is always present on field lines equatorward of the OCB. This type of aurora is dim compared with the discrete aurora and is best observed using cameras mounted on spacecraft in polar orbits (Prölss, 2004).

Discrete Aurora

Discrete auroral forms are generally much brighter and sharper than diffuse aurora when observed from Earth. They are located equatorward of the OCB, although unlike the diffuse aurora they are not always present. The increased brightness of the discrete aurora over the diffuse is due to the increased energy of the incoming electrons and ions. The field aligned current systems outlined in Section 1.3.6 accelerate electrons in the field parallel (or anti-parallel) direction and can lead to both large and small-scale discrete aurora. Reconnection at the magnetopause or in the tail also accelerates particles down field lines; examples of reconnection-driven aurora include phenomena such as cusp spots which will be investigated further in Chapter 6.

Auroral generation mechanisms

Electrons reach lower altitudes than ions as their ionisation efficiency is lower such that the electron-generated aurora is usually at altitudes of approximately 100 km whereas the ion-generated aurora is at greater altitudes (>130 km) (Baumjohann and Treumann, 1997). The energetic protons which reach low enough altitudes to produce aurora primarily undergo charge-exchange interactions with atmospheric neutrals. The proton captures an electron and becomes a high energy hydrogen atom, which emits Lyman-alpha radiation. This energetic hydrogen atom is likely to undergo further collisions with atmospheric neutrals thereby losing and gaining an electron many times. The neutral hydrogen atom is not tied to a field line, so proton aurora are often broader than electron aurora as protons diffuse out of their flux tube. This auroral Lyman-alpha can be distinguished from other Lyman-alpha emissions as it is Doppler shifted due to the

downward motion of the emitting hydrogen atoms and is observed in the UV (~121.6 nm wavelength).

Electrons interact with neutrals in the upper atmosphere in a variety of ways, such as:

1. Elastic collisions with neutral particles.

2. Collisional ionisation, which is the removal of an electron from an atom or ion via a collision. The ionisation rate per unit volume at a given altitude is dependent on the ionisation energy of the atomic electron, the number of collisions per unit height, and the ionisation efficiency (Baumjohann and Treumann, 1997). Higher energy particles are able to penetrate further into the ionosphere and therefore different colour aurora (due to complete or partial ionisation of atmospheric atoms or ions) originate at different altitudes.

3. Collisional dissociation, which is the splitting of a molecule into ions via electron collision, for example molecular oxygen (Wolden, 2004):

$$O_2 + e^- \rightarrow 2O + e^- \qquad [1.38]$$

4. Collisional excitation only contributes to a small amount of the auroral emission we observe (Prölss, 2004). An incident electron collides with an atmospheric particle and gives it energy. That energy is then released by the atmospheric particle in the form of a photon, for example:

$$N_2 + e_p \rightarrow {}^*N_2^+ + e_p + e_s$$

$$ {}^*N_2^+ \rightarrow N_2^+ + \gamma \qquad [1.39]$$
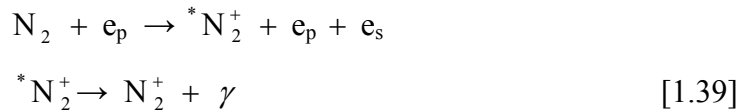
A primary electron (e_p) colliding with a nitrogen molecule (N_2) removes an electron (e_s) and excites the molecule. The excited nitrogen molecule then decays back to a lower energy state, giving off a photon (γ) with wavelength 391.4 nm, which we see as auroral emission (Prölss, 2004).

Having imparted energy to atmospheric particles, this energy is then lost in a variety of ways such as secondary ionisation and scattering, charge exchange,

dissociation exchange, and various recombination processes (see Prölss, 2004 for further detail).

The dominant wavelengths which make up the visible aurora are given in Figure 1.12. Displayed are the primary wavelengths, dominated by processes involving atomic and molecular nitrogen and oxygen. Atomic oxygen and nitrogen also produce UV emission, oxygen primarily at 130.4 and 135.6 nm (Prölss, 2004) and nitrogen at ~150 nm (Baumjohann and Treumann, 1997). Molecular oxygen also generates infrared emission at 1270 and 1580 nm (Baumjohann and Treumann, 1997).

1.4 Coordinate Systems

Many different coordinate systems are used when considering the Sun-Earth system; the primary ones used in this thesis are discussed below.

1.4.1 Geocentric Solar Magnetic Coordinates

The coordinate system that is generally used when studying the Sun's influence on the geomagnetic field is geocentric solar magnetic coordinates (GSM). In this system we have the X direction along the Sun-Earth line, with GSM-$X = 0$ at the centre of the Earth, and positive X is in the sunwards direction. The GSM-Z direction is perpendicular to X and lies in the plane containing the X-axis and Earth's dipole moment, being positive towards the North. The GSM-Y direction completes the right-handed set, and is positive in the direction opposite to the motion of the Earth in its orbit around the Sun.

1.4.2 Geocentric Solar Ecliptic Coordinates

Geocentric solar ecliptic coordinates (GSE) are oriented around the ecliptic plane. In a similar way to the GSM coordinate system, the X-axis is positive towards the Sun with GSM-$X = 0$ at the centre of the Earth. The Z axis is defined as being perpendicular to the ecliptic and the Y direction completes the right-handed set, being positive in the direction opposite to the motion of the Earth around the Sun.
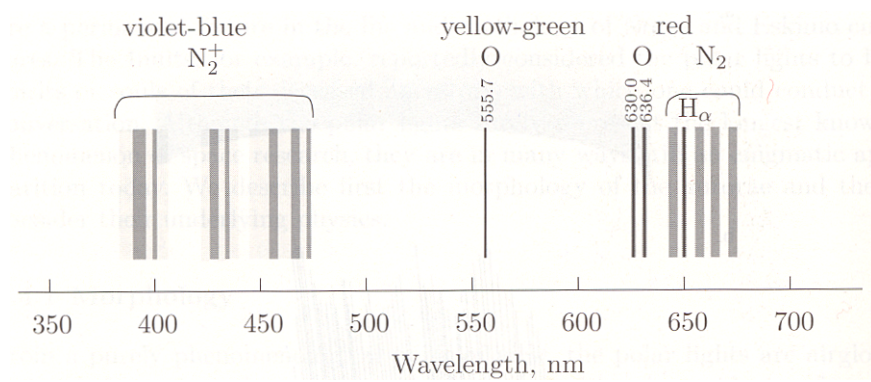
Figure 1.12. The primary wavelengths of auroral emission in the visible range. These wavelengths are produced by energetic particle interaction with neutral and singly charged nitrogen molecules and oxygen atoms. From Prölss, 2004.

1.4.3 Geomagnetic Latitude

The geomagnetic latitude of a point on the Earth's surface is the angle made between the line connecting the point with the centre of the Earth, and the plane perpendicular to the magnetic dipole, which also passes through the centre of the Earth. 90° geomagnetic latitude is the location of the geomagnetic north pole, and -90° is the location of the geomagnetic south pole.

1.4.4 Magnetic Local Time

In order to specify the location of a point on the Earth's surface relative to the magnetic pole, the geomagnetic latitude and the magnetic local time of that point can be specified. Magnetic local time is similar in concept to the familiar geographic longitude except that lines of constant magnetic local time join the two magnetic poles rather than the geographic poles. There are 24 hours of magnetic local time, 12 (noon) pointing towards the Sun, and 24 (midnight) away from the Sun. This frame of reference stays still while the Earth rotates underneath it, rather than the traditional longitudinal system with rotates with the Earth such that Greenwich is always the prime meridian.

1.4.5 Clock Angle

The direction of the interplanetary magnetic field (IMF) has significant implications for determining the location and rate of reconnection at the magnetopause. We define the clock angle to be the angle made by the IMF to geomagnetic north in the GSM *Y-Z* plane, 0° indicating a northwards orientation, +90° (-90°) an eastwards (westwards) orientation, and 180° southwards.

$$\theta = \begin{cases} 90 - \tan^{-1}\left(B_Z / B_Y \right) & B_Y > 0 \\ -90 - \tan^{-1}\left(B_Z / B_Y \right) & B_Y < 0 \end{cases} \qquad [1.35]$$

where B_Y is the IMF component in the GSM-*Y* direction, and B_Z is the GSM-*Z* component.

1.4.6 Magnetometer Coordinate Systems

Geographic coordinates are used to describe the geomagnetic field measured at the surface of the Earth relative to the Earth's rotation axis. X and Y are both defined as being in the plane of the Earth's surface. X is defined as the magnetic field projected into the plane of the Earth and resolved to point in the direction of the Earth's geographic north pole. Y is then the component of the projection perpendicular to the X direction, positive Eastward. Z completes the right handed set, and is positive towards the centre of the Earth.

Another commonly used magnetometer coordinate system is HDZ. Here, H is defined as projection of the magnetic field into the plane of the Earth's surface, while D is the angle between H and the vector pointing towards the geographic north pole. Z is positive towards the centre of the Earth.

Chapter 2. Literature Review

This Chapter outlines the current understanding of dayside solar wind-magnetosphere-ionosphere coupling and provides the basis for the work in this thesis.

2.1 Reconnection at the magnetosphere

2.1.1 Southwards IMF (Bz<0)

When the IMF is directed southwards magnetic reconnection occurs at the subsolar point (Figure 2.1a) where the IMF and geomagnetic fields are anti-parallel (Dungey, 1963). Dayside closed geomagnetic field lines are opened by this process and the newly reconnected field lines have one footprint which maps to the northern or southern polar cap and from there they extend into the IMF. The amount of magnetic flux in the polar cap is therefore increased by this process, and the polar cap area must increase. A combination of the magnetic tension force and the flow of the solar wind past the Earth results in the newly opened field line being dragged tailwards and eventually being added to one of the tail lobes.

In the ionosphere, a proxy for the magnetopause geometry is the shape of the polar cap, which is enclosed by the boundary between the footprints of open and closed field lines. Usually this open/closed field line boundary (OCB) is approximately circular, however during low latitude reconnection the newly reconnected flux is added to a small portion of the dayside polar cap where the footprint of the reconnection site is located (Cowley and Lockwood, 1992). This means that the polar cap is distended sunwards and no longer in a circular equilibrium. The ionospheric flows act to return the polar cap to a more circular configuration, therefore antisunward flows are excited near noon which redistribute the newly added flux, with equatorward flows expanding the OCB to lower latitudes at all local times away from the merging gap.

The lower portion of Figure 2.1a is a schematic looking down on the northern polar cap with the Sun at the top. The solid circle represents the open/closed field line boundary (OCB), within which are open field lines which
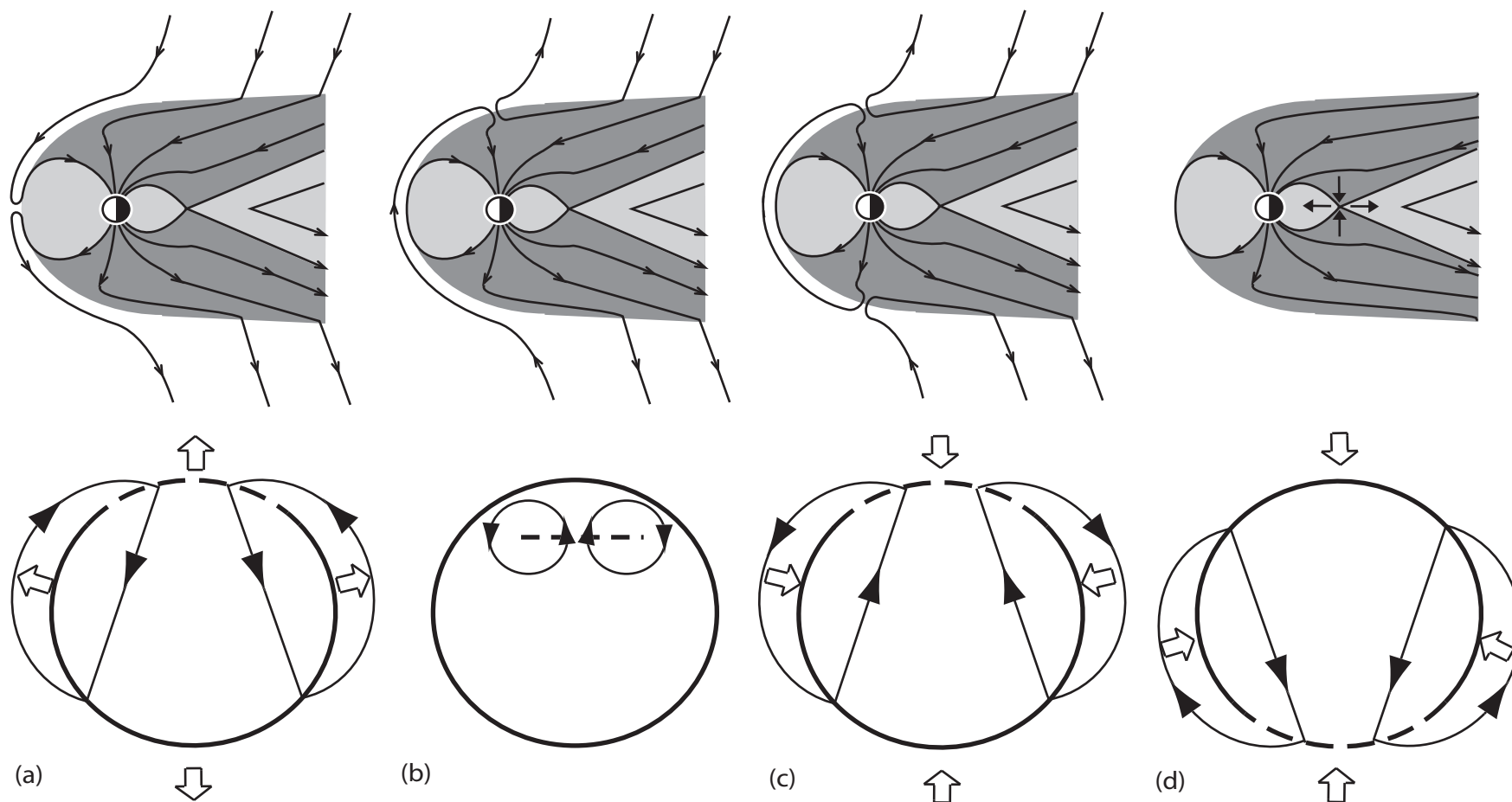
Figure 2.1. Schematic representations of the magnetosphere in the GSM X-Z plane (upper panels) and ionospheric convection patterns (lower panels) during (a) low latitude, (b) single lobe, (c) dual lobe and (d) tail reconnection. The convection schematics look down on the polar cap with local noon at the top of the Figure. The solid circle is the OCB, encircling the polar cap. The dashed portion of the OCB is the merging gap, the arrowed lines are flow streamlines and the large white arrows indicate expansion or contraction of the polar cap.

map to the lobes. Outside of the OCB are closed geomagnetic field lines, and the dashed portion is the merging gap which is the ionospheric footprint of the reconnection site. The black arrowed lines are flow streamlines. The addition of open flux results in the expansion of the polar cap which is indicated by the white arrows.

During a burst of reconnection there is flow across the merging gap therefore the OCB is locally non-adiaroic (i.e. the plasma is not moving with the boundary), but as soon as the reconnection stops (even though flows associated with that reconnection are ongoing), the entire OCB is adiaroic such that the plasma and the OCB move together (Siscoe and Huang, 1985).

2.1.2   *Lobe Reconnection*

During intervals of northward IMF ($B_Z > 0$) it is expected that lobe reconnection will occur (e.g. Dungey, 1963; Russell, 1972; Reiff and Burch, 1985; Milan et al., 2000). The IMF drapes over the magnetopause such that the orientation of the IMF is antiparallel to that of the open lobe field lines tailward of the cusp. Reconnection occurs between the IMF field line and the geomagnetic field line and in most cases the result is a field line with one footprint in the northern or southern hemisphere, and the other end draped around the subsolar magnetopause and into the IMF in the opposite hemisphere (Figure 2.1b shows lobe reconnection in the northern hemisphere). A combination of the magnetic tension force on the bent field line and the flow of the solar wind past the Earth results in the footprint of the field line being dragged initially sunward. Since it has remained open however, the footprint stays within the ionospheric polar cap (the region of open field lines within the auroral oval) and does not cross the open/closed field line boundary (OCB). The field line then moves around the side of the magnetosphere and is added to the magnetotail lobe. For northward IMF the ionospheric flows are expected to form two "reverse" convection cells in the noon sector, contained within the polar cap (Figure 2.1b), with East-West asymmetries introduced by the B_Y component of the IMF (Cowley and Lockwood, 1992, Huang et al., 2000). The open flux of the polar cap that shares in the circulation is said to be "stirred" (Crooker, 1992).

39

The polar cap size is not expected to change during this process as no flux is being added to or removed from the polar cap, unlike, for instance the action of low latitude magnetopause reconnection which causes an expansion of the polar cap (Figure 2.1a) (e.g. Siscoe and Huang, 1985; Cowley and Lockwood, 1992; Milan et al., 2003).

The ionospheric footprint of the reconnection site, or merging gap, shown by the dashed line in the lower portion of Figure 2.1b, is located inside the polar cap. Field lines that have just undergone reconnection contain plasma both of magnetospheric and solar wind origin. The solar wind plasma is able to gain direct entry into the magnetosphere via this field line, and although some of the plasma will mirror at higher altitudes, some particles precipitate into the upper atmosphere. This can lead to an auroral feature called a cusp spot (Milan, 2000; Frey et al., 2002, Fuselier et al., 2002) which is most easily observed using auroral imager data. Cusp spots can be used to indicate the location of the merging gap, and (together with other lobe reconnection ion signatures) are discussed further in Section 2.3 of this Chapter, and Chapter 6.

The electric field associated with the twin reverse convection cells was first observed using polar orbiting spacecraft. Heppner and Maynard (1987) combined electric field measurements made by the Dynamics Explorer 2 satellite with previous modelling work (e.g. Heppner, 1977) to characterise the convection electric field under different IMF conditions. The SuperDARN radar network (Chapter 3.1) enabled simultaneous observations of the entire convection pattern and a combination of statistical studies (such as Greenwald et al., 1995; Ruohoniemi and Greenwald, 1995) with theoretical modelling (Cowley and Lockwood, 1992) have greatly enhanced our understanding of the nature of solar wind-magnetosphere coupling.

Single lobe reconnection is expected to take place simultaneously, though independently, in both hemispheres when $B_Y \neq 0$. As will be described in Chapter 5, we might expect the efficiency in either hemisphere to be affected by the dipole tilt and B_X component of the IMF, the northern hemisphere being favoured for negative B_X and northern hemisphere summer (e.g. Crooker and Rich, 1993; Chisham et al., 2004).

2.1.3   Dual Lobe Reconnection

The site of lobe reconnection on the magnetopause changes with the orientation of the IMF, Milan et al. (2000) having demonstrated a B_Y-dependence of the location of the lobe reconnection footprint in the ionosphere from auroral observations. This was recently confirmed with simultaneous measurements in both hemispheres by Østgaard et al. (2005). When B_Y is non-zero, the displacement of the lobe reconnection sites in the northern and southern hemispheres means that different IMF field lines are reconnected in the North and South – the two processes are independent of each other and we refer to this as single lobe reconnection occurring in the two hemispheres.

If B_Y is close to zero it has been postulated that the same interplanetary magnetic field line can reconnect in both hemispheres. This reconnection process therefore starts with two open lobe field lines and the result is a closed geomagnetic field line, shown in the schematic in Figure 2.1c (after Lockwood and Moen, 1999) we will refer to this process as dual lobe reconnection, or DLR. This was first postulated to take place by Dungey (1963) and ever since has been a subject of some controversy. Conclusive evidence that this process takes place has only recently been observed and will be studied in more detail in Chapters 4 and 7. The ionospheric flows associated with DLR have not previously been discussed; in the lower portion of Figure 2.1c we show the flow pattern that we will propose in Section 4.1.

2.1.4 Tail reconnection

Magnetic reconnection can also take place in the tail as field lines in the northern tail lobe are oppositely directed to those in the southern tail lobe. These regions of oppositely directed field are separated by a thin current sheet. Flux buildup in the tail lobes due to low latitude reconnection results in an increase in the tail flaring angle, presenting a larger obstacle to the flow of the solar wind. The pressure inside the tail lobes therefore increases, which is thought to induce current sheet thinning and filamentation, leading to the onset of reconnection. Reconnection begins between closed geomagnetic field lines embedded within the plasma sheet at a point called the near Earth neutral line (NENL). Eventually open

lobe field lines begin to reconnect. Following reconnection a closed geomagnetic field line is formed which is accelerated earthwards, and an IMF field line is also formed which becomes part of the disconnected tail (Figure 2.1d). The amount of open flux in the polar caps is therefore decreased by tail reconnection, which results in a decrease in the tail flaring angle and induces reconfiguration of magnetic field lines in the lobes. In the ionosphere the polar cap will have magnetic flux removed only from a nightside portion and therefore will be in a non-equilibrium state. The ionospheric flow signatures of the magnetospheric field line reconfiguration will therefore be equatorward flow at the merging gap near midnight with adiaroic poleward flow at the OCB away from the merging gap as the total area of the polar cap has decreased. The resulting twin cell convection pattern is displayed in Figure 2.1d.

It is possible for the current sheet to thin in many places down the tail and many x-lines to be set up. The reconnection rate at each x-line dramatically increases when lobe field lines begin to reconnect, and therefore everything earthward/tailward of the first x-line to reconnect lobe field lines will be carried either earthward or downtail. Between the x-lines are structures called plasmoids which are flux ropes usually aligned in the GSM-Y direction (Figure 2.2). These flux ropes (and the corresponding travelling compression regions caused by the flux ropes compressing the tail lobes) can be detected by spacecraft in the tail and are a signature of tail reconnection taking place (e.g. Slavin et al., 2005).

The entire process from low latitude reconnection increasing the magnetic flux in the lobes, to tail reconnection closing that flux, is called the substorm cycle. Substorms are often identified using the AU or AL geomagnetic indices, discussed in Chapter 1.3.6. They may also be identified using auroral imagery, as tail reconnection accelerates plasma Earthwards, some of which precipitates into the upper atmosphere and generates auroral enhancements (e.g. Frey et al., 2004).

There is some evidence that tail reconnection is driven by overloading of flux in the tail lobes, as the onset of tail reconnection in the form of substorms can be related to upstream conditions with a delay of approximately 30-60 minutes (Cowley and Lockwood, 1992) and therefore the past history of dayside reconnection. Lockwood and Cowley (1992) were the first to directly relate the substorm cycle to Dungey cycle ionospheric convection, developing a model
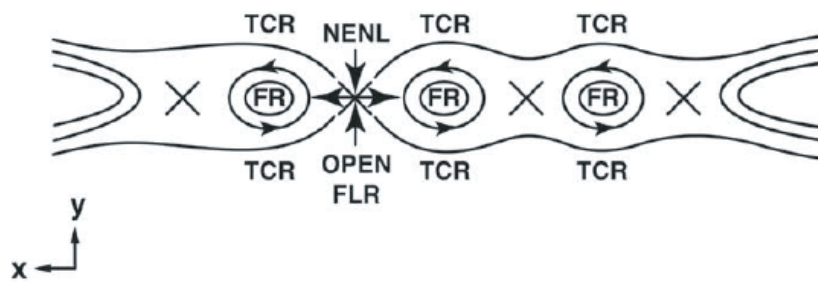
Figure 2.2. A schematic to show plasmoid formation in the tail in the GSM X-Y plane. The near Earth neutral line (NENL) has started to reconnect open field lines. Other reconnection sites in the tail are marked with black crosses, between which are flux ropes called plasmoids. Plasmoids to the left of the NENL will move Earthward, and those to the right will move tailward. From Slavin et al., 2005.

relating the amount of open flux in the polar cap to the dayside and tail reconnection rate.

2.1.5 Reconnection rates

At any given time, regardless of the IMF conditions, it is expected that reconnection will be taking place somewhere along the dayside magnetopause. The rate at which this reconnection is taking place provides information about the rate at which magnetic flux is being added to or removed from the polar cap and the extent of the ionospheric circulation.

The surface integral of the geomagnetic field (**B**) over the polar cap is related to the total amount of flux in the polar cap (F_{PC}) in the following way:

$$F_{PC} = \int_{PC} \mathbf{B}.d\mathbf{s}$$
[2.1]

The rate of change of magnetic flux in the polar cap is given by:

$$\frac{dF_{PC}}{dt} = \frac{d}{dt} \int_{PC} \mathbf{B}.d\mathbf{s}$$
[2.2]

Now applying Faraday's law [1.3] to [2.2]:

$$\frac{dF_{PC}}{dt} = - \int_{OCB} (\nabla \times \mathbf{E}).d\mathbf{s}$$
[2.3]

which by Stoke's Law can be rewritten as:

$$\frac{dF_{PC}}{dt} = - \oint_{OCB} \mathbf{E}.d\mathbf{l}$$
[2.4]

where d**l** is a small section of the OCB. So the rate of change of flux in the polar cap is equal to the integral of the electric field around the entire open/closed field line boundary. It is known that the OCB is adiaroic away from the merging gap, (in the frame of reference of the boundary, $\mathbf{E} = 0$) therefore the electric field need only be integrated along the merging gap in order to determine the rate of change of magnetic flux in the polar cap. This is equivalent to the reconnection rate, (Φ), and is measured in kV:

$$\Phi = \int \mathbf{E}.d\mathbf{l}$$
[2.5]

Depending on the nature and location of the reconnection site, the polar cap may be expanding or contracting, therefore the location of the merging gap is not

stationary. The reconnection rate is therefore the integral (along the merging gap) of the electric field in the frame of reference of the moving boundary:

$$\Phi = \int (\mathbf{E} + \mathbf{v} \times \mathbf{B}).d\mathbf{l} \qquad [2.6]$$

$\mathbf{E}$ is the ionospheric electric field measured in the frame of reference of the Earth, $\mathbf{v}$ is the poleward/equatorward velocity of the OCB.

The potential maps generated using the SuperDARN radar data (Ruohoniemi and Baker, 1998) enable a value of the convection driven electric field in the frame of reference of the Earth ($\mathbf{E}$) to be calculated anywhere within the polar caps (Chapter 3.1), regardless of whether there is data coverage in the sector of interest (although it is more accurate where the spherical harmonic fit of the potential is constrained by radar data points). Auroral images and spacecraft particle precipitation data can be used to determine the size and therefore the rate of expansion or contraction of the polar cap, giving the velocity of the OCB, $\mathbf{v}$. Combining this with the SuperDARN potential maps enables a value of the reconnection rate to be calculated, even if the polar cap is expanding or contracting (e.g. Chisham et al., 2004, 2008; Hubert et al., 2006).

The exact determination of the location of the OCB is often extremely difficult to accomplish. The electrostatic potential pattern produced by the map potential technique is divergence free and the potential is related to the ionospheric electric field by the relation $\mathbf{E} = -\nabla\Phi$. Instead of integrating the electric field along the OCB in order to obtain the reconnection rate, it can therefore also be calculated by the difference between the potential measured at each end of the merging gap, if the assumption of a stationary OCB is applicable. This is a far easier calculation to perform as the exact location of the merging gap along its entire length need not be known.

The lower portion of Figure 2.1 relates the location of the merging gap to the twin cell convection pattern for low latitude, lobe, dual lobe and tail reconnection. The centres of the twin cells in each case mark the edge of the reconnection-driven flow region and therefore the ends of the merging gap. It is important to note that the motion of the OCB must be taken into account when considering low latitude, dual lobe and tail reconnection as the amount of flux in the polar cap is changing. Lobe reconnection does not change the amount of flux in the polar cap, therefore the OCB (and the merging gap) is assumed to be stationary. The calculation of the lobe

reconnection rate can be performed solely using SuperDARN potential maps, as the difference between the potential at the centre of the twin reverse cells. The radar data coverage in the dayside portion of the polar cap must be sufficient to accurately constrain the spherical harmonic fit of the electrostatic potential pattern. Two SuperDARN northern hemisphere convection maps are plotted in Figure 2.3 on a latitude-magnetic local time grid, showing twin reverse cell convection patterns. The coloured vectors are the radar data, the black dots mark the centre of the twin cells, and the contours represent constant electrostatic potential, calculated using a spherical harmonic fit to the radar data as described above. The reconnection rate has been calculated for each example as the difference between the electrostatic potential calculated at the centre of each reverse cell and is recorded in the top right of each panel. Panel (a) shows an ideal example of excellent dayside radar coverage easily constraining the potential pattern, while panel (b) shows the more typical case, with more patchy radar coverage.

Petschek and Thorne (1967) first proposed that the rate of reconnection at a reconnection site should be proportional to $\sin\left(\dfrac{\theta}{2}\right)$, where θ is the angle between the interplanetary and magnetopause field lines. From there, Nishida and Maezawa (1971) and Sonnerup (1974) both developed a similar relation between the polar cap potential and the upstream IMF conditions:

$$\Phi \propto B\sin^2\left(\frac{\theta}{2}\right) \qquad\qquad [2.7]$$

Kan and Lee (1979) used geometrical considerations to include the length and orientation of the x-line and expressed the polar cap potential as:

$$\Phi = v_s B_s \sin^2\left(\frac{\theta}{2}\right)l_0 \qquad\qquad [2.8]$$

where v_s is the inflow speed of the plasma perpendicular to the magnetic field, denoted by B_s, θ is the angle between the two magnetic fields undergoing reconnection, and l_0 is the effective length of the x-line.

Holzer and Slavin (1979) first showed a relation between the geomagnetic activity index AL, and the upstream solar wind conditions, providing conclusive evidence for Dungey's open magnetosphere. Since then, various solar wind-magnetosphere coupling functions have been developed, perhaps the most commonly cited being of the form:
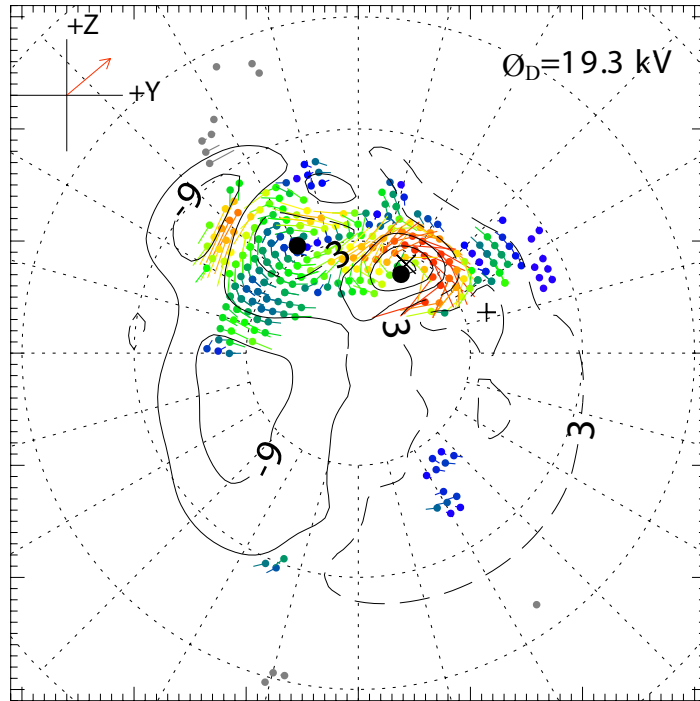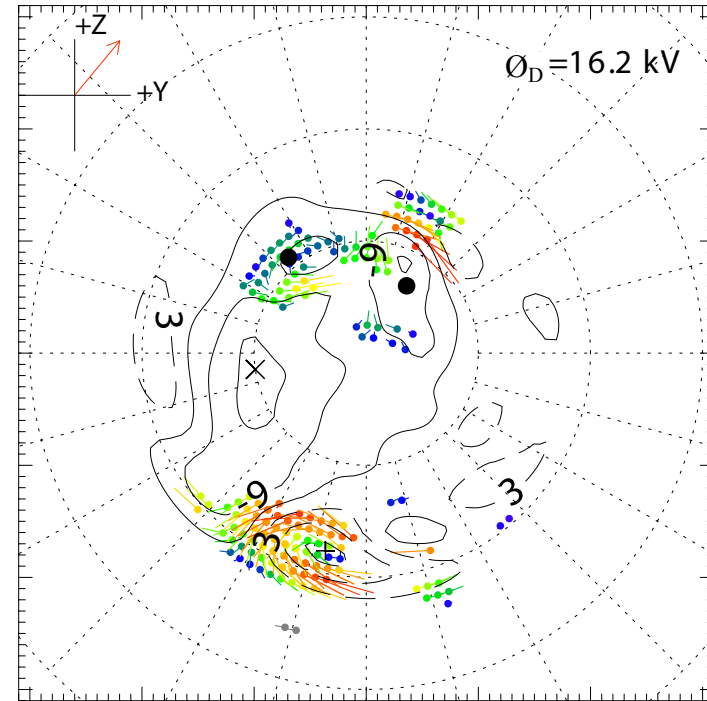
Figure 2.3 (a). An example of a SuperDARN potential map showing clear twin reverse convection cells. The contours are equipotentials and the vectors are SuperDARN convection velocities. The large black dots are the locations of the maximum and minimum of the potential pattern used to calculate $\emptyset_D$. (b). An example of a more typical SuperDARN twin reverse cell convection pattern, with the maximum and minimum in the potential pattern marked by black dots. The clock angle for each case is displayed in the top left corner of each panel.

$$\Phi_D = -L_D V_{SW} B_Z \qquad\qquad [2.9]$$

where L_D is the effective length of the reconnection line at the magnetopause, B_Z is the northward component of the IMF and V_{SW} is the velocity of the solar wind impinging on the magnetopause. $V_{SW} B_Z$ represents the Y-component of the solar wind motional electric field. Milan (2004) used the change in area of the polar cap as a proxy for the reconnection rate and calculated that for two case studies during southward IMF, L_D lies in the range 5-8 R_E.

2.1.6 Global Expanding/Contracting Polar Cap Model

The polar cap is the area of open magnetic flux at the poles, threaded by open, lobe field lines which are swept back by the force of the solar wind and form the lobes of the tail (Figure 2.1). Since closed field lines are defined as having a footprint in both hemispheres, the amount of magnetic flux within the polar cap in each hemisphere must by definition be the same.

The idea of a polar cap which expands and contracts according to the amount of open magnetic flux in the magnetosphere was first proposed by Russell et al. (1972). Later, Siscoe and Huang (1985) considered the implications of dayside merging assuming a circularly expanding polar cap. They developed the ionospheric flow pattern for the situation in which there is no nightside reconnection taking place, but the polar cap is expanding due to ongoing low latitude reconnection. This theory was taken further by Lockwood, Cowley and Freeman (1990) who considered the scenario of simultaneous dayside and nightside reconnection. They concluded that it is the balance between the rate of opening flux on the dayside (Φ_{day}) and the rate of flux closure on the nightside (Φ_{night}) that determines the overall rate of expansion or contraction of the polar cap.

$$\frac{dF_{PC}}{dt} = \Phi_{day} - \Phi_{night} \qquad\qquad [2.10]$$

where F_{PC} is the total magnetic flux within the polar cap (see Section 2.1.5).

It is possible that the dayside and the nightside reconnection rates may be exactly equal, and this would result in a steady auroral oval and a polar cap of constant size (Cowley and Lockwood, 1992). New flux would be created on the

dayside and destroyed on the nightside at an equal rate and therefore the familiar twin cell Dungey cycle flows would be present. Reconnection on the dayside does not tend to be steady due to variations in the magnitude and orientation of the IMF (e.g. Russell and Elphic, 1978, 1979; Haerendel et al., 1978; Kawano and Russell, 1996; Milan et al., 2003) and therefore this scenario is unlikely to exist for prolonged periods of time.

A number of studies have combined auroral imagery with SuperDARN potential maps to obtain the simultaneous dayside and nightside reconnection rates (e.g. Hubert et al., 2006; Chisham et al., 2008). Milan et al. (2003) measured the change in area of the northern polar cap using auroral images and spacecraft flybys and used this to infer the dayside reconnection rate given the assumption of no ongoing tail reconnection using [2.10]. This agreed extremely well with measurements of the dayside reconnection rate calculated using the SuperDARN radars (see Section 2.1.5).

2.2 The cold, dense plasma sheet

The stretched, closed field lines of the magnetotail contain hot, trapped plasma known as the plasma sheet. Embedded within the plasma sheet is the current sheet separating the two lobes of the tail. The average thickness of the plasma sheet is approximately 10 R_E and the average density is ~0.1-1 cm^{-3} (Kivelson and Russell, 1995). The average electron energy is ~ 1 keV, average ion energy is ~ 5 keV and the magnetic field strength is ~ 2-10 nT (Prölss, 2004).

The properties of the plasma sheet are observed to undergo a gradual change under steady northward IMF conditions. The temperature of the plasma decreases to less than 1 keV and the density of the plasma increases to ~1-2 particles cm^{-3} (e.g. Fujimoto et al., 1996; Terasawa et al., 1997; Øieroset et al., 2002). This is called the cold, dense plasma sheet, and its exact formation mechanism is unknown. It appears to contain a mixture of magnetosheath and magnetospheric plasma, primarily H^+. The absence of O^+ also implies that the source of the plasma sheet is the solar wind (Fujimoto et al., 1996, 1998, 2002; Fuselier et al., 1999; Phan et al., 2000; Rème et al., 2001).

The source of plasma sheet particles is thought to be the low latitude boundary layer (LLBL) which is the region near the magnetopause where the

transition from purely magnetosheath to magnetospheric particles is observed. It is thought that LLBL plasma diffuses towards the centre of the tail and can enter the plasma sheet. The plasma transfer mechanism for LLBL plasma across the magnetopause is as yet unclear. Øieroset et al. (2005) outlines three main theories; diffusion, Kelvin-Helmholtz instabilities and dual lobe reconnection.

Eastman et al. (1976) and Eastman and Hones (1979) suggested that the density gradient normal to the magnetopause boundary implies that particles diffuse across the boundary. Gary and Eastman (1979) suggested kinetic instabilities such as the lower hybrid drift instability as the driver of this diffusion, while Miura (1987) and others have suggested MHD instabilities such as Kelvin-Helmholtz waves as the driver.

A number of studies have observed the LLBL to consist of a series of steps in density rather than exhibiting a constant gradient (e.g. Paschmann et al., 1978; Sckopke et al., 1981; Ogilvie and Fitzenreiter, 1989). Song and Russell (1992) suggested that dual lobe reconnection could be the source of this step-like LLBL and enable magnetospheric capture of solar wind particle flux. Le et al. (1996) used spacecraft observations to show that during northward IMF the LLBL appears to consist of two distinct layers of plasma; an inner layer consisting of a mixture of magnetosheath and magnetospheric plasma, and an outer layer containing plasma injected from a single high latitude reconnection site. This was interpreted as evidence for sequential reconnection of an IMF field line with lobe field lines in each hemisphere (DLR). During DLR, newly reconnected field lines at the dayside magnetosphere shorten and sink to form the LLBL (Li et al., 2005; Lin and Wang, 2006). Li et al. (2005) have modelled the progression of these field lines around the flanks and into the tail. This theory is supported by Wing et al. (2006) whose observations show an increase in plasma sheet density in the flanks before the centre, and the CDPS has been observed more often nearer the flanks (Fujimoto et al., 1996, 1998; Phan et al., 1998; Fuselier et al., 1999; Oieroset et al., 2002). Wing et al. (2006) used upstream data to estimate the plasma sheet filling rate due to DLR as ~0.25 cm^{-3} hr^{-1} which was comparable to the observed filling rate of ~0.3 cm^{-3} hr^{-1} during that interval.

Øieroset et al. (2005) observed the formation of a cold, dense plasma sheet on 22nd-24th October 2003. This CDPS was observed both by DMSP and Cluster, with FAST observing a reverse dispersed ion signature indicative of lobe

reconnection taking place at the time. Li et al. (2005) compared the Cluster data with the results of an MHD model (with ACE data as the model input) and showed that the CDPS observed was likely to have been formed by plasma capture due to DLR.

Thomsen et al. (2003) selected 30 "superdense" plasma sheet events measured at geosynchronous orbit and analysed upstream conditions measured by ACE prior to the density enhancements. They concluded that the plasma sheet fills with cool, dense plasma under northward IMF conditions, then either a southward turning of the IMF or an interplanetary shock drives convection which injects plasma deeper into the inner magnetosphere.

2.3 Dispersed Ion Signatures in the Polar Cap

Solar wind/magnetosphere coupling is the main process responsible for the transfer of energy, mass and momentum into the magnetosphere. This coupling takes place via reconnection at the magnetopause; the exact location of the reconnection site has been shown to depend on the orientation of the interplanetary magnetic field (IMF). This section will specifically look at mass injection at the cusp. Lockwood and Smith (1994) and Lockwood (1995b) developed a model to explain the precipitation characteristics observed during southward IMF and this is reviewed below.

2.3.1 Southward IMF

Newly opened field lines generated by low latitude reconnection enable direct entry of solar wind plasma into the magnetosphere. Depending on the pitch angle of an individual particle, it may mirror at low altitudes or precipitate into the ionosphere. As the newly opened field line is dragged tailward by the magnetic tension force and the flow of the solar wind, plasma continues to cross the magnetopause. A wide spectrum of ion energies will cross the magnetopause from the magnetosheath along a given field line at any one time, dependent on the particle distribution in the magnetosheath. The position at which the field line crosses the magnetopause, at time t_n after reconnection, is denoted P_n in Figure 2.4a. The fastest ions will precipitate into the ionosphere first, and the slower ones will
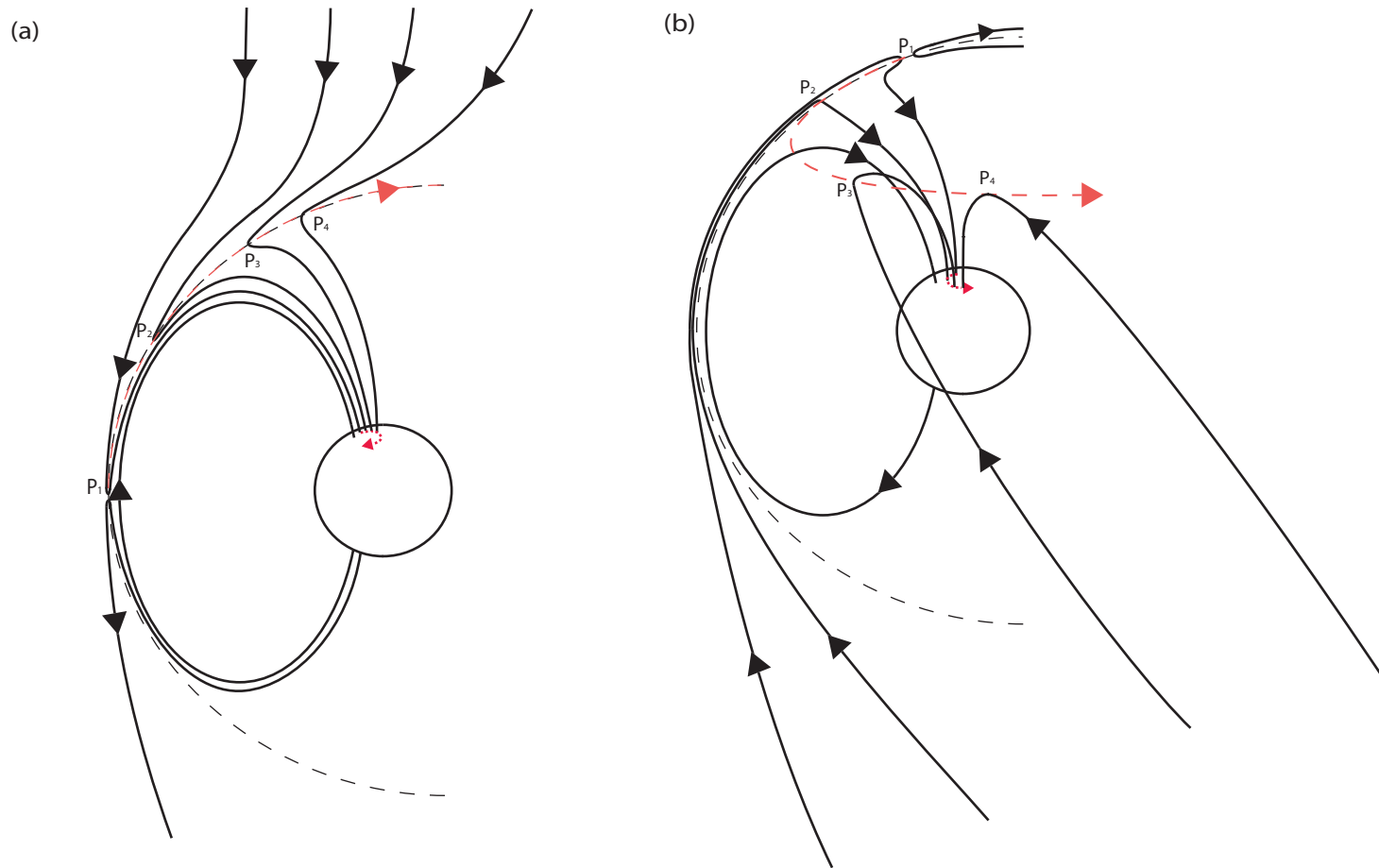
Figure 2.4. (a) A schematic to demonstrate the tailward progression of a newly reconnected field line. The IMF is southward therefore low latitude reconnection has taken place at the point P1. The point at which the reconnected field line crosses the magnetopause at a given time is represented by the points Pn which follow the trajectory of the red dashed line tailwards. The footprint of this field line is shown as the dashed red line in the ionosphere, which therefore also represents the associated ionospheric convection pattern. (after Lockwood, 1995b Figure 1). (b) A schematic to represent the evolution of a field line reconnected at high latitudes. The reconnection site is again denoted P1 with subsequent Pn values representing the point at which the field line crosses the magnetopause at later times. The field line initially moves sunward, then is swept around the flank and into the tail; the footprint of this field line is shown as the small red line in the ionosphere which forms a reverse convection cell.

take longer to reach the ionosphere. Since the footprint of the field line is moving polewards, the highest energy ions will be seen at the lowest latitudes and the ion energies detected will decrease with increasing latitude (Rosenbauer et al., 1975). This is called the velocity filter effect and is the main cause of the ion dispersion signatures seen by low altitude spacecraft, although many other effects also have an impact on the observed ion dispersion signature such as transient reconnection (e.g. Lockwood et al., 2001 and references therein). An example of a dispersed ion signature as seen by the Akebono spacecraft is displayed in Figure 2.5a (Mukai et al., 1990). The spacecraft is moving to higher latitude with time, and as it passes through the cusp it observes an ion population which is characterised by a decrease in energy with time.

2.3.2 Northward IMF

Under conditions of northward IMF, ion signatures with the opposite sense of direction have been observed (e.g. Bosqued et al., 1985; Woch and Lundin, 1992). In a similar way to the low latitude reconnection case, the highest energy ions injected at each position P_n (the point that a newly reconnected field line crosses the magnetopause) will travel fastest down the field line and be seen in the ionosphere first, while slower, lower energy ions will be seen later (Figure 2.4b). For lobe reconnection this therefore means that the highest energy ions will be seen at the highest latitudes, and the energy distribution of the detected ions will decrease as the footprint of the field lines initially moves sunward and to lower latitudes (Figure 2.5b). The ion dispersion signature is of the reverse sense to that seen during southward IMF conditions (Figure 2.5a). If the solar wind density is sufficiently high, an associated auroral signature, a cusp spot, can be identified poleward of the open/closed field line boundary (OCB) (e.g. Milan et al., 2000; Frey et al., 2002, Fuselier et al., 2002).

If the magnetosheath velocity at P_n (the point at which a newly reconnected field line crosses the magnetopause) is less than the Alfvén speed then it is expected that P_n will initially move sunward under the magnetic tension force and then antisunwards due to the tailward force of the solar wind on the open end of the field line. This is the condition required for steady rather than sporadic reconnection to take place, as a magnetosheath speed faster than the Alfvén speed will not allow
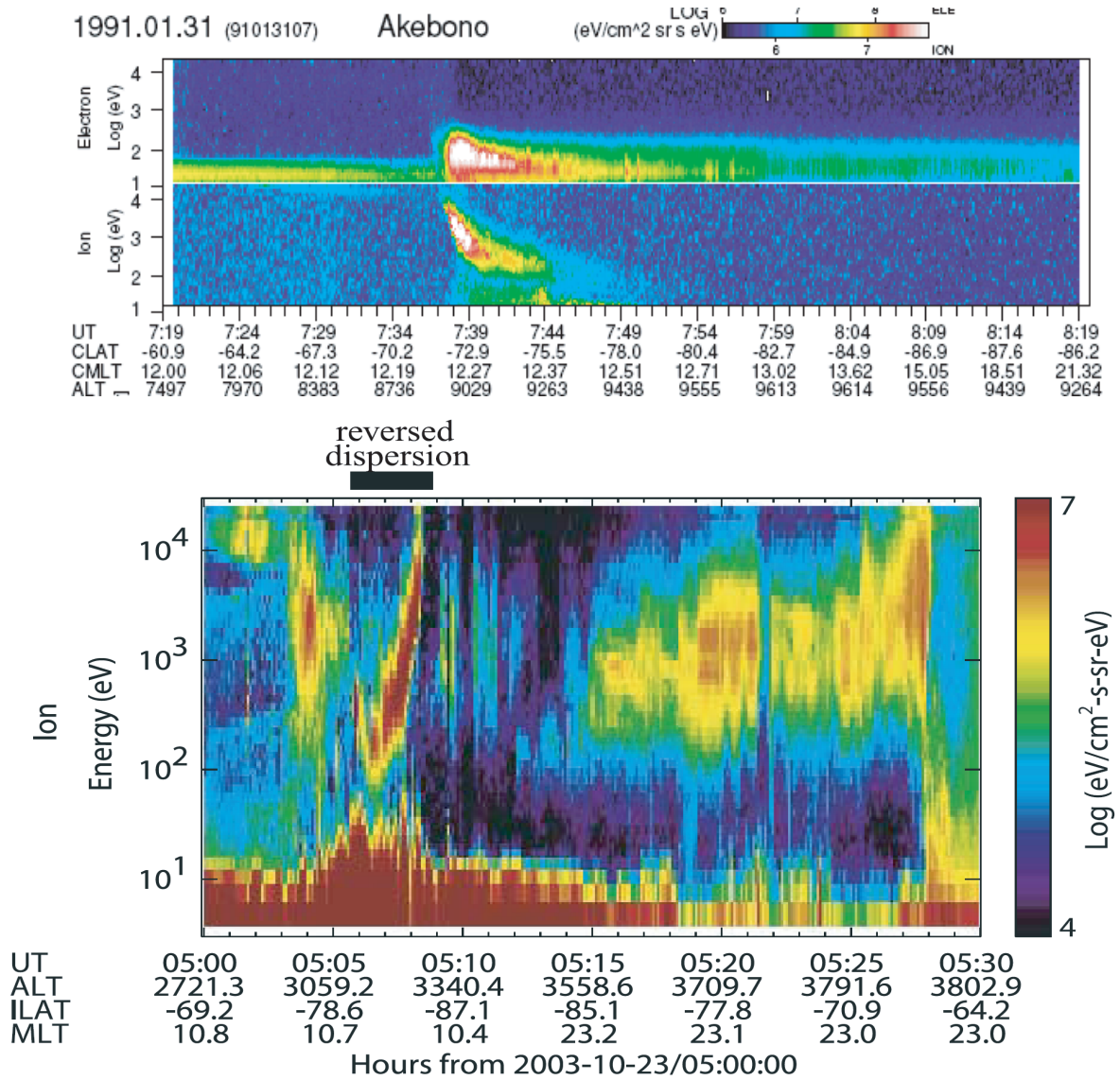
Figure 2.5. (a) A dispersed ion signature measured by the Akebono satellite on 31st January 1991. The field-aligned electron and ion differential energy fluxes are plotted against energy and time. The ion energies are decreasing with increasing latitude. From Asai et al., 2005. (b) A reverse dispersed ion signature measured by FAST on 23rd October 2003. Ion energies are observed to increase with increasing latitude in the region indicated by the black line. From Øieroset et al., 2005.

newly reconnected field lines to move sunward away from the reconnection site, and the reconnection site cannot remain static (Cowley and Owen, 1989).

2.3.3 The Cooling Model

The Cooling model (Cooling et al., 2001) was developed to ascertain the motion of newly-reconnected flux tubes over the magnetopause. The basis of the model is a combination of the Spreiter et al. (1966) magnetosheath gas dynamic model and models developed by Cowley and Owen (1989) and Kobel and Flückiger (1994). The user inputs the solar wind density, speed, the three components of the IMF and the bow shock and magnetopause standoff (R_{MP}) distances. The Cooling model then derives the shape of the magnetopause and bowshock based on a paraboloid fitted to the standoff distances defined by the user. The magnetopause and bowshock standoff distances and IMF strength and orientation are fed into the Kobel and Flückiger model in order to determine the magnetosheath field strength and direction. The magnetosheath flow speed and density can then calculated at any point on the magnetopause using the Spreiter et al. gas dynamic model given the assumption of a solar wind mach number of 8. The magnetosheath temperature and Alfvén speed at any point just outside the magnetopause can therefore also be calculated.

Having defined these parameters, the Cooling model then uses the user input of the reconnection site to decide the likelihood of reconnection taking place given those specific magnetosheath conditions. If this initial test is passed then the reconnection is initiated at a number of points along a merging gap and the Cowley and Owen model is used to determine the velocity of the newly reconnected flux tubes along the magnetopause. The cusp location in GSM coordinates is set to be [½R_{mp},0,±R_{mp}] and the geomagnetic field just inside the magnetopause is assumed to be always tangential to the magnetopause.

The Cooling model then moves the position P_n of the flux tube on the magnetopause one time step forwards based on the Cowley and Owen flux tube velocity model and then recalculates the magnetosheath parameters at the new position using the Spreiter et al. model. The Cowley and Owen model is then applied again to determine the velocity of the flux tube along the magnetopause and in this way the position of the flux tube can be calculated over a finite number of

timesteps or until the extent of one of the models is reached, for example at large distances from the subsolar point where the model magnetosheath parameters become unphysical.

A depletion layer is often thought to be formed under northward IMF conditions where field lines can be draped over the dayside of the magnetosphere for comparatively long periods of time (e.g. Zwan and Wolf, 1976; Petrinec et al., 2003). Plasma on these field lines is squeezed away from the field line stagnation point by the pressure of field lines piling up behind it and therefore the magnetosheath density just outside the magnetopause is lower than expected. The Cooling model magnetosheath density can be modified to include this effect simply by multiplying the magnetosheath density everywhere by a density reduction factor, which is an optional input to the model.

2.3.4 The Lockwood model of ion dispersion under Southward IMF

Lockwood and Smith (1994) and Lockwood (1995b) developed a model to consider the ion population seen by a low-altitude spacecraft flying at the base of newly-reconnected field lines such as the signature observed by the satellite Akebono in 1991 displayed in Figure 2.5a. Reconnection is initiated at low latitudes and the highly kinked, newly reconnected field line moves poleward under the magnetic tension force and the force of the solar wind (Figure 2.4a). The point P_n at which the newly reconnected field line crosses the magnetopause is considered a site at which ions are injected from the magnetosheath and is calculated according to the model of Spreiter et al. (1966). The injected ion distribution function depends on the magnetosheath properties at the point P_n, and these vary across the magnetopause. The rotational discontinuity in the field line is assumed to obey ideal MHD as ions are accelerated across the magnetopause (MP) boundary but not heated, and the pitch angle of the particles is assumed to be conserved.

The ion energy distribution at the footprint of a newly reconnected field line as it evolves with time is dependent upon four factors:

1. The incident ion population

The ion population on the magnetosheath side of the newly reconnected field line is assumed to have a Maxwellian form, with ion energies dependent upon the magnetosheath conditions at the point P_n. Those ions crossing the magnetopause at low latitudes come from a dense, hot, slow magnetosheath, therefore the bulk energy of the incident ion population will be lower than at later times when the field line has evolved to higher latitudes, the magnetosheath density is lower and the magnetosheath velocity is higher.

2. The topology of the rotational discontinuity

The energy of the injected ion population will also depend upon the amount of energy given to each ion as it travels along the newly reconnected and highly kinked field line and crosses the MP. At the initial time of reconnection the energy of each ion crossing the MP increases by an amount corresponding to the de Hoffman Teller (DHT) velocity, V_{fx}, which is the velocity of the field line (the point P_n) away from the x-line in the frame of reference of the Earth. As the newly reconnected field line moves tailward and to higher latitudes, the kink in the field line will straighten out (Figure 2.4a) and ions travelling down this field line will receive less energy as they cross the MP. When the field line has evolved to sufficiently high latitudes to pass through the cusp, ions passing across the MP will be decelerated and lose energy as the field line has straightened out.

3. The velocity filter effect

The ion population injected at a point P_n on the magnetopause will not be the same as that seen at low altitudes as the highest energy ions move down the field line the fastest and therefore will reach low altitudes in less time than the lowest energy ions. Ions are injected continually across the MP along the newly opened flux tube following reconnection. A low altitude spacecraft will therefore see a range of ion energies at any one time; each ion energy corresponds to a different injection point P_n on the magnetopause. The

highest energy ions will be ones that were injected most recently, and the lowest energy ions will have been injected earlier.

4. The distance from P_n to the ionosphere (*di*)

From Figure 2.4a it is clear that the distance that the injected ions have to travel to the ionosphere changes as the field line evolves to higher latitudes. As the field line goes from P_1 to P_4 (the cusp) this distance, *di*, is decreasing, therefore lessening the velocity filter effect on the ion energy distribution seen at low altitudes. From position P_4 onwards the distance *di* is increasing, therefore the ion energies injected beyond this point will be observed over an increasingly longer time frame.

Figure 2.6 taken from Lockwood (1995b) shows the distribution of ion energies seen at the footprint of a field line as it reconnects and moves poleward. The time at which the field line reconnected is t_s=0, and in order to follow the signature at low altitudes on a single field line, time increases from right to left. The dashed lines show the ion energies injected at various points P_n along the magnetopause.

At point P_1 in Figure 2.4a when the field line has just reconnected, only the highest energy ions are seen at low altitudes. With time, the slower ions from the point P_1 also reach low altitudes, along with faster ions subsequently injected along that field line (for instance at P_2), therefore a spread of ion energies is observed. The solid lines show the maximum and minimum ion energies reaching low altitudes at time *t* (E_{max} and E_{min}). By the velocity filter effect, E_{min} at low altitudes will be the lowest energy ion injected at the earliest detectable point. The ion population incident on the MP along a field line after it has passed through P_1 will be increasing in energy with time, as the magnetosheath velocity increases away from the subsolar point. The amount of energy given to each ion as it crosses the MP will be decreasing with time as the field line straightens out. Near the subsolar point the minimum energy of injected ions will increase as the changing magnetosheath conditions dominates the other effects, however as P_n moves to high latitudes and the field line straightens out, the injected ion population will decrease
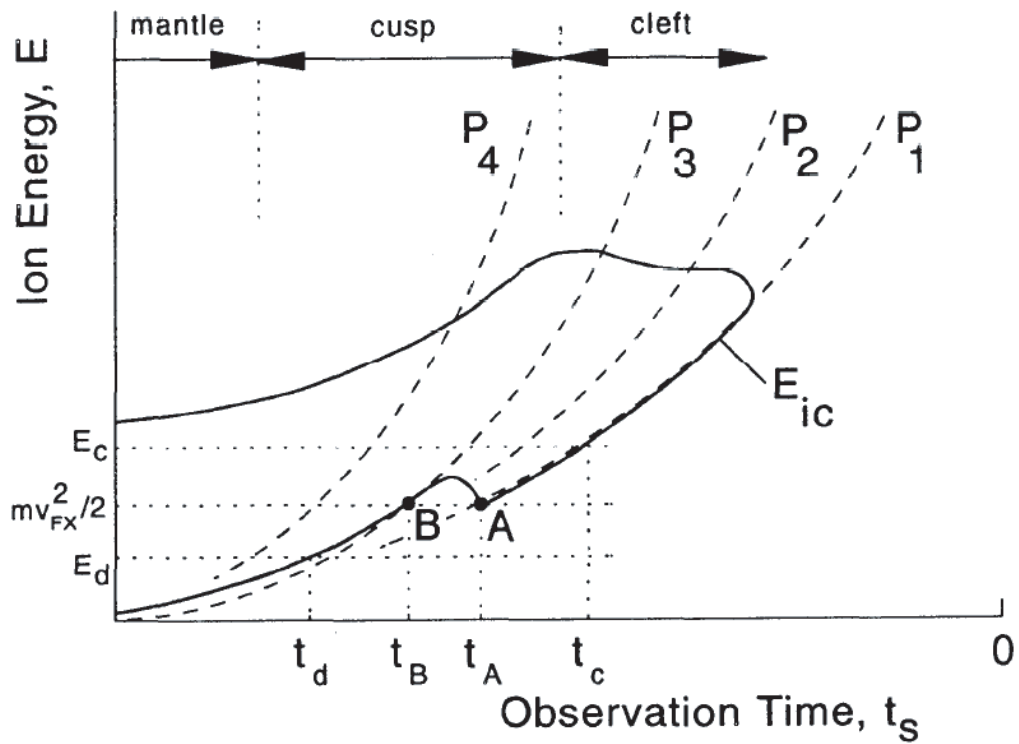
Figure 2.6.   Modelled cusp ion precipitation seen by a satellite moving equatorward following a period of low latitude reconnection. P_1 represents the position at which reconnection took place and the field line the evolves to positions P_2, P_3 and P_4. A range of ion energies are injected at any one time, here represented by dashed lines. E_{ic} in this Figure is the same as E_{min} and represents the minimum observable energy at a given time, while E_{max} is the maximum observable energy. (Taken from Lockwood, 1995b Figure 2).

in energy. This results in a small local maximum both in E_{max} and in E_{min} between points P_1 and P_3 but following this the ion energies decrease with time as the ions are decelerated across the MP.

When considering the particle signature seen by a low altitude spacecraft, it is assumed that the velocity of the spacecraft is much higher than the convection velocity of the individual field lines, such that it appears to fly through a static feature. Lockwood is considering a spacecraft moving sunward over the polar cap. The ion dispersion signature seen by the spacecraft is therefore the reverse of that seen at the footprint of a moving field line following reconnection, as the spacecraft will observe the ion signature of field lines at the higher latitudes first, then subsequent field lines until it approaches the footprint of the merging gap. The spacecraft will stop seeing ions some time before it reaches the footprint of the merging gap, equal to the time of flight of the highest energy ions from the point P_1. The spacecraft will measure the energy of the ion population such that this time of flight and therefore the location of the merging gap can be estimated.

The spectrum of ion energies observed by the low altitude spacecraft will also depend upon the trajectory of the spacecraft relative to the velocity of convecting field lines. If the spacecraft is making a longitudinal rather than a latitudinal cut across the polar cap then it is unlikely that it will see a significant ion dispersion signature as the convection direction of the field line footprints is assumed to be antisunward.

The particle energy distribution in the magnetosheath is considered isotropic, but only those particles with a field parallel component of velocity that is towards the magnetopause can enter the magnetosphere. Crossing the magnetopause these particles are accelerated along the field direction, resulting in the Cowley-D ion distribution (Cowley, 1982) displayed in Figure 2.7 on log-linear axes. The ion distribution function marked P_1 is that injected across the magnetopause at the time of reconnection. Each particle crossing the reconnection site is given a velocity equal to the DHT velocity of the field line, V_f, tangential to the magnetopause such that the distribution function is a truncated maxwellian with a minimum velocity equal to V_f. Subsequent distribution functions injected across the magnetopause are marked P_n where the approximate location of the corresponding field line is shown in Figure 2.4a.
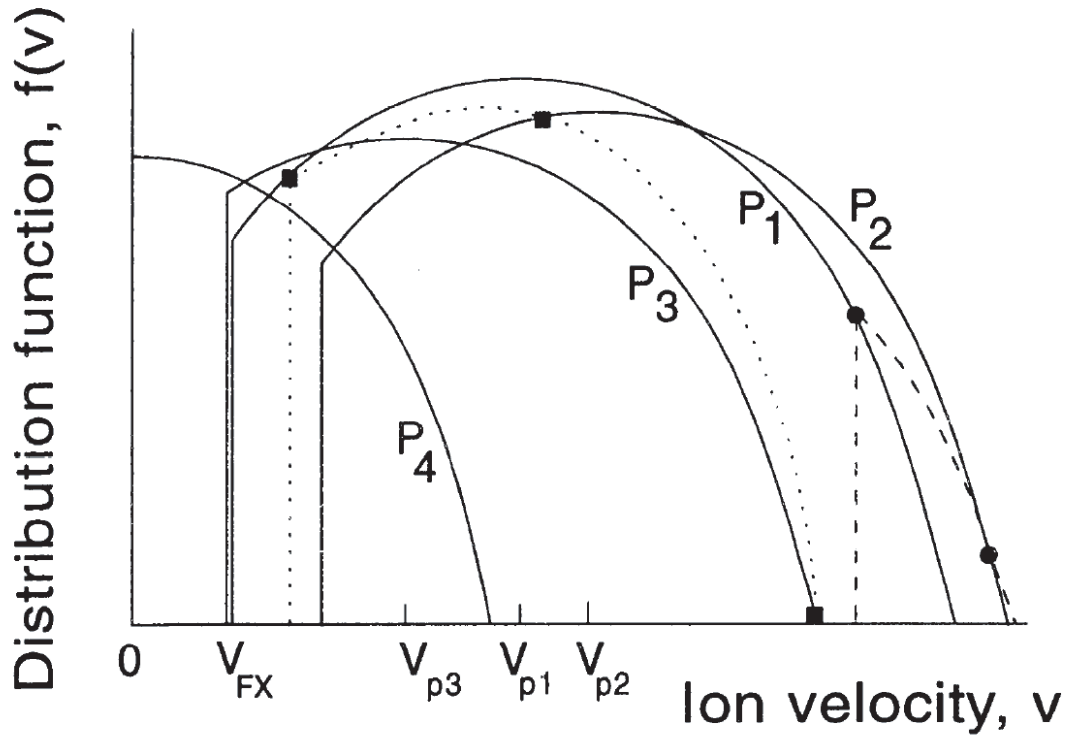
Figure 2.7. The modelled distribution function of ions reaching low altitudes. Only ions with a strong field-aligned component of velocity will reach low altitudes without mirroring. The initial Maxwellian distribution function is therefore truncated such that particles travelling anti-parallel to the field will not be observed at low altitudes, and the entire distribution function is dispersed according to Figure 2.7. (From Lockwood, 1995b, Figure 4).

Figure 2.8 shows the rotational discontinuity of a newly reconnected field line in the GSM *X-Z* plane, and in velocity space, V_X-V_Z. The vertical Z axis corresponds to the magnetopause, with the magnetosheath on the left and the magnetosphere on the right. Lockwood assumes that the Alfvén speed and the magnitude of the magnetic field is the same on both sides of the boundary. V_f is the velocity of the point P_n along the boundary. θ and ϕ are the angles between the magnetopause and the newly reconnected field line on the magnetopause and sheath sides respectively.

Plasma travels with a velocity equal to the sheath velocity, and P_n travels with velocity equal to the de Hoffman-Teller velocity in the Earth's reference frame. Plasma will cross the magnetopause only if the de Hoffman-Teller velocity is greater than the particle (i.e. sheath) velocity. The lowest velocity of any injected ion at a time *t*, will therefore be an ion with zero velocity in the de Hoffman-Teller frame, i.e.

$$V_{min} = V_f \cos\theta \qquad [2.9]$$

where the velocity of the point P_n along the magnetopause in the Earth's frame is given by:

$$V_f = V_{sh} + V_A \cos\phi \qquad [2.10]$$

V_A is the Alfvén velocity at the point P_n. Pressure balance conditions dictate that the peak of the Maxwellian distribution must be travelling at the Alfvén speed in the de Hoffman-Teller frame, such that this peak velocity in the frame of reference of the Earth is:

$$V_p = V_f \cos\theta + V_A \qquad [2.11]$$

The cutoff energy of the Cowley-D distribution for a given P_n is therefore

$$E_{min} = m\frac{v_{min}^2}{2} = \frac{m}{2}\left[\left(V_{sh} + V_A \cos\phi\right)\cos\theta\right]^2 \qquad [2.12]$$

which represents the minimum injected energy at the point P_n. Lockwood (1995b) modelled the distance, from the point P_n along the field line to the ionosphere (*di*), and together with the equations given above, and the Spreiter gas dynamic model supplying the magnetosheath parameters at each P_n, modelled the ion dispersion signature that a low altitude spacecraft flying over the polar cap would see.

Lockwood further studied the effects of time-dependent reconnection which results in steps in the ion dispersion signature (e.g. Lockwood, 1995a; Lockwood
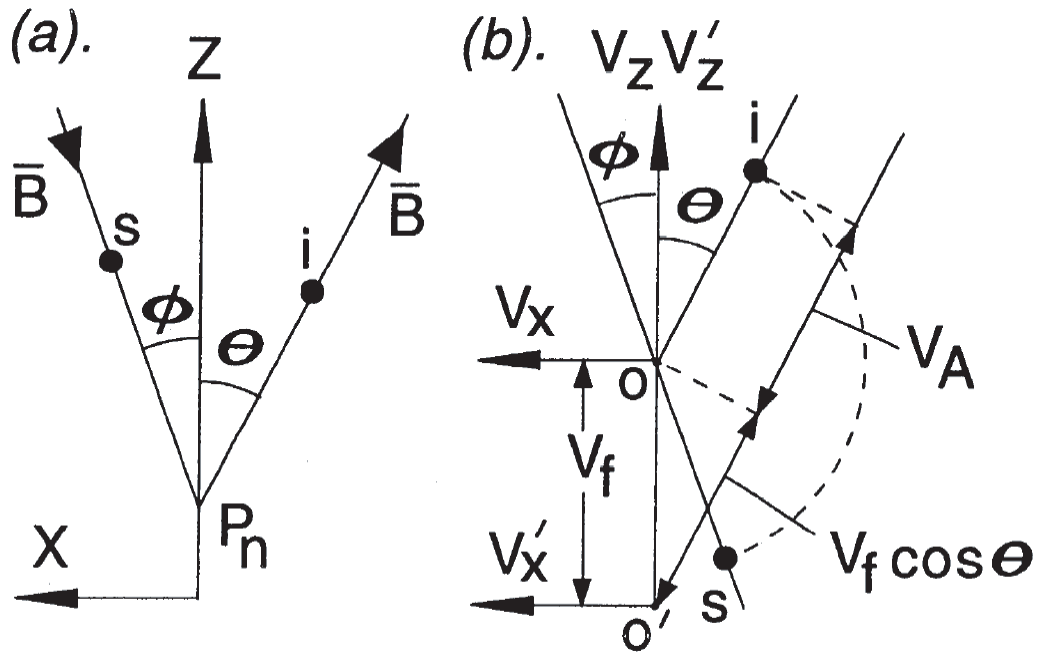
Figure 2.8. A schematic to show the topology of the rotational discontinuity in the Lockwood model for low latitude reconnection. (a) The Z-axis represents the magnetopause, so to the left of that is sheath field, and to the right magnetospheric field. The angles phi and theta are the angles between the sheath and magnetospheric field and the magnetopause current sheet itself. P_n, the point at which the field line crosses the magnetopause is also shown. (b) A schematic of the rotational discontinuity in velocity space, with the V_Z-axis representing the magnetopause. The newly reconnected field line initially moves away from the reconnection site with velocity $V_f = V_A$. Each ion crossing the magnetopause is given a minimum energy V_{min} corresponding to $V_f \cos\theta$. (Taken from Lockwood, 1995b, Figure 3).

and Davis, 1995; Lockwood et al., 1998; Lockwood et al., 2001; Morley and Lockwood, 2003) however this is not relevant to the work in this thesis and will not be discussed further.

Chapter 3. Instrumentation

In this thesis, a significant number of different observations and measurement techniques will be used, some ground-based and some space-based. This chapter will summarize the main features of the instruments.

3.1 The SuperDARN radar network

The Super Dual Auroral Radar Network (SuperDARN) consists of twelve radars in the northern hemisphere and seven in the southern hemisphere (Greenwald et al., 1995; Chisham et al., 2007). These radars are coherent high frequency radars which are designed to measure ionospheric plasma $\mathbf{E} \times \mathbf{B}$ motion. All of the radars are virtually identical in design. Each consists of two arrays of antennas; one is made up of sixteen masts which transmit the high frequency radar beam and receive the backscattered signal, and the other is an interferometer array consisting of four masts which receive only. The radars are capable of transmitting radio waves in the frequency range 8-20 MHz. The radar beam is steerable using a phasing matrix and in normal operations mode it looks in 16 beam directions, sweeping over a total azimuthal angle of 52°. The dwell time on each beam is 7 seconds such that a full beam sweep takes 2 minutes. If greater temporal resolution is required then the dwell time can be reduced to 3 seconds such that each full sweep takes one minute. SuperDARN can run in many modes, most often doing a beam sweep through all 16 beams with a dwell time of 7 seconds per beam, sweeping quickly through a small number of beams concentrating on a specific area, or sweeping through frequency bands to find the band which generates the most backscatter. The fields of view of these radars are displayed in Figure 3.1.

3.1.1 The HF radar technique

There are two main types of plasma instability present in the E and F regions of the ionosphere which can lead to scatter of a radar signal. The first is present in the E region only and is due to the ions suffering collisions with the neutrals while the electrons convect with the $\mathbf{E} \times \mathbf{B}$ drift velocity (see Chapter 1.3.7). This
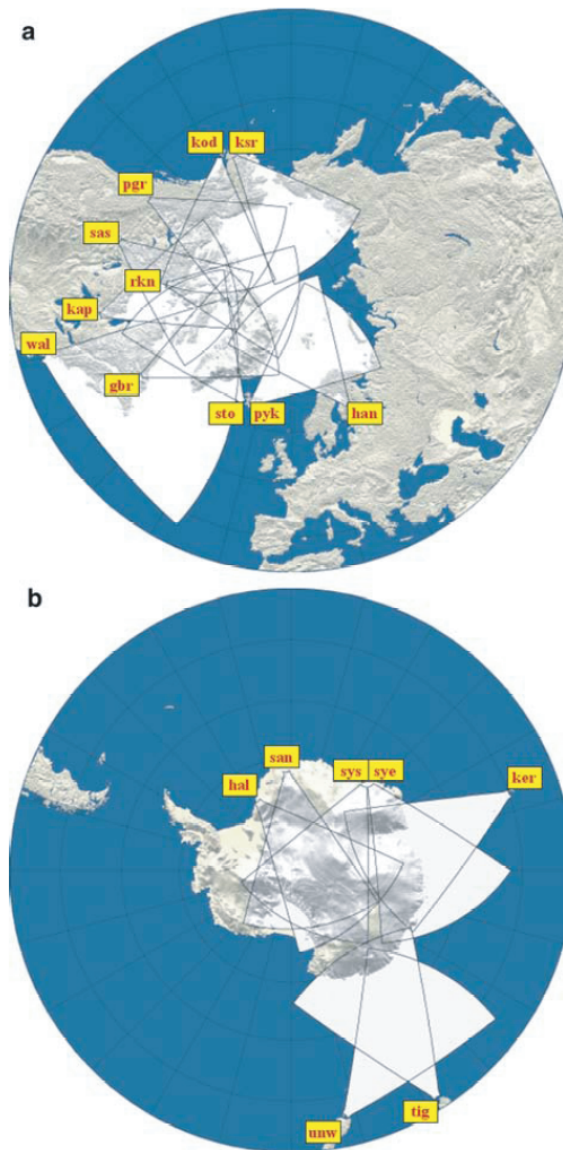
Figure 3.1. Fields of view of (a) northern and (b) southern hemisphere SuperDARN radars. From Chisham et al., 2007.

difference in the velocities of ions and electrons leads to the two stream instability. This generates irregularities typically at the ion-acoustic speed, ~400 m s^{-1}, which move more slowly than the $\mathbf{E} \times \mathbf{B}$ convection velocity. The second type of plasma instability is the gradient-drift instability which produces irregularities moving at the $\mathbf{E} \times \mathbf{B}$ convection velocity in the F region. In this region neither the electrons nor the ions are impeded by collisions with neutrals and the two-stream instability does not form. In order to measure the $\mathbf{E} \times \mathbf{B}$ convection velocity it is therefore necessary to receive backscatter only from F region plasma, therefore frequencies in the HF rather than the VHF range are used (Milan et al., 1997).

The atmosphere appears horizontally stratified on the scale length of a high frequency radio wave passing through it such that it will be refracted as it travels. In addition, each time the incident wave encounters an irregularity it will scatter in all directions with most of the power continuing on the original ray path. The scattered power from each irregularity will either constructively or destructively interfere; with the greatest amplitude created by irregularities that are regularly spaced such that the distance between them is equal to an integer number of half wavelengths of the incident wave. Irregularities in the E and F regions tend to be field aligned because ions and electrons are frozen to the field such that they can easily travel along field lines but not easily travel perpendicular to them (Chapter 1.1.6). The result of this is that in order for radio waves to constructively scatter from the irregularities and return to the radar along the same ray path the incident radar beam must be refracted until its direction of travel is perpendicular to the magnetic field lines (and therefore also perpendicular to the irregularities). Figure 3.2 shows various modes of propagation. Some rays penetrate the ionosphere (ray C). Others can be refracted back to the ground, resulting in some energy being scattered back to the radar to be detected as ground backscatter. Energy is also forward-scattered into subsequent hops and the signal returning from the F region ionosphere (ray B) can give the following information about the ionospheric conditions:

1. The Doppler shift of the return signal allows the velocity of the irregularities along the line-of-sight to be determined. Given the frozen-in approximation, the velocity of the irregularities is the $\mathbf{E} \times \mathbf{B}$ convection of the bulk plasma in the ionosphere which corresponds approximately to the convection of the footprint of the magnetic field lines along which the irregularities are

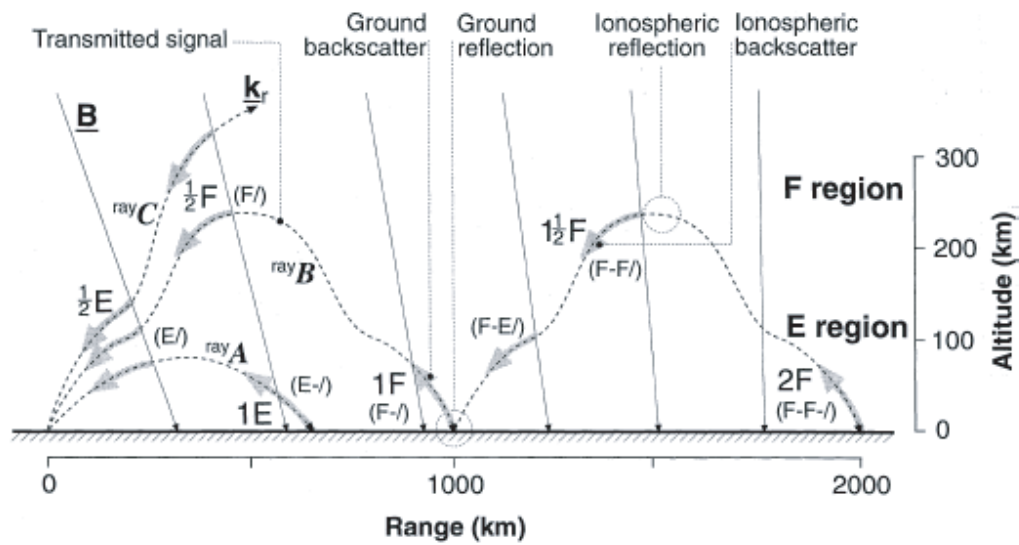Figure 3.2. A schematic to show the primary propagation paths of a transmitted radar beam. Some of the beam is not scattered at all and penetrates the ionosphere (ray C). Some is backscattered from the F region having performed a non-integer number of hops, and some is scattered from the ground (ray B). Other return signals received by the radars could be due to E region scatter (ray A). From Milan et al., 1997.

aligned. The main driver of this ionospheric convection is reconnection both at the dayside and in the tail, therefore analysis of the global ionospheric convection pattern provides information on processes taking place in the outer magnetosphere.

2. It is also possible to calculate the spectral width of the return signal. Perfect reflection would give a return signal that had the same spectral width as the incident ray, however usually the return signal is spectrally broadened, and this can be due to a number of causes, two of which will be outlined here.

    The first is that within the same beam width or integration time it is unlikely that all of the convection will be constant. There may be flow reversals or small scale structures which give a range of Doppler shifts, resulting in the reflected beam having a range of frequencies rather than just the incident frequency.

    The second is due to the nature of the density irregularities which scatter the incident ray. These irregularities are not stable and therefore grow and decay with time. The result of this is that a number of return frequencies can be returned from a single incident beam and this acts to broaden the spectral width of the return signal.

    The spectral width therefore gives information about the nature of the density perturbations in the E and F region, specifically their spatial uniformity and their transience.

3. The final piece of information about the return beam that is of use is the backscatter power. This gives a measure of the regularity and depth of the density perturbations off which the radar wave is scattering. If the irregularities in density are large and uniformly spaced then the power of the return signal will be greater. This is because more of the incident beam will have reflected from each irregularity, and the scatter from each will have constructively interfered with the others to create a stronger signal. Power can also be affected by focusing or defocusing of the radio waves and attenuated by non-deviative absorption in the D-region.

3.1.2 The SuperDARN pulse sequence

The radars do not transit continuously, but in a sequence of 7 pulses. The separation of the pulses allows an autocorrelation function (ACF) to be measured, from which power, Doppler shift and spectral width can be determined.

The radars are unable to transmit and receive pulses simultaneously therefore it is only some time following transmission of a pulse that the radars can then receive the scattered signal. There is a short period of time after transmission during which there is no return as the radar beam has not had time to reach any scattering irregularities and return to the radar; this is called the time to first range, or t_0 and is usually of the order of 1200 μs, corresponding to 180 km in the ionosphere. The radars usually bin the scatter they receive back in 75 range gates. The transmitted pulse length determines the length of these range cells which are usually 45 km each. When the radar is running 2 minute beam sweeps then the range to the first gate is 180 km and the range to the furthest gate is 3550 km with a pulse length of 300 μs. Thus it takes approximately 24 ms for pulses to return from the furthest ranges.

3.1.3   Determination of the range, velocity, spectral width and backscatter power

During normal operating mode the SuperDARN radars emit a sequence of seven pulses in a cycle. This cycle is 100 ms in duration, and is repeated 70 times during the 7 second dwell time on each beam direction. The pulse sequence for each cycle is displayed in Figure 3.3. Each pulse is 300 μs long, spaced in such a way that it is possible to compare returning pulses sent out at different times. The time between two pulses that are to be compared will be an integer number of "lags", with one lag usually being 2.4 ms. The pulse sequence shown in Figure 3.3 maximises the number of returning signals with different lags between them that it is possible to compare; the arrowed lines demonstrate the pulses to be compared in order to obtain the corresponding integer number of lags, marked 0 to 27 in the left hand column. The lines marked "missing" are where it is not possible to compare two signals with that number of lags between them. In most data analysis techniques, the first calculable 18 lags are used. Since each cycle is repeated 70
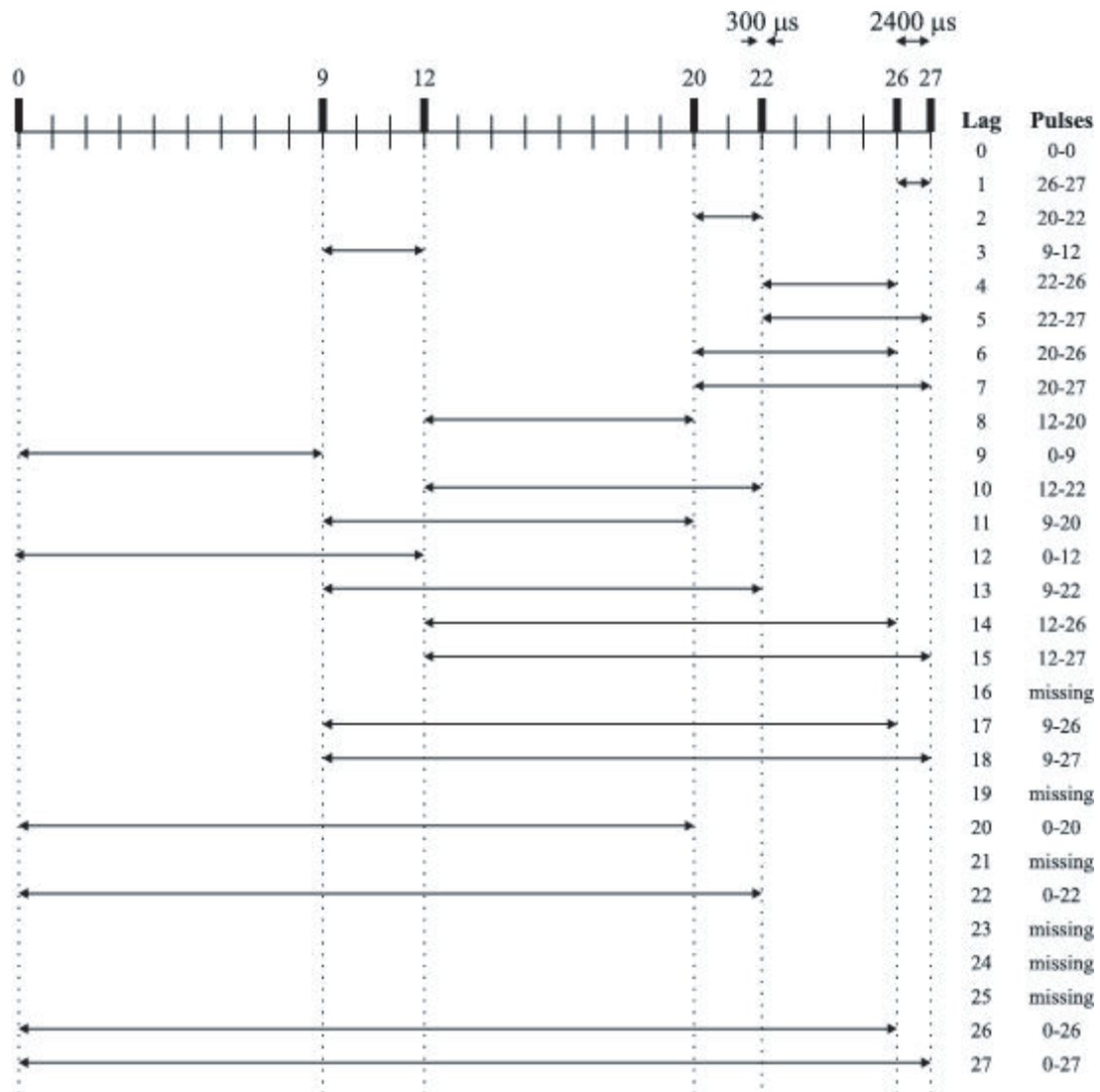
Figure 3.3. Pulse sequence for standard radar operating mode. Pulses are sent out at the times given by the thick black lines at the top of the Figure. Returning signals from various combinations of pairs of these pulses can be compared to obtain a signal at a variety of lags. From McWilliams, 2001.

times during each 7 second beam time, the 70 autocorrelation functions produced for each lag are averaged for greater accuracy.

The autocorrelation function (ACF) of each of the pairs of pulses separated by increasing lag times are computed and the phase difference between the real and the imaginary parts are plotted for each lag. The gradient of the phase against lag graph gives the Doppler frequency which can then be transformed into the Doppler velocity. The ACF will decorrelate with increasing lag, as the time separation of the returning signals increases. The spectral width and the backscatter power can be determined from the amplitude of the ACF with increasing lag.

3.1.4 The map potential technique

The map potential technique is a method of combining all of the SuperDARN radar data available in one hemisphere at a given time into a single convection map (Ruohoniemi and Baker, 1998). The individual radars are only able to provide line-of-sight velocity information and therefore traditionally it has only been possible to know the 2-D velocity of the plasma in the regions where radar fields of view overlap. Although the number of SuperDARN radars has increased in recent years providing much improved coverage of the northern and southern polar caps, there are still many areas in which there are no overlapping fields of view, so a technique such as map potential which does not require this in order to produce 2-D convection maps has been extremely valuable.

The map potential technique uses line of sight convection velocities measured by the radars to constrain a spherical harmonic fit of the electrostatic potential. In areas where the radar coverage is sparse a statistical electrostatic potential pattern helps to constrain the fit. This statistical model is based on average potential maps given specific upstream IMF orientation and magnitude. The input of the model to the final potential map is weighted such that the map is driven by the radar data available and the model is only used to constrain the spherical harmonic fit where there is no data. From this potential map the ionospheric convection flow can be determined and is usually plotted only at the location of real radar data (Figure 3.4).

It is possible to change the order of the spherical harmonic fit that is used to represent the potential, however usually orders higher than 8 do not significantly
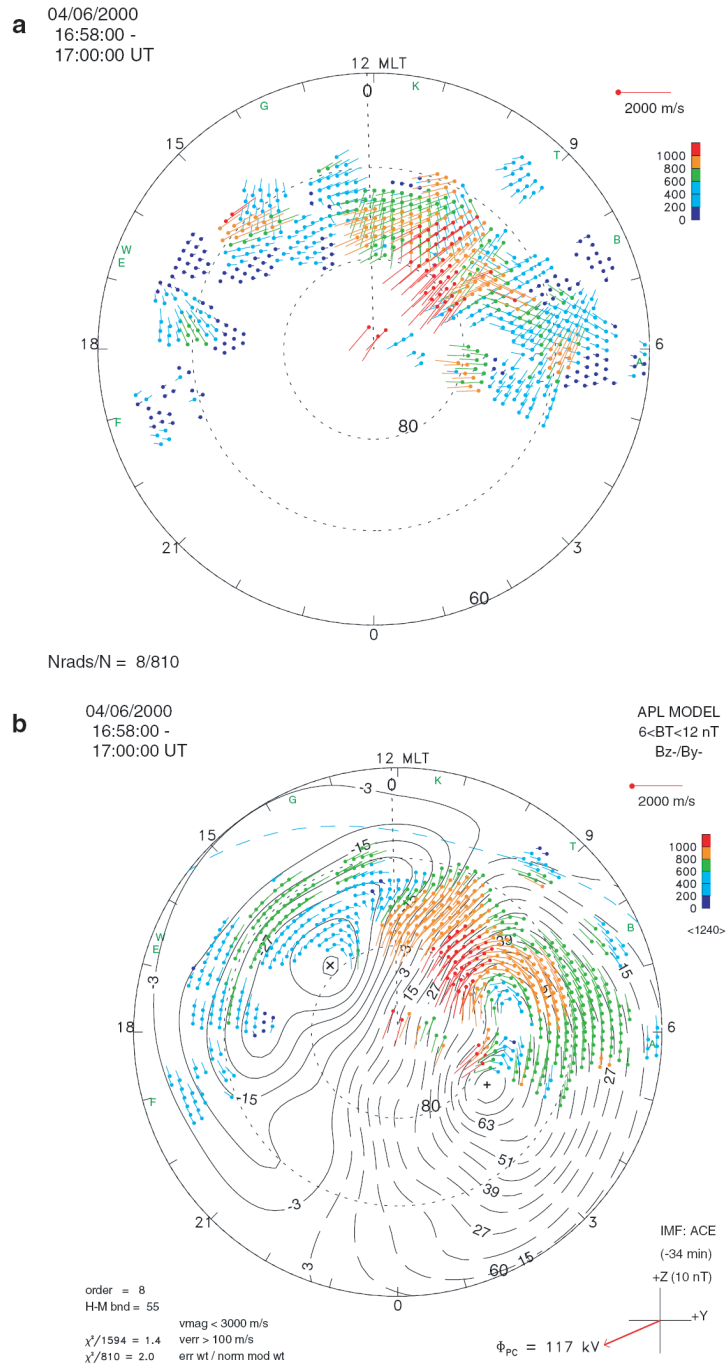
Figure 3.4 (a) An example of a latitude-MLT plot of line-of-sight velocity data from all northern hemisphere radars during a 2 minute interval 16:58-17:00 on 4th June 2000. The data from the radars are represented by coloured dots; the length and colour of the vectors gives the magnitude of the flow. (b) shows the processed radar data; a global convection map has been generated using an 8th order spherical harmonic fit to the raw data displayed in (a). The contours represent the corresponding electrostatic potential pattern. From Chisham et al., 2007.

alter the potential map produced and can add spurious vorticity. It is also possible to fix the statistical model input used in the generation of the global convection map such that no model bias is introduced which may affect a comparison of potential maps produced under different IMF conditions.

3.2 Spacecraft Instrumentation

Spacecraft instrumentation is available to measure in situ magnetic fields, electric fields and plasma populations. Some of the instrument types that are relevant to this thesis are described below.

3.2.1 The fluxgate magnetometer

A fluxgate magnetometer consists of two primary coils wound in opposite directions around ferromagnetic cores such that when an AC current is passed through the coils, at any one time it will induce magnetic fields of the same strength but opposite orientation in each coil. Any external field will create an existing field in the cores that will either be added to or detracted from by the additional field induced by the AC current. If the current is detracting from the existing magnetic field in one core then saturation will occur later than in the other core, where the induced magnetic field due to the current is adding to the existing field.

Without an existing field the magnetic field induced in each coil would be equal and opposite and therefore no net field would be detected. The net field induces a voltage in a secondary coil which is wound around both primary coils and this voltage enables a value of the external field to be determined.

This system enables a knowledge of the external magnetic field parallel (or antiparallel) to the primary coil axis. In order to get a three dimensional magnetic field measurement it is necessary to have three fluxgate magnetometers, aligned orthogonally.

3.2.2 Search coil magnetometers

Search coil magnetometers consist of a single coil aligned with the spin axis of the spacecraft. They detect changes in the external magnetic field by measuring the induced emf (due to Faraday's law) in the coil. Search coil magnetometers need to be carefully calibrated and cannot give an exact value of the field at a given time, only the variation in the field.

3.2.3 Electrostatic potential analysers

Electrostatic potential analysers are used primarily to detect fluxes of charged particles in different energy bands. They usually work by having an entrance aperture controlling the incident solid angle of particles entering the detector, and then two parallel plates with a potential across them. The charged particles are deflected through the field according to their charge and energy, and then exit through a slit. The range of energies that the instrument is capable of measuring depends on the potential difference between the plates. The energy of the particles within a given range is determined using time of flight analysis as they pass through a carbon foil and are subsequently detected by a microchannel plate (MCP). Retarding potential analysers accelerate low energy particles and thereby extend the range of the instrument.

There are different designs of potential analyser; the one used on many of the instruments described below (e.g. Cluster and Wind) is called a "top-hat" analyser which has a circular entrance aperture and spherical parallel plates; deflecting the particles through 90°.

3.3 Spacecraft data

3.3.1 ACE

The Advanced Composition Explorer (ACE) was launched in 1997 and is an upstream solar wind monitor positioned in a halo orbit about the L1 point approximately 240 R_E upstream of the Earth. It provides information about the solar wind composition, velocity, density, pressure and the interplanetary magnetic field

strength and orientation. The solar wind velocity can then be used to determine the transit time of the solar wind parameters from the ACE location to the magnetopause. Two instruments have been used to provide this upstream data; the magnetometer instrument, MAG, and the Solar Wind Electron, Proton and Alpha Monitor, SWEPAM.

The MAG instrument comprises twin, triaxial fluxgate magnetometers which are mounted on booms to minimise magnetic effects from the spacecraft. The dynamic range and digital resolution of the instrument are displayed in Table I of Smith et al. (1998).

The SWEPAM experiment consists of two electrostatic analysers, one measuring protons, and the other measuring electrons. The ion instrument measures a full three dimensional proton and alpha particle distribution every 64 seconds within the energy range 260 eV/q to 36 keV/q. The electron instrument measures 20 energy levels in the range is 1 eV to 1.35 keV and it measures a full 3-D electron distribution every 64 seconds (McComas et al., 1998).

3.3.2 Geotail

Geotail was launched in 1992 into a highly elliptical orbit closely aligned with the ecliptic plane. It was designed to investigate the magnetotail but its orbit is such that it can also be used to measure the solar wind conditions near the bowshock and the shocked solar wind in the magnetosheath. Geotail has three magnetometers as part of its payload, two dual fluxgate magnetometers and a search coil magnetometer. The primary fluxgate magnetometer (MGF) measures the magnetic field in 7 dynamic ranges, and was operational during the period of study in Chapter 7. During this study it provided essential information about the clock angle of both the solar wind and the shocked magnetosheath magnetic field. For further information about the MGF instrument see Kokubun et al. (1994).

3.3.3 WIND

The WIND spacecraft was launched in 1994 primarily to analyse plasma processes in the solar wind and complement magnetospheric and ionospheric studies. Since October 1998 WIND has been orbiting the Earth with a closest

approach of ~10 R_E and apogee ~80 R_E. The magnetometers on board are exactly the same as those on board the ACE spacecraft (Section 3.3.1); dual, triaxial boom mounted fluxgate magnetometers with eight automatically controlled dynamic ranges. The basic sampling rate is 10.9 vectors/second although special modes exist which provide increased sampling rate (Lepping et al., 1995).

3.3.4 Cluster

The Cluster mission was launched in 2000 and consists of four spacecraft flying in a tetrahedral formation. These spacecraft are in an elliptical polar orbit with a 57 hour period, therefore they fly through the magnetospheric cusp during the months July to October each year. During these cusp crossings it is possible to measure ions of solar wind origin precipitating into the ionosphere down newly opened field lines.

The instrument used to detect these ions is the Cluster Ion Spectrometry (CIS) instrument which consists of two detectors, the COmposition and DIstribution Function (CODIF) detector, and the Hot Ion Analyser (HIA), both of which use a retarding potential analyser to measure ion fluxes. The CODIF instrument operates in the energy range 0-40 keV/e with angular resolution 10.6° x 22.5° and the HIA instrument operates in the energy range ~5-32 keV with higher angular resolution (5.6° x 5.6°) (Escoubet et al., 1997). The CODIF instrument is also capable of determining the composition of the ions detected, specifically the principal magnetospheric ions such as H+, He++, He+ and O+. Both instruments provide full three dimensional ion distributions every four seconds (the spacecraft spin period).

Each of the Cluster spacecraft carries two triaxial fluxgate magnetometers which operate in five ranges (Balogh et al., 1997). The appropriate range is automatically selected when a threshold fluctuation is reached.

3.3.5 IMAGE FUV, SI12 and SI13

The Imager for Magnetopause-to-Aurora Global Exploration (IMAGE) spacecraft was launched in March 2000 into an elliptical polar orbit in order to take global images of the aurora. As part of its payload it carries two wideband imagers that have been used in these studies; the Far-UltraViolet Wideband Imaging

Camera, or FUV WIC, and the Spectrographic Imager instrument (SI). The SI instrument is split into two channels, SI12 and SI13.

The SI12 instument measures Doppler shifted Lyman alpha emission. When a precipitating energetic proton captures an electron from an atmospheric neutral (known as charge exchange) it will become a hydrogen atom. Often during this process the atom ends up in an excited state. It subsequently decays back into the ground state, emitting Lyman-alpha emission. This emission will primarily be moving away from the location of the IMAGE spacecraft, therefore IMAGE must measure the Doppler-shifted Lyman-alpha emission at a wavelength of ~121 nm (Mende et al., 2000c). By targeting this wavelength, it is therefore possible for the SI12 channel to image proton aurora.

Electrons precipitating into the upper atmosphere excite atmospheric atomic oxygen which can decay by a forbidden transition and emit energy with wavelength 135.6 nm. There is another wavelength emitted by atomic oxygen, at 130.4 nm, however emission at this wavelength is scattered in the atmosphere whereas the 135.6 nm wavelength is scattered significantly less. The SI13 channel can separate these wavelengths and only measure the 135.6 nm emission (Mende et al., 2000c). This enables it to image the electron aurora.

The Wideband Imaging Camera (WIC) measures a much broader band of wavelengths than the SI instrument, 140-190 nm. Figure 3.5 shows a typical UV auroral emission spectrum (Mende et al., 2000b). The specific wavelengths targeted by the SI instrument are shown, as well as the broad wavelengths covered by the WIC instrument.

Most of the lines in the WIC wavelength range make up the Lyman-Birge-Hopfield (LBH) system. Precipitating particles excite N_2 molecules into a higher energy state, which subsequently decay back into the ground state via a forbidden transition, emitting energy in the LBH wavelength range. Approximately 20-25% of nightside emission in the LBH bands have been shown to be due to precipitating protons, and most of the remainder is due to precipitating electrons (Dashkevich et al., 1996).

The orbit of the IMAGE spacecraft is such that at apogee it is at an altitude of approximately 44,000 km. In order to image the entire earth at this altitude the field of view of a camera would have to be 16 degrees. The far ultraviolet imagers WIC and SI therefore have fields of view of 17°x17° and 15°x15° which ensures
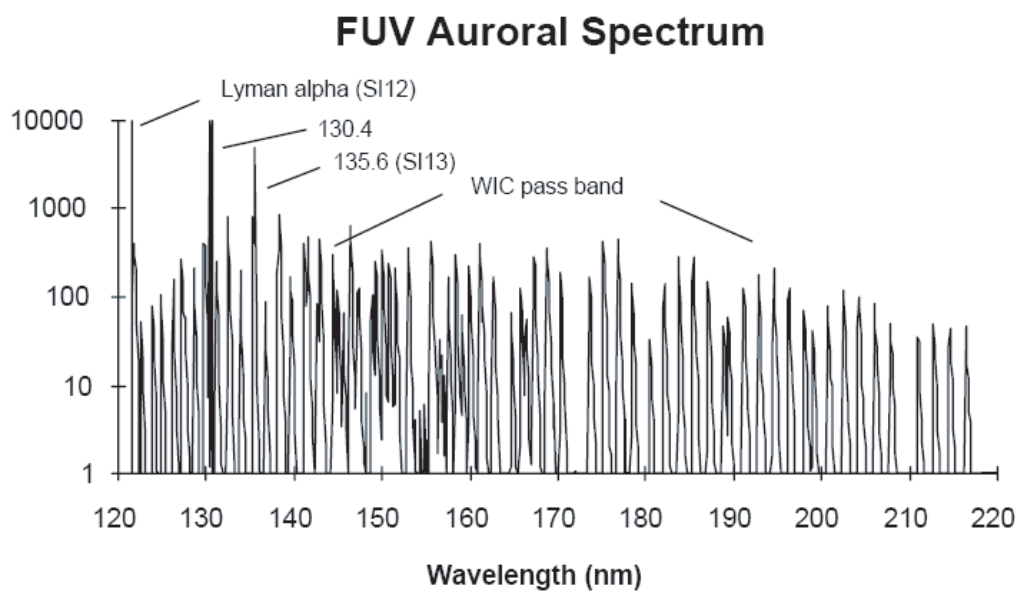
Figure 3.5. Wavelengths measured by the WIC and SI instruments on the IMAGE spacecraft. From Mende et al., 2000.

that even at lower altitudes the entire auroral oval will be imaged. The WIC camera has 256x256 pixels and the SI instrument has 128x128 pixels (Mende et al., 2000b). During each 2 minute orbital period, WIC is in a position to image the Earth for 10 seconds, during which it takes 30 frames per second. Each set of 300 images are combined to create one image every 2 minutes. The SI instrument is able to image the Earth during 5 seconds every 2 minute orbit and again produces one image every 2 minute spin (Mende et al., 2000a).

In order to plot an image taken by either of these instruments onto a polar projection plot of latitude and magnetic local time (MLT), it is necessary to process the data. The latitude and MLT of each pixel is calculated and the number of counts making up each pixel is also known. In this thesis we have chosen to bin the data into a 40x40 grid for SI data and an 80x80 grid for WIC data where rows and columns are aligned along the noon-midnight and dawn-dusk meridians. Each section of the grid therefore contains the number of counts taken by the imager and it is possible to plot this as filled contours on a polar projection plot.

3.3.6 LANL

The Los Alamos National Laboratory (LANL) routinely launches spacecraft into geosynchronous orbit around the Earth, at an altitude of approximately 6.6 R_E. Four LANL spacecraft (1990, 1991, 1994 and 1997) have been used in this thesis to monitor the plasma sheet density (Chapter 7) and all of these spacecraft flew the same plasma instrument, the Synchronous Orbit Particle Analyzer (SOPA).

The SOPA instrument measures electrons, protons and heavy ions using three detectors mounted at different angles relative to the spin axis (30°, 90° and 120°) each with an 11° field of view. The ion flux is measured in 12 channels with energies from 50 keV to 50 MeV and electrons from 50 keV to greater than 1.5 MeV in 10 energy channels; for further information see Belian et al. (1992). A full electron and proton distribution is provided every spin period (~10 seconds).

3.3.7 NOAA POES

The National Oceanic and Atmospheric Administration (NOAA) launched a series of spacecraft known as Polar Orbiting Environmental Satellites, or POES.

These spacecraft are in low altitude (~800 km) polar orbits and their payload includes an instrument called the Medium Energy Proton and Electron Detector (MEPED). This instrument has been used in this thesis to determine the boundary between high and low fluxes of high energy electrons as the spacecraft traverses the polar cap – a proxy for the open/closed field line boundary (OCB).

The MEPED instrument is composed of 22 channels which measure fluxes of ions and electrons in the range 30 keV to >200 MeV with a resolution of 2 seconds, although usually 16 second data is used (Evans and Greer, 2000). Charged particles enter the detector and produce an electrical signal, the amplitude of which enables the energy of the incoming particle to be determined. There are two electron instruments, one pointing directly at the Earth from the satellite, and the other perpendicular to this. In order to determine whether the satellite is on open or closed field lines the perpendicular instrument is used, which measures the flux of trapped electrons (with large velocity components perpendicular to the magnetic field).

3.3.8 DMSP

Data from three Defence Meteorological Satellite Programme (DMSP) spacecraft have been used in this thesis in order to determine the location of the open/closed field line boundary (OCB) as the spacecraft orbit passes over the northern polar cap. This is done by recognising the transition between detection of high fluxes of high energy, trapped electrons on closed field lines, and low fluxes of high energy electrons present on open field lines. The Precipitating Ion and Electron Spectrometer, or SSJ/4 instrument is used, which has been flown on all three DMSP spacecraft considered here; F12, F13 and F15 (Hardy et al., 1984).

The SSJ/4 instrument consists of two pairs of electrostatic analysers, one pair measuring electrons and the other pair measuring ions. These detectors measure particles in 10 logarithmically spaced channels, one in each pair being the low energy detector, and the other, the high energy detector. The dwell time on each energy channel is 0.09 seconds such that the entire range is sampled once per second.

The DMSP spacecraft are in a sun-synchronous, low altitude polar orbit (~835 km), with an orbital period of 101 minutes (Wing et al., 2005). As part of the

Special Sensors-Ions, Electrons, and Scintillation instrument (SSIES), is an Ion Driftmeter (IDM) which measures components of the ion drift relative to the spacecraft trajectory.

The crosstrack component of the ion drift is calculated using a Faraday cup pointing in the direction of motion of the spacecraft, assuming that the bulk plasma flow is smaller than the spacecraft velocity. A slight negative charge is applied to a grid at the front such that only positive ions enter the cup. The ions that reach the four detector plates at the back of the cup are measured as a current. If the ions have a bulk flow component perpendicular to the spacecraft track then the number of ions hitting each plate (and therefore the current measured across each plate) will be different, and this enables the cross-track and vertical bulk velocity of the ions to be determined. Velocities are obtained 6 times per second although usually averaged to give 4 second data. The maximum crosstrack bulk flow that the detector can measure is 3 km s^{-1}.

A similar instrument called the Retarding Potential Analyser measures the along-track ion velocity. It applies a retarding potential to ions entering a Faraday cup aligned with the direction of spacecraft motion, and calculates the current on the collecting plate as a function of the retarding potential which sweeps between -3 and +12 volts every four seconds. This gives the ion bulk flow in the direction of motion of the spacecraft. Measurements of along-track ion velocity are usually considered to be of poorer accuracy than the crosstrack measurements.

3.3.9 FAST

The Fast Auroral SnapshoT (FAST) satellite was developed by NASA to investigate the charged particles giving rise to the aurora and field aligned current systems. It was launched in August 1996 into a near polar, elliptical low altitude orbit, taking only 133 minutes to orbit the Earth (Carlson et al., 1998). In this thesis, FAST has been used both to determine the latitude of the open/closed field line boundary (OCB) and to measure cusp ions injected to low altitudes. The instrument used to make these measurements is called the Electrostatic Analyser (ESA).

The ESA consists of 8 pairs of top hat electrostatic analysers (Section 3.2.3) which are positioned in stacks of four 90 degrees apart. Two pairs of analysers are

ion and electron spectrometers which measure both species at 48 energies in the ranges 4 eV to 32 keV for electrons and 3 eV to 24 keV for ions. A full energy distribution is obtained over 32 pitch angles every 78 ms (Carlson et al., 2001). A deflection plate steers the field of view of each analyser by up to 10° as it crosses the auroral region to align it with the Earth's magnetic field. This therefore enables a full pitch angle distribution to be obtained. When considering precipitating ions on open field lines injected during reconnection, only predominantly field aligned particles are of interest as these reach the lowest altitudes.

Chapter 4. Theory

Dual lobe reconnection (DLR) was a process first proposed by Dungey in 1963. Since that time DLR has been discussed as a possible mechanism for capturing plasma to form the closed low latitude boundary layer and the cold, dense plasma sheet. However, up to this point there has been no conclusive evidence that DLR actually takes place. In order to demonstrate that dual lobe reconnection takes place at Earth, it is necessary first to consider the ionospheric and auroral signatures expected. The purpose of this Chapter is to outline our predicted signatures, some of which will be presented in more detail in Chapter 7.

4.1 Ionospheric convection associated with dual lobe reconnection

During northward IMF lobe reconnection takes place at high latitudes. An interplanetary magnetic field line reconnects with a lobe field line, producing an open field line which drapes over the subsolar point into the opposite hemisphere (Chapter 2.1.2). The location of the lobe reconnection site on the magnetopause has been shown to be dependent on the B_Y component of the IMF (Milan et al., 2000, Østgaard et al., 2005), moving duskward (dawnward) for B_Y positive (negative). If the IMF is very strongly northward with negligible B_Y component, the overdraped field line may then reconnect with a lobe field line in the opposite hemisphere. This process is called dual lobe reconnection (DLR), and a closed field line is formed at the dayside magnetopause (Dungey, 1963).

The ionospheric flow signatures of lobe reconnection are presented in Chapter 2.1.2. The expected convection pattern comprises twin reverse cells on the dayside, contained within the polar cap such that the merging gap is located inside the open/closed field line boundary (OCB). In order to identify the process of dual lobe reconnection from the ionospheric flow signatures, it is necessary to develop a model of the predicted convection pattern.

The shape of the magnetopause is governed by pressure balance between the solar wind ram pressure and the magnetic pressure exerted by the Earth's magnetic field. Closure of lobe field lines on the dayside by DLR will perturb the dayside OCB into a non-equilibrium configuration. Ionospheric flows are then excited to

return the polar cap to a roughly circular shape in a manner similar to that discussed by Cowley and Lockwood (1992). The expected ionospheric flow signature associated with the closure of open, lobe field lines is sunward flow across the dayside OCB with return flow at lower latitudes. The polar cap is expected to shrink during this process as magnetic flux is being closed, and all flow away from the merging gap is expected to be adiaroic.

The simplest scenario considered here is that of ongoing dual lobe reconnection, during which the ionospheric projection of the reconnection site (known as the merging gap) will be co-located with the OCB on the dayside. The signatures of lobe and dual lobe reconnection are very similar – in both cases twin reverse cells on the dayside are expected. The primary difference between the convection patterns is that during DLR the flow crosses the dayside OCB, while during single lobe reconnection there is no flow crossing the OCB and the twin cells are contained with in the polar cap. The upper panels of Figure 2.1b and c show the Earth in the GSM *X-Z* plane, with the Sun to the left. The field line configuration on the left demonstrates the lobe reconnection process, while dual lobe reconnection is taking place in the right hand schematic. The lower portion of this Figure comprises schematics to describe the ionospheric convection patterns associated with lobe and dual lobe reconnection.

4.2 Auroral signatures of dual lobe reconnection

Following a northward turning of the IMF, the first field line to reconnect at the onset of lobe reconnection will map to the OCB on the dayside. When this field line has reconnected it will accelerate away from the reconnection site, allowing another lobe field line to reconnect, and so on. As this process continues, field lines deeper into the lobes will be able to reconnect before other newly-reconnected field lines have moved a significant distance, and therefore the merging gap will move into the polar cap. That is, the location of the merging gap inside the polar cap is dependent on the rate of the lobe reconnection process itself, and the convection of the newly reconnected field lines away from the dayside magnetopause. Solar wind plasma crossing the magnetopause and travelling down newly reconnected field lines may interact with the upper atmosphere and generate an auroral feature called a cusp spot (e.g. Milan et al., 2000). During lobe reconnection this will be located

equatorward of the merging gap (but poleward of the OCB) on open field lines (see Chapter 7).

During the process of dual lobe reconnection, previously open field lines are closed and there is sunward flow across the dayside OCB. We assume that lobe reconnection takes place first in the northern hemisphere and the subsequent overdraped field line then reconnects with a lobe field line in the southern hemisphere. A closed field line is formed on the dayside, which then contracts and sinks into the magnetosphere and subsequently convects around the dawn or the dusk flank and into the tail. For steady, ongoing dual lobe reconnection, the merging gap in both hemispheres associated with this second reconnection site will by definition be located at the dayside OCB. Plasma captured on this closed field line may then generate a cusp spot on closed field lines in both hemispheres. It would therefore be expected that two cusp spots should be observable in the northern hemisphere; one at the merging gap associated with the first single lobe reconnection, and another at the dual lobe merging gap co-located with the OCB (Figure 4.1a). Lobe field lines mapping to the southern hemisphere only reconnect once with overdraped field lines from the northern hemisphere so a single cusp spot is predicted, at the footprint of the dual lobe reconnection site, as sketched schematically in Figure 4.1b. Figure 4.1c shows the cusp precipitation and ionospheric flow pattern expected during single lobe reconnection, for comparison.

The time history of the reconnection will determine the exact location of the dual lobe reconnection-related cusp spots; this will be discussed in further detail below. The hemisphere in which lobe reconnection first takes places is thought to be controlled by the B_X component of the IMF (e.g. Reiff and Burch, 1985). For positive (negative) B_X, reconnection of an individual IMF field line would be expected to take place first in the southern (northern) hemisphere. Draping of magnetosheath field lines subsequently allows reconnection of the overdraped field line in the opposite hemisphere.

4.3 Time history related to the location of the DLR cusp spot

Consider a scenario where lobe reconnection is steady in the northern hemisphere and the southern hemisphere, although the clock angle is too large for dual lobe reconnection to take place. The IMF slowly rotates to smaller clock
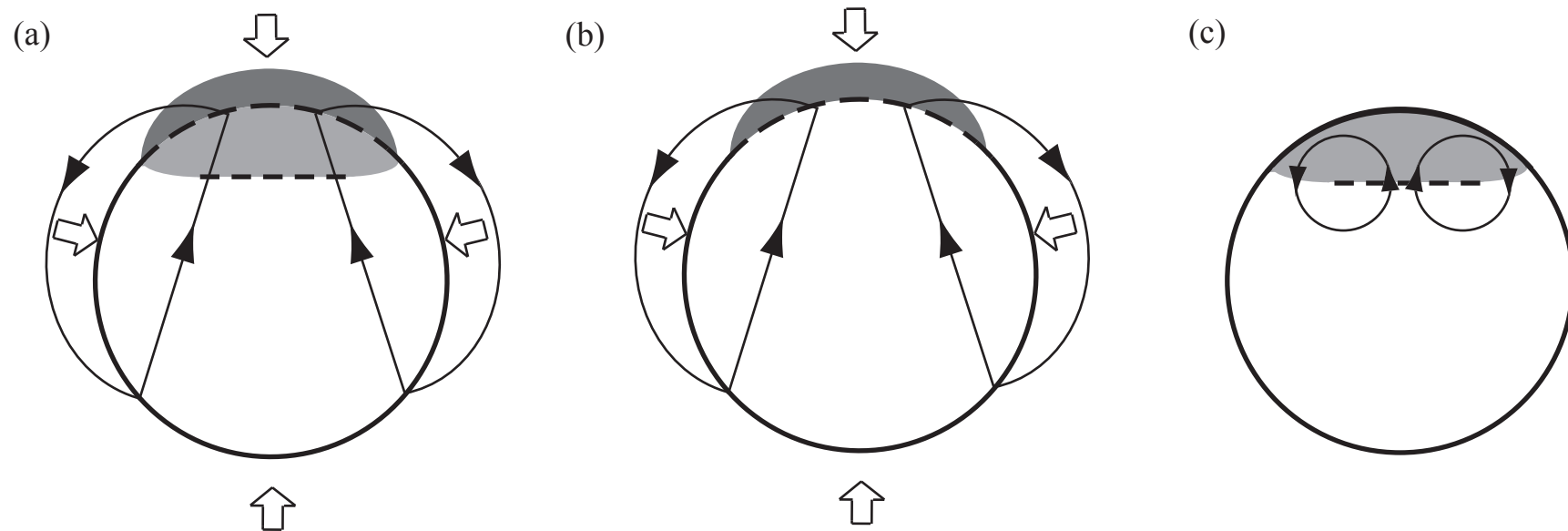
Figure 4.1 A schematic to show the location of the merging gaps and cusp precipitation for DLR in (a) the first and (b) the second hemisphere to reconnect. (c) Single lobe reconnection ionospheric flow and cusp precipitation.

angles until it reaches a threshold angle at which dual lobe reconnection commences. Assuming that reconnection of the overdraped field line in the southern hemisphere takes place shortly after lobe reconnection in the northern hemisphere, the footprint of the first field line to undergo dual lobe reconnection will be inside the polar cap near the lobe reconnection merging gap in both hemispheres. Dual lobe reconnection generates closed magnetic field lines, therefore a closed field line will be formed within the polar cap on the dayside just equatorward of the single lobe reconnection merging gap (Figure 4.2). As dual lobe reconnection continues, the ionospheric footprint of this first field line will move sunward and dusk/dawnward and new closed field lines will form behind it. The lobe field lines equatorward of this region of closed flux will convect sunward and dawn/duskward such that this area of closed flux will move towards the dayside until the dual lobe reconnection merging gap is co-located with the OCB. It is estimated that it would take ~ few minutes for the dual lobe reconnection merging gap to move from the single lobe merging gap location to the dayside OCB. During this time, ions travelling along newly closed field lines may generate a cusp spot poleward of the dayside auroral oval. This cusp spot will move equatorward with the footprint of the field lines until eventually it is co-located with the dayside OCB. Any cusp spot located within the polar cap would usually be assumed to be on open field lines due to single lobe reconnection, although in this case it would be on closed field lines.

4.4 Simultaneous single and dual lobe reconnection

Figure 4.3a presents a schematic demonstrating the threshold clock angle at which dual lobe reconnection can take place based on a static merging gap length. The dashed lines are field lines that are undergoing dual lobe reconnection, while the solid lines are those undergoing single lobe reconnection. A single reconnection line spans the magnetopause in either hemisphere, therefore it is interesting to consider the ionospheric projection of this reconnection and the ionospheric flows associated with it.

If the IMF is northward with a significant B_Y component, single lobe reconnection will be taking place simultaneously in both hemispheres. The reverse twin cell convection pattern will be non-symmetric, with a larger cell at dawn
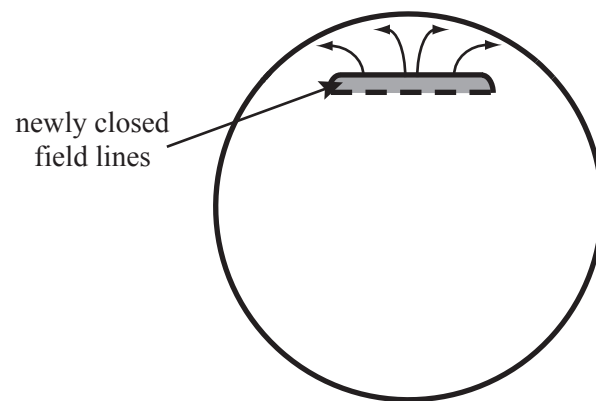
Figure 4.2 A schematic to show the location of newly close field lines at the onset of DLR.
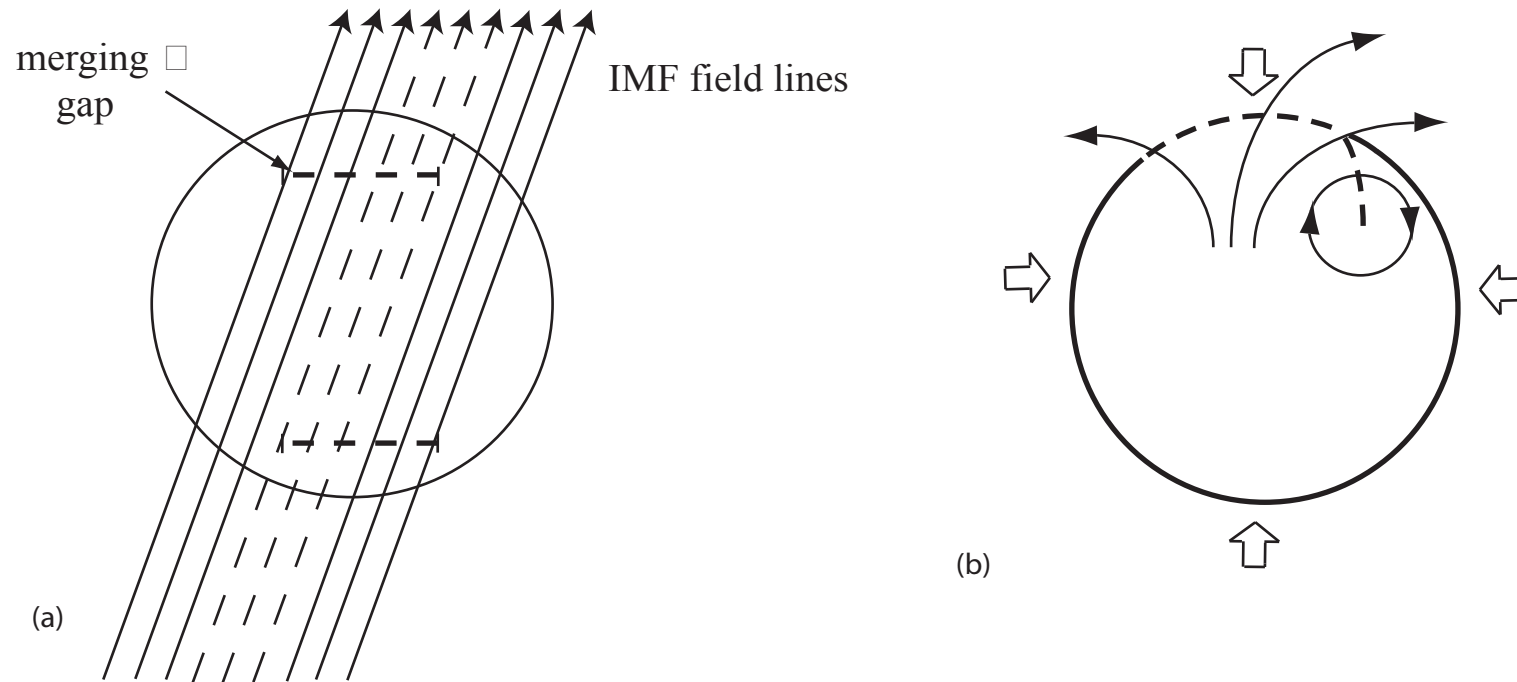
Figure 4.3 (a). IMF field lines in the GSM Y-Z plane; the merging gaps are represented by horizontal dashed lines, field lines undergoing single lobe reconnection are solid arrowed lines, and those capable of dual lobe reconnection are shown as dashed arrowed lines. (b). The ionospheric projection of this reconnection topology, with noon to the top and dawn to the right of the Figure. The solid circle is the northern hemisphere OCB, the dashed portion of which is the merging gap. Black arrows are flow streamlines and white arrows represent the fact that the OCB is expected to shrink as DLR is ongoing. Flow only crosses the OCB along the section of the merging gap mapping to the DLR reconnection site.

(dusk) for B_Y positive (negative) (e.g. Cowley and Lockwood, 1992). Both cells are contained within the OCB. As the IMF rotates and the threshold clock angle for DLR is reached, closed field lines are formed within the polar cap which rapidly move sunward towards the dayside OCB as described in the previous Section. When the merging gap reaches the OCB, the continuation of DLR significantly perturbs the shape of the magnetopause such that flows are excited and the familiar reverse twin cell convection pattern with flow across the dayside OCB is excited. Throughout this time single lobe reconnection is likely to be taking place simultaneously, and as long as the IMF clock angle is not purely northward, one dominant lobe cell is likely to exist contained within the polar cap, perhaps also a significantly smaller second cell. Figure 4.3b shows an example of a possible ionospheric signature of single and dual lobe reconnection taking place along a single x-line. The simplest case is considered here, with a single dominant lobe convection cell and twin reverse dual lobe convection cells, assuming steady DLR along a single portion of the x-line. The true picture is likely to be extremely complicated, with dual lobe reconnection taking place along different portions of the x-line as the IMF changes orientation.

4.5 Ion signatures of dual lobe reconnection

Ions travelling down newly reconnected, open field lines following lobe reconnection are expected to reach low altitudes before mirroring and being lost downtail. Higher energy ions will reach a low altitude spacecraft before lower energy ones, such that the spacecraft would be expected to observe a reverse dispersed ion signature generated by the velocity filter effect on sunward convecting field lines (Chapter 2.3). Depending upon the spacecraft trajectory and altitude, it may also observe an upgoing population of particles which have mirrored at lower altitudes. The expected ion dispersion characteristics of dual lobe reconnection are significantly more complex, as not only are there two reconnection sites, but plasma on the newly reconnected field line is trapped such that it can mirror between hemispheres. The location of the spacecraft relative to each reconnection site, its trajectory, and the time between reconnection in each hemisphere will significantly alter the ion signatures observed by the spacecraft.

The simplest situation to consider is that of a low altitude spacecraft travelling with the same velocity as a reconnected field line. The location of this spacecraft and the reconnection sites are shown in Figure 4.4. Assuming that lobe reconnection takes place first in the northern hemisphere, then subsequently this new overdraped field line reconnects with a lobe field line in the southern hemisphere, the spacecraft will observe the ion signatures outlined in the text below and Figure 4.5.

1. Before the initial lobe reconnection in the northern hemisphere the spacecraft will be on open lobe field lines and therefore will observe low fluxes of ions and electrons.

2. Following lobe reconnection in the northern hemisphere the spacecraft will observe a reverse dispersed ion signature as solar wind plasma travels down the newly reconnected field line and is detected at low altitudes. This signature will consist of heated magnetosheath plasma.

3. Plasma that has reached low altitudes will either interact with the upper atmosphere or will mirror and return up the field line. Returning plasma will pass over the location of the spacecraft for a second time, and may be detected as a dispersed signature; again the higher energy ions will reach the spacecraft location before the low energy ions. The slope of the dispersed signature will be less steep than the initial dispersion signature observed, as the ions have travelled further such that the velocity filter effect will be more pronounced.

4. The exact timing of the two ion signatures described above will depend upon the relative location of the spacecraft to the reconnection site, and the altitude of the spacecraft relative to the mirror point of the plasma. If the field line subsequently reconnects with a lobe field line in the southern hemisphere then a closed field line will be formed. Plasma from this second reconnection site may travel up the field line and be observed by the spacecraft positioned in the northern hemisphere. The timing of the observed signature will depend upon the time that the second reconnection event takes place, which in turn is dependent upon the magnetosheath conditions. The plasma initially travelling along the newly closed field line from the southern hemisphere towards the northern hemisphere will have come from the southern hemisphere lobe. Lobe field lines contain very little
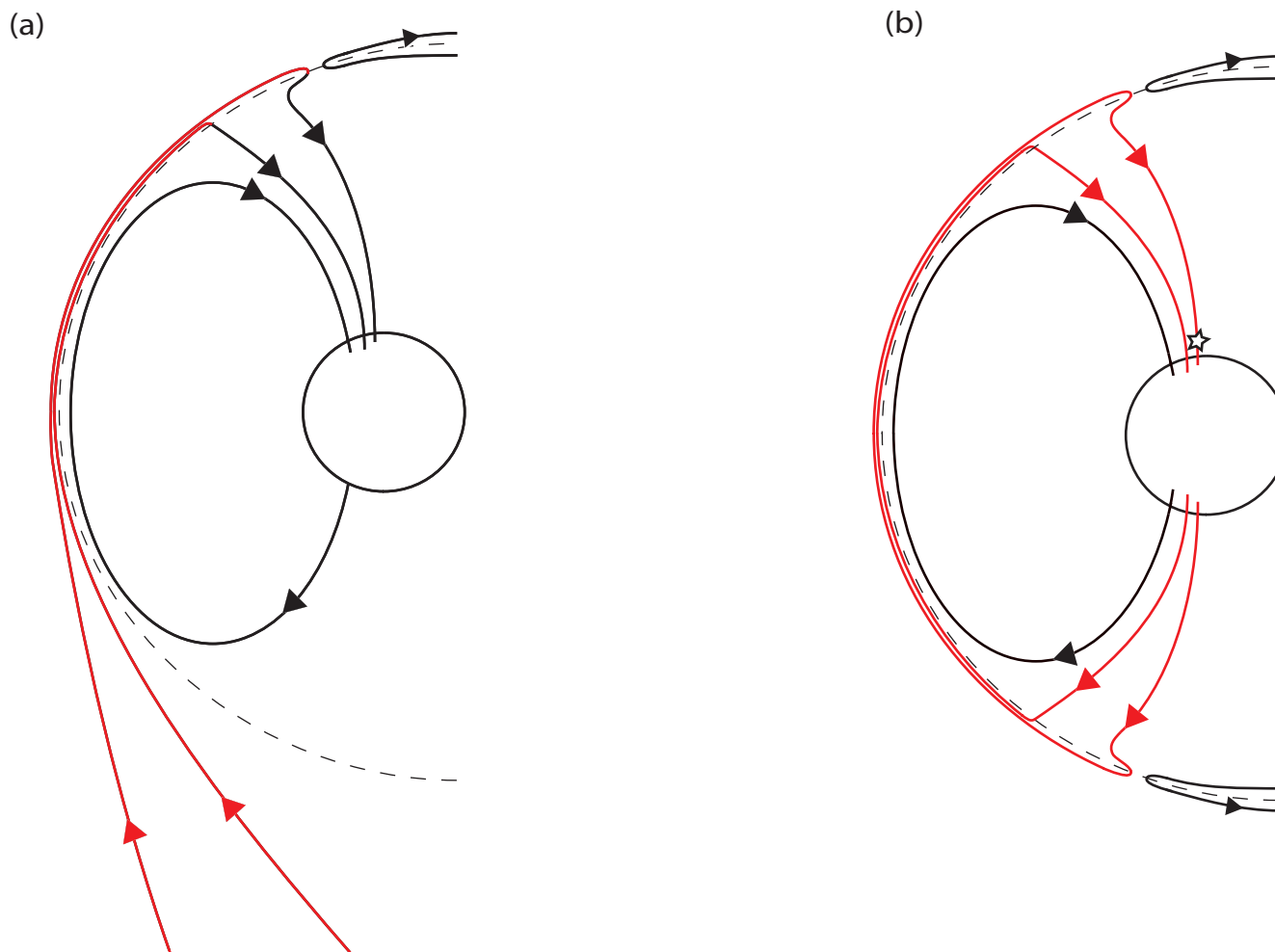
Figure 4.4 (a) Solar wind plasma on a newly reconnected field line may be captured by DLR. This plasma is shown in red following lobe reconnection in the northern hemisphere. (b) It may then mirror in the southern hemisphere and return up the newly closed field line to be detected in the northern hemisphere by a spacecraft located at the position indicated by the star.
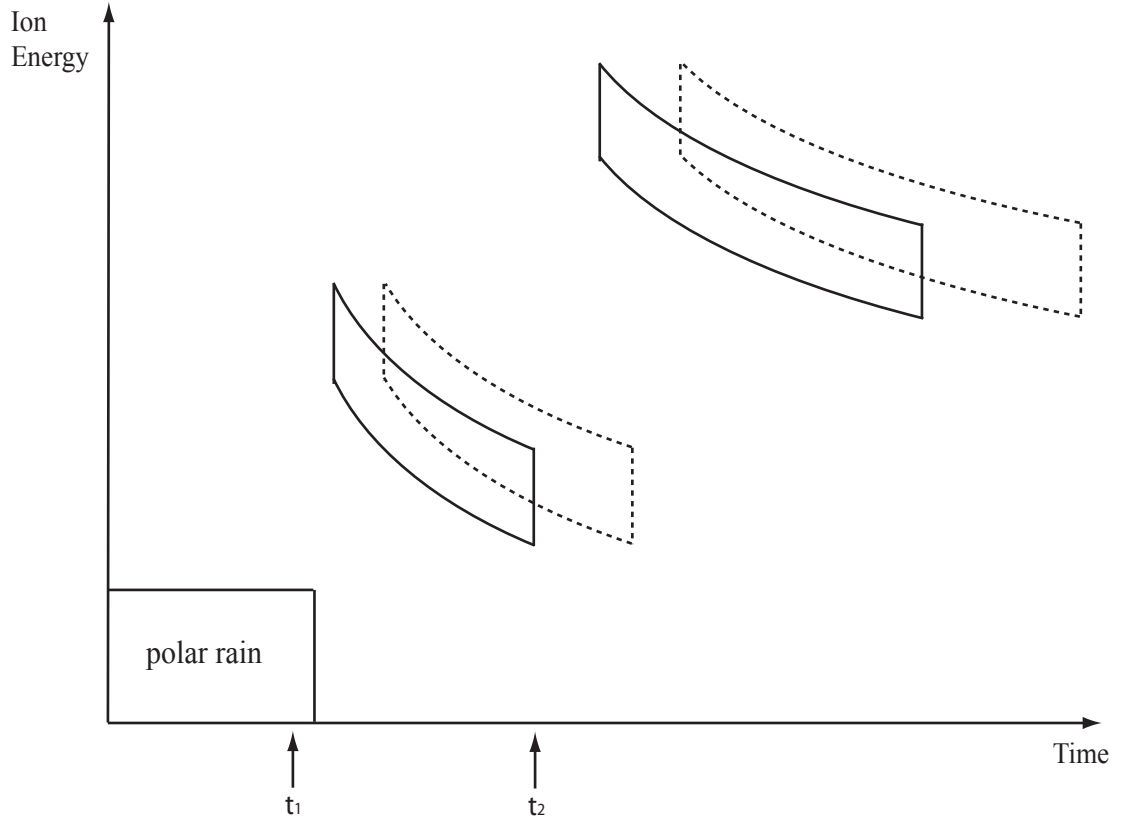
Figure 4.5. Predicted ion dispersion signatures of dual lobe reconnection. A spacecraft located at the foot of a lobe field line initially sees a low flux of low energy ions (polar rain), followed by a dispersed ion signature following reconnection with an interplanetary magnetic field line at time t_1. The upgoing mirrored population is shown as the dashed dispersion signature. The overdraped field line then reconnects in the southern hemisphere at time t_2 and trapped plasma which has mirrored in the southern hemisphere is then trapped on a closed field line and may be observed by the spacecraft in the northern hemisphere. From time t_2 onwards the spacecraft is located on closed field lines.

plasma as they are open, and therefore it is unlikely that the signatures of this plasma will be observable in the northern hemisphere. Following the field line closure, there will be a plasma population travelling along the field line towards the southern hemisphere. This plasma is of solar wind origin and entered the flux tube while it was open. It will pass through the highly kinked portion of newly reconnected field lines in the southern hemisphere, mirror at low altitudes, pass through the same highly kinked field line region, then continue to the northern hemisphere. Here it will travel through another highly kinked region of reconnected field lines in the northern hemisphere and may be detected by low or mid altitude spacecraft. This plasma population will have passed through three acceleration regions in total, and will therefore be of significantly higher energy than the solar wind plasma observed earlier.

5. This second solar wind plasma population will mirror in the northern hemisphere and may be detected by the low altitude spacecraft travelling back along the field line.

All of the plasma described above is captured on a closed field line and will mirror between hemispheres, although the plasma will gradually be lost to the ionosphere such that distinct ion signatures are unlikely to be observed beyond the timescales described above.

Figure 4.5 outlines the main characteristics of the ion populations observed by the spacecraft. The two dispersion signatures generated by downgoing ions are associated with the two merging gaps shown schematically in Figure 4.1a. A spacecraft located in the southern hemisphere would be expected to observe one primary dispersed ion signature (Figure 4.1b), although it may be possible to observe subsequent signatures. It must be noted that in this simplistic model the spacecraft is co-located with the base of a single field line as it undergoes reconnection in both hemispheres. A more realistic picture would be that of a spacecraft travelling through the cusp and therefore observing only part of the signatures described above.

Chapter 5. SuperDARN observations of reverse twin cell ionospheric convection

In this Chapter we investigate the dependence of the lobe reconnection rate on upstream solar wind driving conditions. The reconnection rate is calculated using the SuperDARN electrostatic potential maps and the upstream conditions are measured by the ACE spacecraft. The accuracy of the potential maps in measuring small-scale ionospheric convection features has been a matter of some debate, so an additional study was carried out comparing the convection velocities measured by the SuperDARN potential maps with the comparable crosstrack velocities measured by overflying DMSP spacecraft.

5.1. A statistical study of the dependence of the lobe reconnection rate on upstream solar wind conditions

High latitude magnetic reconnection tailward of the cusp, or lobe reconnection, was first postulated by Dungey (1963), and Russell (1972) later proposed that it could occur independently in both hemispheres under northward IMF conditions. The ionospheric flows corresponding to this high latitude reconnection are presented in Chapter 2.1.2. The response of the twin reverse cells to varying IMF conditions was theorised by Cowley and Lockwood, (1992) and has been extensively studied using SuperDARN radar data (e.g. Huang et al., 2000; Milan et al., 2000; Imber et al., 2006) and spacecraft driftmeter data (e.g. Crooker and Rich, 1993) in conjunction with upstream interplanetary magnetic field (IMF) monitors. The B_Y component of the IMF has been shown to modify the high latitude reconnection rate (e.g. Reiff and Burch, 1985; Huang et al., 2000). It has also been suggested that the high latitude reconnection rates in each hemisphere are dependent upon the season (due to dipole tilt) and the B_X component of the IMF (Luhmann et al., 1984; Reiff and Burch, 1985; Crooker et al., 1992; Crooker and Rich 1993). There is some evidence for this (e.g. Freeman et al., 1993; Lockwood and Moen, 1999; Chisham et al., 2004), although it is also possible that the draping of the field lines over the subsolar point (such that the magnetosheath field is everywhere tangential to the magnetopause) may negate this effect.

This Chapter examines the dayside reconnection rate during conditions of northward IMF and addresses its dependence on upstream IMF conditions. The upstream conditions are monitored by the ACE spacecraft (Stone et al., 1998; Smith et al., 1998; McComas et al., 1998) and lagged to the magnetopause using the Weimer method (Weimer, 2003) and were obtained from the OMNIWeb data facility. The dayside potential Φ_D is calculated by SuperDARN observations of ionospheric flow (e.g. Chisham et al., 2007) using the method outlined in Chapter 2.1.5. The measurement of Φ_D that is being made in this study is a measure of the sunward flow within the polar cap excited by lobe reconnection, with the assumption that there is an equal amount of anti-sunward flow at lower latitudes (although still within the polar cap), to complete the twin cells.

5.1.1 Observations

SuperDARN ionospheric convection maps are available at 2 minute cadence throughout the 12 months beginning December 2000. Ionospheric potential maps are created using a 10th order spherical harmonic fit to the line of sight velocity measurements provided by the northern hemisphere radars (Greenwald et al., 1995a, Ruohoniemi and Baker, 1998). Unsuitable propagation conditions and gaps in the radar coverage mean that there are areas within each map where there are no velocity measurements, so upstream solar wind conditions are fed into a statistical model which is used to complete the potential map. Throughout this study the IMF input to the model has been set to B = [0,0,0] such that the results are not affected by model bias but are solely driven by the radar velocity measurements. A separate study was conducted to ensure that the convection velocity extracted using the electrostatic potential maps is in agreement with in situ measurements made by overflying spacecraft. This study is outlined in Section 5.2.

Each ionospheric convection map to be included in the study had 40 or more radar convection measurements between the magnetic local times of 10 and 14 in order to ensure an accurate representation of the ionospheric potential in the noon sector. Following this, each map was analysed by eye to determine if there were identifiable twin reverse cells on the dayside. In this case Φ_D was calculated by

taking the difference between the maximum and the minimum of the potential between the centre of the cells.

Out of a total of ~245,000 maps, only 1,083 (0.5%) were identified as fitting these criteria. The IMF is assumed to have a B_Z component that is greater than zero 50% of the time, so it is perhaps surprising that we have found so few events if lobe reconnection takes place whenever the IMF is northward. There are a number of explanations for this. Ionospheric propagation conditions mean that the SuperDARN radars do not see scatter all of the time, a particular problem in northern hemisphere summer. In addition, the radar coverage of the northern hemisphere is not complete, such that at certain times of the day there are no radars covering the dayside portion of the polar cap. Ongoing nightside reconnection frequently dominates over the lobe reconnection cells such that picking out clear twin reverse cells on the dayside is impossible if nightside activity is high. Finally if there is a large B_Y component of the IMF then the cells tend to be distorted so that it is not clear whether they are reverse cells or not. This effect is especially noticeable in the summer months (Milan et al., 2001). Figure 2.3 shows some examples of northern hemisphere SuperDARN data plotted on a polar grid with noon at the top of the Figure. Clear twin reverse cells are visible in Figure 2.3a, the black dots representing the locations of the maximum and minimum in the potential pattern used to calculate Φ_D. The number of vectors between 10 and 14 MLT was 104 in this example and the total number of vectors in the map is 320. Figure 2.3b shows a less clear (more typical) example, where twin cells can still be identified, the maximum and minimum again marked by black dots. This map contains fewer vectors than the previous example, with 43 vectors between 10 and 14 MLT and 194 vectors in the whole map. The IMF clock angle was determined from upstream measurements made by the ACE spacecraft and lagged to the magnetopause and is displayed in the upper left corner of each panel. In both cases the B_Z and B_Y components were positive, although the clock angle was smaller for the second example.

5.1.2 Discussion

A statistical study has been performed using all SuperDARN potential maps from December 2000 to November 2001 to determine the dayside lobe reconnection rate during intervals when there are clear twin reverse cells in the potential maps. 1,083 such maps were identified, allowing a comparison of the upstream IMF conditions measured by ACE and the magnetospheric response.

Figure 5.1 shows the distribution of reconnection rates measured. The majority of the reconnection rates fall in the range 5-30 kV, in agreement with previous studies such as Chisham et al. (2004) and Cumnock et al. (1995). Very few values of potential below 5 kV were measured, probably because the cells are so weak that they are not easily identifiable by visual inspection.

The solid lines in the left hand panels of Figures 5.2 and 5.3 show the occurrence distribution of IMF B_X, B_Y and B_Z components, the total interplanetary magnetic field and the clock angle for the 1,083 lobe reconnection events identified, all measured by the ACE spacecraft. As a comparison, the dashed line represents the same data for the entire period December 2000 to November 2001. In order to ascertain whether the lobe reconnection IMF distributions were significantly different from the overall parent distribution, i.e. if they could be taken at random from the parent distribution, Kolmogorov-Smirnoff tests were performed on the data. The maximum distance between the cumulative distribution functions for the two distributions is calculated (right hand panels of Figures 5.2 and 5.3). This can then be used in conjunction with a knowledge of the number of points in each distribution to determine whether it is possible that one distribution could be randomly drawn from the other, or whether they are statistically different. The top number in each panel is the Kolmogorov-Smirnoff number, D, for that variable, while the lower number is the critical limit (CL) above which the two distributions are statistically different to 99% confidence. Lobe reconnection appears to take place preferentially under conditions of northward IMF, positive B_Y, larger total magnetic field, B, and therefore clock angles $|\theta| < 90°$. Twin reverse cells were preferentially observed in the northern hemisphere during summer for negative IMF B_X as predicted by Reiff and Burch (1985).
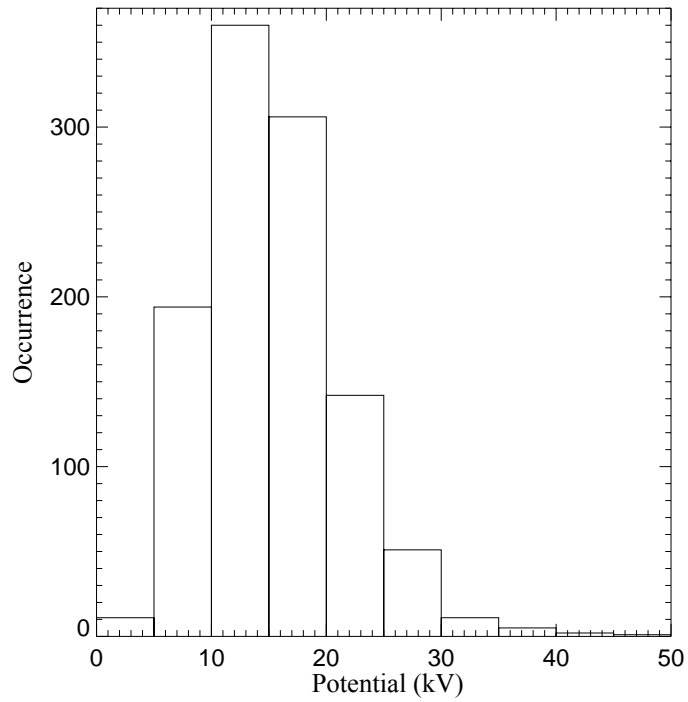
Figure 5.1. An occurrence distribution of the dayside
potential measured from 1,083 SuperDARN potential
maps displaying clear twin reverse convection cells.
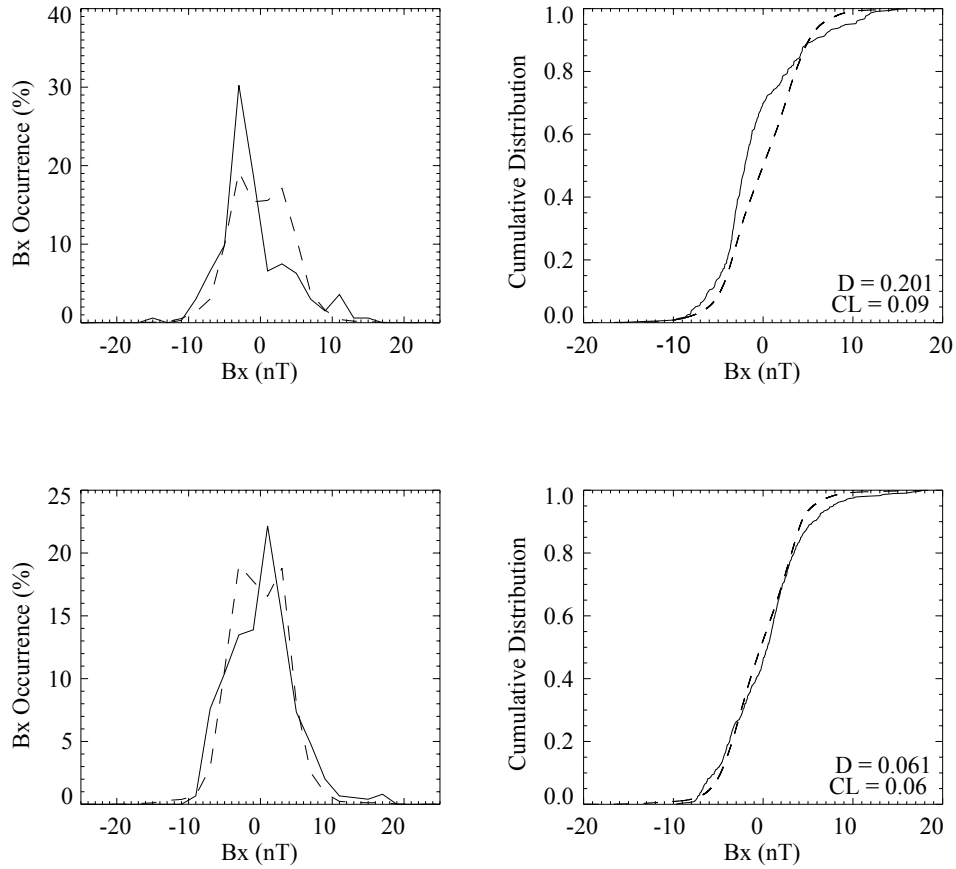
Figure 5.2. Occurrence and Kolmogorov-Smirnov cumulative distribution functions for the solar wind IMF B_X component during March to August (top panels) and September to February (bottom panels). The solid lines are solar wind data at the time of the twin reverse cells and the dashed lines are the solar wind conditions throughout the 6 month period.
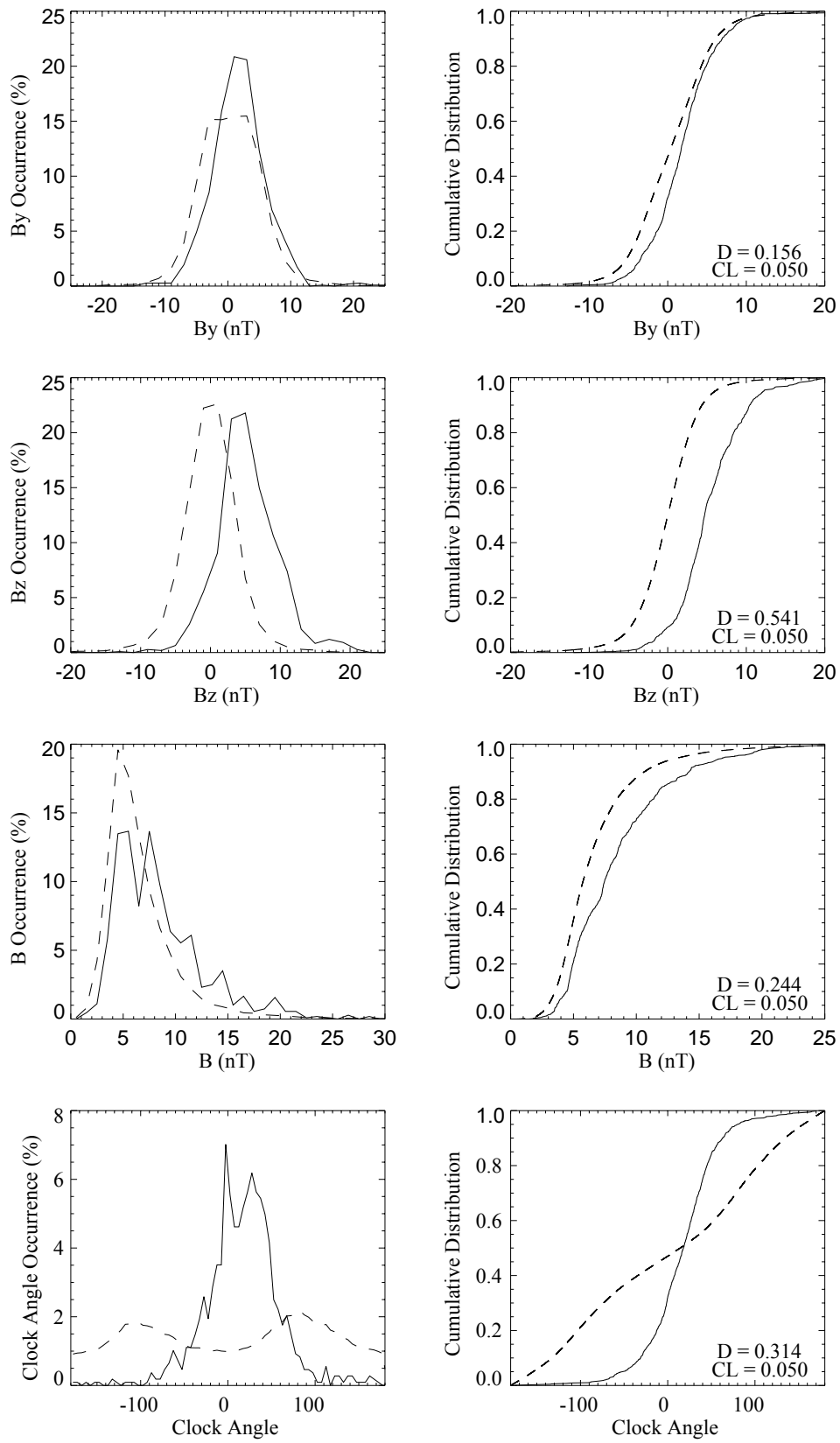
Figure 5.3. Occurrence and Kolmogorov-Smirnov distribution functions for solar wind IMF B_Y, B_Z, B and clock angle. The solid lines are solar wind data during observed twin reverse ionospheric convection cells and the dashed lines are data from the entire period of December 2000 to November 2001.

Figure 5.4 shows the lobe reconnection and yearly distributions (solid and dashed line respectively) for the solar wind speed, the solar wind density, solar wind Alfvén Mach number and Alfvén speed, as well as the Kolmogorov-Smirnov tests. From these data it is clear that there is a higher probability of lobe reconnection taking place under high solar wind densities, therefore lower Alfvén Mach numbers and higher Alfvén speeds.

The lower panels of Figure 5.5 show the potential, Φ_D, calculated from the SuperDARN maps plotted against the GSM B_X, B_Y and B_Z components of the IMF. The grey crosses are the data points, and the black horizontal lines are the mean potential measured in 5 nT bins, shifted by 1 nT. The mean is only plotted where 25 points or more fall within that bin. The thick vertical bars are the error on the mean, and the thin ones are one standard deviation of the data within that bin to give an indication of the spread of the data. The upper panels show the occurrence distribution of the data binned in the panels below, giving an indication of the reliability of the mean potentials. As expected, >95% of the events were observed during northward IMF conditions. There was no IMF constraint on event selection, so this result confirms that twin reverse cells are an IMF $B_Z > 0$ phenomenon. The events for which the IMF B_Z component is negative are probably due to a delay between changing upstream conditions and the response of the ionosphere to those changes.

Figure 5.5c demonstrates that there is a positive correlation between the IMF B_Z and the potential Φ_D in agreement with Freeman et al. (1993). The relation between the potential and the IMF B_Y is less clear than the case for B_Z, although the potential appears to increase with increasing B_Y. There also appears to be an increase in the potential with increasing IMF B_X (Figure 5.5a). It might be expected that for negative B_X the potential would be higher than for positive B_X as this would favour reconnection in the northern hemisphere, although this does not appear to be observed.

Figure 5.6a shows the potential against the total interplanetary magnetic field strength in 5 nT bins. The grey crosses in the Figure are the data points and the black horizontal lines are the mean potential in 4 nT bins, shifted by 1 nT. The mean potential is only plotted where 25 points or more fall within that bin. In all panels the thin vertical lines are one standard deviation of the data within each bin,
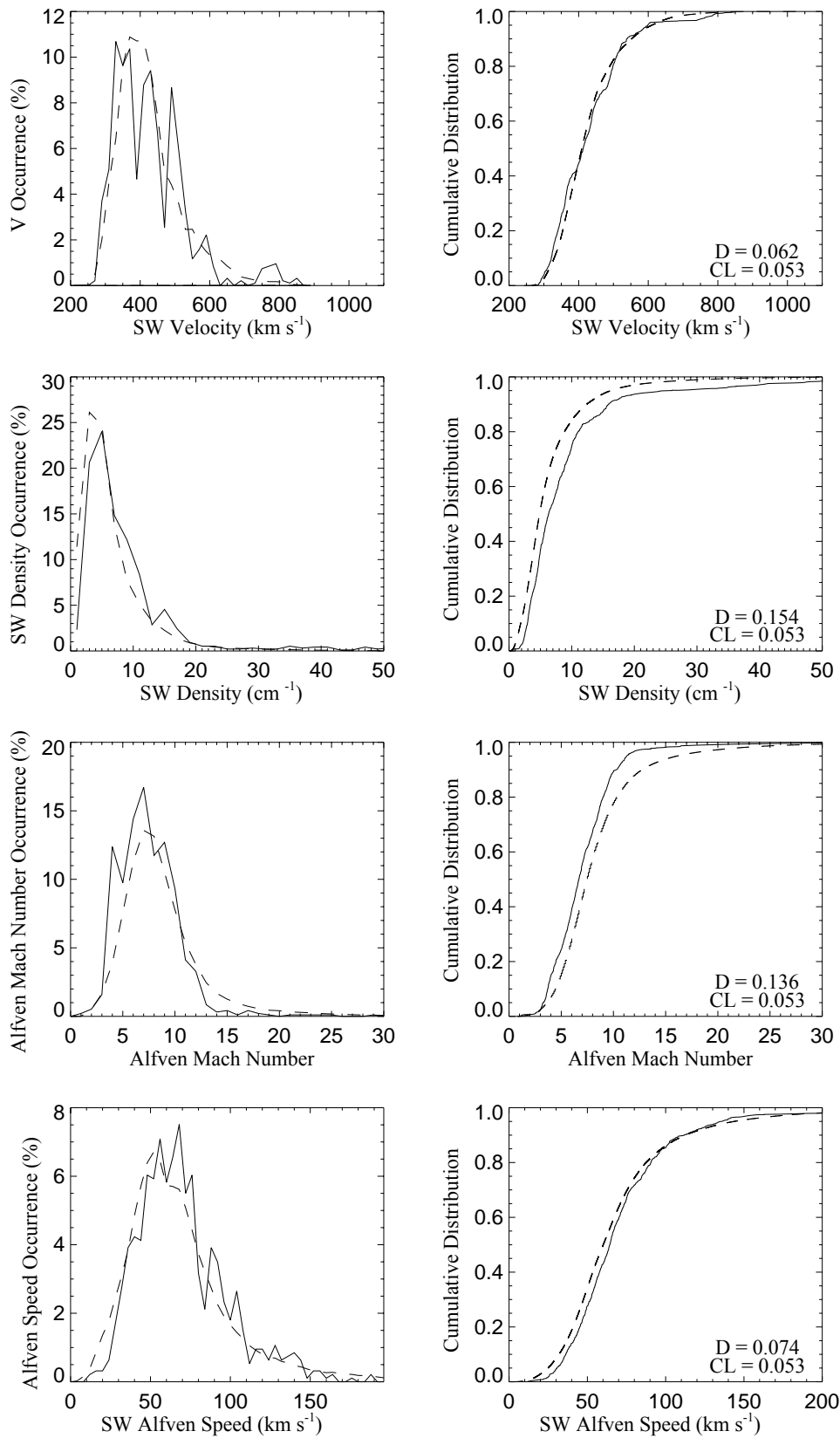
Figure 5.4. Occurrence and Kolmogorov-Smirnov distribution functions for
ACE solar wind V_X, proton density, Alfvén number and Alfvén speed. The
solid lines represent intervals during which twin ionospheric reverse cells
were observed, and the dashed lines are all available ACE data from
December 2000 to November 2001.
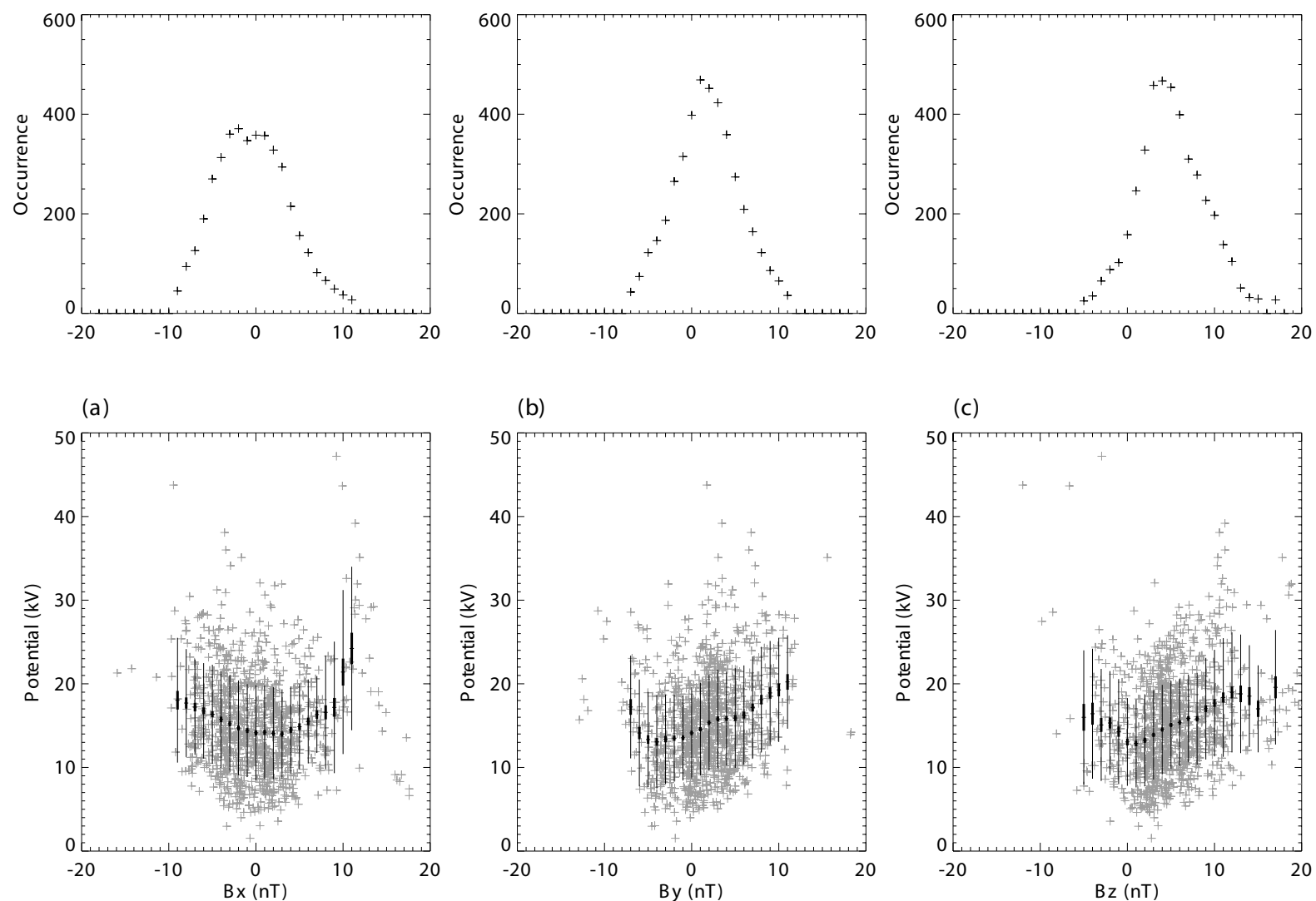
Figure 5.5. The dayside potential measured from the SuperDARN convection maps plotted against the IMF components obtained from ACE data lagged to the magnetopause. The grey crosses in the lower panels are the 1,083 data points and the black horizontal lines are the mean dayside potential in 5 nT bins, each shifted by 1 nT. The thick vertical lines are the standard error on the mean, and the thin lines are one standard deviation of the data in the bin. The upper panels are occurrence distributions of the data in the panels below.
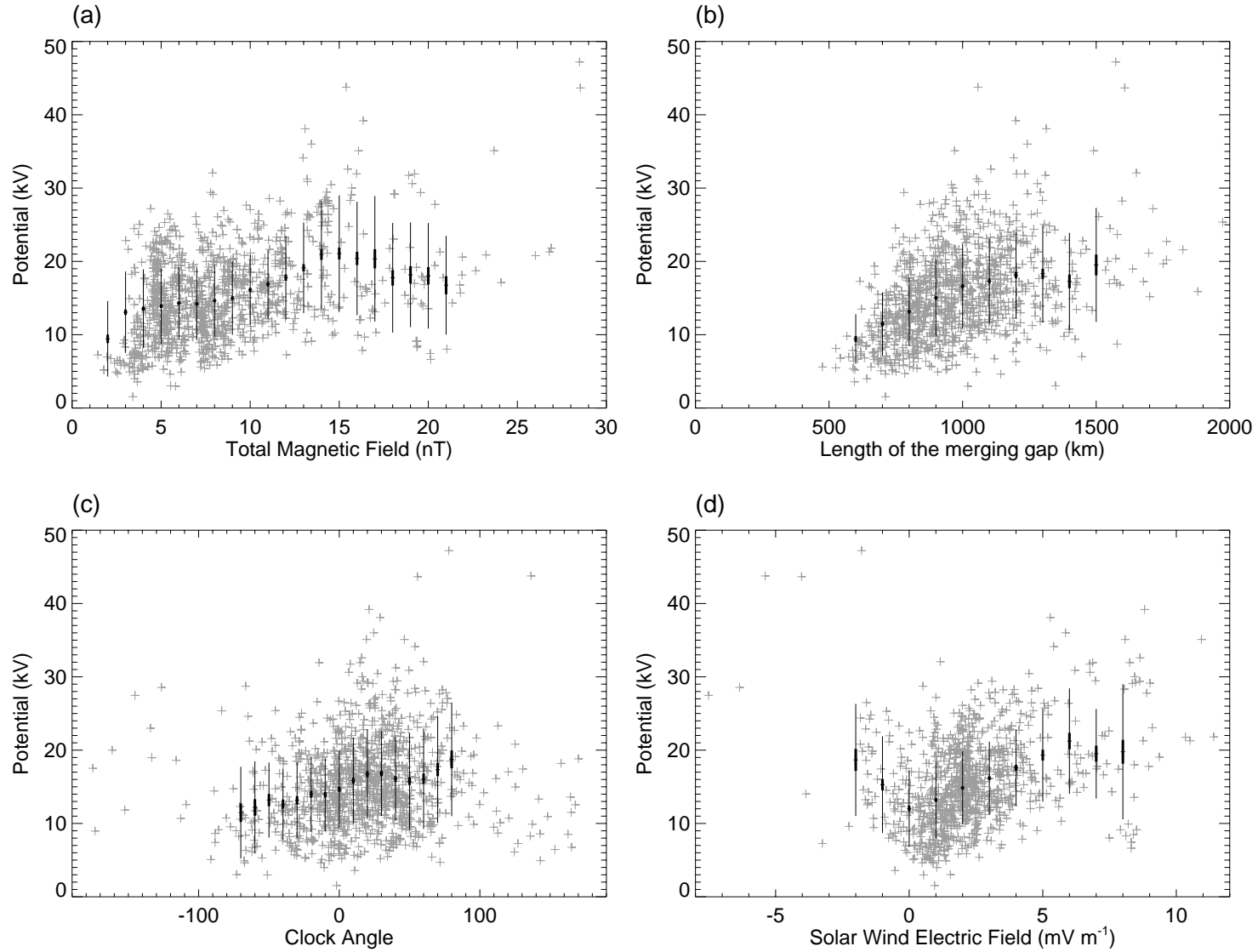
Figure 5.6.   Dayside potential measured from SuperDARN convection maps plotted against (a) the total interplanetary magnetic field, B, (b) the length of the merging gap, (c) the clock angle and (d) the solar wind electric field, total interplanetary magnetic field, $V_X B_Z$. The grey crosses are the data points and the black horizontal lines are the mean potential in sliding bins. The thick black vertical lines are the standard error on the mean and the thin ones are the standard deviation of the data in that bin.

and the thick lines are the error on the mean. There is a positive correlation between upstream magnetic field strength and lobe reconnection rate although there is a large spread. The potential does not appear to depend strongly on the IMF clock angle (Figure 5.6c) which is perhaps surprising as it would be expected that for clock angles approaching ±90° the anti-parallel condition would be increasingly difficult to achieve given the assumption of field line draping. There are fewer data points for clock angles approaching ±90° as these conditions produce highly anti-symmetric reverse twin cells which are difficult to identify. The result of this is that the mean potential is less reliable in these ranges.

Figure 5.6b shows the potential plotted against the merging gap length, which is the distance between the maximum and minimum of the ionospheric potential pattern. The mean potential is plotted in 200 km bins, shifted by 100km. There is a very clear correlation between these two variables, with longer merging gaps on average producing higher potentials. Since the potential is a measure of the amount of sunward flow within the dayside polar cap, it is perhaps to be expected that a longer merging gap would produce more flow as reconnection is taking place over a larger effective length.

The solar wind electric field can be estimated as the upstream solar wind velocity multiplied by the IMF B_Z component (Chapter 2.1.5). The dayside potential is plotted against the solar wind electric field in Figure 5.6d; the two variables appear to be positively correlated. The mean potential is plotted in black in bins of 2 mV m^{-1}, shifted by 1 mV m^{-1}. In previous studies (e.g. Milan, 2004, Milan et al., 2007) a relation has been found between the upstream solar wind electric field, the dayside potential due to low latitude reconnection, and an effective length, L, representing the length of the merging gap given 100% efficient reconnection:

$$\Phi_D \approx -L V_X B_Z \qquad\qquad [3.1]$$

Assuming that the relation takes a similar form to that for southward IMF, the effective length would be approximately 0.15 R_E, far smaller than that found for southward IMF (~5 R_E). We interpret this as an indication that lobe reconnection takes place over a smaller area of the magnetopause than low latitude reconnection, as expected considering the smaller region in which the anti-parallel reconnection condition may be satisfied for northward IMF.

5.2. A statistical comparison of ionospheric plasma flow measurements by the SuperDARN radar network and DMSP spacecraft

The aim of this study is to investigate the accuracy of the SuperDARN ionospheric convection velocities; in particular whether SuperDARN is capable of resolving small scale features such as the twin reverse cells described above. The main advantage of using the SuperDARN radars to determine the ionospheric convection pattern is that they are capable of providing data covering a large portion of the entire northern hemisphere polar cap every two minutes. Due to the necessity of using a statistical model to constrain the electrostatic potential fit, as well as creating a 2-D convection map using one-dimensional line-of-sight velocities, the reliability of this method has been a matter of debate. This Section aims to address the accuracy of the convection maps generated using the map potential technique by comparing the ionospheric velocity measured by overflying DMSP spacecraft with the corresponding convection velocity calculated from the SuperDARN convection maps.

5.2.1. Observations

During January 2001 there were eight northern hemisphere coherent HF SuperDARN radars in operation. Data from each of the radars is combined to produce a global ionospheric convection map by constraining a 10th order spherical harmonic fit of the ionospheric electrostatic potential pattern (Ruohoniemi and Baker, 1998). The potential map is driven by the radar observations, but in areas where radar coverage is poor a statistical model is used to constrain the fit (see Chapter 3.1).

During this time there were four DMSP satellites in orbit. They were all in sun synchronous, polar orbits passing over the northern polar cap approximately every 101 minutes. The altitude of the spacecraft was ~835 km therefore they were situated in the F region of the ionosphere. These satellites took in situ measurements of ionospheric plasma convection using particle driftmeters (Hardy et al., 1984). There are two instruments measuring plasma flow on board each satellite, one measures the plasma bulk flow in the direction of travel of the satellite,

and the other measures the crosstrack bulk flow, i.e. the vertical component and the horizontal component perpendicular to the direction of travel (see Chapter 3.2.8).

2.3 Data analysis

Of the four DMSP spacecraft in orbit in January 2001, reliable data were available from F12, F13 and F15. The corresponding 10th order SuperDARN convection map was generated, and the ionospheric velocity at the footprint of the DMSP spacecraft was calculated from the potential map. The convection velocity was separated into its components in the direction parallel and perpendicular to the spacecraft track, such that the corresponding SuperDARN and DMSP plasma velocities could be directly compared. This analysis was performed on all northern hemisphere DMSP passes during January 2001 at magnetic latitudes greater than 70°. Both panels of Figure 5.7 show a SuperDARN convection map plotted on a latitude-MLT grid with noon to the top and dawn to the right of the panels. The coloured vectors are SuperDARN velocity data points and the contours are the corresponding 10th order electrostatic potential map. Overlaid are the corresponding DMSP passes mapped into the ionosphere with the crosstrack component of the flow plotted as vectors perpendicular to the track. It is important to note each DMSP pass takes ~10 minutes so a comparison is only made between each DMSP vector and the corresponding 2 minute SuperDARN electrostatic potential map. Figure 5.7a demonstrates a single F13 pass over an area with excellent SuperDARN data coverage. The satellite passes through the centre of both convection cells identified by the SuperDARN convection pattern, and the velocities measured by the radars and satellite appear to be similar. The SuperDARN coverage of the pre-noon sector is not good, however this example serves to demonstrate how data from overflying satellites could be used to fill in the gaps in the SuperDARN convection maps. Figure 5.7b shows passes from three spacecraft passing over the polar cap within a 30 minute period. This demonstrates broad agreement between the satellites themselves and the radar data, although again only a representative convection map is shown.

(a) 2nd January 2001, 19:50
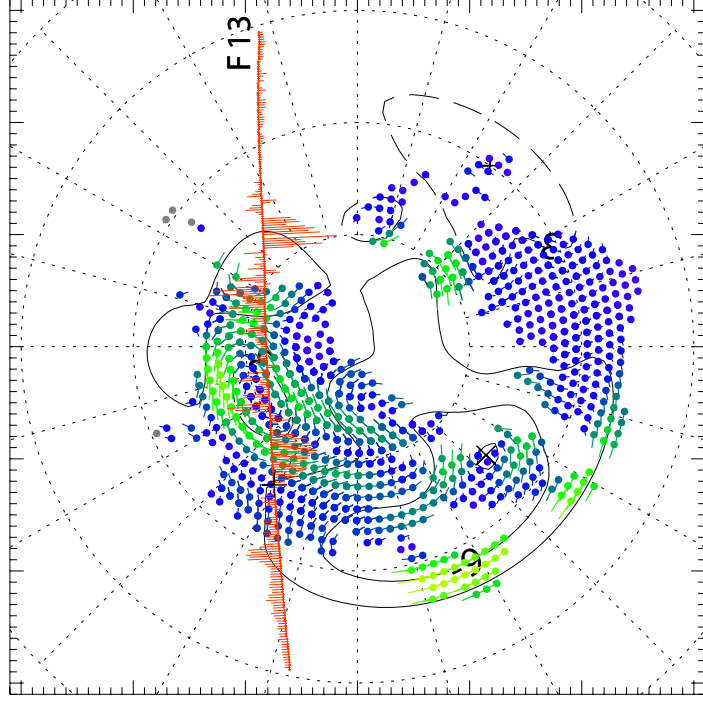
(b) 17th January 2001, 23:06
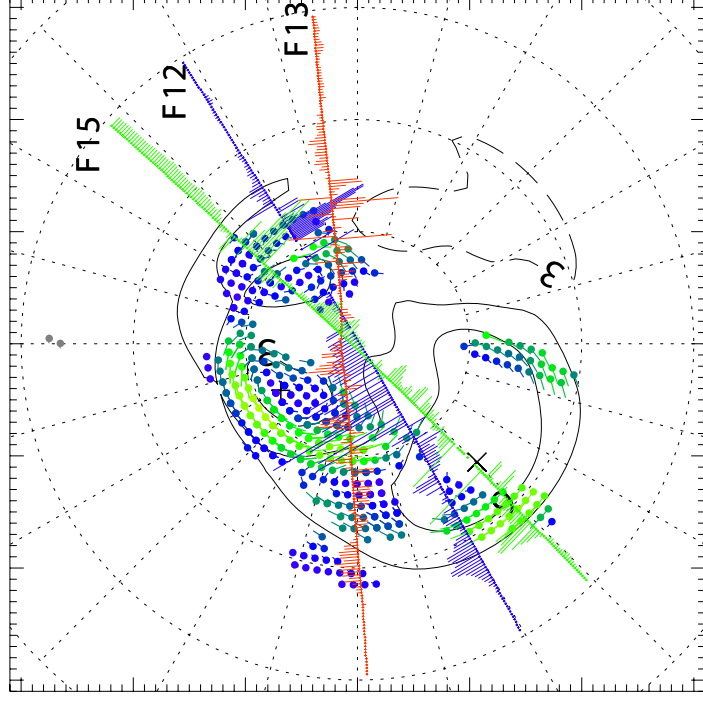
Figure 5.7. SuperDARN radar data plotted as coloured vectors on an MLT-latitude grid with noon at the top and dawn to the right. The tracks of overflying DMSP spacecraft are overlaid along with the measured crosstrack velocity. (a). An example of excellent agreement between the two measurement techniques, with F13 resolving the twin reverse cells in the same location as the SuperDARN convection map. (b). An example of multi-spacecraft observations of the convection velocity; these spacecraft all crossed the polar cap in the space of approximately 30 minutes. The SuperDARN convection maps presented are those closest in time to the midpoint of the track to give an idea of the comparative convection pattern; during the data analysis many maps are used for each spacecraft pass.

5.2.2. Discussion

The DMSP F13 crosstrack velocity measurements are plotted against the velocity obtained from the corresponding SuperDARN potential map at the spacecraft magnetic footprint in Figure 5.8a. The SuperDARN velocity is resolved in the direction perpendicular to the spacecraft direction of travel such that a direct comparison between the ionospheric velocities measured by the two methods can be performed. Figure 5.8a contains velocity measurements for every F13 pass over the northern hemisphere in January 2001; in total over 26,000 data points. The solid red line is a least squares fit of the DMSP velocity measurements to the SuperDARN velocity measurements, and the dashed red line is a least squares fit of SuperDARN to the DMSP measurements. The coefficients of these fits can be found in Table 5.1. It has previously been reported that the SuperDARN potential map technique consistently underestimates high convection velocities due to the potential map technique smoothing out small scale and high velocity features (e.g. Drayton et al., 2005). Figure 5.8a appears to support this theory as SuperDARN measures similar velocities to DMSP in the range -400 to 400 m s^{-1}, however when DMSP measures high velocity flow, SuperDARN frequently appears to measure slightly lower velocities. The coefficients of the DMSP fit to the SuperDARN velocity show that overall SuperDARN agrees with DMSP velocities extremely well, although the tendancy of SuperDARN to measure a slightly lower velocity in high velocity regimes results in the dashed red line being a poor fit.

Figure 5.8b shows the ionospheric plasma velocity measured in the direction of travel of the DMSP spacecraft (using the RPA instrument) plotted against the SuperDARN convection velocity resolved in this direction. Table 5.2 contains the coefficients of the least squares fit of the velocity measured by DMSP to that measured by SuperDARN (solid red line) and vice versa (dashed red line). It is immediately clear from Figure 5.8b that the RPA instrument on the DMSP spacecraft shows a significantly poorer agreement with the SuperDARN velocity data.

In order to see what effect the potential mapping model has on the velocity measured by the SuperDARN radars, any data points where the footprint of the DMSP spacecraft did not fall within 0.5° magnetic latitude and 0.3 MLT of a measured SuperDARN velocity vector were discarded. This means that data from
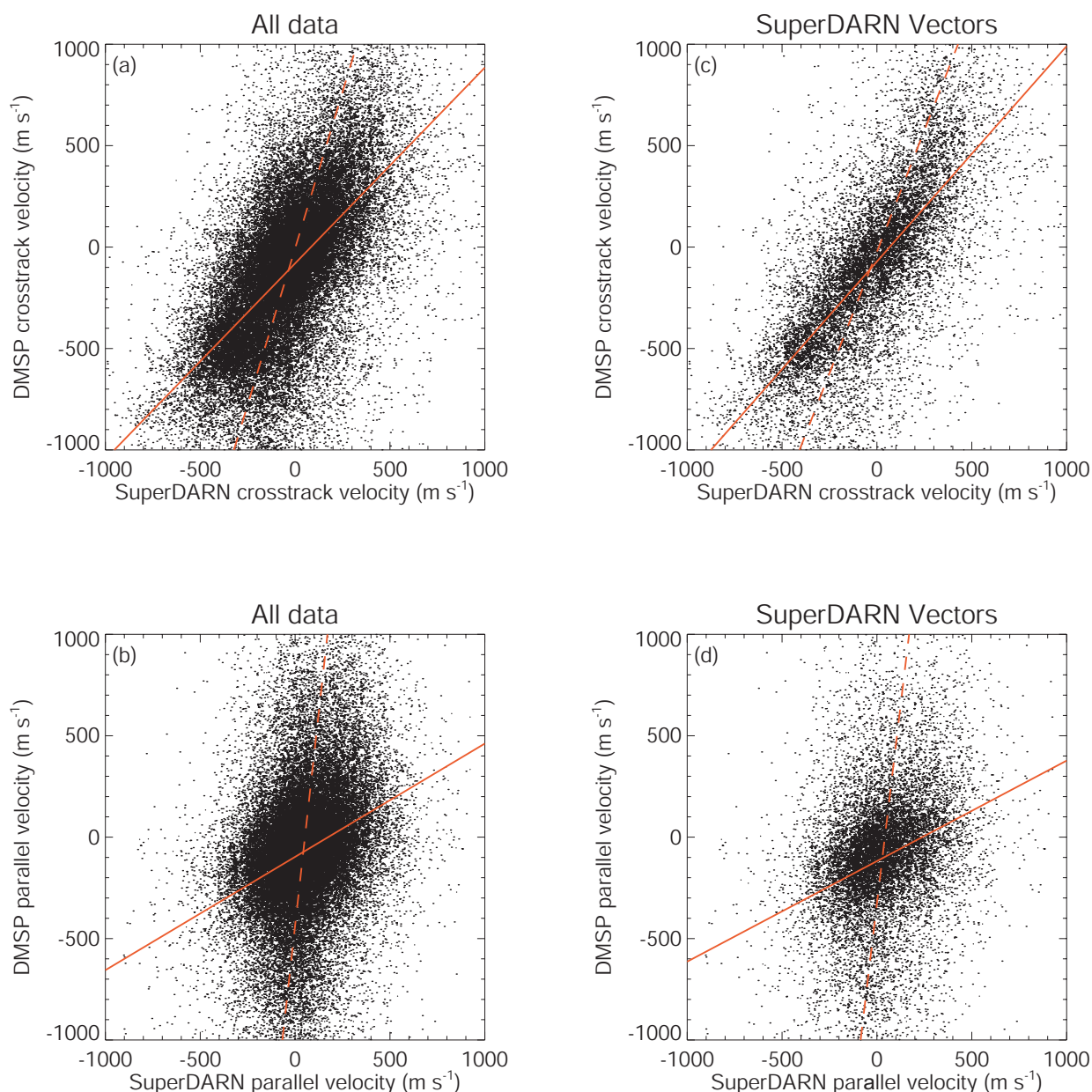
Figure 5.8. The DMSP F13 velocity data plotted against the coincidental SuperDARN velocity for all F13 passes over the northern hemisphere during January 2001. The solid red line is a least squares fit of the DMSP velocity to the SuperDARN velocity, and the dashed red line is a similar fit of the SuperDARN velocity to the DMSP velocity. (a) The crosstrack component of the velocity measured by the DMSP IDM instrument plotted against the SuperDARN velocity resolved in the same crosstrack direction. (b) The along track velocity measured by the DMSP RPA instrument plotted against the SuperDARN along track component. (c) and (d) are the same format as (a) and (b) except they show a reduced data set, with the criteria that the DMSP footprint must be within 0.5° magnetic latitude and 0.3 MLT of a SuperDARN radar velocity measurement.

Crosstrack Data				
	DMSP least squares fit to SuperDARN		SuperDARN least squares fit to DMSP	
	Gradient	Intercept	Gradient	Intercept
DMSP F12 All data	0.98	69.57	0.27	-39.58
DMSP F12 SuperDARN vector criteria	0.95	14.09	0.47	-27.11
DMSP F13 All data	1.01	-80.35	0.34	5.22
DMSP F13 SuperDARN vector criteria	1.10	-70.88	0.42	11.43
DMSP F15 All data	0.88	-157.04	0.29	15.52
DMSP F15 SuperDARN vector criteria	0.92	-140.93	0.37	33.27

Table 5.1. Coefficients of least squares fits of DMSP and SuperDARN crosstrack velocity data for all northern hemisphere passes of F12, F13 and F15 in January 2001.

Along track Data				
	DMSP least squares fit to SuperDARN		SuperDARN least squares fit to DMSP	
	Gradient	Intercept	Gradient	Intercept
DMSP F12 All data	0.60	-162.79	0.16	62.83
DMSP F12 SuperDARN vector criteria	0.69	-183.74	0.27	24.43
DMSP F13 All data	0.61	-97.22	0.13	49.19
DMSP F13 SuperDARN vector criteria	0.54	-119.10	0.13	41.52
DMSP F15 All data	0.68	-145.88	0.22	41.56
DMSP F15 SuperDARN vector criteria	0.70	-176.57	0.20	-18.00

Table 5.2. Coefficients of least squares fits of DMSP and SuperDARN along track velocity data for all northern hemisphere passes of F12, F13 and F15 in January 2001.

areas where there are large gaps in the SuperDARN coverage were removed, as the data from these areas are largely model driven. Figures 5.8c and 5.8d show the crosstrack and along track velocity measured by DMSP F13 plotted against the corresponding SuperDARN velocity. Removing data from areas where there is no SuperDARN data coverage significantly improves the agreement between the two velocity measurements as there is significantly less scatter in these panels. Again the coefficients of the fits are displayed in Tables 5.1 and 5.2, and the agreement between the crosstrack velocity instrument on DMSP and the SuperDARN radar network is extremely good. The DMSP F13 least squares fit to the SuperDARN data has gradient 1.10 and offset -70.88 m s^{-1}. The along track data again shows significant discrepancy between the spacecraft and the radar data, and we conclude that the RPA is significantly less accurate than the IDM instrument.

Figure 5.9 shows the mean DMSP F13 crosstrack velocity plotted against the SuperDARN velocity data averaged in bins of 50 m s^{-1} for the reduced data set described above, i.e. only where the magnetic footprint of the spacecraft is located near a SuperDARN data point. The thin vertical bars are one standard deviation of the data in each bin to give an indication of the spread of the data, the thick bars are the error on the mean, and only bins containing 50 or more data points are shown. The black line shows a theoretical perfect fit between the two data sets and is plotted to guide the eye. This Figure clearly demonstrates the excellent agreement between the two data sets covering most of the velocity range, however there is not sufficient data to analyse the very high velocity case. It must be noted that the DMSP data used here is the 4 second average of the ionospheric convection velocity, whereas the SuperDARN radars complete a beam sweep every 2 minutes in normal operating mode. Each radar range gate has a length ~45 km, whereas the spacecraft is making a point measurement, potentially causing significant discrepancy between the two measured velocities during small scale, high velocity convection regimes. This could be the cause of much of the scatter observed in Figure 5.8 and the discrepancy between the two measuring techniques at high convection velocities.

This study was repeated for DMSP F12 and F15 passes over the northern polar cap in January 2001, with similar results to the F13 study. Least squares fits were again performed to compare the DMSP data with the corresponding SuperDARN data and the coefficients these fits can be found in Tables 5.1 and 5.2.
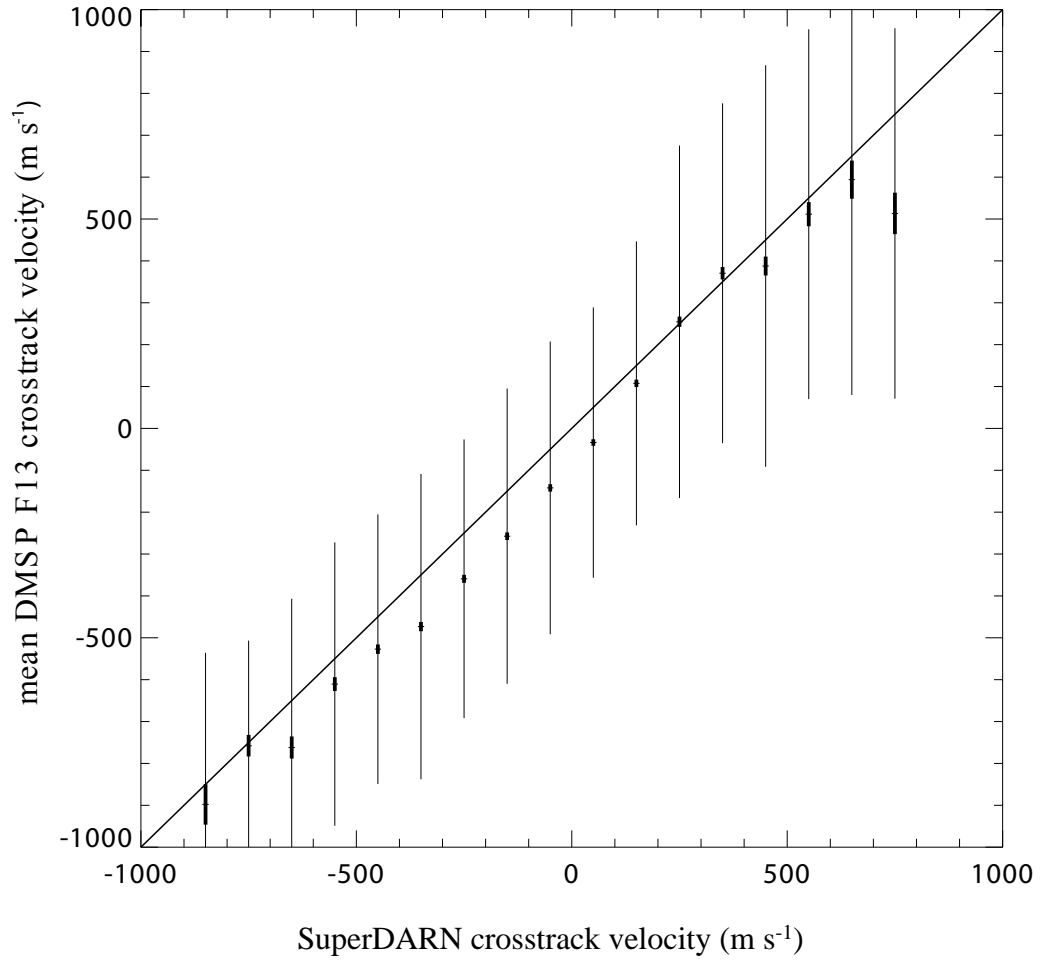
Figure 5.9. The mean DMSP crosstrack velocity plotted against the SuperDARN velocity for the reduced data set described in the text. The data are binned in 50 m s^{-1} bins with the thin error bars showing one standard deviation of the binned data and the thick lines are the error on the mean. Only bins containing a minimum of 50 data points are shown. The solid black line is y = x.

It is interesting to note that although the gradient of the fits are similar for each spacecraft, they have significantly different offsets.

5.3 Conclusion

A statistical study of 12 months of northern hemisphere SuperDARN potential maps has been performed and 1,083 maps were selected within which there are identifiable twin reverse convection cells. The occurrence of twin reverse cells was highest during conditions of northward IMF, positive B_Y and stronger total B field. Higher solar wind densities and lower solar wind velocities also resulted in more twin reverse cells being identified in the SuperDARN radar data.

The lobe reconnection rate was found to depend on all three components of the IMF, B_X, B_Y and B_Z, although most strongly on B_Z. The reconnection rate was also dependent on both the merging gap length and the total IMF, B, although not on the clock angle. A relation was found between the solar wind electric field (VB_Z) and the potential, $\Phi_D \approx LV_X B_Z$ for $B_Z > 0$ with the effective length, $L \sim 0.15\ R_E$. This is significantly smaller than the effective length for low latitude reconnection ($\sim 5\ R_E$), possibly due to a comparatively lower lobe reconnection merging gap length.

In order to ensure that the SuperDARN potential maps used in the study outlined above are capable of accurately representing the ionospheric convection pattern, a further study was carried out. The ionospheric convection velocity measured by three DMSP spacecraft for each northern hemisphere pass in January 2001 was compared with coincident SuperDARN velocity measurements. The level of agreement between the SuperDARN and DMSP crosstrack velocity measurements was extremely good (Table 5.1) with SuperDARN only slightly underestimating the higher velocity measurements. SuperDARN was found to be in greater agreement with DMSP when the DMSP magnetic footprint was located near a SuperDARN data point, as opposed to an area of the potential map that was model driven. It is therefore conceivable that overflying spacecraft data could be an additional input to the SuperDARN potential map model, particularly if the spacecraft instrument offsets can be accurately determined using statistical techniques.

Chapter 6. Reverse dispersed ion signatures: modelling and observation

Magnetic reconnection at the dayside magnetopause is the primary mechanism allowing solar wind plasma to enter the magnetosphere. During southward IMF the plasma injection process is generally well understood; this Chapter aims to address the northward IMF case.

6.1 The high latitude reconnection ion dispersion model

Lockwood and Smith (1994) and Lockwood (1995b) developed a model to predict the ion dispersion signature observed by a low altitude spacecraft during low latitude reconnection. The details of this model are presented in Section 2.3. Briefly, the model uses fixed magnetosheath and solar wind conditions based upon gas dynamic modelling (Spreiter et al., 1966) to calculate the ion signature observed at low altitudes on a newly reconnected field line. Magnetosheath plasma is injected along the newly reconnected field line where it crosses the magnetopause, the point P_n, and this is assumed to move to higher latitudes along the magnetopause at the de Hoffman-Teller velocity, V_{fx}. Variables such as the angles between the newly reconnected field line and the magnetopause (θ and φ) are inferred from geometrical arguments.

Figure 2.4a is a schematic after Figure 1 of Lockwood (1995b). It shows the evolution of the newly reconnected field line in the GSM *X-Z* plane. In contrast, Figure 2.4b is the northward IMF case, with lobe reconnection at high latitudes and the subsequent progression of the field line sunwards, then dusk/dawnwards and antisunwards. Two ion dispersion signatures measured by the low altitude FAST spacecraft are presented in Figure 6.1. Panel (a) shows a normally dispersed ion signature of the sense expected during low latitude reconnection, while panel (b) shows a reverse dispersed ion signature; the ion energy is seen to increase with increasing latitude from 22:48 UT onwards. This signature will be further studied below. A comparison of these two Figures clearly shows that many changes must be made to the low latitude reconnection model when applying it to the high latitude reconnection case.
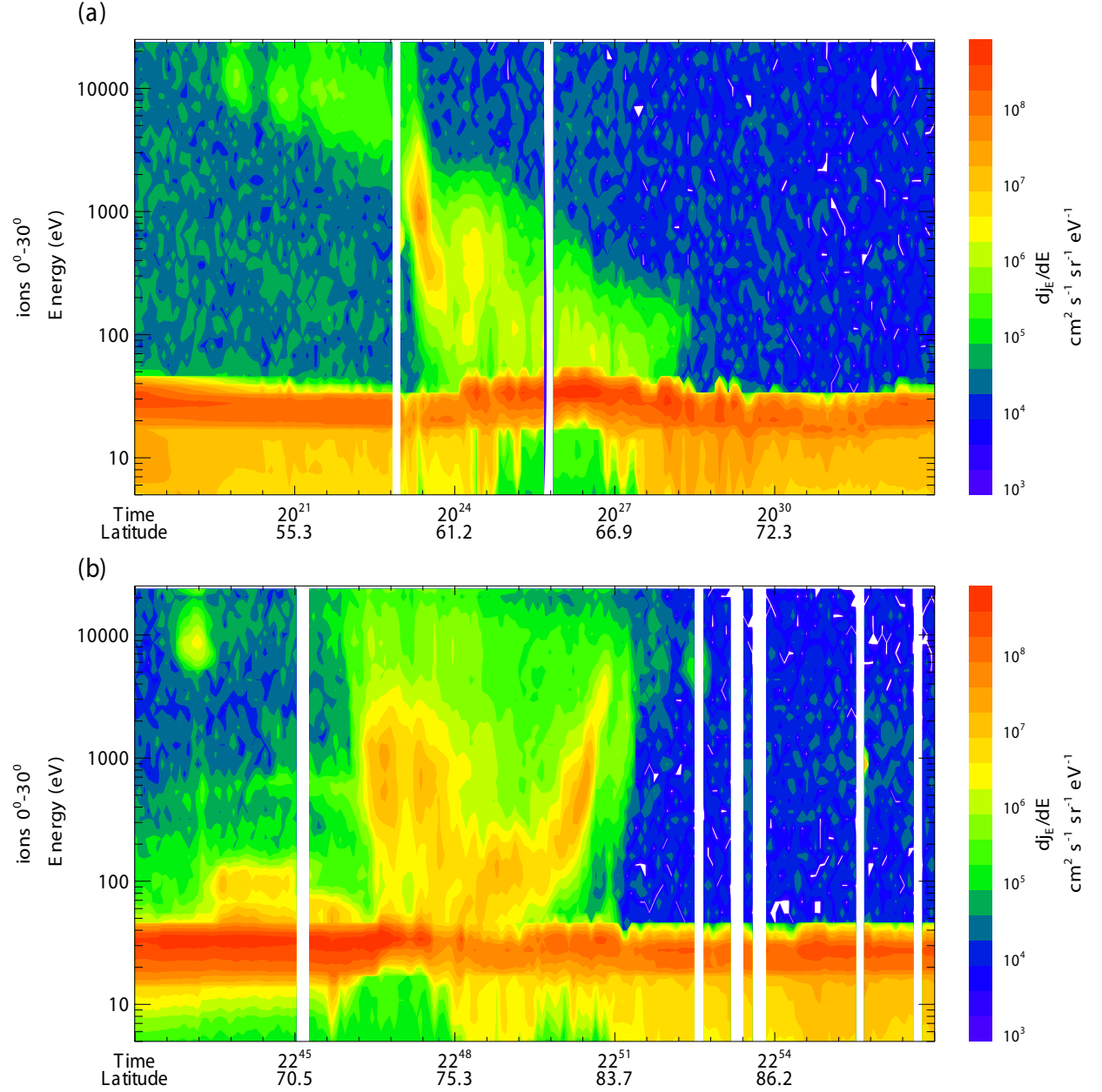
Figure 6.1. Differential energy flux measured for ions with pitch angle 0-30° in the energy range 5 eV to 12 keV measured by the low altitude FAST spacecraft. (a) An example of a dispersed ion signature observed during low latitude reconnection; the ion energy is decreasing with increasing latitude. (b) An example of a reverse dispersed ion signature observed during lobe reconnection; from 22:48 UT onwards the ion energy is increasing with increasing latitude.

The Cooling model enables the user to input solar wind conditions such as the interplanetary magnetic field (IMF), solar wind velocity and density and performs an initial likelihood of reconnection test. If this test is passed then reconnection is initiated at a specified magnetopause location and the progression of the reconnected flux tubes along the magnetopause is calculated, along with the magnetosheath conditions at that point (see Section 2.3.3). Our northward IMF model uses the Cooling model to provide some of the inputs for an adapted version of the Lockwood (1995b) model. It is then possible to predict the ion dispersion signature seen by an observer in the ionosphere moving with a newly reconnected field line. In addition to the inputs provided by the Cooling Model, the Lockwood model also requires some geometrical parameters such as the angles θ and φ, and the distance di from P_n to the ionosphere. These values cannot be determined by the Cooling model or the Spreiter gas dynamic model.

φ is the angle between the magnetosheath field and the magnetopause (Figure 2.8). A field line that has just reconnected at high latitudes has a footprint in one hemisphere, and is also connected to the solar wind in the opposite hemisphere (Figure 2.4b). This field line is draped along the magnetopause, therefore for the purposes of this model, φ will always be very small.

θ is the angle between the magnetospheric field line and the magnetopause (Figure 2.8). Initially the field line is highly kinked and therefore this angle is extremely small. As the field line initially moves sunward this angle increases (Figure 2.4b) and as the field line is then dragged antisunward and dawn/duskward it eventually tends to 180 degrees. The Cooling model provides the location of the point P_n where the field line crosses the magnetopause, but uses an extremely simplistic model to obtain the magnetospheric field. Once the time evolution of P_n has been calculated using the Cooling model, an approximation for θ is made, whereby it starts at an extremely low value, reaches 90 degrees as P_n reaches its most sunward location, then continues to increase until it reaches 180 degrees as the field line is added to the tail lobe.

The distance di to the ionosphere from the point P_n is also unknown. Initially di is estimated to be a distance corresponding to a straight line between the Earth and the reconnection site, d_0. At all subsequent times the distance di is estimated to be d_0 plus the distance along the magnetopause that P_n has moved since

t_0. Overall this results in an overestimate of *di*, which may act to enhance the velocity filter effect and therefore stretch out the ion dispersion signature.

As with the southward IMF case, the energy of the ions observed at low altitude depends not only on the velocity filter effect, but also on the energy of the ion population just inside the magnetopause. Again, the ion population incident on the magnetopause is assumed to be Gaussian and dependent on the magnetosheath parameters at the injection site P_n. This incident ion population is then accelerated as it crosses the magnetopause.

6.2. Modelling results

Ion dispersion signatures observed by a spacecraft at low altitudes travelling with a newly reconnected field line were calculated under a variety of upstream solar wind conditions. The main parameters that were changed were:

- The upstream solar wind density (N_{SW}=2,5,10,20 cm^{-3})
- The upstream solar wind velocity (V_{SW}=300,500,700 km s^{-1})
- The IMF components ($[B_x,B_y,B_z]$=[0,3,5],[0,3,10],[0,3,15],[0,3,20])

In all cases a plasma depletion factor of 0.2 was assumed. It is necessary to either introduce a solar wind V_Y component or an IMF B_Y component if reconnection is being initiated along the Sun-Earth line, as this enables the reconnected field line to eventually escape around the dawn or dusk flank of the magnetosphere. Without this component the reconnected field line feels no force in the dawn- or duskward direction and stagnates as it drapes over the subsolar point.

A representative subset of model results are displayed in Figure 6.2. These show low altitude precipitating ions as a function of time since reconnection. The most prominent feature in all of the panels is the decrease in ion energy with time. Assuming initial sunward ionospheric convection (given the northward IMF conditions) this results in a reverse dispersion signature, where the ion energies decrease with decreasing latitude. Another prominent feature in some of the modelled signatures is a small increase in ion energy immediately following the reconnection of the field line (see for example Figure 6.2b); we call this feature a "hook". This is then followed by the expected decrease in energy with time seen in
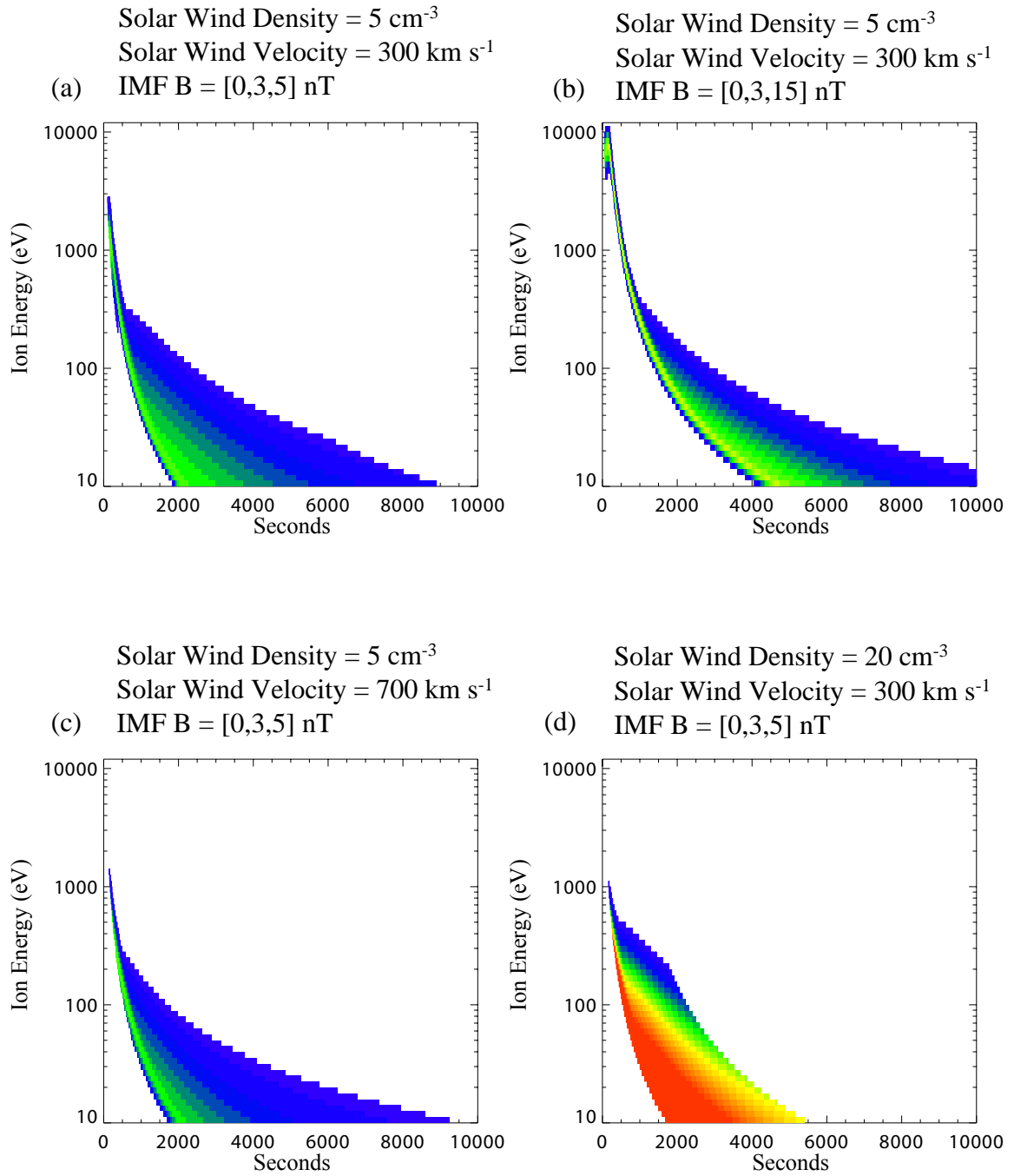
Figure 6.2. Modelled ion dispersion signatures for different solar wind density, velocity and magnetic field conditions.

the modelled signature under all northward IMF conditions. Having analysed the modelled conditions at the position P_n when the hook is seen, it has become clear that the hook is only observed during the time that P_n, (the position of the reconnected field line on the magnetopause) is moving sunward. This hook is characterised by an increase in ion energy with time. The energy of the detected low altitude ions depends upon the four factors outlined in Section 2.3.4, namely the energy of the incident ion population, the topology of the rotational discontinuity, the velocity filter effect, and the distance from P_n to the ionosphere. The sunward motion of P_n would be expected to result in an increased thermal spread of the incident ion population as the magnetosheath plasma is hotter nearer the subsolar point. This effect will dominate over other geometrical effects such as the predicted increase in di and θ and therefore the high energy particles detected while the field line is moving sunward are increasing in energy. As P_n moves antisunward and around the flank of the magnetopause, the magnetosheath temperature, pressure and density decrease, as well as θ increasing, resulting in a decrease of the energy of the incident population and that of the particles reaching low altitudes.

Panel (a) of Figure 6.2 shows the modelled dispersion signature for IMF conditions given by $\mathbf{B}=[0,3,5]$ nT, solar wind velocity of 300 km s^{-1} and solar wind number density of 5 cm^{-3}. The observed ion energy is observed to fall sharply with time; the fastest ions taking ~few minutes to reach low altitudes. Panel (b) is a modelled signature under the same conditions as panel (a) except that the B_Z component of the IMF is now increased to 15 nT. The magnetosheath Alfvén speed is given by $V_A = \sqrt{\dfrac{B^2}{\mu_0 n}}$ where B is the magnetic field strength, n is the magnetosheath mass density and μ_0 is the permeability of free space. Increasing the solar wind magnetic field strength increases the Alfvén velocity in the magnetosheath, which in turn increases the likelihood that the magnetosheath Alfvén speed exceeds the magnetosheath velocity and the newly reconnected field line will initially move sunward. This then produces a small "hook" feature, as seen by comparing panels (a) and (b).

Panel (c) is a modelled dispersion signature with the same upstream parameters as those in panel (a) except that the solar wind velocity has increased from 300 to 700 km s^{-1}. It can be seen that increasing the solar wind velocity (but

keeping the other parameters the same), appears to have little effect on the particle fluxes observed, but the signature is significantly shorter and steeper. This implies that the point P_n follows a similar path in both cases, but the magnetosheath velocity is higher for higher solar wind velocities such that P_n moves to higher latitudes faster where the injected ion population is of lower energy.

Panel (d) was also generated using the same upstream model parameters as those in panel (a), except that the solar wind density has been increased from 5 to 20 particles cm^{-3}. This increase in the solar wind density results in an increase in the magnetosheath density, which leads to more particles precipitating to low altitudes and therefore the particle flux observed by the low-altitude spacecraft is increased.

6.3. Observation of reverse dispersed ion signatures and comparison with model results

In this Section we compare observations of a reverse-dispersed ion signature seen at low altitude by the FAST spacecraft (Carlson et al., 1998) with predictions from our model. The interval of interest is 22:35-22:55 UT on 1st June 2001. This period was chosen because it displayed the correct solar wind conditions for reverse dispersed cusp ion signatures to be observed, there was a suitable pass of FAST at the footprint of the cusp, and there were also concurrent observations from the IMAGE spacecraft (Mende et al., 2000a, c) and the SuperDARN radars (Greenwald et al., 1995), which allow the auroral and convection characteristics to be determined.

Figure 6.3 shows the upstream IMF conditions spanning the interval of interest measured by the ACE spacecraft (Stone et al., 1998; Smith et al., 1998; McComas et al., 1998) located at GSM-X=236 R_E, Y=41 R_E and Z=6 R_E. A time lag of approximately 74 minutes was added to the data in order to allow for the propagation delay from the spacecraft to the magnetopause based on the solar wind velocity as measured by ACE. The top three panels show the IMF B_Y, B_Z and clock angle in GSM coordinates (0° is purely northward IMF and 180° southward), and the bottom two panels show the solar wind GSM V_X component and the solar wind density. The dashed lines show the time interval during which the FAST spacecraft passed over the polar cap. It can be seen from this Figure that prior to and during the time when the FAST spacecraft was over the northern auroral oval, the IMF was

124
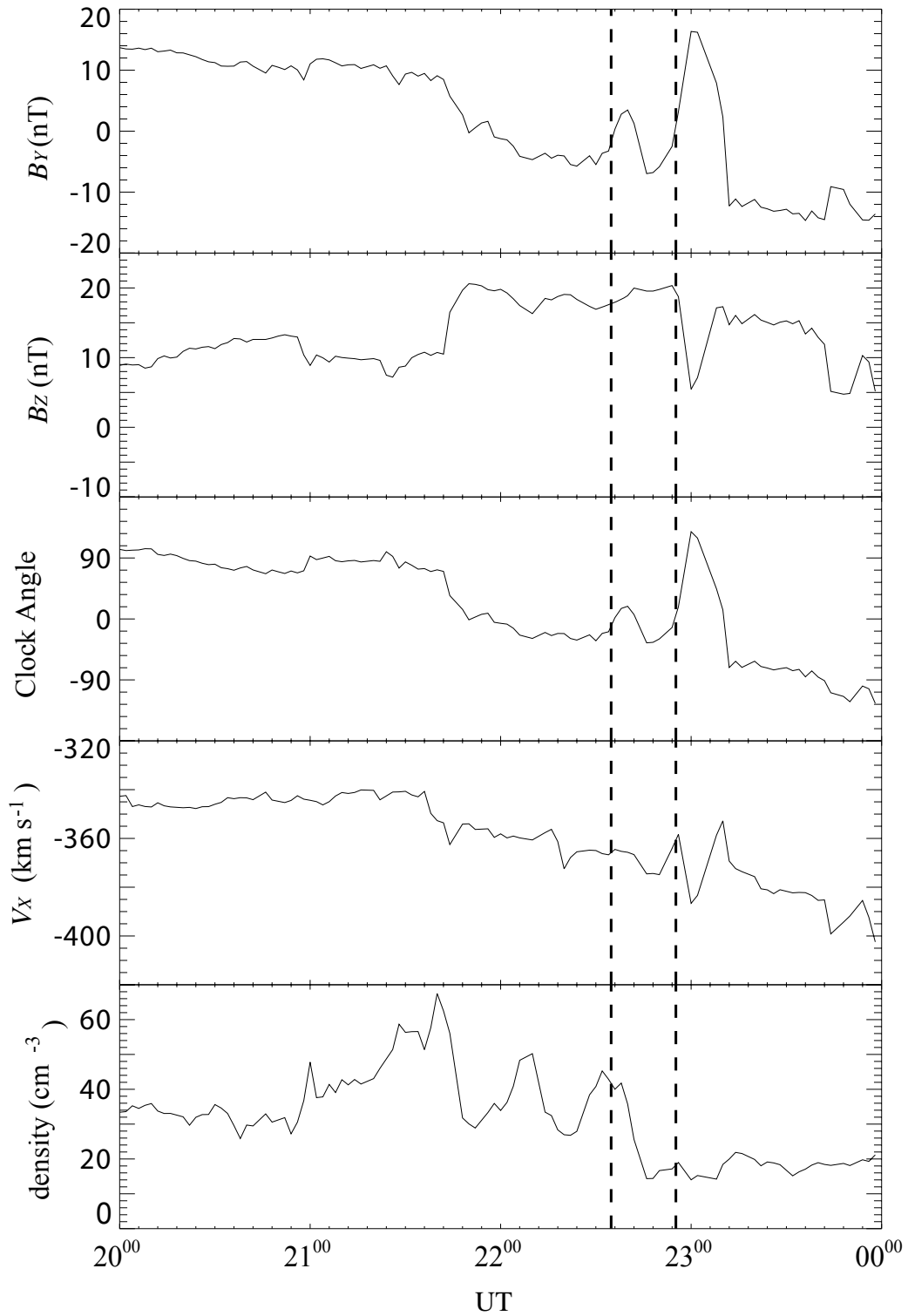
Figure 6.3. ACE solar wind B_Y, B_Z, clock angle, V_X and density data for the period 20:00 to 24:00 UT on 6th June 2001. A time delay of 74 minutes has been added to the data to allow for solar wind propagation to the magnetopause. The dashed lines span 22:35 to 22:55 UT during which time a reverse dispersed ion signature was observed by the low altitude FAST spacecraft.

northward, therefore lobe reconnection would be expected to be taking place. The solar wind speed was lower than the average value for that year (436 km s^{-1}) and the solar wind density was exceptionally high compared to the average yearly value of ~6 cm^{-1}.

In order to verify that lobe reconnection is taking place, it is possible to look at the ionospheric convection pattern measured by the northern hemisphere SuperDARN radars and the concurrent auroral images.

Figure 6.4 presents three images taken by the SI12 instrument on the IMAGE spacecraft in a latitude-MLT frame with noon to the top and dawn to the right. The images were taken just before, during, and just after the interval of interest on 1st June 2001. A clear cusp spot is seen near noon and between approximately 83 and 86 degrees latitude, particularly clearly in panels (a) and (c). The main auroral oval is also visible equatorward of 80 degrees in all three panels. The auroral features equatorward of the main auroral oval in the post noon sector are "sub-auroral proton flashes" associated with the very high solar wind ram pressure caused by high solar wind density at this time (Hubert et al., 2003). Overlaid on the IMAGE data are the SuperDARN potential maps during the interval. The coloured dots represent radar data, while the black contours are the electrostatic potential pattern. The radar coverage is not complete on the dayside, however there are clear twin reverse cells indicative of lobe reconnection taking place at this time. The solid line in panel (b) approximately following a noon-midnight cut over the polar cap is the trajectory of FAST between 22:36 and 22:54 UT. A comparison of the spacecraft trajectory with the SuperDARN convection pattern indicates that FAST crosses the location of the cusp spot observed most clearly in panels (a) and (c) but also visible in panel (b). Unfortunately the amount of SuperDARN backscatter is reduced during the exact time period of the FAST pass, however the FAST trajectory appears to be closely aligned with the direction of the sunward flow in panels (a) and (c) at the latitude of the cusp spot. This indicates that if a reverse dispersed ion signature was generated at the cusp footprint, the FAST footprint would cut through this signature. The crosses marked on panel (b) represent the approximate location of the merging gap at 86° between 9 and 15 MLT. This was estimated from the location of the cusp spot and the twin reverse cells in the SuperDARN convection flow maps during the interval.
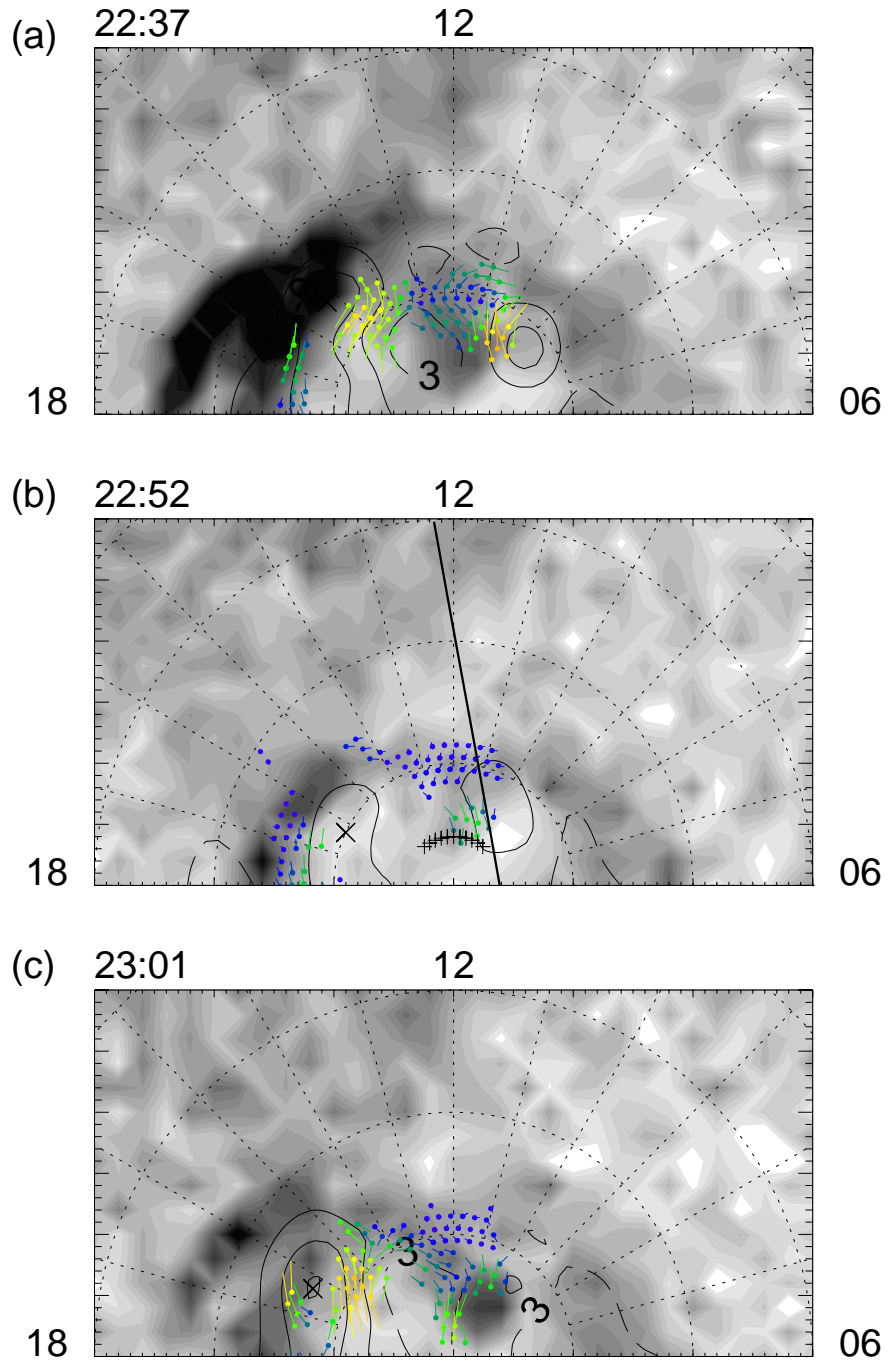
Figure 6.4. 1st June 2001: IMAGE SI12 images of the dayside polar cap are plotted as filled contours on an MLT-latitude grid with noon at the top. The black line contours are the electrostatic potential calculated from the SuperDARN radar observations, which are plotted as coloured vectors. (a) Clear twin reverse cells are observed at 22:37 UT with a cusp spot near noon. (b) The SuperDARN velocities decrease at the time of the FAST overpass, the footprint of which is shown as a black line from near noon towards midnight. The black crosses are the estimate of the merging gap location at 86°. (c) Clear twin reverse cells are again observed at 23:01 UT with a cusp spot in the pre-noon sector.

The top panel in Figure 6.5 is an image from the SI12 camera on the IMAGE spacecraft, with the simultaneous SuperDARN radar data overlaid. The trajectory of the FAST spacecraft is marked by a line of crosses which goes from noon to near midnight. Panel (c) shows the differential energy flux of ions with pitch angles between 0 and 30° measured by the FAST spacecraft during the interval 22:40 to 22:55 UT on 1st June 2001. The red crosses overlaid on the spacecraft track in panel (a) correspond to the times marked by the vertical dashed lines in panels (c) and (d). The first vertical line marks the beginning of a population of high fluxes of high energy ions. The source of these ions is unclear, although they line up with the spacecraft passing through the auroral oval. Other possible sources of such a particle population are discussed in Chapter 4. The second line marks the end of this population and the start of the reverse dispersed ion signature. This signature is characterised by high fluxes of ions at low energies (~100 eV) increasing in energy with time and reaching energies just below 10 keV at the location of the third dashed line. The flux of ions then decreases although it is possible to see a hook-shaped extension of this signature. Panel (d) is the pitch angle distribution of ions with energy between 1 and 25 keV. A clear double loss cone is visible until the time of the first dashed line, indicating closed field lines. After this only a single loss cone is observed, although this is only an indicator of particle injection at some point along the field line and it is not clear whether the field line is open or closed.

Knowing the trajectory of FAST across the polar cap and the solar wind conditions at the time that the reverse dispersed ion signature was seen, a modelled dispersion signature can be generated using the model described in Section 6.2. An approximate reconnection location from the SuperDARN convection map (Figure 6.4b) and the solar wind conditions measured by ACE and lagged to the magnetopause (Figure 6.3) were used as inputs into the Cooling model, which then produced the magnetosheath conditions at the points P_n. A plasma depletion value of 0.2 was again used to account for a plasma depletion layer and the ion dispersion signature at the footprint of the moving field line was obtained. The convection footprint of this newly reconnected field line must now be calculated.

The ionospheric convection maps generated using SuperDARN radar data enable identification of the twin reverse convection cells. The centre of these cells marks the approximate extent of the merging gap. Assuming that the merging gap
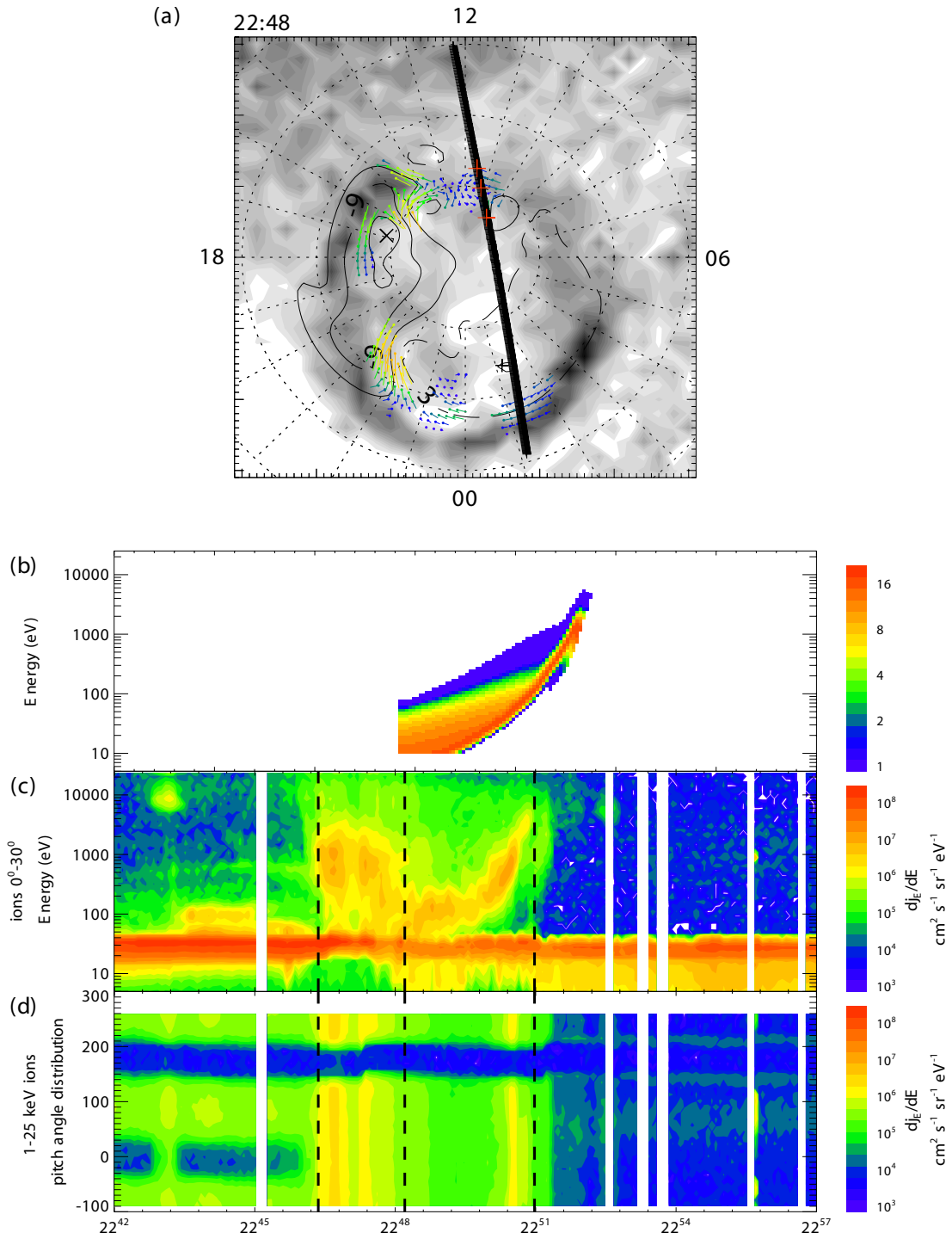
Figure 6.5. (a) IMAGE SI12 data from 22:48 UT on 1st June 2001 plotted as filled contours on an MLT-latitude grid with noon at the top. The SuperDARN convection velocities are plotted as coloured vectors with the corresponding electrostatic potential map as line contours. The FAST footprint is shown as a series of black crosses passing from near noon to 01 MLT. The 0-30° pitch angle ion differential energy flux is plotted in panel (c), and the 1-25 keV ion pitch angle distribution is plotted in panel (d). The times of the vertical dashed lines correspond to the red crosses on the FAST trajectory. Panel (b) contains the modelled ion signature for the FAST spacecraft.

can be approximated to be at constant latitude between these points (Figure 6.4b), the latitude of the first detectable injected ions is estimated to be 86°. Approximating the speed of the sunward convecting plasma to be 250 m s^{-1}, and modelling the twin reverse cells initially as sunward streamlines of constant MLT originating at the merging gap latitude, it is possible to model the ion signature seen at each point in the polar cap. The duration of the ion dispersion signature is much shorter than the time for the footprint of a field line to begin convecting dusk/dawnward and poleward, so the entire signature will be seen during the initial sunward convection of the field line.

The modelled ion dispersion signature is displayed in Figure 6.5b. It can be seen that there are some good similarities between the modelled and the observed signatures. The onset of the observed signature occurs close to the start of the modelled dispersion signature, and the signature gradient and energy range in both the modelled and dispersed signatures appear to be well matched. As discussed above, there is a high energy (~1 keV) ion population observed by the FAST spacecraft prior to the reverse dispersed ion signature and therefore at lower latitudes. Further work is necessary to understand the origin of this signature.

Finally the modelled signature displays a hook signature made up of high fluxes of ions on the poleward edge of the dispersion signature. This hook signature is generated as the point at which the reconnected field line crosses the magnetopause, P_n, moves initially sunward due to the magnetic tension force, before convecting dawn/duskward and antisunward into the tail. This hook signature is perhaps visible at the end of the ion dispersion signature measured by FAST, although it is significantly less clear than that seen in the model.

6.4. Cluster statistics

In order to verify whether the dispersion signatures observed by overflying spacecraft display the same solar wind dependence as the modelled reverse dispersed ion signatures, it is necessary to analyse many spacecraft passes over the dayside polar cap under varying solar wind conditions. A list of ion dispersion signatures observed by the CIS instrument (Rème et al., 2001) on the mid-altitude Cluster spacecraft during 2001 and 2002 was provided by Frederick Pitout. An example of a reverse dispersed ion signature as observed by three of the Cluster

spacecraft is presented in Figure 6.6. The top panel shows the solar wind data measured by the WIND spacecraft and a time delay of 20 minutes has been added to account for the travel time to the magnetopause. The IMF is northward throughout the interval, such that reverse dispersed ion signatures would be expected to be observed. The lower three panels show the differential energy flux of ions with a pitch angle between 140 and 180 degrees, i.e. field-aligned as the spacecraft are at the southern cusp. Clear signatures are observed by all three spacecraft, with the black lines indicating the approximate slope of the dispersion. The black circles highlight a high energy population observed at lower latitudes than the dispersed signatures; the nature of which is unclear but which matches closely a similar feature in the previous FAST observations. Another observed feature is a "hook" shape at the high latitude end of the dispersion signature, similar to those discussed earlier.

The database of ion signatures observed by Cluster can be combined with the simultaneous solar wind conditions using ACE data lagged to the magnetopause. The top row of Figure 6.7 shows the occurrence distribution of the upstream solar wind data lagged to the magnetopause during intervals of 15 reverse dispersed ion signatures observed by the Cluster spacecraft. The centre row shows the occurrence distribution of solar wind conditions during intervals of 30 normally dispersed ion signatures, and the lower row shows the occurrence distribution of all ACE solar wind data during the years 2001 and 2002. $\sqrt{N}$ error bars converted into percentages are plotted on all of the histograms, where N is the number of data points in a given histogram bin. The far left column shows the IMF B_Z component during these intervals. As expected, the IMF is predominantly northward during the times when reverse ion dispersion signatures were observed, and southward for the normally dispersed signatures. The centre column displays the solar wind velocity in the Earthward direction. There does not appear to be an obvious tendency for reverse or normally dispersed signatures to be observed during particular solar wind velocity conditions. The model signature density increases with increasing solar wind density, therefore it might be expected that in order for a low altitude signature to be observed by a spacecraft, significant plasma injection may be required at the magnetopause. The right hand column of Figure 6.7 displays the upstream density during the reverse and normally dispersed signatures, to be compared with the
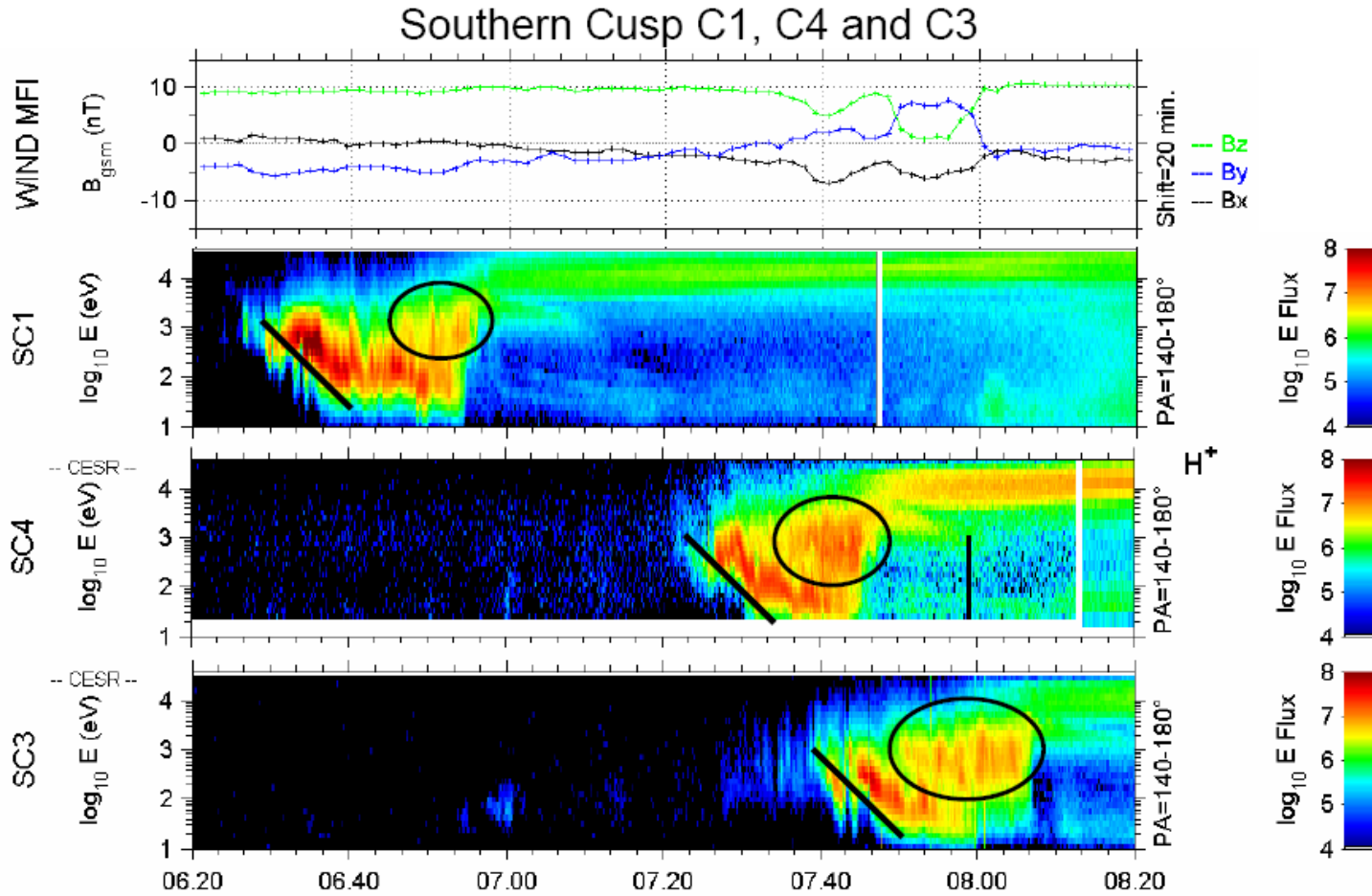
Figure 6.6. An example of a reverse dispersed ion signature observed by three Cluster spacecraft. (a) WIND IMF data with a 20 minute time shift to allow for solar wind propagation to the magnetopause. (b), (c) and (d). The differential energy flux observed by Clusters 1, 4 and 3. The black lines give an idea of the gradient of the reverse dispersed signature and the black circles highlight a high energy ion population equatorward of the main dispersion signature, the source of which is unclear. A clear "hook" signature is observed poleward of the main dispersion signature by each of the Cluster spacecraft. Plot provided by F. Pitout.
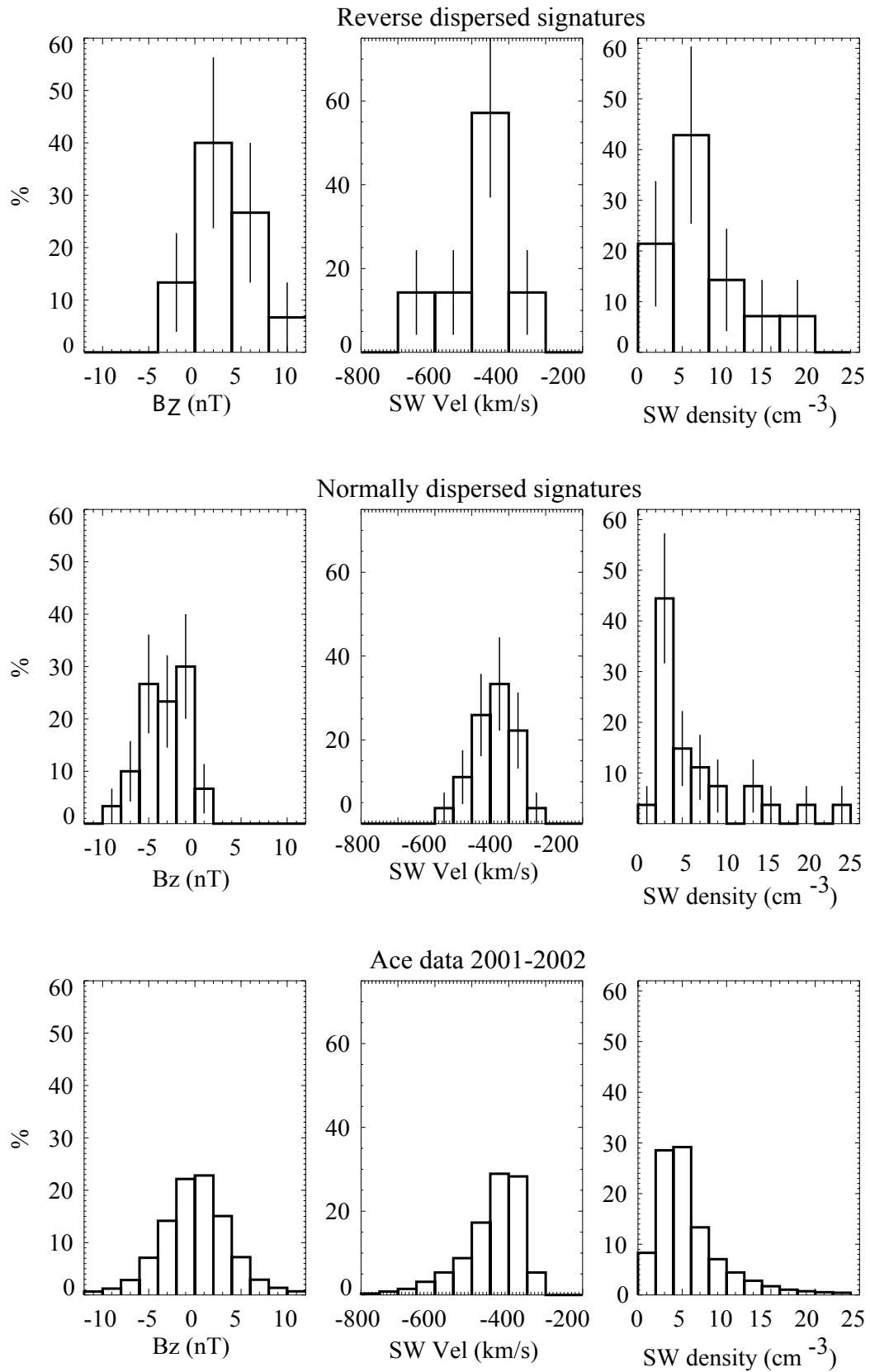
Figure 6.7. Occurrence distributions of solar wind B_Z, V_X and density during times of observed reverse dispersed ion signatures (top row), normally dispersed ion signatures (middle row) and all data throughout 2001-2002 (bottom row).

133

parent distribution in the lower panel. The number of events for which ACE solar wind density was available is low, particularly for the reverse dispersed signatures, however this preliminary result does not show a significant bias towards higher solar wind densities for either the normal or the reverse dispersed signatures.

Figure 6.8 shows the maximum signature density measured by the Cluster spacecraft plotted against the upstream solar wind density. As previously mentioned, the model outlined in Section 6.2 predicts that the density of the observed low altitude signature should be proportional to the upstream solar wind density. The black crosses show the normally dispersed signatures while the red crosses show the reverse dispersed signatures. It is clear from this Figure that even with the limited statistics available, the density of the observed signatures does appear to increase with increasing solar wind density.

Further comparisons between statistical data and the modelling work are beyond the scope of this study, however building up a larger statistical database of normal and reverse dispersed ion signature from a variety of spacecraft would be of interest in the future.

6.5. Conclusion

A model has been developed to simulate the low altitude particle signatures of high latitude reconnection. The model is based on the theory of Lockwood (1995) in which particle signatures of low latitude reconnection are studied. The Cooling model is also introduced into the high latitude model in order to provide the location of the reconnection site, reconnected field line motion and magnetosheath conditions. The dependence of the modelled signature on upstream solar wind conditions is analysed and appear to be in agreement with a small statistical study undertaken using dispersion signatures observed by Cluster. A very clear reverse dispersed ion signature observed by FAST was analysed; the upstream conditions fed into the model and good agreement obtained between the modelled dispersion signature and the observed signature.
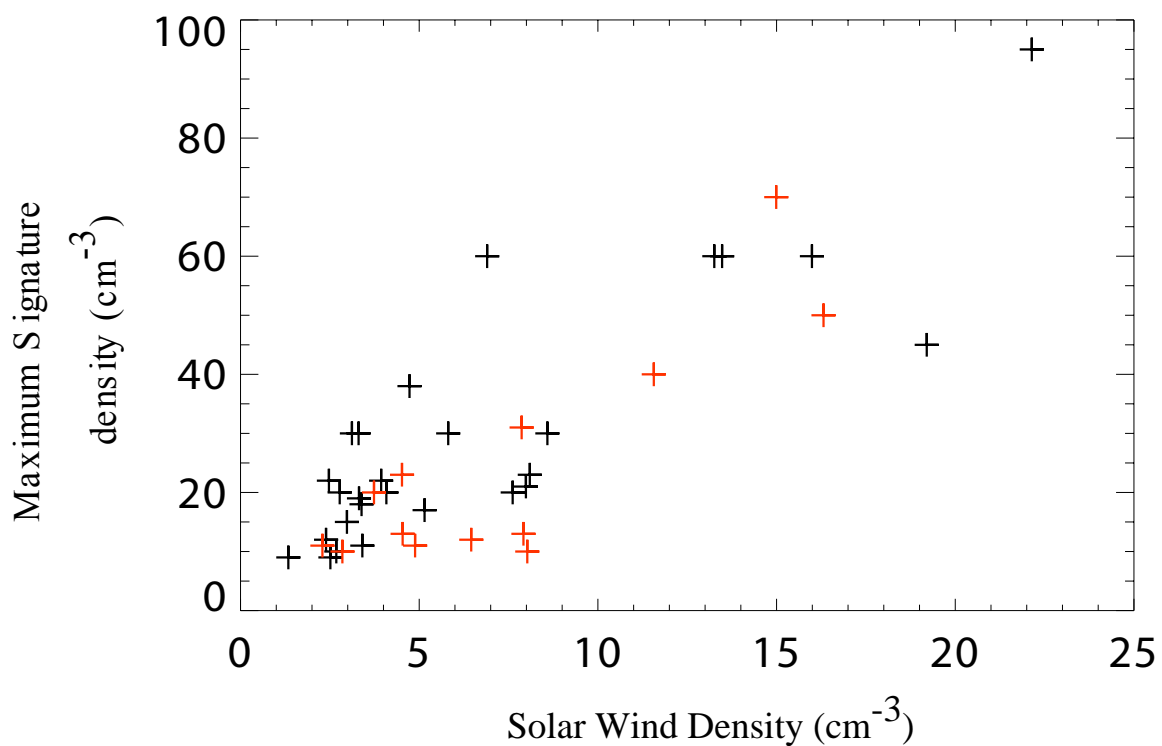
Figure 6.8. Maximum observed ion density in the reverse dispersed ion signatures (red crosses) and normally dispersed ion signatures (black crosses) measured by the Cluster spacecraft in 2001 and 2002, plotted against the upstream solar wind density measured by the ACE spacecraft and lagged to the magnetopause.

Chapter 7. The Auroral and Ionospheric Flow Signatures of Dual Lobe Reconnection

Two case studies demonstrating the first observational evidence for the occurrence of dual lobe reconnection (DLR) are discussed in this Chapter. The first study was based on a time interval previously studied by McFadden (private communication) following which he noted the formation of a cold, dense plasma sheet and postulated that DLR might be the plasma capture mechanism. A detailed analysis of ground-based and spacecraft data was performed and the first conclusive evidence of DLR is reported, along with calculations of the DLR threshold clock angle, the amount of flux closed, the amount of solar wind plasma captured by the magnetosphere, and the possible implication for the formation of a cold, dense plasma sheet.

The second study was selected because multiple upstream spacecraft showed that the clock angle passed extremely slowly through zero, and good auroral and SuperDARN radar coverage were also available. Dual lobe reconnection was shown to close a large amount of flux (~10% of the flux in the polar cap), and as the solar wind density was high, a very large amount of solar wind plasma was captured during the process.

7.1 First Observations of DLR

The first time interval studied was 03:30-06:00 UT on 18th December 2002. This period of continuous imaging of the northern hemisphere by the IMAGE FUV instrument was chosen because the IMF was strongly northward throughout, and the clock angle was observed to pass through zero several times (Figure 7.1).   In addition to this the coverage of the northern polar region by SuperDARN was good, and there were several spacecraft passing over the northern polar cap during the interval. Finally, it has been speculated that dual lobe reconnection may have been occurring at this time and was responsible for the population of a cold, dense plasma sheet (J. P. McFadden, private communication).
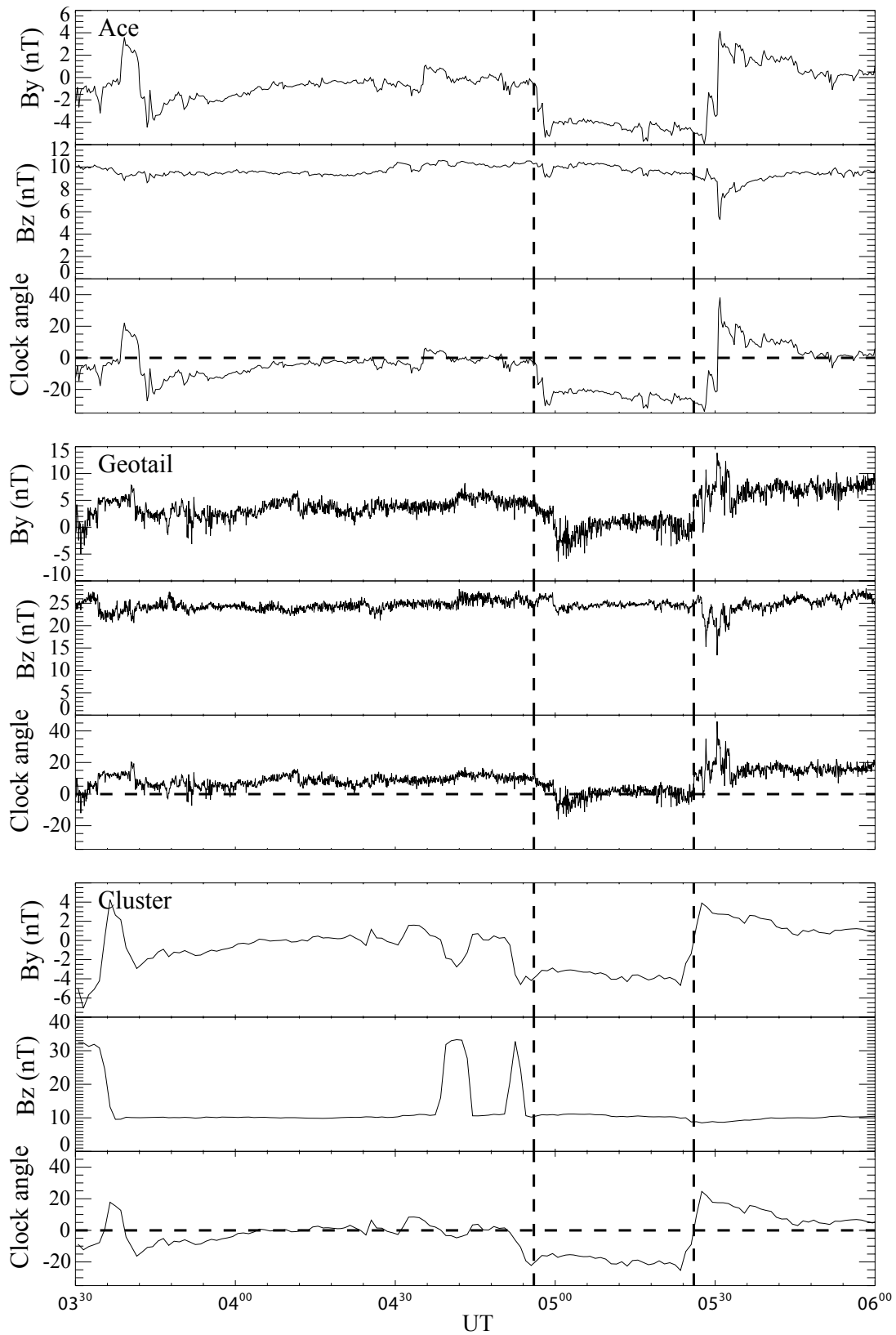
Figure 7.1. GSM BY and BZ interplanetary magnetic field components along with the corresponding clock angle, measured by ACE in the solar wind and Geotail and Cluster-3 within the magnetosheath, 03:30-06:00 UT on 18th December 2002. Vertical lines mark the average time that the clock angle passed through zero at Cluster and Geotail.

137

7.1.1 IMF conditions

It is important to accurately determine the IMF clock angle during the interval as this should give an indication of the times that dual lobe reconnection might be expected to occur (see Section 2.1.3 and Chapter 4). The upstream solar wind and IMF measurements were made by ACE, Cluster and Geotail. Ace was located at GSM $X = 241$, $Y = 8$ and $Z = 11$ R_E during the interval; Cluster was in the magnetosheath, near the bowshock at GSM $X = 5.2$, $Y = 18.4$, $Z = -2.4$ R_E; and Geotail was in the magnetosheath at GSM $X = -8.0$, $Y = -22.0$, $Z = 4.3$ R_E. A propagation delay of 65 minutes was added to the ACE data, based on an observed solar wind velocity of $V_X = -380$ km s^{-1}. This delay does not take into account the slowing of the solar wind as it crosses the bowshock, introducing some uncertainty into the timing of the ACE clock angle. The GSM B_Y component was approximately 0 nT for most of the interval, falling to -6 nT at 05:00-05:30 UT. The GSM B_Z component was close to 10 nT throughout although it dropped very briefly to 5 nT at 05:30 UT. The GSM B_X component remained constant at approximately 5 nT during the interval.

The GSM B_Z component of the IMF measured by Geotail was observed to be approximately 25 nT throughout the interval, elevated above the ACE measurements due to compression of the solar wind as it crossed the bowshock. The GSM B_Y component was around 5 nT at the start of the interval, falling to around -5 nT at 05:00 UT and recovering to approximately 7 nT at 05:30 UT. The GSM B_X component was approximately constant at 5 nT, briefly falling to -3 nT between 05:00 UT and 05:30 UT. The differences between the Geotail and Cluster B_Y magnetic field measurements could be due to field line draping, as Geotail is located 8 R_E downstream of the Earth.

Despite the passage of the solar wind and IMF through the bowshock and the compression of the plasma, the clock angle variation of the magnetosheath field was very similar to that of ACE, though rotated clockwise (when looking from the Sun) by ~10°. This indicates that there is some uncertainty in the clock angle of the field near the lobe reconnection sites. This will be discussed more fully below.

Cluster was just outside the bowshock for much of the interval, and made very similar measurements to ACE. Brief enhancements in the field strength around 04:45 UT and 04:53 UT, most noticeable in B_Z, were due to excursions of

the bowshock outwards, over the spacecraft, which correspondingly entered the magnetosheath. A comparison of the magnetic signatures seen at ACE and Cluster indicate that an ACE lag of approximately 60 minutes may have been more accurate.

At all three spacecraft the clock angle showed a very similar variation, with a sudden anticlockwise rotation of the IMF (when viewed from the Sun) of ~20° at 04:56 UT, followed by a clockwise rotation by ~20° at 05:28 UT, both indicated by vertical dashed lines in Figure 7.1. Although the variations are the same, there are offsets at each spacecraft due to their spatial separation. As will be discussed below, we believe that two bursts of dual lobe reconnection occurred at the times of these rotations, possibly suggesting that the clock angle at the lobe reconnection sites went through 0° at each turn.

Cluster and Geotail were both in the magnetosheath, Cluster near the bowshock and Geotail near the magnetopause, 8 R_E downstream of the Earth. There was a delay of a few minutes between seeing clock angle changes at Cluster and Geotail, which we assume was due to propagation delays within the slowed magnetosheath flow. Since neither of these spacecraft was exactly at the reconnection site, we have initially taken the times of the clock angle rotations to be half way between that recorded at Geotail and that recorded at Cluster. We estimate a ±4 minute uncertainty in the time that the clock angle first passed through 0°.

7.1.2 IMAGE

The IMAGE spacecraft was located over the northern polar cap throughout the interval, 03:30-06:00 UT on 18th December 2002. Images were taken approximately every two minutes using the Wideband Imaging Camera (WIC) which measures the UV aurora, and Spectrographic Imager instruments (Mende et al., 2000a,b) which measure the proton and electron aurora (Section 1.3.7 and 3.3.5).

These images were plotted on a geomagnetic polar grid as presented in Figure 7.2. A typical image from ~ 05:03 UT is shown in a magnetic latitude and magnetic local time frame with 12 MLT at the top of the Figure. Presented as a colour scale are the intensities measured by the WIC instrument on an arbitrary scale. Dayglow is apparent at the top of the image. The auroral oval is clearly
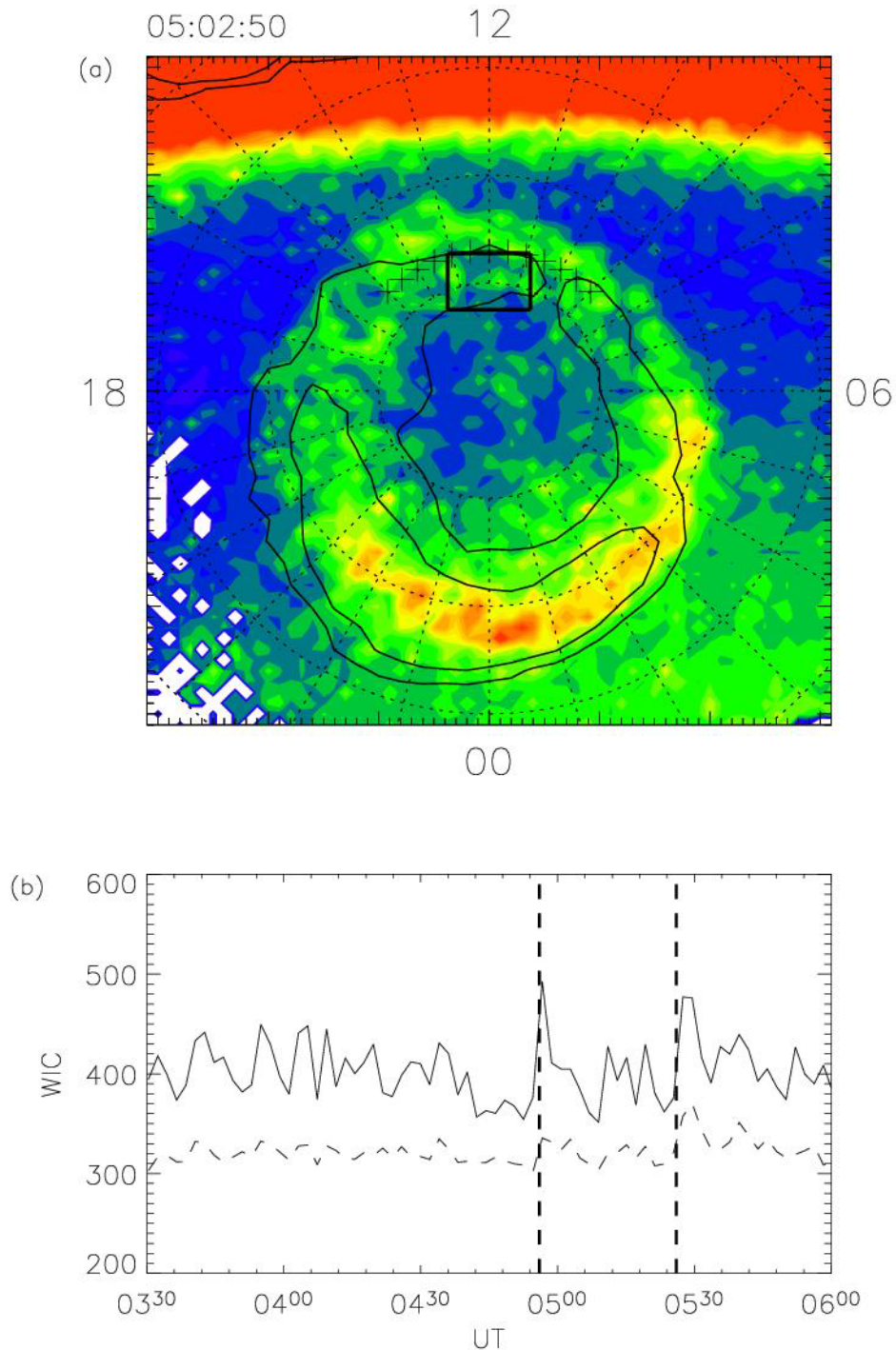
Figure 7.2. (a) A typical image of the Northern polar cap from the WIC instrument on the IMAGE spacecraft, 05:02:50 UT on 18th December 2002. The black square outline represents the area used to observe the change in brightness of the dayside aurora with time. The contours are the superposition of the intensity of the corresponding SI12 image, demonstrating that the proton aurora appear at higher latitudes than the electron aurora on the dayside. The location of the OCB is marked by black crosses between 9 and 15 MLT. (b) Maximum (solid line) and mean (dashed line) brightness of a small section of the WIC images. The vertical dashed lines represent the time that the clock angle passed through 0°, derived from the observations of ACE, Cluster and Geotail. The WIC image clearly shows an enhancement in the mean and maximum brightness just after the zero clock angle as measured by the spacecraft.

visible, with the presence of a relatively dim transpolar arc also evident. Superimposed on this as line contours is the intensity of the proton aurora measured by SI12, again on an arbitrary scale. This demonstrates the relative locations of the electron and proton aurora. In most local time sectors the two are co-located, but near noon there is a clear offset, with the proton aurora displaced polewards of the electron aurora. As described below, we interpret the lower latitude region of noon-sector electron aurora as located on closed field lines and the higher latitude region of proton aurora as being associated with the cusp on open field lines. In this case we would place the OCB at the equatorward edge of the proton aurora, at ~77° latitude near noon (represented by the black crosses in Figure 7.2). Further supporting evidence for locating the OCB at this latitude will be presented below.

Keograms were generated with cuts from noon to midnight, and dawn to dusk using WIC data (Figure 7.3). These clearly show that the auroral oval remains stationary throughout the interval, suggesting that the polar cap is neither expanding nor contracting significantly. We note also the clear presence of a transpolar arc near the noon-midnight meridian, evident in the dawn-dusk keogram. The location of the dayside OCB is marked with a horizontal dashed line at 77° latitude in the noon-midnight keogram.

7.1.3 Identifying the OCB

Identification of the open/closed field line boundary (OCB) is extremely important in determining whether dual lobe reconnection has taken place. Sunward flow is expected during single and dual lobe reconnection and therefore cannot distinguish between the two processes; only sunward flow across this boundary, representing the closure of open flux, is a signature of dual lobe reconnection.

As a spacecraft traverses the polar cap it will see different particle populations (Figure 7.4). When it is within a region of closed field lines at auroral latitudes, it will see high energy electrons that are trapped and mirror between hemispheres without escaping. On open field lines however, any high energy particles will mirror once near the Earth before escaping along the open field line into the magnetotail. Hence, open field lines are usually devoid of high energy particles except where they are being injected into the magnetosphere from the magnetosheath, such as ions in the cusp region, and for this reason the polar cap
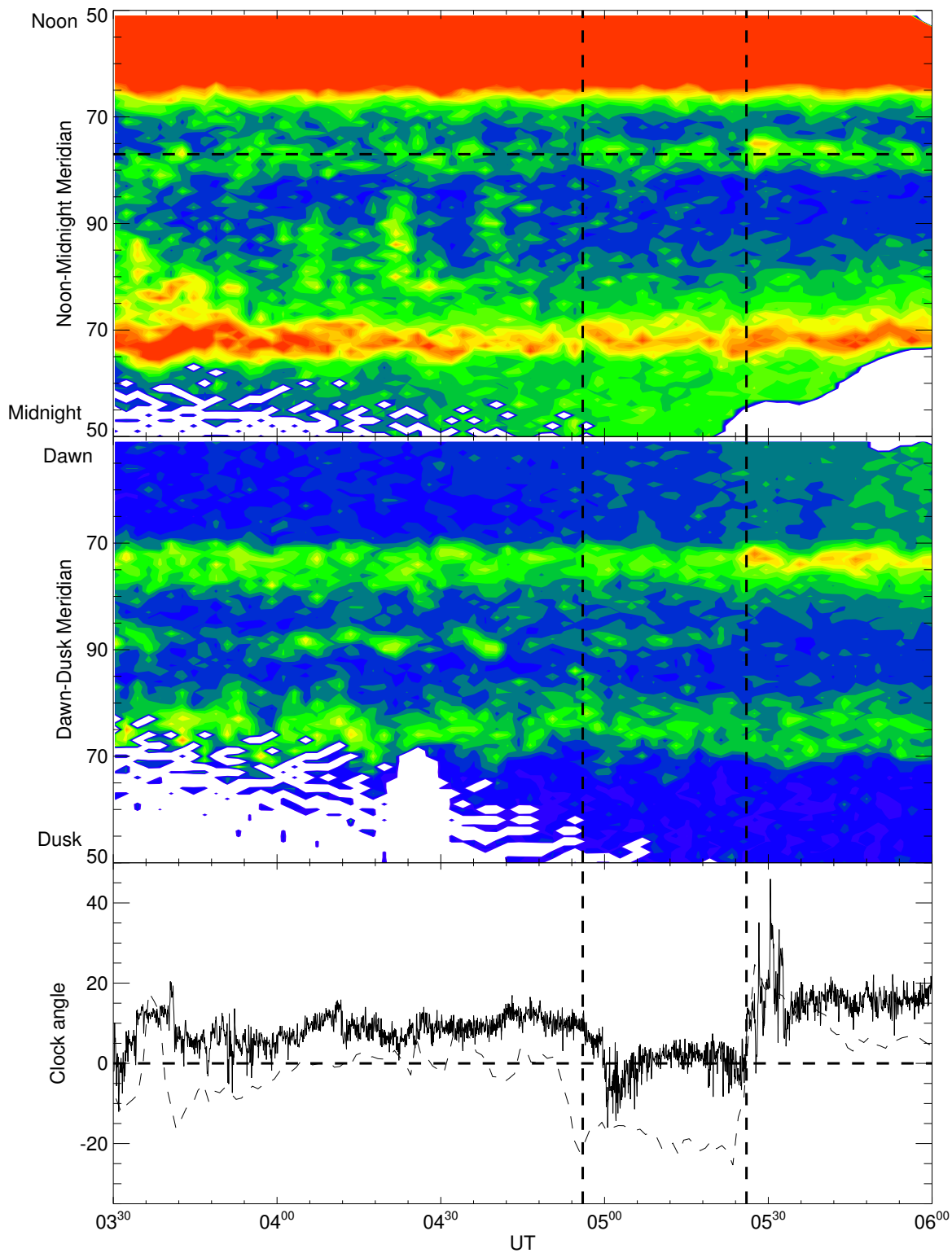
Figure 7.3. Noon-midnight and dawn-dusk keograms of the WIC data during the interval of interest, 03:30-06:00 UT on 18th December 2002. In the first panel noon is at the top and midnight at the bottom, in the second, dawn is at the top and dusk at the bottom. These demonstrate that the auroral oval stays at approximately the same latitude throughout. The horizontal dashed line in the noon-midnight keogram represents the latitude of the OCB. Below this is the clock angle measured by Geotail (black line) and Cluster (dashed line).
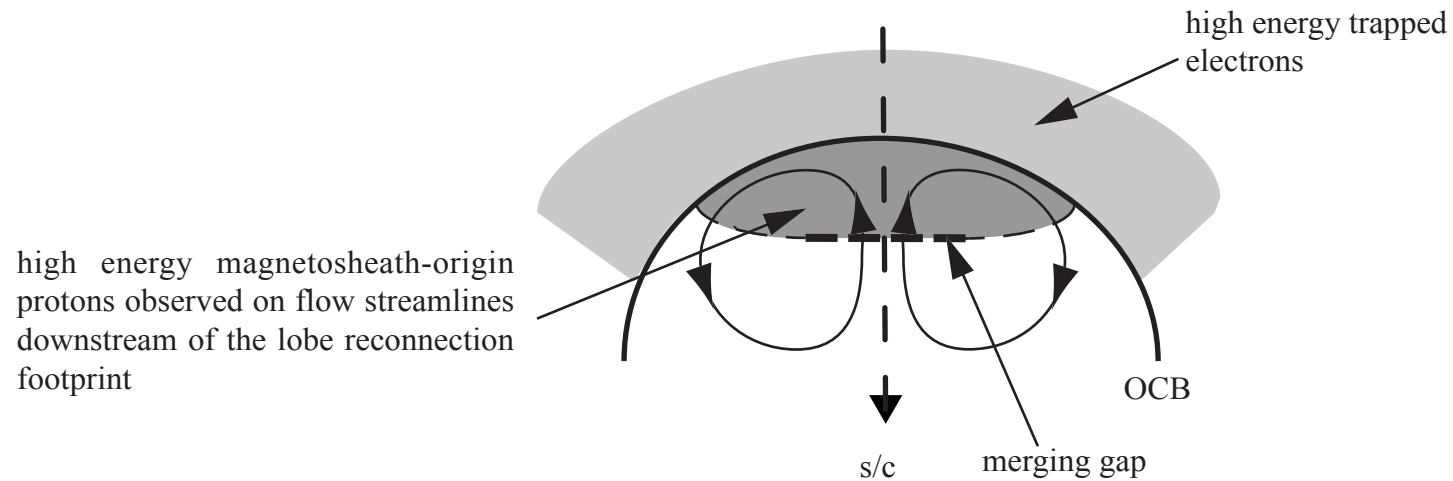
Figure 7.4. A schematic to illustrate the important features and particle populations in the vicinity of the dayside polar cap during single lobe reconnection. Looking down on the northern hemisphere with the Sun to the top of the Figure, the solid semi-circle represents the OCB. Field lines that map to within this region are open, whereas those outside it are closed. The thick dashed line within this is the merging gap, which is the ionospheric foorprint of the lobe reconnection site. The thin lines with black arrows are flow streamlines and demonstrate the reverse twin cell convection pattern of single lobe reconnection. The thick vertical dashed line is the trajectory of a poleward moving spacecraft. The light grey shaded area is a region of high energy trapped electrons on closed field lines and the darker grey region represents high energy protons that have travelled down newly-reconnected field lines.

tends to appear dim in auroral images. A good signature of the OCB would therefore be the sharp transition between high energy trapped electrons and high energy ions as the spacecraft traverses from the noon-sector auroral zone into the polar cap (as discussed by e.g. Milan et al., 2003). For lobe reconnection a poleward moving spacecraft would observe a "reverse-dispersed" ion signature (Woch and Lundin, 1992; Øieroset et al., 1997), encountering increasingly higher energy ions as it approaches the merging gap, located some distance poleward of the OCB (see Section 2.3).

The NOAA 15, 16 and 17 (Evans and Greer, 2000), and FAST (Carlson et al., 1998) spacecraft all passed over the polar cap during the interval of interest. For each spacecraft the electron and proton measurements were plotted, along with the superposition of the footprint of the orbital field lines over a typical WIC image. In this way it was possible to associate the high energy electron/ion boundary with a specific location on Earth, and relative to the aurorae. From Figure 7.5 it can be seen that both FAST and the NOAA spacecraft observed a sharp decrease in the flux of high energy electrons polewards of 77° latitude. In addition FAST sees an increase in the flux of low energy electrons and an increase in the flux of high energy protons poleward of this latitude, the signature of cusp-like precipitation on open field lines. The latitude of the dayside OCB was therefore determined to be 77°, which also corresponds to the equatorward edge of the proton aurora as identified using the IMAGE data (Figure 7.5). This latitude is marked on Figure 7.5 by black crosses. No dispersion was observed in the protons as FAST made a longitudinal, not latitudinal, cut through this region.

It is widely acknowledged that open field lines considerably broaden the spectral width of a radar backscatter echo in comparison with closed field lines (e.g. Baker et al., 1995; Milan et al., 1999, 2000; Moen et al., 2001, 2002; Chisham and Freeman, 2003, 2005; Oksavik et al., 2004) and therefore the spectral width of radar backscatter can be used to identify the OCB. The two radars of the CUTLASS array, the Iceland East and Finland radars, part of the SuperDARN network, were in the correct location to observe this backscatter on the dayside. During the interval both radars had good coverage of the dayside polar cap, and the boundary between broad and narrow spectral widths was determined to be ~77° magnetic latitude, in agreement with the spacecraft observations described above.
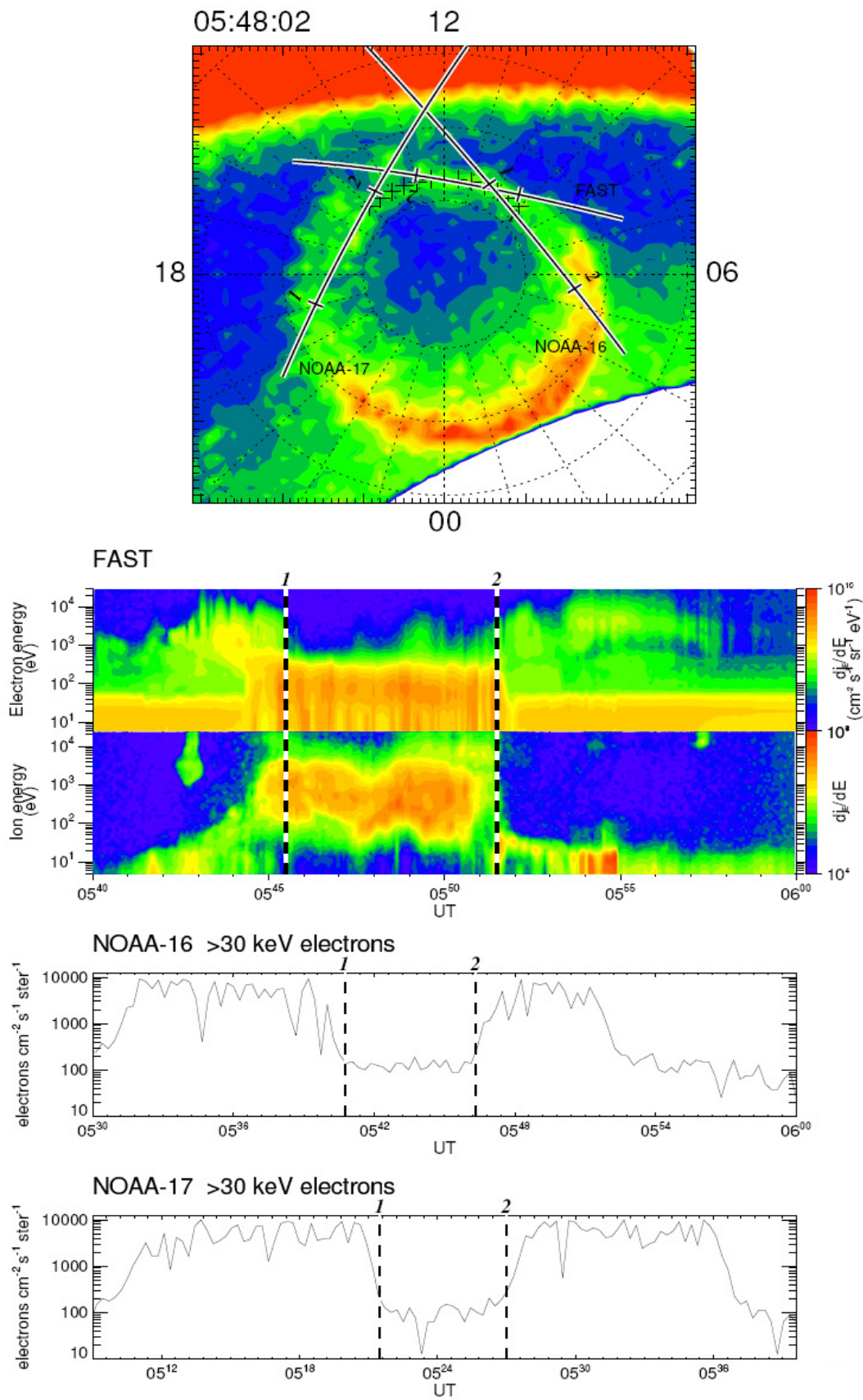
Figure 7.5. Spacecraft trajectories during the interval of interest superimposed over a WIC image of the Northern polar cap. The location of the OCB is marked by black crosses between 9 and 15 MLT. Below are the particle data recorded by these spacecraft and used to define the OCB, marked by the vertical dashed lines.

Having previously observed from keograms of the IMAGE data that the size of the polar cap did not significantly change with time during the interval, it is a reasonable assumption that the OCB did not move a significant amount and therefore it is taken as 77° throughout this analysis.

7.1.4 Radar Data

Using the SuperDARN network of radars it is possible to create a map of the electrostatic potential pattern associated with the ionospheric convection over the polar regions (Ruohoniemi and Baker, 1998). In regions where observations are sparse a statistical convection pattern, parameterised by IMF orientation and magnitude, is used to help constrain the fit (see Section 3.1). For this study the model input was fixed to $B_Z > 0$, $B_Y = 0$ to prevent possible bias by the IMF input and ensure that all changes in the convection pattern are driven by the flow observations. The flow patterns, determined at 2 minute cadence, were superimposed over the simultaneous WIC, SI12 and SI13 images. These flow patterns were used to accurately determine the flow in the vicinity of the OCB, 77° magnetic latitude, marked by the crosses in Figure 7.6. During the majority of the interval of study the flow pattern was consistent with lobe reconnection (Section 2.1.2). That is, sunward flows were seen near noon, but with the reverse cells contained within the open polar cap (Figure 7.6a), with only small flows relative to the boundary which we assume are motions of the boundary itself – i.e. we assume that the boundary is adiaroic throughout most of the period. The radar data is sparse in the post-noon sector such that only the pre-noon reverse cell is identifiable from the convection map, however it is expected that a post-noon cell would be observed given increased radar coverage of the region. During the period 04:58 to 05:15 UT, however, there is flow observed crossing the location of the OCB (Figure 7.6b). Comparing the time of this reconnection burst with the IMF clock angles in Figure 7.1, it can be seen that this follows closely after the first of the clock angle turnings through 0°. This, therefore, would be the optimum time for dual lobe reconnection to have occurred. Coupled with our theoretical expectation of flow across the OCB, we interpret this as strong evidence for dual lobe reconnection.

The magnitude of the flow across the boundary provides a measure of the reconnection electric field, which when integrated along the boundary gives the
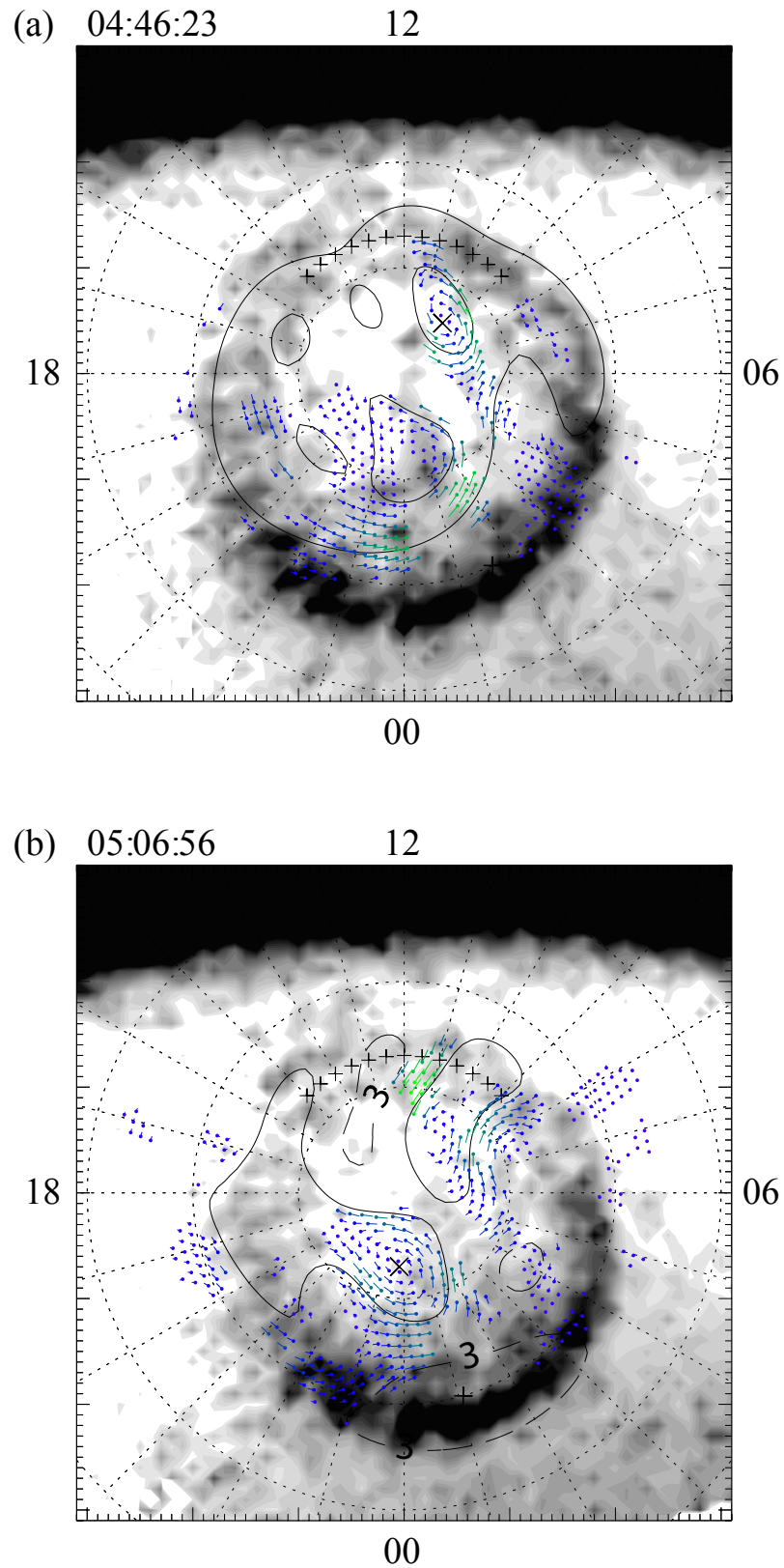
Figure 7.6. WIC images of the Northern polar cap, superimposed over which are the potential contours and flow pattern determined by analysis of SuperDARN radar data. The location of the OCB is marked by the crosses between 9 and 15 MLT. (a) All flow contained within the polar cap (b) Equatorward flow across the OCB.

reconnection voltage, that is the rate of transport of magnetic flux from one side of the boundary to the other. When this is integrated over time it gives the flux closed by the dual lobe reconnection (Section 2.1.5). The flow perpendicular to the boundary, and the associated electric field parallel to the boundary were derived directly from the SuperDARN potential maps. The IMF input to the model was fixed such that any changes in the flows were driven solely by the radar data. The electric field and flow were determined every 0.25 hours of MLT between 09 and 15 MLT at a latitude of 77°, our estimate of the location of the OCB. The time history of the flow between 03:30 and 06:00 UT is shown as a contour plot in Figure 7.7, with time along the X-axis and MLT on the Y-axis. The contours are the velocity of the ionospheric convection perpendicular to the OCB, with positive flows into the polar cap, and negative flows out of the polar cap. Before 04:55 UT the observed flows are small, in general of order ± 50 m s^{-1}. Two strong bursts of flow out of the polar cap are seen near noon, at 05:00-05:24 UT and 05:30-05:40 UT. These are accompanied by weaker poleward flows away from noon. We interpret the equatorward (sunward) flows as plasma flow out of the polar cap along the length of the merging gap due to the closure of open flux by dual lobe reconnection; the poleward flows are associated with the contraction of the polar cap, along adiaroic portions of the OCB.

The noon portion of the dayside aurora was analysed for each of the 2 minute WIC images during the 2½ hour interval. The maximum brightness within the box indicated in Figure 7.2a was plotted with time in Figure 7.2b and it is clear that the brightness peaks at the time of the onset of each burst of reconnection (marked by the vertical dashed lines).

7.1.5 Plasma Sheet

To investigate the effect of dual lobe reconnection on the plasma sheet, the high energy proton density within the inner edge of the plasma sheet was measured by four LANL spacecraft at geosynchronous orbit between 17th and 22nd of December 2002 (Figure 7.8). The plasma density from four spacecraft, located at four geographic locations spaced around the equator, have been superimposed. This gives an indication of the plasma density as the spacecraft sweep through local time; the highest densities are found on the nightside, in the inner edge of the plasma

148
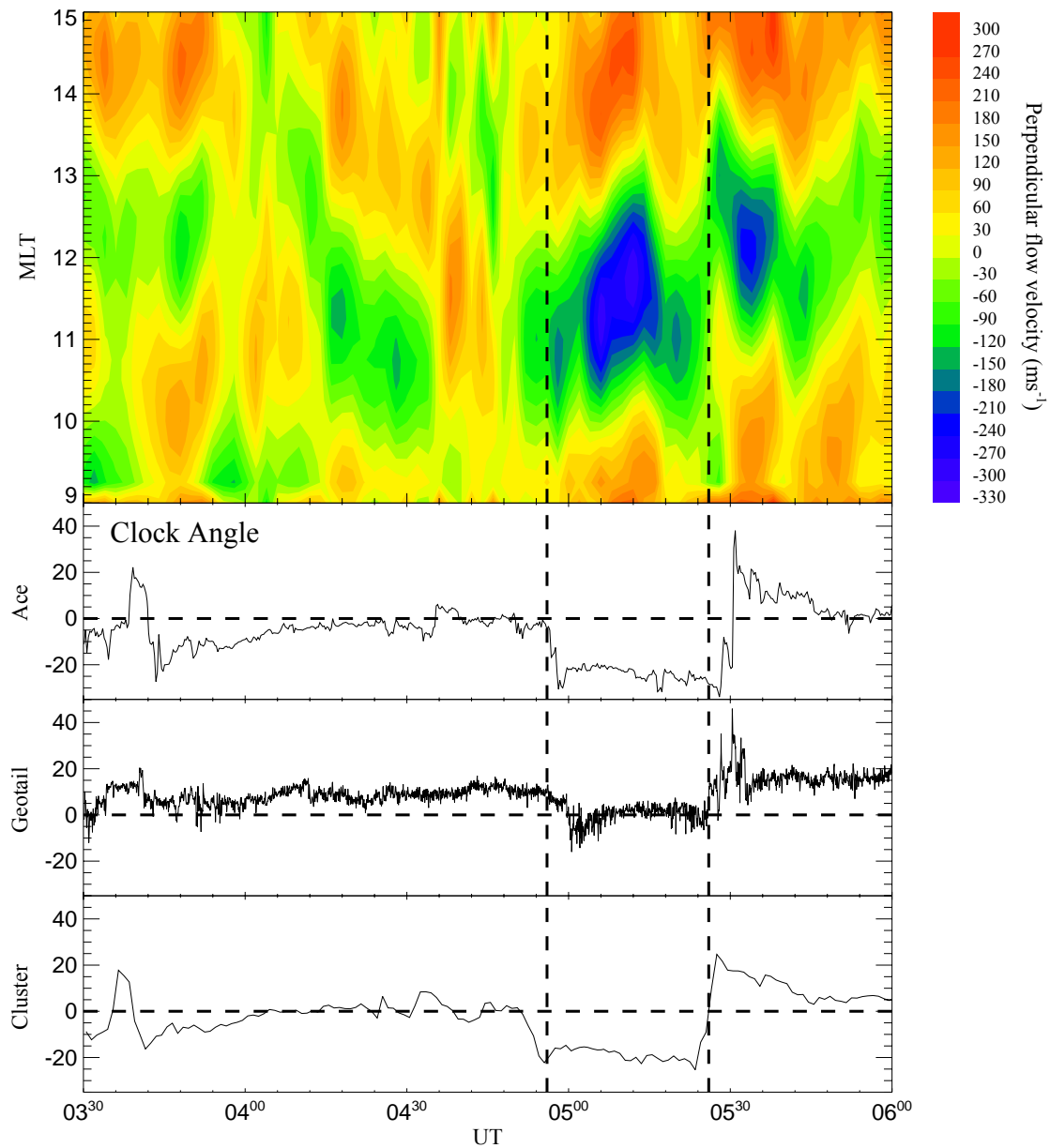
Figure 7.7. A contour plot showing the velocity of plasma flow across the OCB, previously determined to be at 77° magnetic latitude. Blue represents flow equatorward while red represents flow poleward. Two intervals of equatorward flow across the OCB can be clearly identified beginning at 05:00 UT and 05:30 UT. The clock angles from ACE, Geotail and Cluster displayed below show that the start of these flows corresponds to the time when the clock angle passes through zero, represented by vertical dashed lines.
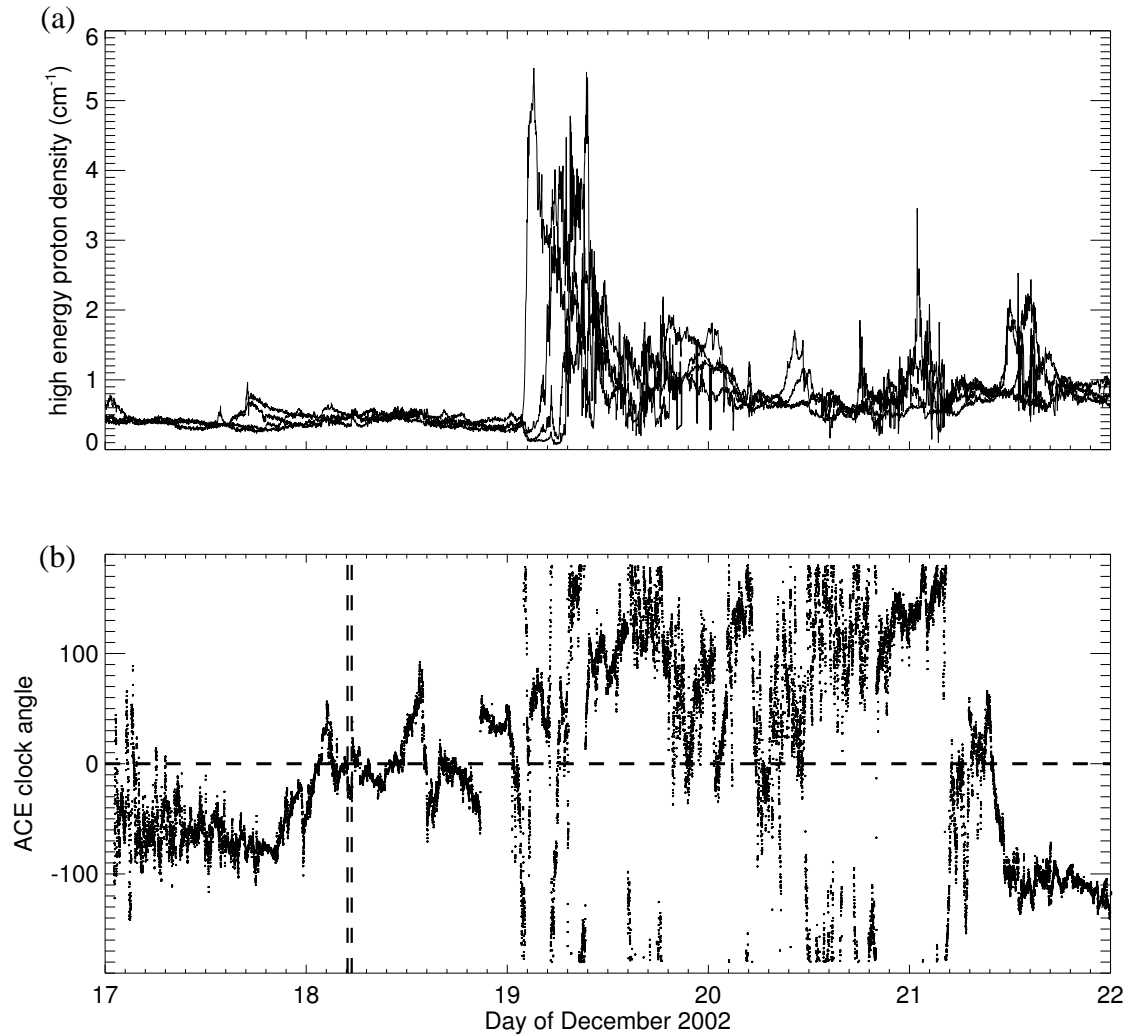
Figure 7.8. (a) High energy proton density measured by LANL 1990-095, 1991-080, 1994-084, and LANL-97A in the interval 17th-22nd December 2002. (b) Clock angle measured by ACE (lagged to the magnetopause). The horizontal dashed line represents $0°$ and the vertical dashed lines represent the times at which the clock angle passed through zero.

sheet. Prior to our interval of interest the plasma sheet density was ~0.4 cm^{-3} which is a standard quiet time value (Øieroset et al., 2005). It remained at this density until approximately 00:30 UT on 19th December when it abruptly increased to ~5 cm^{-3}. The density then decreased to a value of ~ 1 cm^{-3} over the next 24 hours, which was then maintained for several days. Øieroset et al. [2005] define the threshold density for the cold, dense plasma sheet to be 1-2 cm^{-3} therefore it is thought that the increase in density observed here is due to the formation of such a plasma sheet; confirmed with observations by FAST (J. P. McFadden, private communication). The bottom panel in Figure 7.8 shows the clock angle from the 17th to the 22nd of December. The extended period of observations of IMF clock angle show that during the 18th the IMF clock angle is directed mainly northward, with a distinct swing to more southerly directions on the 19th. It is striking that the increase in plasma sheet density appears to occur at approximately the same time as a southward turning of the IMF following the intervals of DLR (marked by the vertical dashed lines). It could be that the southward turning (and therefore the onset of low latitude reconnection) increases the rate of transport of cold, dense plasma within the magnetosphere such that it reaches the LANL spacecraft rapidly. The clock angle passes through zero a number of times before and after the two times identified in this study. These other crossings cannot be studied in as much detail due to a lack of radar and imager data, but it should be noted that dual lobe reconnection would be expected to have occurred at each of these crossings which would contribute more plasma to the cold, dense plasma sheet. We will estimate the plasma capture efficiency of dual lobe reconnection in Section 7.3.5.

7.2 Observation of significant flux closure by dual lobe reconnection

The interval studied here is 18:00 – 24:00 UT on the 21st October 2001. It was chosen primarily because the SuperDARN radars provided excellent coverage of the ionospheric convection flows near the dayside auroral oval during a period when the upstream solar wind monitors showed the IMF clock angle passing gradually through zero. In addition the IMAGE spacecraft provided good coverage of the auroral configuration in the northern hemisphere.

7.2.1 IMF conditions

The upstream solar wind conditions were measured by three spacecraft: ACE, Geotail and WIND (Chapter 3) shown in Figure 7.9. ACE was located at GSM X=221, Y= 8.8 and Z=-25.2 R_E and the ACE data was lagged by 37.5 minutes to allow for the spacecraft position ~220 R_E upstream of the Earth, using an average solar wind velocity of -624.6 km s^{-1}. ACE observed the GSM B_Z component to be at approximately -20 nT until 20:55 UT when it passed through zero to ~22 nT. It then fell again to negative values peaking at -30 nT before the end of the interval. There was therefore an interval between 20:35 UT and 21:35 UT during which the GSM B_Z component was positive (Figure 7.9). The B_Y component of the IMF was observed to increase from -10 nT to 20 nT, then decrease steadily to -20 nT at 20:55 UT. Following this it returned to ~25 nT before falling to negatives values again towards the end of the interval. The clock angle was therefore observed to pass gradually from -180° (southward), through zero (northward) to +180° over a timescale of just over 3 hours. It should be noted that relatively high magnetic field strengths in the solar wind are due to a co-rotating interaction region.

During the interval Geotail was near the bowshock, at GSM X = 2, Y = -19 and Z = 0 R_E. It observed very similar variations in the GSM B_Y and B_Z components, and the clock angle was observed to pass through zero at exactly the same time as for ACE. For short periods during the interval Geotail measured enhanced values of B_Y and B_Z relative to those measured by ACE. This is due to compression of the field when Geotail was located within the magnetosheath. Despite this the clock angle variation was very similar to that at ACE. Although data were not observed for the full interval, the location of Geotail relatively close to the magnetopause gives us confidence in the time lag calculated for the ACE data.

WIND was located at GSM X = 40, Y = -10 and Z = 3.5 R_E and the data was lagged by 6.5 minutes to take into account the upstream location of the spacecraft. Again there was excellent agreement with the ACE data in the IMF B_Y and B_Z components, and again the clock angle passed through zero at the same time: 20:55 UT. The excellent agreement between the solar wind monitors gives us confidence that we know the time at which DLR might be expected to occur to a reasonable degree of accuracy.
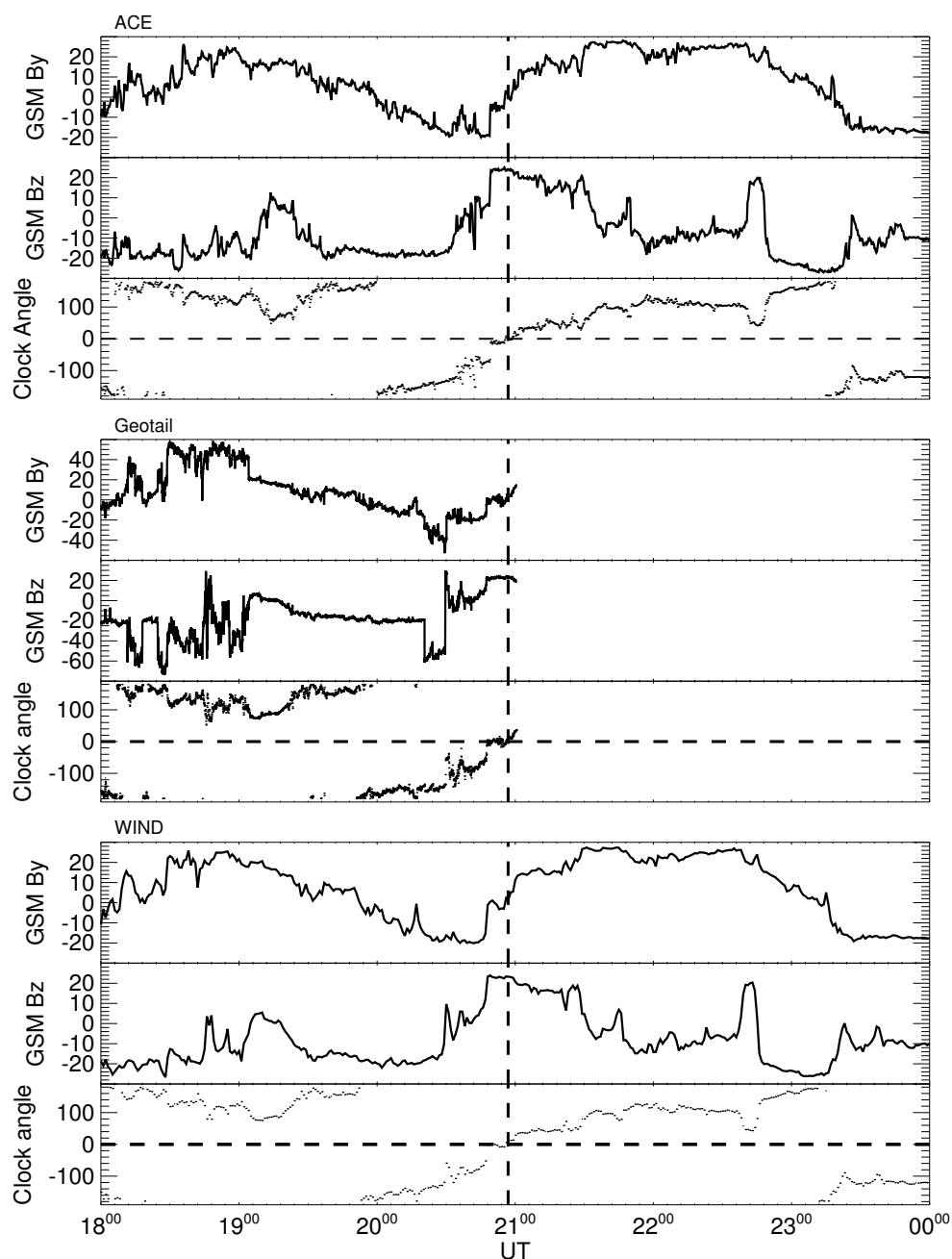
Figure 7.9. GSM B$_Y$ and B$_Z$ interplanetary magnetic field components along with the corresponding clock angle, measured by ACE and WIND in the solar wind and Geotail in the upstream solar wind and occasionally within the magnetosheath, 18:00-24:00 UT on 21st October 2001. Vertical lines mark the average time that the clock angle passed through zero - 20:55 UT.

The IMAGE spacecraft passed over the northern polar cap between 18:00 and 24:00 UT on 21st October 2001. Images are available from the Wideband Imaging Camera (WIC), and the Spectrographic Imager instrument, measuring UV, and electron and proton aurora respectively. Both WIC and the SI13 images were obscured by dayglow on the dayside so the SI12 proton aurora images, relatively unaffected by dayglow, are used in this study. Figure 7.10 shows a typical SI12 image during this interval taken at 21:08 UT. The image is plotted on a polar grid looking down on the northern hemisphere with noon at the top of the image. The auroral oval is clearly visible, as is a prominent cusp auroral spot in the noon sector associated with the northward IMF conditions (Milan et al., 2000). This cusp spot is caused by solar wind plasma travelling down newly reconnected field lines and is seen both in the SI12 (proton) and SI13 (electron) images. In order for a spot to appear the solar wind density has to be sufficiently high for a significant number of solar wind particles to be present on reconnecting IMF field lines (Frey et al., 2002). The spot is particularly important in this event as it represents the footprint of the reconnecting field lines and therefore enables us to observe the location and motion of the merging gap with changing IMF conditions. High luminosities in the top-left of the image are an artefact.

Noon-midnight and dawn-dusk keograms were generated from the auroral observations and are presented in Figure 7.11, the vertical dashed line marks the time at which the clock angle is observed to pass through zero. It is clear from the keograms that the auroral oval is located at relatively low latitudes due to intense solar wind-magnetosphere coupling under southward IMF conditions prior to 20:35 UT. During the interval the auroral oval is observed to move both equatorwards and polewards indicating changes in the open flux content of the magnetosphere (e.g. Milan et al., 2003). There is also a cusp spot observed near noon in the noon-midnight keogram of Figure 7.11. The spot is first formed at 20:54 UT when the IMF turned strongly northward. As $B_Y < 0$ at this time the spot forms in the prenoon sector as reported by Milan et al. (2000). Analysis of subsequent auroral images shows that as B_Y changes the spot moves, through noon at 21:10 UT when it would be expected that $B_Y = 0$. As B_Y becomes more positive, the spot is observed to move
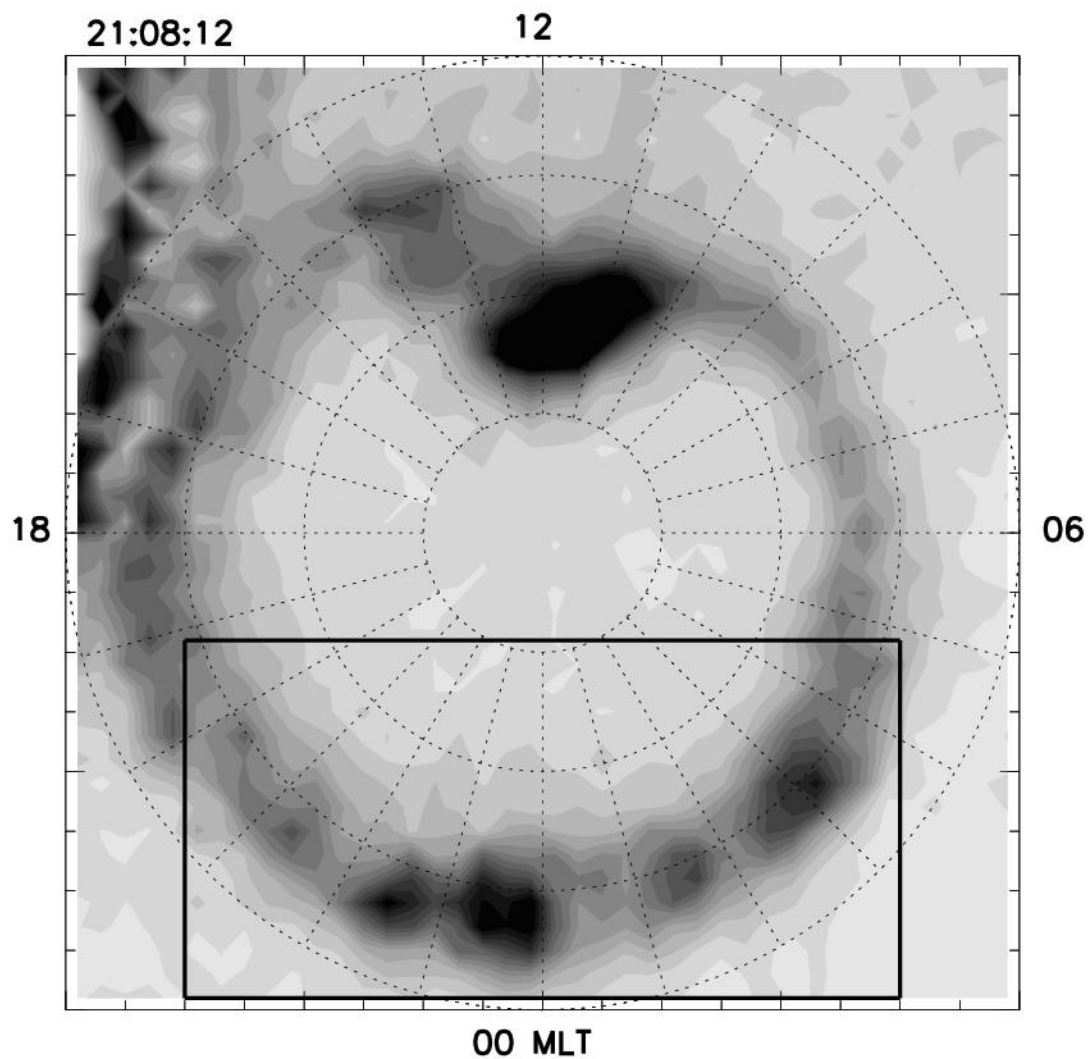
Figure 7.10. A typical image from the SI12 instrument on the IMAGE spacecraft. The image is looking down on the northern polar cap with noon to the top. The proton aurora is clearly visible as the darker portion of the image. The black rectangle represents the area used to observe the change in brightness of a nightside portion of the auroral oval during the interval.
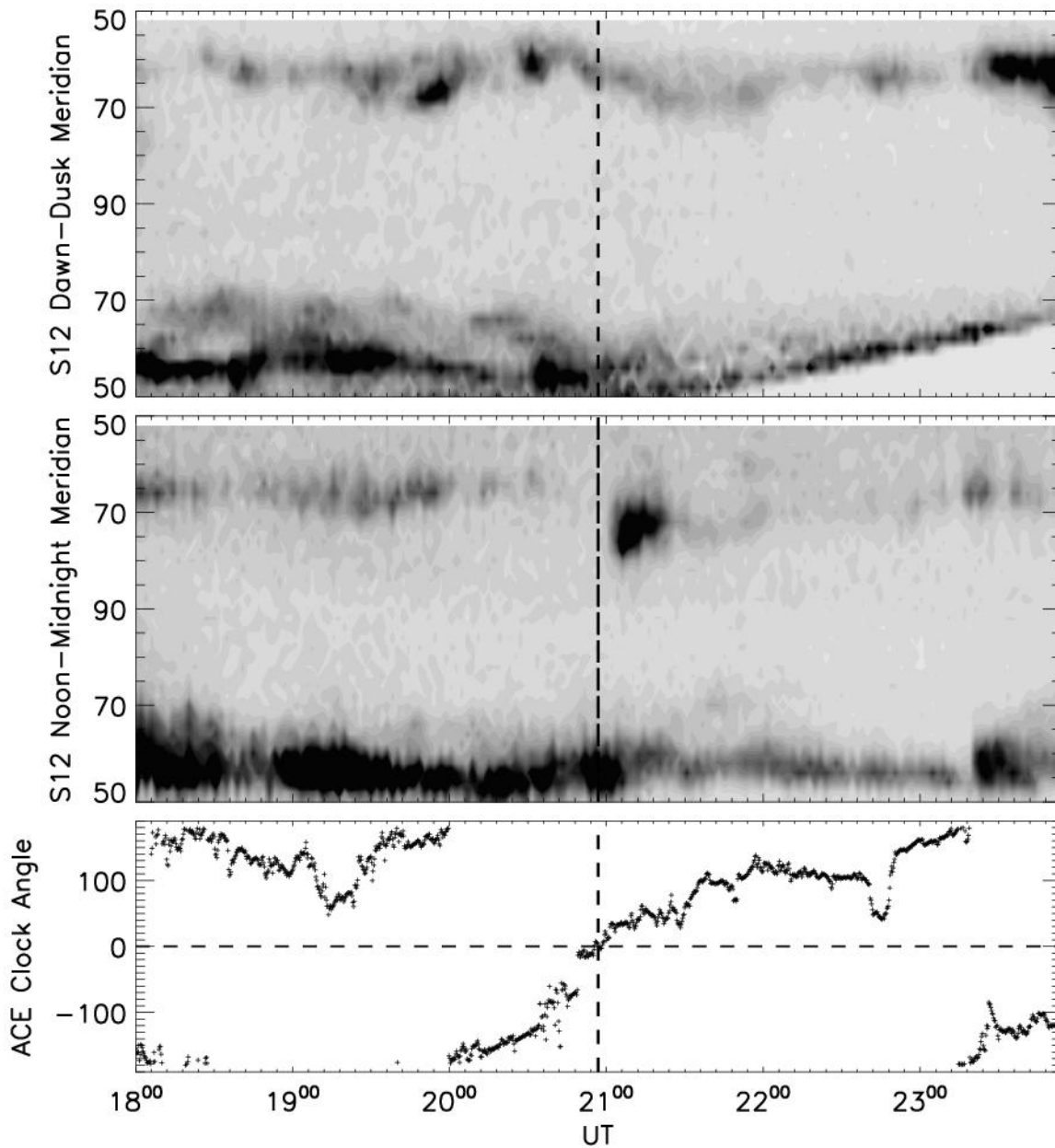
Figure 7.11. Dawn-dusk and noon-midnight keograms of the SI12 data during the interval of interest, 18:00 to 24:00 UT on 21st October 2001. In the first panel dawn is at the top and dusk at the bottom, in the second, noon is at the top and midnight at the bottom. These demonstrate that the auroral oval expands and contracts throughout the interval. Below this is the clock angle measured by ACE with the vertical dashed line representing the time at which the clock angle passed through zero.

into the postnoon sector, reaching 13:30 MLT. The intensity of the spot decreases and it finally disappears at approximately 22:00 UT.

7.2.3 SuperDARN radars

Throughout the interval the SuperDARN radar coverage of the dayside portion of the northern auroral oval was excellent. The SuperDARN ionospheric convection maps were plotted over the simultaneous SI12 images at 2 minute cadence. When the IMF is southward, prior to 20:35 UT, the convection cells are typical of low latitude dayside reconnection with anti-sunward flow across the dayside OCB, as would be expected during this time (Figure 7.12a). As the clock angle approaches zero however, some sunward flow is observed in the noon portion of the auroral oval (Figure 7.12b). This sunward flow crosses the dayside auroral oval, extending down to magnetic latitudes of approximately 63° and is observed between 20:58 UT and 21:14 UT. During this time the sense of the convection cells is observed to reverse, with sunward flow at high latitudes and return flow at lower latitudes. Sunward flow near noon is the expected signature of both single and dual lobe reconnection. The inclusion of sunward flow extending to such low latitudes indicates the possibility that the flow crosses the OCB, therefore that dual lobe reconnection has taken place. In order to determine whether this has taken place however, it is necessary to first calculate the position of the OCB.

7.2.4 Identifying the OCB

An interval of sunward flow near noon extending to latitudes ~63° has been identified from ionospheric flow patterns generated using data from the northern hemisphere SuperDARN radars. In order to ascertain whether dual lobe reconnection has taken place it is necessary to determine whether the flows crossed the dayside OCB, therefore the latitude of the dayside OCB must be identified to a reasonable degree of accuracy. In our previous study we were able to assume the location of the OCB to be constant throughout the interval as the polar cap did not contract significantly. In the present case however, the keograms (Figure 7.11) show that the location of the aurora (and therefore the OCB) moves considerably during the interval and cannot be approximated to constant latitude.
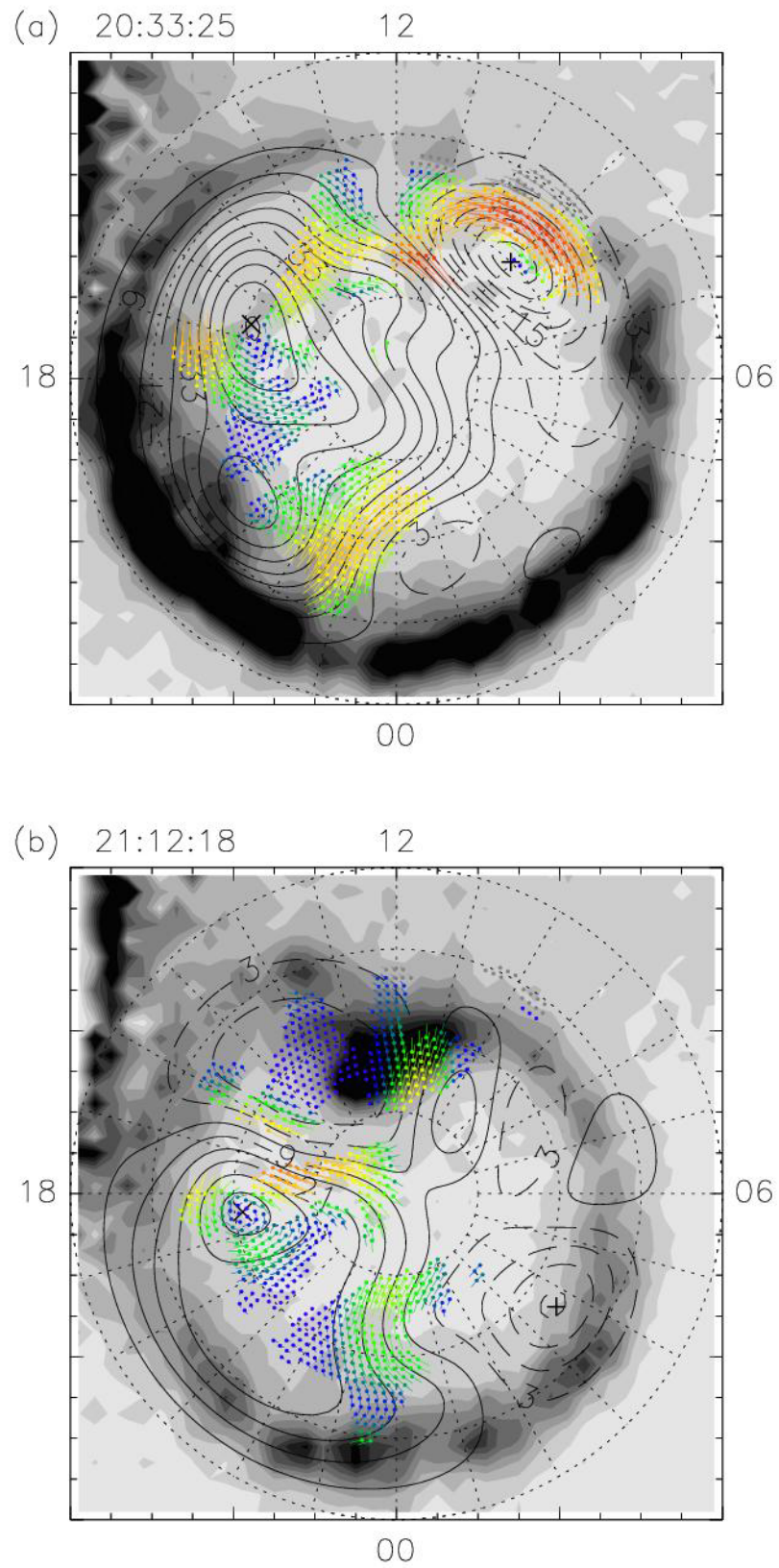
Figure 7.12. SI12 images of the northern polar cap, superimposed over which are the potential contours and flow pattern determined by analysis of SuperDARN radar data. (a) a typical southward IMF twin cell convection pattern (b) Equatorward flow across the OCB.

We took the poleward boundary of the main proton auroral oval, measured with the SI12 camera, as a proxy for the OCB. The proton auroral spot is associated with the cusps but it is unclear whether the cusp spot is on open or closed field lines, and in fact this will depend upon the reconnection mechanism that has taken place. For this analysis we have assumed that it is on open field lines, (therefore that single lobe reconnection has taken place) and have placed the boundary equatorwards of it (Figure 7.13a). During dual lobe reconnection the merging gap is collocated with the OCB at the poleward edge of the proton spot, and sunward flows across this merging gap are in response to the closing of open field lines (Figure 7.13b). Once this process has stopped, the OCB will not be circular therefore in order to return to an equilibrium shape the boundary will move sunwards in the noon sector, resulting in corresponding sunward flow signatures (Figure 7.13c). These flows are not crossing the OCB itself as DLR has stopped, but instead are adiaroic, and moving with the OCB. It is not possible to distinguish between the flows associated with the DLR process itself, and the ensuing adiaroic flows, as both demonstrate sunward flow, so it is not possible to observe the exact time at which DLR stops.

The latitude of the OCB at 06, 12 and 18 MLT was estimated from the keograms in Figure 7.11 and the location of the OCB was then determined by interpolating between these latitudes at intervals of 0.25 hours of MLT, estimating the location of the equatorward edge of the cusp spot from the latitude of the poleward edge of the aurora either side of it where necessary. The estimated OCB latitudes at 06, 12 and 18 MLT are plotted in panels b, c and d of Figure 7.14.

The ionospheric flow across the dayside OCB can now be determined from the SuperDARN convection maps at 2 minute cadence, i.e. that of the SI12 images. Figure 7.14a shows the velocity of the flow perpendicular to the OCB in the frame of reference of the boundary with time between 18:00 and 24:00 UT along the x axis, and magnetic local time (MLT) between 09 and 15 along the y axis. Blue contours represent sunward flow and red contours represent poleward flow. Plotted below this is the clock angle determined from the ACE spacecraft, lagged by 37.5 minutes to take into account the location of ACE ~220 R_E upstream (Figure 7.14e). The vertical dashed lines mark times of specific interest to be discussed later. The second vertical dashed line represents the time at which the clock angle passed through zero. When $B_Z < 0$ (prior to 20:35 UT) there is strong antisunward flow, at times covering the entire MLT range. The strength of this flow is severely

(a)

cusp spot observed polewards of the OCB but equatorwards of the merging gap

high energy trapped electrons

(b)

OCB

merging gap

cusp spot observed polewards of the OCB but equatorwards of the merging gap

OCB

merging gap

(c)

OCB
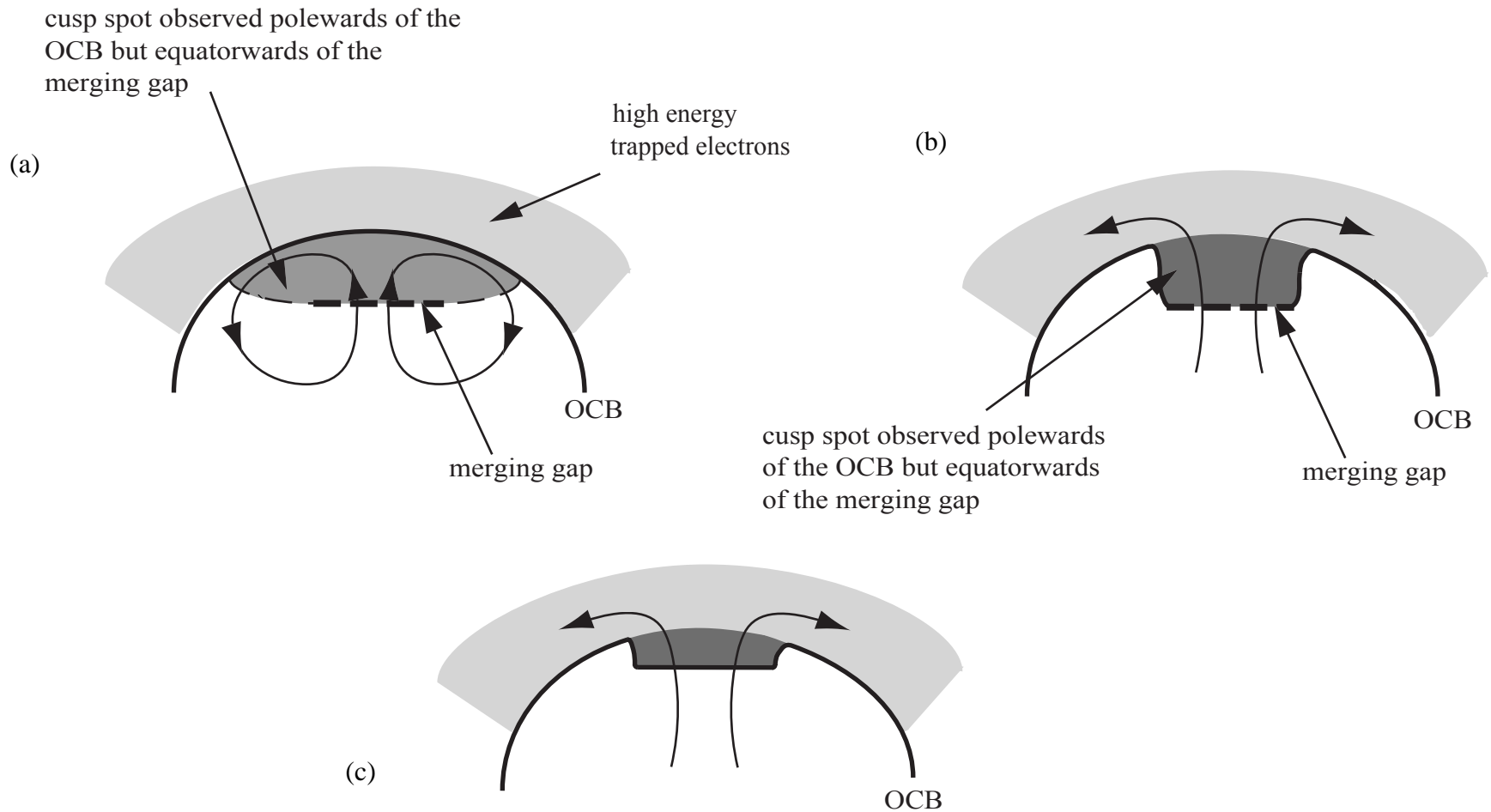
Figure 7.13. Schematics of the northern polar cap with noon to the top of the diagram, thick dashed lines represent the merging gap, solid lines the OCB and the black arrowed lines are flow streamlines. These demonstrate expected particle populations and ionospheric convection for (a) single lobe reconnection where twin reverse cells are observed (b) ongoing dual lobe reconnection where there is sunward flow across the dayside OCB (c) magnetospheric reconfiguration following dual lobe reconnection, where the OCB is an adiaroic boundary, i.e. there is no flow crossing the OCB.
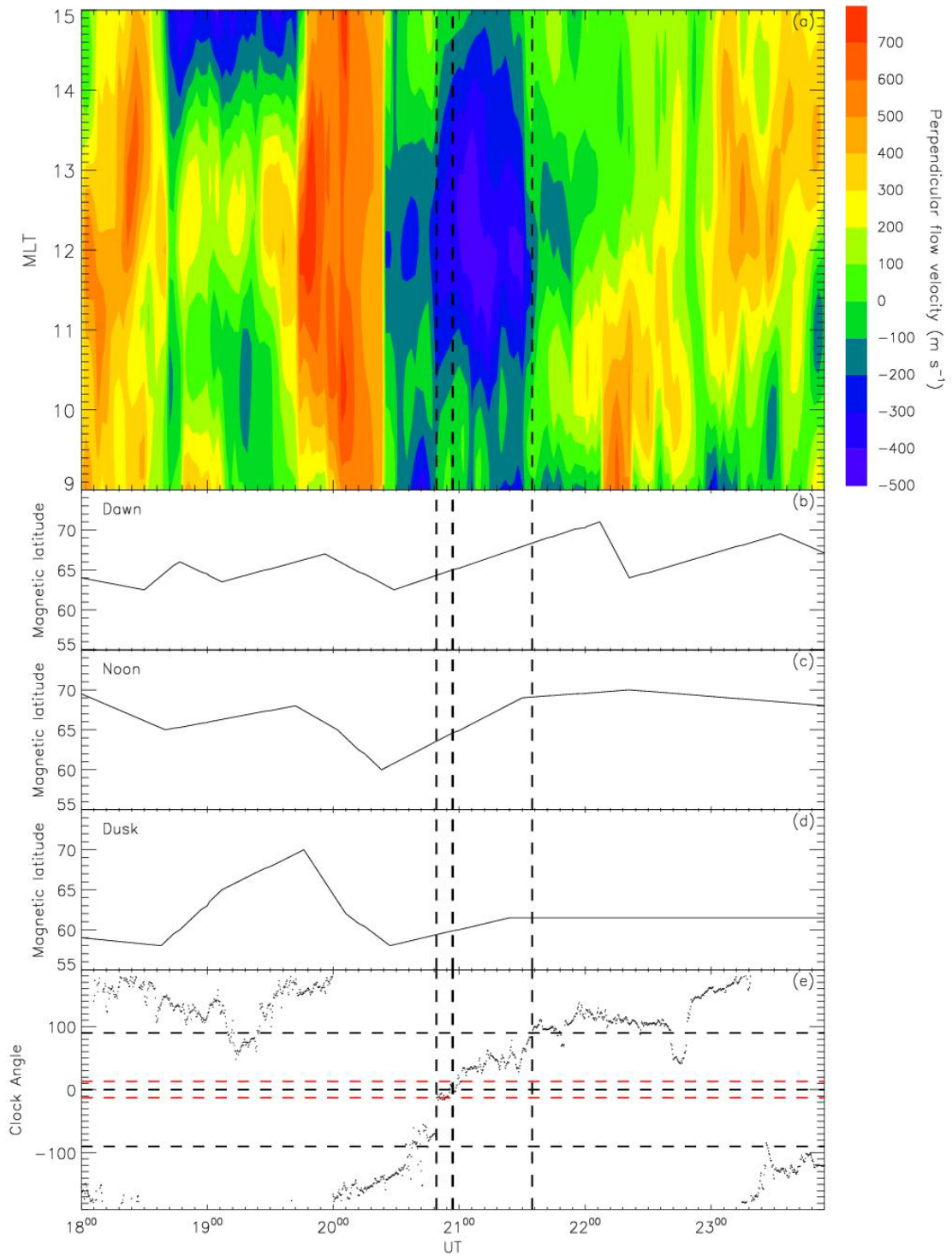
Figure 7.14. (a) A contour plot showing the velocity of plasma flow across the OCB, determined from the keograms in Figure 7.11. Blue represents flow equatorward while red represents flow poleward. (b), (c), (d) show the latitude of the OCB at 06, 12 and 18 MLT. (e) is the clock angle measured at the ACE spacecraft lagged to the magnetopause. One interval of equatorward flow across the OCB can be clearly identified beginning at 20:49 UT. The first vertical dashed line marks the time at which the clock angle passed through -15°, the angle at which it has been calculated that DLR would be expected to commence. The second vertical line represents the time at which the clock angle passes through zero. The third vertical line marks the time at which the IMF turns southwards and coincides with the end of the sunward flow.

decreased when the IMF turns northward (20:35 UT) and it is only observed over a range of a few hours of MLT. A large patch of sunward flow is observed crossing the dayside OCB which lasts approximately 35 minutes and begins just prior to the clock angle passing through zero. The length of the patch of sunward flow is 4 hours of MLT from Figure 7.14a, and we assume that this represents the length of the ionospheric projection of the dual lobe merging gap. The sunward flow reached a maximum velocity of 478 m s^{-1} relative to the boundary, at 21:08 UT. We take this signature of sunward flow across the boundary as an indication that dual lobe reconnection has taken place.

7.3. Discussion

Two intervals have been identified during which the interplanetary magnetic field as measured by upstream solar wind monitors appeared to pass through zero and dual lobe reconnection might be expected to occur, which would manifest itself as a sunward ionospheric convection flow across the dayside OCB.

In the first event the OCB was determined from radar and spacecraft data. For the spacecraft, the boundary was determined using the sharp transition between high energy electron and high energy ion precipitation observed as it crossed the noon sector auroral oval and polar cap (Figure 7.5). Data taken from NOAA 15, 16 and 17, and FAST are all in agreement that the OCB was approximately at 77° magnetic latitude. Backscatter from the SuperDARN radars demonstrated that the high/low spectral width boundary and therefore the OCB was at ~77° latitude in agreement with the spacecraft data. This also marked the equatorward edge of the proton aurora near noon, the protons being of magnetosheath origin and associated with open field lines.

Potential maps were created from SuperDARN data and these were converted into flow maps. The velocity of the plasma across the OCB was calculated from the radar data and plotted in Figure 7.7. Two clear periods of sunward flow across a 2 hour MLT portion of the OCB are visible and appear to begin exactly at the two times that the clock angle is observed to pass through zero. Single lobe reconnection produces sunward flow but this is contained within the polar cap. We interpret flow across the OCB as strong evidence for the occurrence of dual lobe reconnection and the closure of open magnetic flux at the dayside.

Simultaneous anti-sunward flows away from noon are interpreted as a contraction of the polar cap, associated with the closure of open flux.

In the second study, IMAGE Spectrographic Imager data and the SuperDARN radar network were used to identify the OCB (Section 7.2.4). The interval was selected as the clock angle observed by ACE, Geotail and WIND passed relatively slowly through zero (Figure 7.9) therefore dual lobe reconnection would be expected to take place for a longer period of time than in the first study. The OCB was identified from the SI12 images as the poleward edge of the dayside aurora and sunward flow crossing this boundary was observed for a period of 35 minutes. The OCB was observed to move poleward during the interval, indicating that a significant amount of magnetic flux was closed. A cusp auroral spot was observed at noon near the time of the onset of dual lobe reconnection.

7.3.1 Constraining the clock angle

During the first study the clock angle measured by the three upstream spacecraft differs depending on location; however all are close to 0° and all show the same variation. Our observation of dual lobe reconnection following the times of the clock angle rotation suggests that at the reconnection sites the clock angle passes through 0°. If this is the case we estimate that the clock angle at the reconnection sites can be no larger than ±10° at other times. This puts a constraint on the range of clock angles for which dual lobe reconnection can occur, which we suggest is $|\theta|<10°$. We can also estimate this from the geometry of the reconnection site at the magnetopause.

Figure 7.15a is a schematic showing the front of the magnetosphere looking from the Sun, to demonstrate how single lobe reconnection can occur simultaneously in both hemispheres during periods of northward IMF. The solid lines of IMF are those reconnecting at the merging gaps, shown by horizontal dashed lines. This case shows lobe reconnection occurring in the two hemispheres with different IMF field lines, i.e. single lobe reconnection at both the northern and the southern magnetopause. Figure 7.15b shows the limiting case, i.e. the maximum clock angle for which a single field line can undergo dual lobe reconnection. From the dimensions of the two bursts of flow identified in Figure 7.7, we conclude that the merging gaps are approximately 2 hours of MLT in
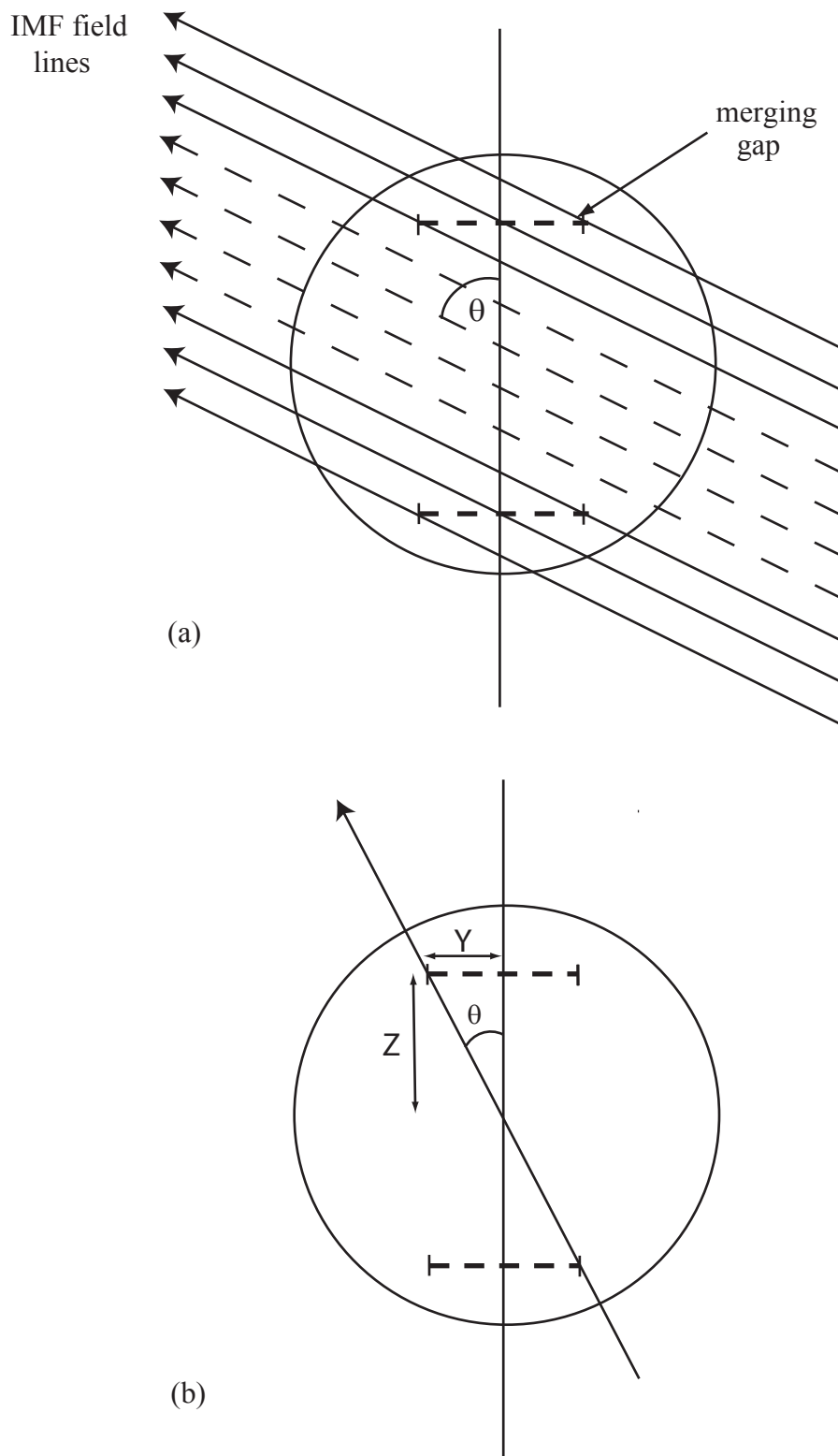
Figure 7.15. Schematics to show (a) single lobe reconnection in both hemispheres during northward IMF, and (b) the maximum clock angle for the same IMF field line to reconnect in both hemispheres simultaneously, i.e. dual lobe reconnection to occur.

length. Assuming that the reconnection point is at $Z = \pm10$ R_E, $X = 5$ R_E (Figure 7.16), the length of each merging gap can be calculated to be approximately 2.6 R_E in Y. From this we can determine θ_{max} (Figure 7.15b) to be approximately 8°, in excellent agreement with the estimate of $|\theta| \leq 10^o$ made by comparing the time of the onset of reconnection with the IMF clock angles.

The same geometrical consideration can be applied to the second study. Again assuming that the reconnection points are tailward of the cusp, at GSM $Z = \pm10$ R_E and $X = 5$ R_E on the magnetopause and having estimated the length of the merging gap to be 4 hours of MLT (Section 7.2.4), we estimate that in this case the threshold clock angle for dual lobe reconnection is $\pm15°$ which is comparable to the $\pm10°$ determined in the first study.

The first vertical dashed line in Figure 7.14 represents the approximate time at which the clock angle passed through -15° during the second interval. It is clear from comparing the time of the onset of the sunward flow with the dashed line that reconnection does appear to begin promptly at the time predicted by the threshold clock angle calculated from the length of the merging gap. The second vertical dashed line marks the time at which the clock angle passed through 0°. Dual lobe reconnection would be expected to cease when the clock angle exceeds ±15°; at which time single lobe reconnection would be expected to recommence. The third vertical dashed line marks the time at which the clock angle passed through 90°, that is the IMF turned southwards. This is the time at which the flows associated with lobe reconnection would be expected to decrease and low latitude reconnection commences. During low latitude reconnection an IMF field line reconnects with a geomagnetic field line at the subsolar point (Figure 2.1a). The first field lines to reconnect will be the ones most recently formed during the process of dual lobe reconnection. This means that following a southward turning of the IMF, the sense of the ionospheric dual cell convection patterns will reverse from lobe reconnection convection patterns to low latitude convection patterns and the sunward flow (interpreted as the magnetospheric reconfiguration following the burst of dual lobe reconnection, see below) would be expected to cease. Comparing the time when the clock angle passes through 90° with the time when the sunward flow across the OCB is observed to cease, this does appear to be the case.
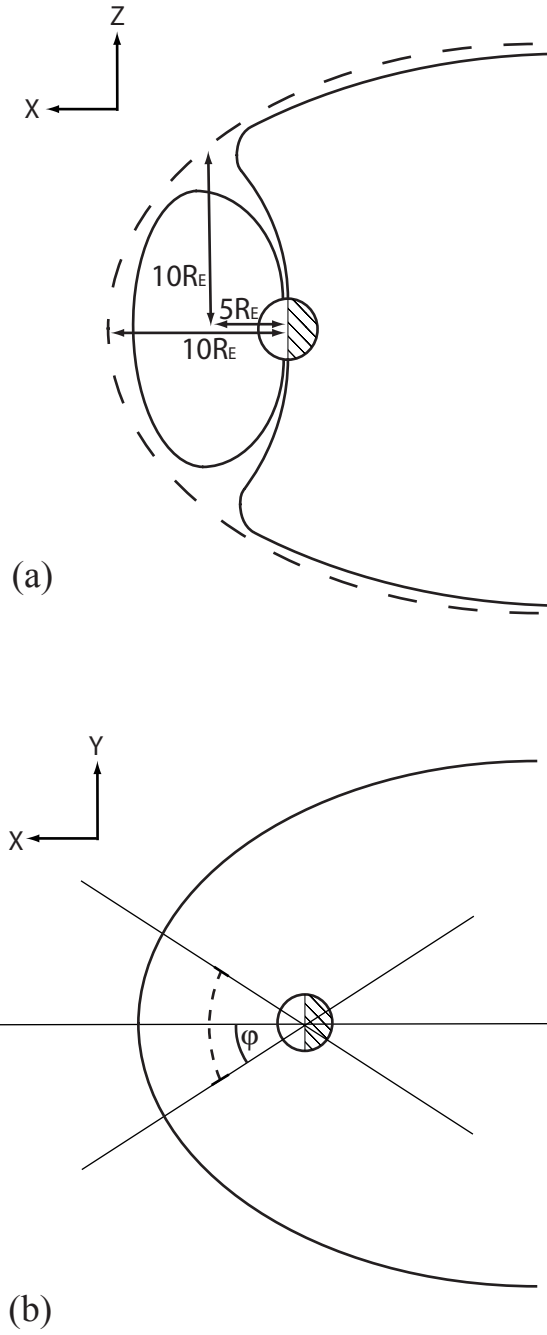
Figure 7.16. Schematics to show (a) the estimated position of the reconnection point in the X-Z plane, $X = 5\ R_E$, $Z = 10\ R_E$ and (b) the merging gap (dashed line) in the X-Y plane, $\varphi = 1$ hr MLT.

7.3.2 Reconfiguration of the magnetosphere

The bursts of sunward flow observed in the first study at 05:00 UT and 05:30 UT (Figure 7.7) have durations of approximately 25 and 10 minutes, respectively. The rearrangement of the magnetic field by DLR modifies the shape of the magnetosphere such that it no longer presents a streamlined shape to the flow of the solar wind. Flows are excited within the magnetosphere to return it to equilibrium (see also Cowley and Lockwood, 1992). The duration of each burst of flow represents the time taken for the magnetosphere to reconfigure; we assume that reconnection occurred for the relatively short period of time that the clock angle passed through 0° (also the duration of the luminosity enhancements presented in Figure 7.2). These times are therefore in agreement with Cowley and Lockwood (1992) who suggested that the magnetosphere takes approximately 15 minutes to re-adjust following a perturbation away from equilibrium.

The duration of the sunward flow across the OCB in the second interval was determined from Figure 7.14 to be approximately 35 minutes. The dual lobe reconnection itself is only thought to take place while the clock angle is within approximately 15° of zero (~10 minutes). The period of sunward flow in this interval is significantly longer than previous studies have identified (e.g. Sandholt et al., 2000). This is likely to be due to the clock angle passing very slowly through zero, therefore dual lobe reconnection taking place for a longer period of time than in previous cases. The result is a larger amount of flux being closed and therefore as expected the magnetosphere takes more time to adjust to this. This theory is in agreement with the keograms (Figure 7.11) which clearly show that during this event the polar cap is observed to shrink, indicating that a large amount of flux has been closed.

Previous studies (e.g. Lavraud et al., 2006) have concluded that DLR can take place for clock angles significantly larger than those identified here. It is possible that DLR continues beyond a value of +15° in this study as it is not possible to determine the time that the reconnection stops. The threshold angles for which DLR takes place depend on the length and location of the merging gap in each hemisphere.

7.3.3 Flux capture

The total magnetic flux crossing the OCB during each interval can be calculated from the SuperDARN potential maps by integrating the potential along the boundary with respect to time. During the first study this was found to be 9.1×10^6 Wb for the period 05:00-05:24 UT and 3.2×10^6 Wb for the period 05:30-05:40 UT. As a percentage of the total flux within the polar cap (calculated to be approximately 0.5 GWb in total), these are 1.8 and 0.6% and therefore we conclude that dual lobe reconnection closes only a small amount of flux during this interval. Clearly the clock angle would have to remain near 0° for long periods of time for significant flux closure to occur. Given the total amount of flux closed and assuming that the OCB remains circular, the poleward motion of the OCB would be ~0.15° magnetic latitude during the interval. It is not surprising therefore that it is not possible to identify this contraction in the keograms in Figure 7.3.

We cannot measure the flux closure rates for the two bursts of reconnection directly as we measure the flux transport in response to the magnetospheric reconfiguration, which occurs over a longer timescale than the reconnection itself. However, if reconnection during the first burst is assumed to occur for 4 minutes, the approximate duration of the clock angle rotation, then we can estimate a flux closure rate of ~35 kV.

Again by consideration of the potential along the OCB, the total flux closed during the second study was calculated to be 0.13 GWb, a significantly larger amount than in the first study. Another method used to determine the flux closed during the interval is to calculate the total flux in the polar cap before the burst of reconnection began, and then recalculate it at the end of the interval. It was not possible to perform this calculation in the first study as the amount of flux closed was so small that the polar cap was not observed to shrink. Reconnection in the tail must also be taken into consideration as it will also result in the polar cap shrinking. Figure 7.17d displays the AL and AU indices during this period, and these indicate that a substorm took place just prior to the start of our event. The maximum and mean brightness of a section of the nightside auroral oval (Figure 7.10) are plotted in Figure 7.17a. It suggests that the substorm activity is decreasing at the time of the onset of DLR (marked by the vertical dashed line in Figure 7.17), and although substorm activity is likely to account for the shrinking of the auroral oval before the
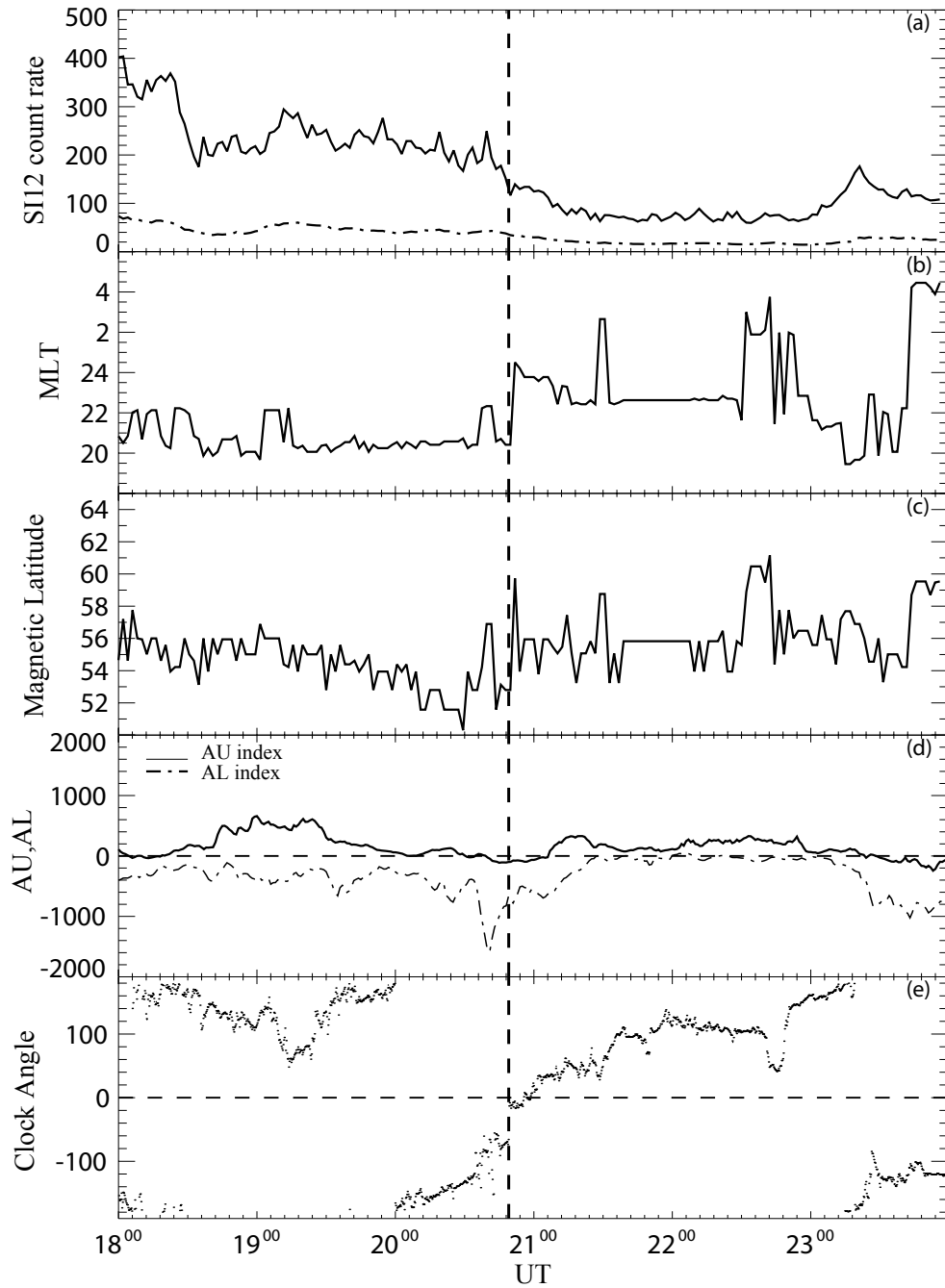
Figure 7.17. (a) Maximum and mean brightness of a nightside portion of the auroral oval, this portion being outlined in Figure 7.10 (b) The magnetic local time of the brightest pixel within this area (c) The magnetic latitude of the brightest pixel within the area (d) the AL and AU indices during the interval of interest (e) the clock angle measured by ACE lagged to the magnetopause. The vertical dashed line marks the onset of dual lobe reconnection as calculated from Figure 7.14.

start of the interval, it is unlikely to account for the significant polewards motion of the OCB during the interval itself. The latitude and MLT of the area of maximum brightness are plotted in panels b and c, and these demonstrate that for most of the interval this bright area remains fairly stationary. The substorm auroral bulge was located in the pre-midnight sector, but this fades by 20:50 UT such that the maximum brightness is in the midnight sector (i.e. the nightside activity level has fallen to a significantly lower level). Hence we assume that the nightside reconnection rate is small during the burst of DLR.

The polar cap contained 1.51 GWb of flux before the interval of reconnection, and 1.35 GWb after the interval, and therefore the total flux closed during the interval is the difference between these values, 0.16 GWb. The amount of flux closed estimated from the two methods are in close agreement, any discrepancy possibly being accounted for by ongoing nightside reconnection. These two values represent approximately 10% of the total flux in the polar cap prior to the onset of DLR, as well as corresponding to a reconnection rate of $\frac{0.13\,\text{GWb}}{600\text{s}} \approx 200\text{kV}$ if it is assumed that the dual lobe reconnection lasts 10 minutes. This reconnection rate is extremely high when compared to results of other studies, such as Chisham et al. (2004), and serves to highlight the significance of dual lobe reconnection under specific IMF conditions, namely a strong, northward pointing IMF.

7.3.4 Further evidence of DLR

The brightness of a small portion of the dayside aurora (marked by the black rectangle in Figure 7.2a) throughout the 2½ hour interval of the first event is plotted in Figure 7.2b. The brightness peaks at the time of the onset of DLR, marked by the vertical dashed lines. Since the IMF is northward throughout the interval, it would be expected that single lobe reconnection is occurring throughout and there will be aurora associated with particles accelerated at the magnetopause. These give the aurora poleward of the OCB and the proton fluxes observed by FAST. We interpret the enhanced luminosity as a contribution of magnetosheath particles injected at the southern lobe reconnection site during dual lobe reconnection increasing the particle

flux into the northern hemisphere ionosphere. This, then, is an additional signature of the interconnection of the two hemispheres by dual lobe reconnection.

The maximum and mean brightness of each SI12 image between 9.5 and 14.5 MLT and 65-75° latitude was determined throughout the interval studied in the second event. There is a large increase in both the maximum and the mean brightness at the time of the sunward flow (Figure 7.18a) due to the presence of the cusp spot. We expect that single lobe reconnection is taking place throughout the interval whenever the IMF is northward. The enhanced brightening again coincides with the onset of dual lobe reconnection, identified in Figure 7.14 and marked by the vertical dashed line. As in the case of the first event, we interpret this brightening as the signature of additional particle flux from the southern hemisphere travelling up newly reconnected field lines and being detected in the northern auroral oval. The extremely large increase in the maximum brightness suggests that a significant number of particles were captured onto closed field lines during the reconnection. During the interval the solar wind density fluctuates between ~5 and 55 cm^{-3}, therefore it is also possible that an increase in the solar wind density could have been responsible for some of the observed brightening (Frey et al., 2002).

Figure 7.18b shows the variation in MLT of the brightest portion of the dayside auroral oval. During the period prior to the cusp spot (and after it has disappeared) there is no consistently bright location, however the formation and subsequent duskward motion of the cusp spot is clearly visible, closely following IMF B_Y as it moves from negative through to positive values. Figure 7.18c is the magnetic latitude of the brightest portion of the dayside auroral oval and it is clear that following the onset of reconnection this moves poleward and remains so after the cusp spot has disappeared. This indicates that the polar cap has decreased in size, and therefore that significant amounts of flux have been closed by DLR. The polar cap is only observed to move to lower latitudes again when the IMF turns southward.

The maximum and the mean flow speed calculated from the SuperDARN convection maps between 9.5 and 14.5 MLT and 65-75° are plotted in Figure 7.19a. At the observed onset of the reconnection, marked by the vertical dashed line in Figure 7.19, the maximum flow clearly decreases from approximately 1800 m s^{-1} to 500 m s^{-1}. Sandholt et al. (2000) theorised that this decrease in the velocity of newly reconnected field lines could be due both to ionospheric resistance and the
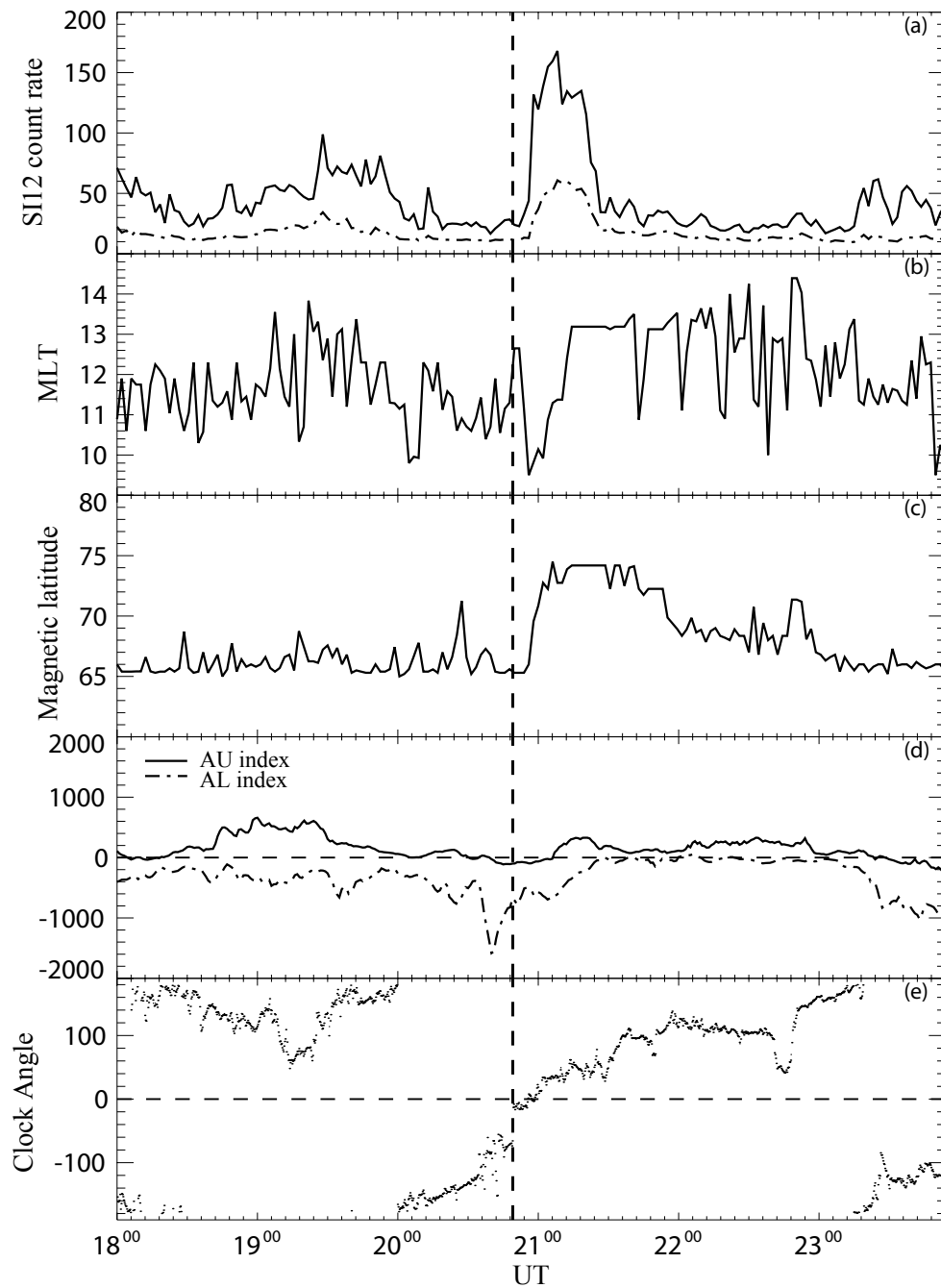
Figure 7.18. (a) The maximum and mean brightness of a dayside portion of the auroral oval, between 9.5 and 14.5 MLT and 65-75° latitude. (b) The magnetic local time of the brightest pixel within this area (c) The magnetic latitude of the brightest pixel within this area (d) The AL and AU indices during the interval of interest (e) the clock angle measured by ACE, lagged to the magnetiopause. The vertical dashed line marks the onset of dual lobe reconnection.

172
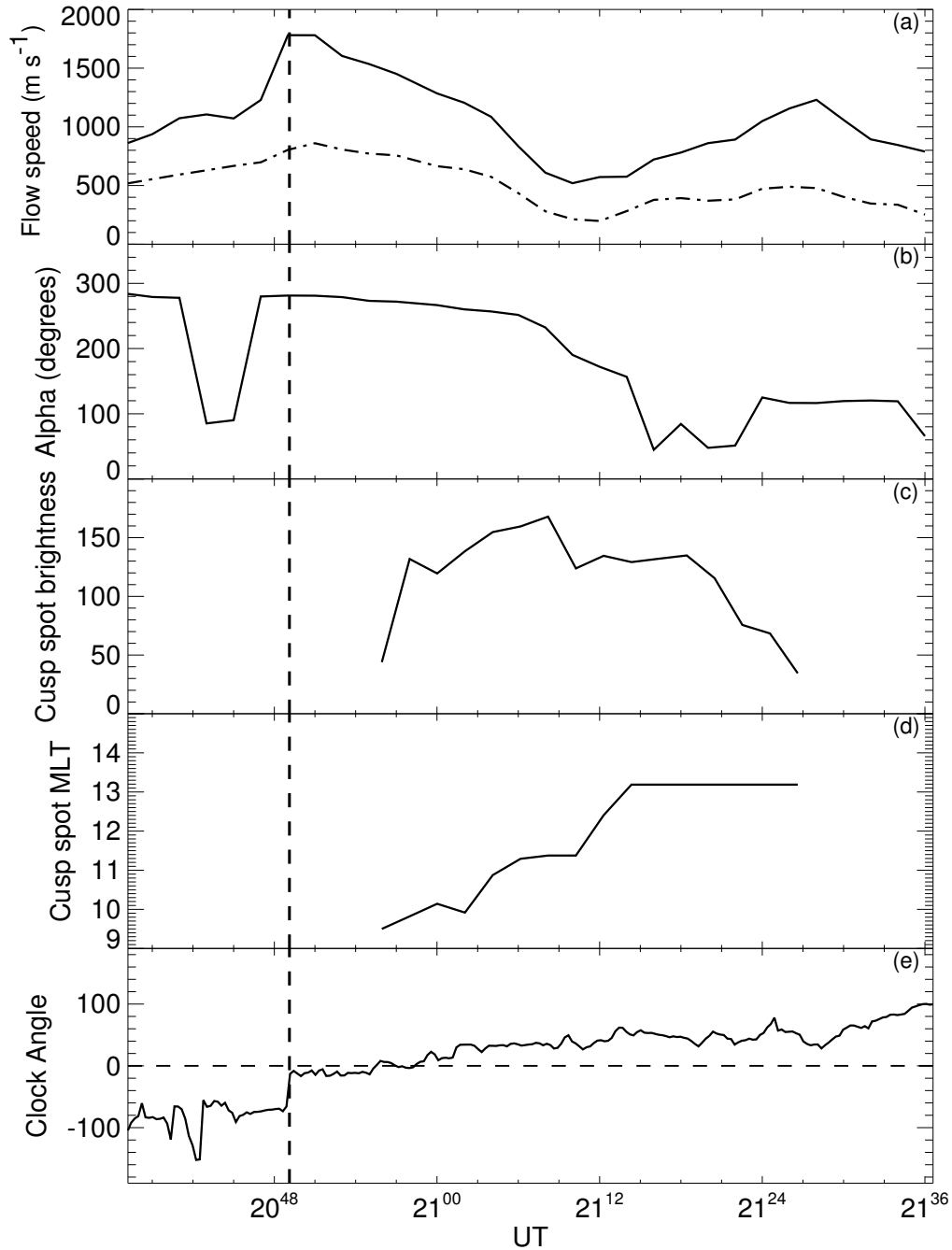
Figure 7.19. (a) The maximum and mean velocity of ionospheric flow measured by the SuperDARN radars within a sector 9.5-14.5 MLT and 65-75° magnetic latitude between 20:36 and 21:36 UT (b) The angle of the maximum velocity vector to North, clockwise in degrees (c) The brightness of the cusp spot (d) The MLT of the cusp spot (e) The clock angle measured by ACE, lagged to the magnetopause. The vertical dashed line represents the time at which the reconnection is thought to have commenced.

newly reconnected field lines no longer being directly connected to the fast flowing magnetosheath field. α is defined as the angle of the maximum velocity vector, measured clockwise in degrees from 0° (North). This is plotted in Figure 7.19b, with the brightness and MLT of the cusp spot in Figures 7.19c and d. These show that at the time when the cusp spot is passing through 12 MLT and at its brightest, the maximum and mean flows reach a minimum. The maximum flow vectors appear also to rotate with the cusp spot, pointing eastwards initially, passing through 180° (Sunward) as the cusp spot passes through 12 MLT, then pointing westwards. This is consistent with the expected variation in convection as the B_Y component of the IMF goes from negative, through zero, to positive values.

7.3.5 Plasma Capture

It has been postulated that dual lobe reconnection should be an extremely efficient solar wind plasma capture mechanism for the magnetosphere (e.g. Sandholt et al., 1999, 2000), and hence may be a mechanism for the population of the cold dense plasma sheet which sometimes occurs after prolonged periods of northward IMF (e.g. Øieroset et al., 2005, and references therein). Closed field lines that have undergone dual lobe reconnection will proceed into the tail. These field lines contain a large amount of solar wind plasma that was captured during DLR. This plasma would be of solar wind origin and would therefore be cold (defined by Oieroset et al. [2005] as < 1 keV), and if the solar wind density was high enough and the reconnection proceeded for enough time, it is thought that sufficient particles would be captured to significantly enhance the density of the plasma sheet. The plasma sheet density is usually ~ 0.3 cm^{-3} and Oieroset et al. [2005] define the threshold density for the cold, dense plasma sheet to be 1-2 cm^{-3}. The exact plasma transfer mechanism from the dayside to the tail once the plasma has been captured is as yet unclear.

It is possible to put an upper limit on the amount of plasma captured during each interval by calculating the amount of plasma on the interplanetary field lines that reconnected in both hemispheres. If the flux closed during the reconnection is known, it is possible to calculate the volume of the upstream solar wind that contains this amount of flux. Then knowing the density of the solar wind from the

upstream measurements it is possible to calculate the number of particles captured during the interval.

The total magnetic flux closed during both bursts of reconnection in the first study was calculated earlier to be $\sim 1.2 \times 10^7$ Wb. The equatorial cross-sectional area of the upstream volume containing $\sim 1.2 \times 10^7$ Wb of magnetic flux is given by $A=F/B$ where F is the flux closed and B is the average B_Z component of the IMF (~ 10 nT). The GSM Z dimension of this volume is given by the distance between the two cusps, here estimated to be ~ 20 R_E. Given that the upstream proton number density is measured by ACE to be 16 cm^{-3} at this time, the number of ions captured is of the order of 2.5×10^{30} representing a mass of approximately 4 tonnes of protons. We stress that this represents an upper limit in which it is assumed that no plasma is lost by mirroring in the near-Earth magnetic field after reconnection has taken place in one hemisphere but before field lines become closed by reconnection in the other hemisphere. We also have not accounted for the formation of a plasma depletion layer near the subsolar magnetopause.

The same calculation can be performed in order to estimate the number of particles captured during the interval of the second study. The magnetic flux closed during the reconnection was calculated earlier to be ~ 0.13 GWb, the average B_Z component of the IMF is 17.2 nT, the distance between the cusps is estimated again to be ~ 20 R_E and the upstream proton number density is 23 cm^{-3}. The number of protons captured given these conditions is therefore calculated to be of the order of 2×10^{31}.

To assess the implications of this plasma capture for the magnetotail and plasma sheet we can imagine transferring this plasma into the tail to determine its contribution to the pre-existing plasma content. Estimating the plasma sheet dimensions to be 50 R_E, 35 R_E and 5 R_E in X, Y and Z, the density of the plasma sheet would increase by ~ 1 cm^{-3} following the interval in the first study, and by a factor of ~ 20 (to be >10 particles per cubic centimetre) following the second interval. This demonstrates that dual lobe reconnection could be an extremely efficient method of populating the plasma sheet.

7.3.6 Plasma Sheet Observations

Data from the LANL spacecraft (Bame et al., 1993; McComas et al., 1993) passing through the plasma sheet indicates that a dense plasma sheet appears to have been detected following the first study of dual lobe reconnection, at approximately 02:00 UT on 19th December (Figure 7.8). The density of the plasma sheet will not increase immediately following the plasma capture on the dayside as the mass loaded field lines must migrate to the tail and the plasma be distributed through the plasma sheet. Clearly the newly-closed field lines must remain closed during this migration; if the IMF were to turn southward shortly after the plasma capture the field lines could be reopened and the plasma lost. Hence we expect that the formation of a cold dense plasma sheet requires long periods of northwards IMF, even if dual lobe reconnection occurs for only a small fraction of this time. The IMF was observed by ACE to be northward until 00:32 UT on 19th December, approximately 19 hours after the second interval of dual lobe reconnection (Figure 7.8). Following the initial increase in the near-Earth plasma sheet density to ~5 cm^{-3} at 02:00 UT on 19th December, the density then decays to ~1 cm^{-3} at approximately 05:00 UT which represents an overall increase in density of 0.5 cm^{-3}. This is in good agreement with our predicted plasma sheet density increase of 1 cm^{-3} from the number of upstream particles captured by reconnection. The decay from 5 cm^{-3} to 1 cm^{-3} might indicate that plasma first enters the plasma sheet near the Earth (close to geosynchronous altitude) before being distributed more evenly throughout the tail. This decay could also be explained by loss processes including precipitation into the ionosphere and loss down the tail due to substorms, or more gradual loss processes which could deposit particles into the ionosphere (e.g. Oksavik et al., 2006).

Following the second interval on 21st October 2001, data from the LANL spacecraft passing through the plasma sheet indicates that a dense plasma sheet does not appear to have been detected. It is believed that the formation of a cold dense plasma sheet takes considerable time (Terasawa et al., 1997), and the interval between the dual lobe reconnection closing field lines on the dayside and these field lines entering the tail might be expected to be of the order of 9 hours. An analysis of the IMF conditions during the event show that the sunward flow abruptly ends as the IMF turns southward at 21:35 UT (Figure 7.14). This is thought to be because

low latitude reconnection commences at this time and the newly closed field lines are therefore opened again. A cold dense plasma sheet would not be expected to form in this case as the closed field lines would not have had time to convect into the tail before the onset of low latitude reconnection. This example therefore serves to show that DLR is capable of capturing sufficient plasma to populate the cold dense plasma sheet, but that crucially the IMF must remain northwards for some considerable amount of time after the reconnection has ceased in order to allow the newly captured particle flux to enter the plasma sheet.

7.4 Conclusion

In the first interval we have presented the first substantial evidence for dual lobe reconnection from ionospheric flows and auroral signatures. Strongly northward IMF with a clock angle close to 0° provides the necessary conditions for this process. The specific signature identifying dual as opposed to single lobe reconnection is sunward flows across the noon portion of the OCB. These were observed in the SuperDARN radar data. The OCB is identified by the high energy electron/ion precipitation boundary observed from spacecraft, from radar backscatter, and auroral observations. Two separate intervals of sunward flow across the OCB are identified (Figure 7.7) and these are associated with the reconfiguration of the magnetosphere in response to two bursts of dual lobe reconnection occurring at rotations of the IMF through 0° clock angle.

From this study we conclude that: (1) Dual lobe reconnection does occur under conditions of strongly northward IMF; (2) In order for this process to take place the clock angle must be within approximately ±10° of zero; (3) The total flux crossing the OCB during each burst is small; (4) The flux closure rates observed enable a rough calculation of the number of particles captured during reconnection. This suggests that sufficient particles were captured to populate the cold, dense plasma sheet observed in subsequent hours, despite the fact that dual lobe reconnection only occurred for a few minutes.

In the second study we have presented an interval of dual lobe reconnection during which a significant amount of flux is closed (~10% of the pre-existing polar cap). Noon-midnight and dawn-dusk keograms show that the polar cap shrank visibly during the interval and although a small amount of this flux closure may be

due to nightside reconnection, we have calculated that 0.13 GWb of flux are closed by the process of dual lobe reconnection. This represents significantly more flux than was closed in the first study. The reason for this is thought to be that the clock angle passed extremely slowly through zero and therefore the reconnection took place for longer than previously. We were also able to estimate that $\sim 2 \times 10^{31}$ protons were captured by the magnetosphere by estimating the upstream volume of the solar wind containing the amount of magnetic flux closed during the event. This number of particles would be more than capable of populating a cold, dense plasma sheet, although in this case the IMF turned southwards shortly after the occurrence of the DLR, so the newly closed flux was opened again before the particles could be transferred into the plasma sheet. We can therefore conclude that in order for dual lobe reconnection to populate the cold, dense plasma sheet, the IMF is required to pass slowly through zero, and stay northward for a considerable period of time afterwards.

Chapter 8. Summary and Future Work

8.1 Summary

We have investigated the nature of the dayside reconnection process under northward IMF. A statistical study of the lobe reconnection rate for 12 months of northern hemisphere SuperDARN data has been performed. During this time period 1083 convection maps containing clear reverse twin cells were identified, and the reconnection rate was calculated as the difference between the electrostatic potential measured at the centre of each cell. The corresponding upstream conditions were measured by the ACE spacecraft and lagged to the magnetopause. The reconnection rate was found to depend upon each of the IMF components, and therefore the magnitude of the IMF, B. It also depended upon the length of the merging gap, and the solar wind electric field, $V_X B_Z$.

A modified version of the Lockwood ion dispersion model (Lockwood, 1995b) has been combined with the Cooling Model (Cooling et al., 2001) to model ion dispersion signatures associated with lobe reconnection. The dependence of the modelled signature on upstream solar wind conditions was analysed and appeared to be in agreement with a small statistical study undertaken using dispersion signatures observed by Cluster. Also a very clear reverse dispersed ion signature observed by FAST was analysed; the upstream conditions were fed into the model and good agreement was obtained between the modelled and the observed dispersion signature.

Finally we have modelled, and then identified the ionospheric signatures of dual lobe reconnection (DLR), and thereby provided the first conclusive evidence that this process takes place at Earth. We have calculated the threshold clock angle for DLR to take place, as well as calculating the amount of magnetic flux closed during two case studies. We have also calculated the amount of solar wind plasma captured and demonstrated that it is sufficient to populate the cold, dense plasma sheet observed following the first case study. We have concluded that in order for a CDPS to be formed by the process of DLR, a prolonged period of subsequent northward IMF is necessary.

In the three years since this work began, the process of DLR has received renewed interest within the international community. Although proposed several decades ago, the work presented within this thesis (and published as Imber et al., 2006; 2007) represents the first conclusive evidence for the occurrence of DLR. There remains controversy, however, especially surrounding the threshold clock angle for DLR occurrence. Lavraud et al. (2006) suggested that DLR could occur for clock angles up to ±60° using Cluster observations of heated magnetosheath electrons. Hu et al. (2008) also observed magnetosheath plasma signatures which they interpret as DLR for significantly larger clock angles than predicted by the geometrical considerations laid out in Chapter 7. Finally DLR has also been of interest to the planetary community, McComas and Bagenal (2007) controversially suggesting that it could be the primary flux closure mechanism at Jupiter.

The following section summarises some of the many ways in which it is possible to build upon this work in the future, particularly given the current and proposed space missions.

8.2 Future Work

8.2.1 Dual Lobe Reconnection

The study of magnetic flux closure via dual lobe reconnection (DLR) has been a large part of the work in this thesis, and remains a key area of interest. There are a number of future studies that can be recommended in order to better characterise the process of DLR and assess its importance in terms of magnetic flux transfer and solar wind plasma capture.

Statistical DLR study

Chapter 7 contains two case studies conclusively demonstrating that DLR takes place at Earth under specific interplanetary magnetic field (IMF) conditions. These case studies are important as subtle differences in the ionospheric convection associated with lobe as opposed to dual lobe reconnection make distinguishing between the two processes particularly complex. A statistical study of DLR events would provide useful insight into how the reconnection rate changes with upstream

conditions. It would be interesting to ascertain the impact of solar wind density, velocity and IMF clock angle on the dual lobe reconnection rate and the location of the merging gap on the magnetopause. This may, in turn, enable the likelihood of DLR taking place at a given time to be estimated based solely on the upstream conditions.

The difficulty in performing a large statistical study of DLR events is that to conclusively show that dual lobe reconnection is taking place, it must be shown that there is ionospheric plasma flow across the dayside open/closed field line boundary (OCB) and in order to do this the exact location of the dayside OCB must be determined. The method used in the two case studies presented in Chapter 7 requires good SuperDARN coverage on the dayside in order to ascertain the nature of the flows, as well as either overflying spacecraft capable of measuring electron fluxes at different energies, or auroral images.

It is possible to estimate the location of the OCB using auroral images alone, as the poleward edge of the electron aurora. In the past, automating the OCB location has been complicated during northward IMF as auroral arcs appear within the polar cap but can be mistaken for the aurora associated with the OCB. I propose developing a method of identifying the dayside OCB in each image using the maximum brightness along a series of cuts of constant MLT. This would allow identification of auroral arcs or cusp spots as double peaks in the intensity-latitude profile. Then, given sufficient SuperDARN coverage, the flow across the OCB could be calculated, and therefore DLR events could be identified. The times of the DLR events could then be combined with upstream measurements of the solar wind made by the ACE spacecraft.

The IMAGE spacecraft was operational for just under 6 years, from 2000 to 2005, providing images of the electron and proton aurora at 2 minute cadence. During this time period the SuperDARN radars had good northern hemisphere coverage, capable of determining plasma flow across the dayside OCB given suitable radar propagation conditions. The ACE spacecraft was located at the L1 point approximately 240 R_E upstream of the Earth throughout 2000-2005, and was therefore capable of determining the IMF clock angle, solar wind density, and velocity. Given the length of time that reliable data from these instruments has been available, it would be possible to combine these data to build up a large statistical data set of DLR events.

DLR plasma capture statistical study

The first case study in Chapter 7 has demonstrated that even a relatively short burst of DLR is capable of capturing a huge number of solar wind particles, and this has been proposed as a plasma capture mechanism for the cold, dense plasma sheet (CDPS). The results of modelling the motion of newly closed field lines on the dayside show that they appear to sink into the dayside magnetosphere and move dusk or dawnward to the flanks (e.g. Li et al., 2005; Wing et al., 2006). It is not clear exactly how the plasma on these newly closed field lines then enters the plasma sheet. The second case study of Chapter 7 is thought to have captured significantly more plasma than the first, however the IMF turned southward again, and we proposed that the plasma on the newly closed field lines was lost when low latitude reconnection commenced. We therefore concluded that the IMF must remain northward for some time following DLR to allow the closed field lines on the dayside to convect into the tail and the plasma to enter the plasma sheet.

If a database of DLR events could be developed it would then be possible to use the LANL spacecraft which pass through the plasma sheet to determine whether a CDPS is subsequently formed. A statistical analysis of the occurrence of the CDPS following DLR would help to clarify the importance of DLR in CDPS formation. In cases where a CDPS is not formed it would be of interest to analyse both the amount of plasma captured during DLR and the subsequent upstream conditions.

DLR plasma capture case study

In Chapter 7 we analysed an episode of DLR and concluded that sufficient particles were captured to populate the subsequent CDPS observed by the LANL spacecraft. We have not provided any conclusive evidence that the particles injected into the plasma sheet were captured by DLR, and there are several alternative CDPS formation mechanisms which have been proposed, mainly involving diffusive entry through the magnetotail flanks (Terasawa et al., 1997) or reconnection in Kelvin-Helmholtz vortices (Fujimoto and Terasawa, 1994; Fairfield et al., 2000; Hasegawa et al., 2004). It would therefore be of interest to

conclusively demonstrate that plasma captured during DLR does enter the plasma sheet and contribute to the formation of a CDPS.

The solar wind contains varying quantities of highly ionised heavy ions such as iron which act as tracers of the coronal conditions at their point of origin. One example is that the relative abundance of Fe with charge states between 6+ and 15+ depends on the coronal temperature (Grande et al., 1996, Perry et al., 2000). In order to demonstrate that solar wind plasma has been captured by DLR and has resulted in the formation of a CDPS, it may be possible to relate changes in the CDPS composition with upstream measurements of the highly ionised solar wind plasma population, lagged according to the estimated transit time from dual lobe reconnection on the dayside, to particles reaching the plasma sheet in the tail.

In order to do this an upstream solar wind monitor capable of distinguishing between different high energy, highly ionised ion populations is required. The ACE spacecraft has such a detector called the Solar Wind Ion Composition Experiment (SWICS) (Gloeckler et al., 1998) which determines a full Fe spectrum every 12 minutes. This spacecraft is also used to determine the upstream solar wind magnetic field conditions as well as the solar wind density and velocity. An interval of DLR must be identified in a similar way to the two case studies presented in Chapter 7, therefore good SuperDARN coverage of the dayside auroral oval in one hemisphere is essential, as well as auroral imagery and overflying spacecraft capable of measuring electron fluxes in both high and low energy ranges. A spacecraft just inside the magnetopause, or near the dawn or dusk flank which is capable of measuring the in situ particle population would then be able to identify the particle signatures of DLR (ion dispersion signatures) and the composition of the plasma on those newly closed field lines. If the plasma composition observed by this spacecraft matched the upstream plasma composition and it was clearly positioned on closed field lines, then we may conclude that the spacecraft has observed the particles captured by DLR. Finally both the LANL and POLAR spacecraft are capable of determining the composition of the plasma sheet, and LANL also measures the plasma sheet temperature and density. As mentioned above, it may be possible to relate changes in the relative quantities of highly ionised heavy solar wind particles impinging on the magnetopause with changes in the composition of both the dayside/flank magnetospheric plasma and the plasma sheet. This would provide excellent evidence that DLR contributes to the CDPS.

8.2.2 Northward IMF Plasma Depletion Layer

Chapter 5 presents a statistical study of lobe reconnection rates, and relates these to the upstream conditions. Cowley and Owen (1989) postulated that in order for steady lobe reconnection to take place, the magnetosheath velocity at the reconnection site must be less than the local Alfvén velocity. This allows newly reconnected field lines to move sunward away from the reconnection site such that reconnection can continue to take place. It can be assumed that in order for clear twin reverse cells to be identified in the SuperDARN convection maps, lobe reconnection must be steady for some period of time. It would therefore be of interest to use ACE solar wind data combined with the Cooling Model to calculate the Alfvén velocity near the reconnection site and compare this to the modelled magnetosheath velocity, with the knowledge that lobe reconnection was taking place during each interval. Petrinec et al. (2003) combined 61 passes of the Polar spacecraft through the cusp with both a hydrodynamic and a magnetic field model to estimate the Alfvén velocity and magnetosheath velocity at the reconnection site. Assuming that the Alfvén velocity must be greater or equal to the magnetosheath velocity, it was possible to estimate the ion density of the necessary plasma depletion layer. Using the lobe reconnection data set already developed this study could be performed on a much larger scale and under a range of northward IMF solar wind conditions.

8.2.3 Reconnection rates in opposite hemispheres

The Kua Fu mission is currently in the pre-phase A stage, and is scheduled to be launched in 2012. This mission consists of an upstream solar wind monitor and two spacecraft in highly elliptical polar orbits, both of which carry an auroral imager. The orbit of these spacecraft is such that at any given time there is always coverage of the northern hemisphere auroral oval, and for a short period every orbit there is simultaneous coverage of the southern hemisphere auroral oval.

Østgaard et al. (2005) identified a short interval in September 2000 during which the IMAGE spacecraft was over the northern hemisphere polar cap and Polar was simultaneously imaging the southern hemisphere auroral oval. They observed a cusp spot in both hemispheres indicative of lobe reconnection, as well as a theta

aurora in the southern hemisphere. They concluded from this that the reconnection rate was higher in the southern hemisphere due to a positive IMF B_X component. It would be of particular interest to use Kua Fu simultaneous auroral images in both hemispheres to test this theory.

The predicted ionospheric signatures of dual lobe reconnection were presented in Chapter 4. Two case studies presented in Chapter 7 identified sunward flow across the OCB which provided evidence that DLR does take place at Earth. In both cases at the times of the DLR itself the auroral brightness on the dayside was observed to increase, and it was postulated that this was due to particles from the opposite (southern) hemisphere reconnection site travelling up the newly reconnected field line and precipitating in the northern hemisphere. It would therefore be of great interest to analyse simultaneous auroral images during an interval of dual lobe reconnection in order to ascertain whether this brightening occurs in both hemispheres, as theory would predict. The timing of the brightenings in each hemisphere would also provide information about which tail lobe reconnected first, which would be of significant value when modelling the expected low altitude spacecraft signature, as discussed in Chapter 4. The proposed imagers on the Kua Fu spacecraft image the aurora at 30 second cadence, therefore may be able to observe the timing difference in the cusp spot brightening in opposite hemispheres.

Bibliography

Asai, K. T., Maezawa, K., Mukai, T., and Hayakawa, H., Latitudinal and longitudinal displacement of cusp ion precipitation controlled by IMF BY and BZ, *Earth Planets Space*, *57*, 627-641, 2005.

Baker, K. B., Dudeney, J. R., Greenwald, R. A., Pinnock, M., Newell, P. T., Rodger, A. S., Mattin, N., and Meng, C.-I.: HF radar signatures of the cusp and low-latitude boundary layer, *J. Geophys. Res.*, *100*, 7671–7695, 1995.

Balogh, A., Dunlop, M. W., Cowley, S. W. H., Southwood, D. J., Thomlinson, J. G., Glassmeier, K. H., Musmann, G., Luhr, H., Buchert, S., Acuna, M. H., Fairfield, D. H., Slavin, J. A., Riedler, W., Schwingenschuch, K., and Kivelson, M. G., The cluster magnetic field investigation, *Space Sci. Rev.*, *79*, 65–91, 1997.

Bame, S. J., McComas, D. J., Thomsen, M. F., Barraclough, B. L., Elphic, R. C., Glore, J. P., Gosling, J. T., Chavez, J. C., Evans, E. P., and Wymer, F. J., Magnetospheric plasma analyzer for spacecraft with restrained resources, *Rev. Sci. Instrum.*, *64*, 1026–1033, 1993.

Baumjohann, W. and Treumann, R. A., Basic Space Plasma Physics, Imperial College Press, 1997.

Belian, R. D., Gisler, G. R., Cayton, T., and Christensen, R., High Z energetic particles at geosynchronous orbit during the great solar proton event of October 1989, *J. Geophys. Res.*, *97*, 16,897, 1992.

Bosqued, J. M., Sauvaud, J. A., Réme, H., Crasnier, J., Galperin, Y. I., Kovrazhkin, R. A., and Gladyshev, V. A., Evidence for Ion Energy Dispersion in the Polar Cusp related to a Northward-directed IMF, *Adv. Space Res.*, *5*, 149-153, 1985.

Carlson, C. W., Pfaff, R. F., and Watzin, J. G., The Fast Auroral SnapshoT (FAST) mission, *Geophys. Res. Lett.*, *25*, 2013-2016, 1998.

Carlson, C. W., McFadden, J. P., Turin, P., Curtis, D. W., and Magoncelli, A., The Electron and Ion Plasma Experiment for Fast, *Space Sci. Rev.*, *98*, 2001.

Chisham, G., and Freeman, M. P., A technique for accurately determining the cusp-region polar cap boundary using SuperDARN HF radar measurements, *Ann. Geophys.*, *21*, 983-996, 2003.

Chisham, G., Freeman, M. P., Coleman, I. J., Pinnock, M., Hairston, M. R., Lester, M., and Sofko, G., Measuring the dayside reconnection rate during an interval of due northward interplanetary magnetic field, *Ann. Geophys.*, *22*, 4243-4258, 2004.

Chisham, G., Freeman, M. P., Sotirelis, T., Greenwald, R. A., Lester, M., and Villain, J.-P., A statistical comparison of SuperDARN spectral width boundaries and DMSP particle precipitation boundaries in the morning sector ionosphere, *Ann. Geophys.*, *23*, 733–743, 2005.

Chisham, G., Lester, M., Milan, S. E., Freeman, M. P., Bristow, W. A., Grocott, A., McWilliams, K. A., Ruohoniemi, J. M., Yeoman, T. K., Dyson, P. L., Greenwald, R. A., Kikuchi, T., Pinnock, M., Rash, J. P. S., Sato, N., Sofko, G. J., Villain, J.-P., Walker, A. D. M., A decade of the Super Dual Auroral Radar Network (SuperDARN): scientific achievements, new techniques and future directions, *Surveys in Geophysics*, *28*, 33-109, 2007.

Chisham, G., Freeman, M. P., Abel, G. A., Lam., M. M., Pinnock, M., Coleman, I. J., Milan, S. E., Lester, M., Bristow, W. A., Greenwald, R. A., Sofko, G. J., and Villain, J.-P., Remote Sensing of the Spatial and Temporal Structure of Magnetopause and Magnetotail Reconnection from the Ionosphere, *Rev. Geophys.*, *46*, 2008.

Cooling, B. M. A., Role of the magnetosheath flow in determining the motion of open flux tubes, *J. Geophys. Res.*, *106*, 18,763-18,775, 2001.

Cowley, S. W. H., The causes of convection in the Earth's magnetosphere: A review of developments during the IMS, *Rev. Geophys.*, 20, 531-565, 1982.

Cowley, S. W. H., and Owen, C. J., A simple illustrative model of open flux tube motion over the dayside magnetopause, *Planet. Space Sci.*, *37*, 1461-1475, 1989.

Cowley, S. W. H., and Lockwood, M., Excitation and decay of solar wind-driven flows in the magnetosphere-ionosphere system, *Ann. Geophys.*, *10*, 103-115, 1992.

Crooker, N. U., Reverse Convection, *J. Geophys. Res.*, *97*, 19,363–19372, 1992.

Crooker, N. U., and F. J. Rich, Lobe cell convection as a summer phenomenon, *J. Geophys. Res.*, *98*, 13,403, 1993.

Cumnock, J. A., Heelis, R. A., and Hairston, M. R., High-latitude ionospheric convection pattern during steady northward interplanetary magnetic field, *J. Geophys. Res.*, *100*, 14,537-14,555, 1995.

Dashkevich, Z. V., Kozelov, B. V., and Ivanov, V. Y., Lyman-Birge-Hopfield bands in proton auroras, *Geomagnetism and Aeronomy*, *35*, 1996.

Dendy, R., Plasma Physics An Introductory Course, Cambridge University Press, 1993.

Drayton, R. A., Koustov, A. V., Hairston, M. R., and Villain, J.-P., Comparison of DMSP cross-track ion drifts and SuperDARN line-of-sight velocities, *Ann. Geophys.*, *23,* 2479-2486, 2005.

Dungey, J. W., Interplanetary magnetic field and the auroral zones, *Phys. Rev. Letters*, *6*, 47-48, 1961.

Dungey, J. W., The structure of the ionosphere, or adventures in velocity space, in Geophysics: The Earth's Environment, edited by C. DeWitt, J. Hiebolt, and A. Lebeau, 526-536, Gordon and Breach, New York, 1963.

Eastman, T. E., Hones, E. W., Jr., Bame, S. J., and Asbridge, J. R., The magnetospheric boundary layer: Site of plasma, momentum and energy transfer from the magnetosheath into the magnetosphere, *Geophys. Res. Lett.*, *3*, 685, 1976.

Eastman, T. E., and Hones, E. W., Jr., Characteristics of the magnetospheric boundary layer and magnetopause layer as observed by IMP 6, *J. Geophys. Res.*, *84*, 2019, 1979.

Escoubet, C. P., Schmidt, R., and Goldstein, M. L., Cluster − Science and Mission Overview, *Space Sci. Rev.*, *79*, 11–32, 1997.

Evans, D. S., and Greer, M. S., Polar orbiting environmental satellite space environment monitor - 2: Instrument descriptions and archive data documentation, NOAA Technical Memorandum OAR SEC-93, Space Environment Center, Boulder, Colorado, 2000.

Fairfield, D. H., and Scudder, J. D., Polar rain: Solar coronal electrons in the Earth's magnetosphere, J. Geophys. Res., 90, 4055-4068, 1985.

Fairfield, D. H., Lazarun, A. J., Otto, A., Mukai, T., Kokubun, S., Lepping, R. P., Steinberg, J. T., and Yamamoto, T., Geotail observations of the Kelvin-Helmholtz instability at the equatorial magnetotail boundary for parallel northward fields, *J. Geophys. Res.*, *105*, 21,159-21,173, 2000.

Freeman, M. P., Farrugia, C. J., Burlaga, L. F., Hairston, M. R., Greenspan, M. E., Ruohoniemi, J. M., and Lepping, R. P.: The interaction of a magnetic cloud with the Earth: Ionospheric convection in the northern and southern hemispheres for a wide range of quasi-steady IMF conditions, *J. Geophys. Res.*, *98*, 7633–7655, 1993.

Frey, H. U., Mende, S. B., Immel, T. J., Fuselier, S. A., Claflin, E. S., Gérard, J-C., and Hubert, B., Proton aurora in the cusp, *J. Geophys. Res.*, *107*, 1091, 2002.

Frey, H. U., Mende, S. B., Angelopoulos, V., and Donovan, E. F., Substorm onset observations by IMAGE-FUV, *J. Geophys. Res.*, *109*, 2004.

Fujimoto, M., and Terasawa, T., Anomalous ion mixing within an MHD scale Kelvin-Helmholtz vortex, *J. Geophys. Res.*, *99*, 8601-8613, 1994.

Fujimoto, M., Nishida, A., Mukai, T., Saito, Y., Yamamoto, T and Kokubun, S., Plasma entry from the flanks of the near-Earth magnetotail: Geotail observations in the dawnside LLBL and the plasma sheet, *J. Geomagn. Geoelectr.*, *48*, 711, 1996.

Fujimoto, M., Terasawa, T., Mukai, T., Saito, Y., Yamamoto, T., and Kokubun, S., Plasma entry from the flanks of the near-Earth magnetotail: Geotail Observations, *J. Geophys. Res.*, 103, 4391-4408, 1998.

Fujimoto, M., Mukai, T., and Kokubun, S., Cold-dense plasma sheet and hot-dense ions in the inner-magnetosphere, *Adv. Space Res.*, *30*, 2279-2288, 2002.

Fuselier, S. A., Elphic, R. C., and Gosling, J. T., Composition measurements in the dusk flank magnetosphere, *J. Geophys. Res.*, *104*, 4515-4522, 1999.

Fuselier, S. A., Frey, H. U., Trattner, K. J., Mende, S. B., and Burch, J. L., Cusp aurora dependence on interplanetary magnetic field BZ, *J. Geophys. Res.*, *107*, 1111, 2002.

Gary, S. P., and Eastman, T. E., The lower hybrid drift instability at the magnetopause, *J. Geophys. Res.*, *84*, 7378, 1979.

Gloeckler, G., Cain, J., Ipavich, F. M., Tums, E. O., Bedini, P., Fisk, L. A., Zurbuchen, T. H., Bochsler, P., Fischer, J., Wimmer-Scweingruber, R. F., Geiss, J., and Kattenbach, R., Investigation of the Composition of Solar and Interstellar Matter Using Solar Wind and Pickup Ion Measurements with SWICS and SWIMS on the ACE Spacecraft, *Space Sci. Rev.*, *86*, 497-539, 1998.

Grande, M., Perry, C. H., Blake, J. B., Chen, M. W., Fennell, J. F., and Wilken, B., Observations of iron, silicone, and other heavy ions in the geostationary altitude region during late March 1991, *J. Geophys. Res.*, *101*, 24,707-24,718, 1996.

Greenwald, R. A., Bristow, W. A., Sofko, G. J., Senior, C., Cerisier, J.-C., and Szabo, A., Super Dual Auroral Radar Network radar imaging of dayside high-latitude convection under northward interplanetary magnetic field: Toward resolving the distorted two-cell versus multicell controversy, *J. Geophys. Res., 100,* 19,661-19,674, 1995.

Greenwald, R. A., Baker, K. B., Dudeney, J. R., Pinnock, M., Jones, T. B., Thomas, E. C., Villain, J.-P., Cerisier, J.-C., Senior, C., Hanuise, C., Hunsucker, R. D., Sofko, G., Koehler, J., Nielsen, E., Pellinen, R., Walker, A. D. M., Sato, N., and Yamagishi, H., DARN/SuperDARN: a global view of the dynamics of high-latitude convection, *Space Sci. Rev.,* 71, 761, 1995.

Hardy, D. A., Yeh, H. C., Schmitt, L. K. Schumaker, T. L., Gussenhoven, M. S., Huber, A., Marshall, F. J., and Pantazis, J.: Precipitating electron and ion detectors (SSJ/4) on the block 5D/Flights 6-10 DMSP satellites: Calibration and data presentation, Tech. Rep. AFGL-TR-84- 0317, Air Force Geophys. Lab., Hanscom Air Force Base, Mass., 1984.

Hasegawa, H., Fujimoto, M., Phan, T.-D., Rème, H., Balogh, A., Dunlop, M. W., Hashimoto, C., TanDokoro, R., Transport of solar wind into Earth's magnetosphere through rolled-up Kelvin–Helmholtz vortices, *Nature,* 430, 755-758, 2004.

Haubold, H. and Mathai, A. M., Sun, *Encyclopedia of Planetary Sciences,* 786-794, Chapman and Hall, 1997.

Heppner, J. P., Empirical Models of High-Latitude Electric Fields, *J. Geophys. Res., 82,* 1115-1125, 1977.

Heppner, J. P., and Maynard, N. C., Empirical High-Latitude Electric Field Models, *J. Geophys. Res., 92,* 4467-4489, 1987.

Haerendel, G., Paschmann, G., Sckopke, N., Rosenbauer, H., and Hedgecock, P.C., The frontside boundary layer of the magnetopause and the problem of reconnection, *J. Geophys. Res., 83,* 3195, 1978.

Holzer, R. E., and Slavin, J. A., A correlative study of magnetic flux transfer in the magnetosphere, *J. Geophys. Res.*, *84*, 2573-2578, 1979.

Hu, R., Bogdanova, Y. V., Owen, C. J., Foullon, C., Fazakerley, A. N., and Rème, H., Cluster observations of the midlatitude cusp under strong northward interplanetary magnetic field, *J. Geophys. Res.*, *113*, 2008.

Huang, C., Sofko, G. J., Koustov, A. V, Andre, D. A., Ruohoniemi, J. M., Greenwald, R. A., and Hairston, M. R., Evolution of ionospheric multicell convection during Northward interplanetary magnetic field with |Bz/By|>1, *J. Geophys. Res.*, *108*, 27,095–27, 2000.

Hubert, B., Gérard, J. C., Fuselier, S. A., and Mende, S. B., Observation of dayside subauroral proton flashes with the IMAGE-FUV imagers, *Geophys. Res. Lett.*, *30*, 1145-1178, 2003.

Hubert, B., Milan, S. E., Grocott, A., Blockx, C., Cowley, S, W, H., and Gérard, J.-C., Dayside and nightside reconnection rates inferred from IMAGE FUV and Super Dual Auroral Radar Network data, *J. Geophys. Res.*, *111*, A03217, 2006.

Ijima, T. and Potemra, T.A., Large-scale characteristics of field-aligned currents associated with substorms. *J. Geophys. Res*, *83*, 599, 1978.

Imber, S. M., Milan, S. E., and Hubert, B., The auroral and ionospheric flow signatures of dual lobe reconnection, *Ann. Geophys.*, *24*, 3115-3129, 2006.

Imber, S. M., Milan, S. E., and Hubert, B., Observations of significant flux closure by dual lobe reconnection, *Ann. Geophys.*, *25*, 1617-1627, 2007.

Kan, J. R., and Lee, L. C., Energy Coupling Function and Solar Wind-Magnetosphere Dynamo, *Geophys. Res. Lett.*, *6*, 577-580, 1979.

Kawano, H., and Russell, C. T., Survey of flux transfer events observed with the ISEE 1 spacecraft: Rotational polarity and the source region, *J. Geophys. Res.*, *101*, 27,299-27,308, 1996.

Kivelson, M. G. and Russell, C. T., Introduction to Space Physics, Cambridge University Press, 1995.

Kobel, E., and Flückiger, E. O., A model of the steady state magnetic field in the magnetosheath, *J. Geophys. Res.*, *99*, 23,617-23,622, 1994.

Kokubun, S., Yamamoto, T., Acuña, M. H., Hayashi, K., Shiokawa, K., and Kawano, H., The GEOTAIL magnetic field experiment, *J. Geomagn. Geoelectr.*, *46*, 7–21, 1994.

Lavraud, B., Thomsen, M. F., Lefebvre, B., Schwartz, S. J., Seki, K., Phan, T. D., Wang, Y. L., Fazakerley, A., Rème, H., and Balogh, A., Evidence for newly closed magnetosheath field lines at the dayside magnetopause under northward IMF, *J. Geophys. Res.*, *111*, A05211, 2006.

Le, G., Russell, C. T., Gosling, J. T., and Thomsen, M. F., ISEE observations of low-latitude boundary layer for northward interplanetary magnetic field: Implications for cusp reconnection, *J. Geophys. Res.*, *101*, 27,239–27,249, 1996.

Lepping, R. P., Acuna, M. H., Burlaga, L. F., Farrell, W. M., Slavin, J. A., Schatten, K. H., Mariani, F., Ness, N. F., Neubauer, F. M., Whang, Y. C., Byrnes, J. B., Kennon, R. S., Panetta, P. V., Scheifele, J. and Worley, E. M., The Wind Magnetic Field Investigation, *Space Sci. Rev.*, *71*, 207-229, 1995.

Li, W., Raeder, J., Dorelli, J., Oieroset, M., and Phan, T., Plasma sheet formation during long period of northward IMF, *Geophys. Res. Lett.*, *32*, L12S08, 2005.

Liemohn, M. W., and A. A. Chan, Unraveling the mechanisms responsible for radiation belt enhancements, *EOS*, *88*, 2007.

Lin, Y., and Wang, X. Y., Formation of low-latitude boundary layer under northward interplanetary magnetic field, *Geophys. Res. Lett.*, *33*, L21104, 2006.

Lockwood, M., Cowley, S. W. H., and Freeman, M. P., The excitation of plasma convection in the high latitude ionosphere, *J. Geophys. Res.*, *95*, 7961, 1990.

Lockwood, M., and Cowley, S. W. H., Ionospheric Convection and the Substorm Cycle, in Proceedings of the International Conference on Substorms (ICS-1), 99–109, 1992.

Lockwood, M., and Smith, M. F., Low and middle altitude cusp particle signatures for general magnetopause reconnection rate variations: 1. Theory, *J. Geophys. Res.*, *99*, 8531-8553, 1994.

Lockwood, M., Overlapping cusp ion injections: An explanation invoking magnetopause reconnection, *Geophys. Res. Lett.*, *22*, 1141-1144, 1995a.

Lockwood, M., Location and characteristics of the reconnection X line deduced from low-altitude satellite and ground-based observations: 1. Theory, *J. Geophys. Res.*, *100*, 21,791-21,802, 1995b.

Lockwood, M., and Davis, C. J., Occurrence probability, width and number of steps of cusp precipitation for fully pulsed reconnection at the dayside magnetopause, *J. Geophys. Res.*, *100*, 7627-7640, 1995.

Lockwood, M., Davis, C. J., Onsager, T. G., and Scudder, J. D., Modelling signatures of pulsed magnetopause reconnection in cusp ion dispersion signatures seen at middle altitudes, *Geophys. Res. Lett.*, *25*, 591-594, 1998.

Lockwood, M., and Moen, J., Reconfiguration and closure of lobe flux by reconnection during northward IMF: possible evidence for signatures in cusp/cleft auroral emissions, *Ann. Geophys.*, *17*, 996-1011, 1999.

Lockwood, M., Milan, S. E., Onsager, T., Perry, C. H., Scudder, J. A., Russell, C. T., and Brittnacher, M., Cusp ion steps, field-aligned currents and poleward moving auroral forms, *J. Geophys, Res.*, *106*, 29,555-29,569, 2001.

Luhmann, J.G., R.J. Walker, C.T. Russell, N.U. Crooker, J.R. Spreiter, and S. S. Stahara, Patterns of potential magnetic field merging sites on the dayside magnetopause, *J. Geophys. Res.*, *89*, 1739, 1984.

McComas, D. J., Bame, S. J., Barraclough, B. L., Donart, J. R., Elphic, R. C., Gosling, J. T., Moldwin, M. B., Moore, K. R., and Thomsen, M. F., Magnetospheric Plasma Analyzer: Initial three spacecraft observations from geosynchronous orbit, *J. Geophys. Res.*, *98*, 13 453–13 465 , 1993.

McComas, D.J., Blame, S.J., Barker, P., Feldman, W.C., Phillips, J.L., Riley, P., Griffee, J.W., Solar Wind Electron Proton Alpha Monitor (SWEPAM) for the Advanced Composition Explorer, *Space Sci. Rev.*, *86*, 563-612, 1998.

McComas, D. J., and Bagenal , F., Jupiter: A fundamentally different magnetospheric interaction withthe solar wind, *Geophys. Res. Lett.*, *34*, 2007.

McWilliams, K. A., Ionospheric Signatures of Dayside Reconnection Processes, PhD Thesis, 2001.

Maxwell, J. C.: A Treatise on Electricity and Magnetism, New York, Dover, Third edn., 2 vols., reprint (1954), 1891.

Mende, S.B., Heetderks, H., Frey, H.U., Lampton, M., Geller, S.P., Habraken, S., Renotte, E., Jamar, C., Rochus, P., Spann, J., Fuselier, S.A., Gerard, J.-C., Gladstone, R., Murphree, S., Cogger, L., Far ultraviolet imaging from the IMAGE spacecraft. 1. System design, *Space Sci. Rev.*, *91*, 243 – 270, 2000a.

Mende, S. B., Heetderks, H., Frey, H. U., Lampton, M., Geller, S. P., Abiad, R., Siegmund, O. H. W., Tremsin, A. S., Spann, J., Dougani, H., Fuselier, S. A., Magoncelli, A. L., Bumala, M. B., Murphree, S., Trondsen, T., Far ultraviolet imaging from the IMAGE spacecraft. 2. Wideband FUV imaging, *Space Sci. Rev.*, *91*, 271 – 285, 2000b.

Mende, S. B., Heetderks, H., Frey, H. U., Stock, J. M., Lampton, M., Geller, S. P., Abiad, R., Siegmund, O. H. W., Habraken, S., Renotte, E., Jamar, C., Rochus, P., Gerard, J.-C., Sigler, R., and Lauche, H., Far Ultraviolet Imaging from the IMAGE Spacecraft: 3. Spectral Imaging of Lyman-α and OI 135.6 nm, *Space Sci. Rev.*, *91*, 2000c.

Milan, S. E., Yeoman, T. K., Lester, M., Thomas, E. C., and Jones, T. B., Initial backscatter occurrence statistics from the CUTLASS HF radars, *Ann. Geophys.*, *15*, 703-718, 1997.

Milan, S. E., Lester, M., Cowley, S. W. H., Moen, J., Sandholt, P. E., and Owen, C. J., Meridian-scanning photometer, coherent HF radar, and magnetometer observations of the cusp: a case study, *Ann. Geophys.*, *17*, 159, 1999.

Milan, S.E., Lester, M., Cowley, S.W.H., and Brittnacher, M., Dayside convection and auroral morphology during an interval of Northward interplanetary magnetic field, *J. Geophys. Res.*, *105*, 15741-15755, 2000.

Milan, S. E., L. J. Baddeley, M. Lester, and N. Sato, A seasonal variation in the convection response to IMF orientation, *Geophys. Res. Lett.*, *28*, 471– 474, 2001.

Milan, S.E., Lester, M., Cowley, S.W.H., Oksavik, K., Brittnacher, M., Greenwald, R.A., Sofko, G., and Villain, J.-P., Variations in polar cap area during two substorm cycles, *Ann. Geophys.*, *21*, 1121-1140, 2003.

Milan, S. E., A simple model of the flux content of the distant magnetotail, *J. Geophys. Res.*, *109*, A07210, 2004.

Milan, S. E., Dayside and nightside contributions to the cross polar cap potential: placing an upper limit on a viscous-like interaction, *Ann. Geophys.*, *22*, 3771–3777, 2004.

Milan, S. E., Cowley, S. W. H., Lester, M., Wright, D. M., Slavin, J. A., Fillingim, M., Carlson, C. W., and Singer, H. J., Response of the magnetotail to changes in the open flux content of the magnetosphere, *J. Geophys. Res.*, *109*, A04220, 2004.

Milan, S. E., Wild, J. A., Grocott, A., and Draper, N. C., Space and ground-based investigations of solar wind-magnetosphere ionosphere coupling, *Adv. Space. Res.*, *38*, 1671-1677, 2006.

Milan, S. E., Provan, G., and Hubert, B., Magnetic flux transport in the Dungey cycle: A survey of dayside and nightside reconnection rates, *J. Geophys. Res.*, *112*, 2007.

Miura, A., Simulation of Kelvin-Helmholtz instability at the magnetospheric boundary, *J. Geophys. Res*., *92*, 3195, 1987.

Moen, J., Carlson, H. C., Milan, S. E., Shumilov, N., Lybekk, B., Sandholt, P. E., and Lester, M., On the Collocation between dayside auroral activity and coherent HF radar backscatter, *Ann. Geophys.*, *18*, 1531, 2001.

Moen, J., Walker, I. K., Kersley, L., and Milan, S. E., On the generation of cusp HF-backscatter irregularities, *J. Geophys. Res.*, *107*, 1044, 2002.

Morley, S. K., and Lockwood, M., The dependence of cusp ion signatures on the reconnection rate, *Ann. Geophys.*, *21*, 947-953, 2003.

Mukai, T., Kaya, N., Sagawa, E., Hirahara, M., Miyake, W., Obara, T., Miyaoka, H., Machida, S., Yamagishi, H., Ejiri, M., Matsumoto, H., and Itoh, T., Low energy charged particle observations in the "Auroral" Magnetosphere: First results from the Akebono (EXOS-D) satellite, *J. Geomag. Geoelectr., 42,* 479-496, 1990.

Nishida, A., and Maezawa, K., Two Basic Modes of Interaction between the Solar Wind and the Magnetosphere, *J. Geophys. Res.*, *76*, 2254-2264, 1971.

Ogilvie, K. W., and Fitsenreiter, R. J., The Kelvin-Helmholtz Instability at the Magnetopause and Inner Boundary Layer Surface, *J. Geophys. Res.*, *94*, 15,113-15,123, 1989.

Øieroset, M., Sandholt, P. E., Denig, W. F., and Cowley, S. W. H., Northward interplanetary magnetic field cusp aurora and high-latitude magnetopause reconnection, *J. Geophys. Res.*, *102,* 11349-11362, 1997.

Øieroset, M., Phan, T. D., Fujimoto, M., Lin, R. P., and Lepping, R. P., In situ detection of collisionless reconnection in the Earth's magnetotail, *Nature*, *412*, 414-417, 2001.

Øieroset, M., Phan, T. D., Fujimoto, M., Chan, L., Lin, R. P., and Skoug, R., Spatial and temporal variations of the cold dense plasma sheet: Evidence for a low-latitude boundary layer source? AGU Monograph on Earth's Low-Latitude Boundary Layer, edited by P. T. Newell and T. G. Onsager, 253, 2002.

Øieroset, M., Raeder, J., Phan, T. D., Wing, S., McFadden, J. P., Li, W., Fujimoto, M., Rème, H., and Balogh, A., Global cooling and densification of the plasma sheet during an extended period of purely Northward IMF on October 22–24, 2003, *Geophys. Res. Lett.*, *32*, L12S07, 2005.

Oksavik, K., Søraas, F., Moen, J., Pfaff, R., Davies, J. A., and Lester, M., Simultaneous optical, CUTLASS HF radar, and FAST spacecraft observations: Signatures of boundary layer processes in the cusp, *Ann. Geophys.*, *22*, 511-525, 2004.

Oksavik, K., Rouhoniemi, J. M., Greenwald, R. A., Baker, J. B. H., Moen, J., Carlson, C., Yeoman, T. K., and Lester, M., Observations of isolated polar cap patches by the European Incoherent Scatter (EISCAT) Svalbard and Super Dual Auroral Radar Network (SuperDARN) Finland radars, *J. Geophys. Res.*, *111*, 2006.

Østgaard, N., Mende., S. B., Frey, H. U., and Sigwarth, J. B., Simultaneous imaging of the reconnection spot in the opposite hemispheres during Northward IMF, *Geophys. Res. Lett.*, *32*, L21104, 2005.

Parker, E. N., Dynamics of the interplanetary gas and magnetic fields, *Astrophys. J.*, *128*, 664–676, 1958.

Parnell, C., Peeling back the Sun, *Solar Physics*, 1999.

Paschmann, G., Sckopke, N., Haerendel, G., Papamastorakis, J., Bame, S. J., Asbridge, J. R., Gosling, J. T., Hones, E. W. Jr., and Tech, E. R., ISEE Plasma Observations near the Subsolar Magnetopause, *Space Sci. Rev.*, *22*, 717-737, 1978.

Paschmann, G., Haaland, S and Treumann, R., Auroral Plasma Physics, Kluwer Academic Publishers, Space Science Series of ISSI., 2003.

Perry, C. H., Grande, M., Zurbuchen, T. H., Hefti, S., Gloeckler, G., Fennell, J. F., Wilken, B., and Fritz, T., Use of Fe charge state changes as a tracer for solar wind entry to the Magnetosphere, *Geophys. Res. Lett*., *27*, 2441-2444, 2000.

Petrinec, S. M., Trattner, K. J., and Fuselier, S. A., Steady reconnection during intervals of northward IMF: Implications for magnetosheath properties, *J. Geophys. Res.*, *108*, 1458, 2003.

Petschek, H. E., and Thorne, R. M., The Existence of Intermediate Waves in Neutral Sheets, American Astronomical Society, 1967.

Phan, T. D., Paschmann, G., Raj, A., Angelopoulos, V., Larson, D., and Lin, R. P., Wind observations of the halo/cold plasma sheet, in Substorms-4, edited by S. Kokubun and Y. Kamide, Terra Sci., Tokyo, 1998.

Phan, T. D., Lin, R. P., Fuselier, S. A., and Fujimoto, M., Wind observations of mixed magnetosheath-plasma sheet ions deep inside the magnetosphere, *J. Geophys. Res.*, *105*, 5497-5505, 2000.

Prölss, G. W., Physics of the Earth's Space Environment, Springer, 2004.

Reiff, P. H., and Burch, J. L., IMF By-dependent plasma flow and Birkeland currents in the dayside magnetosphere: 2. A global model for Northward and southward IMF, *J. Geophys. Res.*, *90*, 1595-1609, 1985.

Rème, H., Aoustin, C., Bosqued, M., Dandouras, I., and the CIS-Team, First multi-spacecraft ion measurements in and near the Earth's magnetosphere with the identical Cluster Ion Spectrometry (CIS) Experiment, *Ann. Geophys.*, *19*, 1303-1354, 2001.

Rosenbauer, H., Gronwaldt, H., Montgomery, D. M., Paschmann, G., and Sckopke, N., Heos 2 Plasma Observations in the Distant Polar Magnetosphere The Plasma Mantle, *J. Geophys. Res., 80,* 2723-2737, 1975.

Ruohoniemi, J. M., and Greenwald, R. A., Observations of IMF and seasonal effects in high-latitude convection, *Geophys. Res. Lett.*, *22*, 9, 1995.

Ruohoniemi, J. M., and Baker, K. B., Large-scale imaging of high-latitude convection with Super Dual Auroral Radar Network HF radar observations, *J. Geophys. Res.*, *103*, 20,797–20,811, 1998.

Russell, C. T., The configuration of the magnetosphere, in Critical Problems of Magnetospheric Physics, edited by E. R. Dyer, Inter-Union Comm. on Sol. Terr. Phys., Natl. Acad. of Sci., Washington, D.C., 1972.

Russell, C. T., and Elphic, R. C., Initial ISEE magnetometer results: Magnetopause observations, *Space Sci. Rev.*, *22*, 681, 1978.

Russell, C. T., and Elphic, R. C., ISEE observations of flux transfer events at the dayside magnetopause, *Geophys. Res. Lett.*, *6*, 33, 1979.

Sandholt, P. E., Farrugia, C. J., Cowley, S.W.H., Denig, W.F., Lester, M., Moen, J., and Lybekk, B., Capture of magnetosheath plasma by the magnetosphere during Northward IMF, *Geophys. Res. Lett.*, *26*, 2833-2836, 1999.

Sandholt, P. E., Farrugia, C. J., Cowley, S. W. H., Lester, M., Denig, W. F., Cerisier, J.-C., Milan, S. E., Moen, J., Trondsen, E., and Lybekk, B., Dynamic cusp aurora and associated pulsed reverse convection during northward interplanetary magnetic field, *J. Geophys. Res.*, *105*, 12869-12894, 2000.

Sckopke, N., Paschmann, G., Haerendel, G., Sonnerup, B. U. Ö., Bame, S. J., Forbes, T. G., Hones, E. W. Jr., and Russell, C. T., Structure of the Low-Latitude Boundary layer, *J. Geophys. Res.*, *86*, 2099-2110, 1981.

Siscoe, G. L., and Huang, T. S., Polar cap inflation and deflation, *Geophys. Res. Lett.*, *90*, 543–547, 1985.

Slavin, J. A., Smith, E. J., Sibeck, D. G., Baker, D. N., Zwickl, R. D., and Akasofu, S.-I., An ISEE 3 study of average and substorm conditions in the distant magnetotail, *J. Geophys. Res.*, *90*, 1985.

Slavin, J. A., Tanskanen, E. I., Hesse, M., Owen, C. J., Dunlop, M. W., Imber, S. M., Lucek, E. A., Balogh, A. and Glassmeier, K.-H., Cluster observations of traveling compression regions in the near-tail, *J. Geophys. Res.*, *110*, A06207, 2005.

Smith, C.W., Acuna, M.H., Burlaga, L.F., L'Heureux, J., Ness, N.F., Scheifele, J., The ACE Magnetic Fields Experiment, *Space Sci. Rev.*, *86*, 611-632, 1998.

Song, P., and Russell, C. T., Model of the Formation of the Low-Latitude Boundary Layer for Strongly Northward Interplanetary Magnetic Field, *J. Geophys. Res.*, *97*, 1411-1420, 1992.

Sonnerup, B. U. Ö., Magnetopause Reconnection Rate, *J. Geophys. Res.*, *79*, 1546-1549, 1974.

Spreiter, J. R., Summers, A. L., and Alksne, A. Y., Hydromagnetic flow around the magnetosphere, *Planet. Space Sci.*, *14*, 223-253, 1966.

Stone, E.C., Frandsen, A.M., Mewaldt, R.A., Christian, E.R., Margolies, D., Ormes, J.F., Snow, F., The Advanced Composition Explorer, *Space Sci. Rev.*, *86*, 1-22, 1998.

Terasawa, T., Fujimoto, M., Mukai, T., Shinohara, I., Saito, Y., Yamamoto, T., Machida, S., Kokubun, S., Lazarus, A. J., Steinberg, J., T., and Lepping, R. P., Solar Wind Control of Density and Temperature in the Near-Earth Plasma Sheet: WIND-GEOTAIL Collaboration, *Geophys. Res. Lett.*, *24*, 935-938, 1997.

Thomsen, M. F., Borovsky, J. E., and Skoug, R. M., Delivery of cold, dense plasma sheet material into the near-Earth region, *J. Geophys. Res.*, *108*, 2003.

Weimer, D. R, Ober, D. M., Maynard, N. C., Collier, M. R., McComas, D. J., Ness, N. F., Smith, C. W. and Watermann, J., Predicting interplanetary magnetic field (IMF) propagation delay times using the minimum variance technique, *J. Geophys. Res.*, *108*, 2003.

Wing, S., Newell, P. T. and Meng, C.-I., Cusp Modelling and Observations at Low Altitude, *Surveys in Geophysics*, *26*, 341-367, 2005.

Wing, S., Johnson, J. R., and Fujimoto, M., Timescale for the formation of the cold-dense plasma sheet: A case study, *Geophys. Res. Lett.*, *33*, L23106, 2006.

Woch, J. and Lundin, R., Magnetosheath plasma precipitation in the polar cusp and its control by the interplanetary magnetic field, *J. Geophys. Res.*, *97*, 1421–1430, 1992.

Wolden, C. A., The Role of Oxygen Dissociation in Plasma Enhanced Chemical Vapor Deposition of Zinc Oxide from Oxygen and Diethyl Zinc, *Plasma Chemistry and Plasma Processing*, *25*, 2005.

Zwan, B. J., and Wolf, R. A., Depletion of solar wind plasma near a planetary boundary, *J. Geophys. Res.*, *81*, 1636– 1648, 1976.